HYPERSONIC NOZZLE/AFTERBODY PERFORMANCE AT LOW MACH NUMBERS

THESIS

R. Bruce Cochran

AFIT/GAE/~~[illegible]~~/89J-2
AA

DEPARTMENT OF THE AIR FORCE
AIR UNIVERSITY
AIR FORCE INSTITUTE OF TECHNOLOGY

Wright-Patterson Air Force Base, Ohio

1

AFIT/GAE/AA/89J-2

HYPERSONIC NOZZLE/AFTERBODY PERFORMANCE AT LOW MACH NUMBERS

THESIS

R. Bruce Cochran

AFIT/GAE/[redacted]/89J-2

AA

Approved for public release; distribution unlimited

UNCLASSIFIED

SECURITY CLASSIFICATION OF THIS PAGE

REPORT DOCUMENTATION PAGE

Form Approved OMB No. 0704-0188

1a. REPORT SECURITY CLASSIFICATION Unclassified	1b. RESTRICTIVE MARKINGS
2a. SECURITY CLASSIFICATION AUTHORITY 2b. DECLASSIFICATION / DOWNGRADING SCHEDULE	3. DISTRIBUTION / AVAILABILITY OF REPORT Approved for public release; distribution unlimited
4. PERFORMING ORGANIZATION REPORT NUMBER(S) AFIT/GAE/AA/89J-2	5. MONITORING ORGANIZATION REPORT NUMBER(S)
6a. NAME OF PERFORMING ORGANIZATION School of Engineering 6b. OFFICE SYMBOL *(If applicable)* AFIT/ENG	7a. NAME OF MONITORING ORGANIZATION
6c. ADDRESS *(City, State, and ZIP Code)* Air Force Institute of Technology Wright-Patterson AFB OH 45433	7b. ADDRESS *(City, State, and ZIP Code)*
8a. NAME OF FUNDING / SPONSORING ORGANIZATION Wright Research & Development Center 8b. OFFICE SYMBOL *(If applicable)* WRDC/FI-2	9. PROCUREMENT INSTRUMENT IDENTIFICATION NUMBER
8c. ADDRESS *(City, State, and ZIP Code)* Wright-Patterson AFB OH 45433	10. SOURCE OF FUNDING NUMBERS PROGRAM ELEMENT NO. / PROJECT NO. / TASK NO. / WORK UNIT ACCESSION NO.

11. TITLE *(Include Security Classification)*

HYPERSONIC NOZZLE/AFTERBODY PERFORMANCE AT LOW MACH NUMBERS

12. PERSONAL AUTHOR(S)

R. Bruce Cochran, B.S.

13a. TYPE OF REPORT	13b. TIME COVERED	14. DATE OF REPORT *(Year, Month, Day)*	15. PAGE COUNT
Thesis	FROM ______ TO ______	1989 December	177

16. SUPPLEMENTARY NOTATION

17. COSATI CODES			18. SUBJECT TERMS *(Continue on reverse if necessary and identify by block number)*
FIELD	GROUP	SUB-GROUP	Hypersonic Propulsion, Engine-Airframe Integration, Nozzle/Afterbody Jet Effects, Boattail Drag, Base Drag

19. ABSTRACT *(Continue on reverse if necessary and identify by block number)*

The low speed performance of a generic 2-D hypersonic nozzle/afterbody configuration was studied experimentally. Wind tunnel tests were conducted at simulated flight Mach numbers of 0.6, 0.8, 1.9, and 3.0, in the Wright Research and Development Center (WRDC) Two-Foot Trisonic Gasdynamics Facility (TGF). Parametrics included four cowl configurations and simulated propulsion variations with high pressure, cold (ambient temperature) air. The exhaust flow characteristics, the pressure distributions, pressure coefficients, and pressure drags, were determined. The nozzle/afterbody exhaust flows were overexpanded for all of the configurations and conditions, and produced a pressure drag (thrust loss). The exhaust flow characteristics of the subsonic and supersonic flight Mach numbers were different. The subsonic condition resulted in higher pressure drag levels than for the supersonic conditions. The subsonic pressure drag levels increased with increasing nozzle pressure ratios (NPR), while for the supersonic conditions,

20. DISTRIBUTION / AVAILABILITY OF ABSTRACT ☒ UNCLASSIFIED/UNLIMITED ☐ SAME AS RPT ☐ DTIC USERS	21. ABSTRACT SECURITY CLASSIFICATION Unclassified
22a. NAME OF RESPONSIBLE INDIVIDUAL Paul King, Lt Col, USAF	22b. TELEPHONE *(Include Area Code)* (513)255-2362 22c. OFFICE SYMBOL AFIT/ENY

DD Form 1473, JUN 86 *Previous editions are obsolete.* SECURITY CLASSIFICATION OF THIS PAGE

UNCLASSIFIED

19. ABSTRACT (CONT'D):

the pressure drag levels were nearly constant or decreased with increasing NPR.

AFIT/GAE/AA/89J-2

HYPERSONIC NOZZLE/AFTERBODY PERFORMANCE AT LOW MACH NUMBERS

THESIS

Presented to the Faculty of the School of Engineering

of the Air Force Institute of Technology

Air University

In Partial Fulfillment of the

Requirements for the degree of

Master of Science in Aeronautical Engineering

R. Bruce Cochran, B.S.

December 1989

Approved for public release; distribution unlimited

Acknowledgements

I would like to express my sincere gratitude for the assistance I received during this investigation. I especially would like to thank my advisor, Lt Col P. King, for his advice and guidance. I would also like to acknowledge my faculty committee members, Dr W. Elrod and Capt D. Fant, and my sponsor, Mr D. Stava, WRDC/FI-2, for their support.

I owe a special debt of gratitude for the support from WRDC/FIM for the planning, setup, and the conducting of my test in the Trisonic Gasdynamics Facility. I owe a special thanks to Capt B. Hart and Mr G. Gustafson of FIMM, and to Mr G. Dale and Mr G. Williams of FIMN. I also would like to thank Mr T. Hancock and the AFIT Model Shop for the fabrication of my nozzle/afterbody.

Finally, I would like to express my deepest appreciation to my wife, Kathy, for her patience, understanding, and support during my program at AFIT.

Table of Contents

List of Figures

Figure		Page

Figure		Page

Figure		Page

List of Tables

Nomenclature

Symbol

A	Area (in^2)
A_{ref}	Reference Area (A_{ref} = 7.84 in^2)
C_p	Pressure Coefficient, $C_p = \frac{P - P_o}{Q_o}$
CDP	Pressure Drag Coefficient (pressure integration, based on A_{ref})
M	Mach
NPR	Nozzle Pressure Ratio (P_{Tn}/P_o)
PN	Part Number
P_o	Free-Stream Static Pressure (psf)
P_{Tn}	Total Pressure of Nozzle Exhaust (psf)
P_{To}	Free-Stream Total Pressure (psf)
P_i	Local Pressure At Probe (psf)
TPN	Test Point Number
Q_o	Dynamic pressure
Re	Reynolds Number

Subscripts

e	Afterbody Exit
i	Local Tap Location
n	Nozzle Cowl Exit
o	Free-Stream
t	Nozzle Throat

Cowl Configurations

BL	Baseline Cowl Configuration (no cowl), PN=11
L	Long Cowl Configuration (straight 0.5 in. cowl), PN=12
+5	Positive 5 degree Configuration (0.5 degree cowl), PN=13
-5	Negative 5 degree Configuration (-5 degree cowl), PN=14

Abstract

The low speed performance of a generic 2-D hypersonic nozzle/afterbody configuration was studied experimentally. Wind tunnel tests were conducted at simulated flight Mach numbers of 0.6, 0.8, 1.9, and 3.0, in the Wright Research and Development Center (WRDC) Two-Foot Trisonic Gasdynamics Facility (TGF). Parametrics included four cowl configurations and simulated propulsion variations with high pressure, cold (ambient temperature) air. The exhaust flow characteristics, the pressure distributions, pressure coefficients, and pressure drags, were determined. The nozzle/afterbody exhaust flows were overexpanded for all of the configurations and conditions, and produced a pressure drag (thrust loss). The exhaust flow characteristics of the subsonic and supersonic flight Mach numbers were different. The subsonic condition resulted in higher pressure drag levels than for the supersonic conditions. The subsonic pressure drag levels increased with increasing nozzle pressure ratios (NPR), while for the supersonic conditions, the pressure drag levels were nearly constant or decreased with increasing NPR.

HYPERSONIC NOZZLE/AFTERBODY PERFORMANCE AT LOW MACH NUMBERS

1.0 Introduction

Background

The propulsion system for an airbreathing vehicle that operates over a wide Mach number range, subsonic to hypersonic speeds, must be highly integrated into the airframe. The National Aero-Space Plane, as described in Reference 1, will take off from a runway, accelerate up to 25 times the speed of sound attaining low earth orbit or hypersonic cruise, and descend and land in a conventional manner. This type of vehicle must be designed for hypersonic Mach numbers (on-design) and operate efficiently at these high speeds. The entire flight envelope, however, must be addressed for optimized vehicle performance. A vehicle design for efficient hypersonic speeds may have poor performance at low speed, off-design conditions.

The most promising design concept for hypersonic speeds is an airframe-integrated supersonic combustion ramjet (scramjet) which blends aircraft forebody and afterbody functions in combination with the engine (combustors) modules (2:39). The entire undersurface of the vehicle is part of the propulsion system resulting in lower aerodynamic drag and higher installed specific impulse, as compared to an axisymmetric pod-mounted design (3:2). Figure 1 is a schematic of an integrated hypersonic vehicle propulsion system. The propulsion system-airframe integration deals

with the first-order interactions between the engine and the vehicle's forebody and afterbody (4:38). The forebody is part of the inlet compression system of the engine airflow and the afterbody is a continuation of the nozzle and is the expansion surface for the engine exhaust.

At hypersonic speeds the performance of a scramjet is considerably improved compared to the performance of a subsonic combustion ramjet. As stated in Reference 5, when the combustion process is allowed to occur supersonically, the amount of inlet diffusion is reduced with an accompanying increase in total pressure recovery (total pressure at the combustor entrance divided by the free-stream total pressure). This results in lower static temperatures, with a reduction of the dissociation losses (5:1-2). The vehicle must use a combined propulsion system concept (turbojet-ramjet-scramjet) to cover all of the speed regimes. A scramjet is not efficient at low speeds ($M < 5$), and neither the scramjet nor ramjet can produce static thrust (6:1). Therefore, a low speed propulsion system must be used for low speed flight.

The hypersonic propulsion system operates at extremely high pressure ratios (scramjet total pressure divided by ambient pressure) at hypersonic speeds. The nozzle/ afterbody geometry is very important to extracting thrust from the exhaust plume (7:1). A large nozzle/afterbody area ratio (projected axial area of the nozzle/afterbody divided by the nozzle throat area, A_e/A_t), is required to expand the

nozzle exhaust and maximize the scramjet thrust. For hypersonic speeds, the exhaust flow is generally underexpanded, and exerts high pressures on the afterbody, which translates into additional thrust (7:1). At subsonic and low supersonic Mach numbers, the nozzle/afterbody is operating at an extremely overexpanded condition, and the pressures on the afterbody are below ambient pressure. Therefore, the afterbody behaves as a base region and contributes a significant pressure drag component (boattail drag). This investigation addresses the nozzle/afterbody integration of the hypersonic propulsion system at low speed, off-design conditions between Mach numbers of 0.6 to 3.0.

Problem

The low speed, off-design performance of the hypersonic vehicle will impact the size, weight, and performance of the vehicle by determining the required size of the low speed propulsion system required for acceptable acceleration characteristics (6:2). The low speed nozzle performance must be understood to optimize the vehicle performance throughout the flight envelope. The objective of this investigation was to examine the low speed, off-design exhaust flow and base drag characteristics of a generic hypersonic afterbody.

Scope

An experimental investigation was conducted in the Wright Research and Development Center (WRDC) Two-Foot

Trisonic Gasdynamics Facility (TGF), 10 February through 6 March 1989. The test was conducted on an isolated nozzle/afterbody model at zero degrees angle of attack, at Mach numbers ranging from 0.6 to 3.0, and Reynolds numbers based on model length of 2.0 million and 4.0 million. High pressure cold (ambient temperature) air was used to simulate the jet exhaust at various nozzle pressure ratios (NPR, total pressure of the exhaust divided by tunnel static pressure). Four nozzle cowl variations were tested. Nozzle/afterbody ramp surface pressures were measured at desired NPR. The magnitude of these afterbody ramp pressures were used to determine the base drag.

High pressure air at ambient temperatures was used to simulate the engine exhaust flow. As stated in Reference 8, high pressure cold air at the correct nozzle pressure ratio is generally used to represent the nozzle flow for nozzle/afterbody testing. It would be desirable to simulate the gas properties of the exhaust flow, the high temperature, or the lower ratio of specific heats, but this adds complexity to the test and the TGF does not have this capability. The effects of the engine combustion products, however, must be addressed in the nozzle/afterbody design. An understanding of the overexpanding exhaust flow characteristics over the nozzle/afterbody was obtained with cold flow simulation.

Approach and Presentation

A generic hypersonic nozzle was designed, fabricated, and tested. This thesis describes the test facility, the experimental hardware, and instrumentation (Chapter 2.0), the experimental and data reduction procedures (Chapter 3.0), the experimental results and discussion (Chapter 4.0), and the conclusions and recommendations (Chapter 5.0).

2.0 Apparatus

Test Facility

The Trisonic Gasdynamics Facility (TGF) is a closed circuit, continuous flow, variable density wind tunnel, capable of operating at subsonic, transonic, and supersonic speeds. The subsonic test section has a Mach number range of 0.23 to 0.85. Supersonic Mach numbers of 1.5, 1.9, 2.3, and 3.0 are obtained by installing fixed area ratio nozzles just ahead of the test section. The maximum subsonic Reynolds number is 2.5 million per foot and the maximum subsonic dynamic pressure is 350 psf. The maximum supersonic Reynolds number is 5.0 million per foot and the maximum supersonic dynamic pressure is 1000 psf. The stagnation temperature is maintained at approximately 100 degrees F. The test section of the TGF is two feet square. The TGF Users Manual, Reference 9, contains additional information about the tunnel, its capabilities, and operating characteristics.

Experimental Hardware

The generic hypersonic nozzle/afterbody was attached to a square forebody (cross section) with a 15 degree half-angle conical nose section which was faired into the square forebody. Figure 2 is a photograph of the model installed in the TGF. The model was strut supported and was attached to the tunnel floor by a single cantilever blade support system. A diagram of the hypersonic nozzle/afterbody model and support

strut is presented in Figure 3. The strut had a sweep angle of 31 degrees aft. The hypersonic nozzle/afterbody was mounted inverted to minimize strut interference. The conical nose section had a sharp nosepiece for supersonic testing and a round nosepiece for subsonic testing. The model lengths are 23.33 inches and 22.16 inches for the supersonic and subsonic configurations, respectively. High pressure air for the nozzle exhaust simulation was ducted to the model through the strut and the inner core of the forebody where the flow conditioning devices, flow straightener/choke plates, were located. The nozzle/afterbody instrumentation was also routed in the strut and forebody.

The quasi 2-D hypersonic nozzle/afterbody was designed to be representative of the external geometry of a hypersonic vehicle. The design was based on configurations described in Reference 3. Figure 4 is a three-view drawing of the nozzle/afterbody with the pertinent dimensions. The nozzle/afterbody had a straight 20 degree expansion ramp and a nozzle expansion area ratio (projected axial area of the nozzle/afterbody divided by the nozzle throat area, A_e/A_t) of approximately 6.2. The internal nozzle was convergent and, because of design length constraints (sized to keep the afterbody ramp region free of reflected shock waves at Mach 1.9), and to facilitate fabrication , resulted in a 50 degree straight convergent ramp. The nozzle/afterbody had a sharp corner at the nozzle throat to make the performance independent of throat radius. The throat was the nozzle

exit for the baseline nozzle. To determine the effects of the nozzle lower cowl four different cowl configurations were tested: the baseline (BL, no extended cowl), the long (L, 0.5 in. straight extension), the positive 5 degree (+5, 0.5 in. extension angled 5 degrees towards the nozzle centerline), and the negative 5 degree (-5, 0.5 in. extension angled 5 degrees away from the nozzle centerline). Photographs of the cowls installed on the model are shown in Figures 5a-5d. The cowls have quasi internal expansion area ratios (A_n/A_t) of 1.0, 1.4, 1.3, and 1.5, respectively. The extended cowls do not have sidewalls, which allow the nozzle exhaust flow to expand into the external flow, downstream of the nozzle throat. The cowls were 0.125 inches thick with trailing edges that were squared-off blunt.

Instrumentation

The primary instrumentation for this investigation measured the external nozzle ramp static pressures. There were 61 static pressure taps located on the afterbody expansion ramp and 10 located on the internal convergent ramp. Tap locations are shown in Figure 4, and in Tables 1a and 1b, for the nozzle/afterbody left and right sides, respectively. Sixteen (16) pressure taps were located along the centerline of the external ramp. Pressure taps distributed across the external and internal ramps were used to determine the lateral pressure variance. Figure 6 is a photograph of the nozzle/afterbody pressure instrumentation (tygon) tubing and shows the interior design of the

nozzle/afterbody ramps. In addition to the surface pressure measurements, internal nozzle flow pressures were measured with a five probe total pressure rake. The rake location was 3.25 inches upstream of the nozzle throat (Figure 3). The nozzle flow total pressure (P_{Tn}) equals the average of these five probes.

Standard facility instrumentation was used to measure the pressures. Reference 10 contains information as to the facility measuring devices. Five multiport scanivalves were used to measure the static pressures on the ramps (internal and external). The five internal nozzle total pressure probes were plumbed to individual transducers. The measurement uncertainties of the sensors used are presented in Table 2.

3.0 Procedures

Experimental Procedures

Ramp pressure distributions were obtained over a range of nozzle pressure ratios (NPR) for each Mach number, cowl configuration, and Reynolds number tested. The NPR is the nozzle exhaust flow total pressure divided by the tunnel static pressure. Test conditions are listed in Table 3 and plotted in Figure 7. Included in Table 3 are the test point numbers (TPN) for each Mach number, cowl configuration, and NPR tested.

The ranges of NPR vary for the subsonic and supersonic Mach numbers. This variation occurs because of the constant pressure air supply for the nozzle exhaust flow and the variation of tunnel static pressures with Mach numbers. The NPR tested covers the expected flight conditions.

For each test configuration, the tunnel flow conditions (Mach and Reynolds numbers) were established, and the nozzle exhaust flow-off data were obtained. The high pressure air was then established through the model and nozzle exhaust flow set to the desired NPR. Data were obtained at each NPR. Data acquisition time, for a test point, was approximately one minute. The five multiport scanivalves, used for the nozzle/afterbody static pressure measurements, were set at three seconds per step (measurement reading) and 18 steps were required. For each test point the tunnel and nozzle flow parameters were recorded during a scanivalve reading and used for the data reduction. A significant

variation of a test parameter invalidated the data. Repeats of test points were conducted throughout the test to determine data repeatability.

Data Reduction

The net thrust of an airbreather is the difference between the nozzle gross thrust and the inlet ram drag. To determine the net propulsive force (installed thrust), one must account for the installation effects. These installation effects include the inlet spillage drag and the nozzle/afterbody drag. As stated in Reference 11, to completely account for all the (thrust) forces, an additional force must be included in the net thrust equation. This pressure force is the difference in the base pressure of the hypersonic vehicle and the free-stream static pressure (11:16). This can result in a thrust increment and increase the net thrust, or a drag increment and decrease the net thrust.

The main performance parameter for the test was the nozzle/afterbody pressure drag force, which was calculated in dimensionless form as the pressure drag coefficient (CDP). CDP was calculated from the integrated (summed) external ramp pressure coefficients, C_p, by assigning an appropriate area to each pressure tap location and resolving the area into the projected axial component. Thus, the

nozzle/afterbody base pressure drag coefficient becomes

$$CDP = -\frac{1}{(2.0*A_{ref})} \sum_{i=X}^{L} (C_{p_i} + C_{p_{i+1}}) A_i \tag{1}$$

where A_{ref} is the reference cross sectional area (7.84 in^2), and i refers to the conditions at the local static pressure taps. The A_i term is the projected axial area between the two adjacent pressure taps (i.e., summing over the average pressures on this projected area). The C_{p_i} term is calculated from the locally measured static pressure (P_i) using the following relationship

$$C_{p_i} = \frac{P_i - P_o}{Q_o} \tag{2}$$

where P_o and Q_o are the tunnel test section static and dynamic pressures, respectively.

For this investigation, the centerline pressures were used to calculate the pressure drag coefficient calculation (as stated, the off centerline pressures were used to determine the lateral variation of the flow). The centerline pressure were used because of the higher density of pressure taps which characterized the nozzle exhaust flow and the afterbody ramp pressures more accurately (as compared to using the less dense off centerline taps). The centerline pressures were also used for the test parameters (Mach, cowl, and NPR) data comparisons.

When the pressure tap measurement is below the tunnel

static pressure, the result is a suction force, or a drag increment. Conversely, if the pressure is above the tunnel static pressure, the result is a push, or a thrust increment.

4.0 Experimental Results and Discussion

General

The hypersonic nozzle exhaust flow, for all test conditions, was dominated by an initial overexpansion of the flow downstream of the nozzle throat. Overexpansion occurs when the static pressure of the flow expands below the tunnel static pressure. The sudden increase in exhaust flow area of the (diverging) afterbody expansion ramp and the effect of the sharp corner at the throat (possible flow separation) caused the flow to quickly overexpand to a low pressure. This low pressure (0.25 inches downstream of the throat) was the minimum pressure obtained on the ramp for the subsonic Mach numbers. The recompression characteristic, after this overexpansion, varied for the test parameters: Mach number, cowl configuration, nozzle pressure ratio, and Reynolds number. The overexpansion and recompression characteristics are similar to those reported in References 6 and 12.

The nozzle exhaust static pressure distribution of the afterbody ramp are presented (in the appendices) for an assumed Mach number and nozzle pressure ratio (NPR) schedule. These static pressure distributions are representative of the characteristics and trends of the entire NPR ranges tested (exhaust off to maximum). The NPR schedule was 2.0, 3.0, 7.0, and 16.0, for the Mach numbers 0.6, 0.8, 1.9, and 3.0, respectively, and is depicted in Figure 7. This NPR schedule is representative of a generic

flight path. The external ramp pressure distributions, for each cowl configuration, are presented in Appendix A. Presented in Appendix A are the ramp pressure coefficient (C_p) contours which show that the exhaust flow is symmetric about the centerline of the ramp. Because of the symmetry of the nozzle exhaust flow, only the data from the "left hand side" (i.e., left of the centerline) of the afterbody ramp will be presented. The nozzle/afterbody ramp left hand side pressure coefficient (C_p) plots and pressure ratio (P_i/P_{Tn}) plots, for the NPR schedule, are presented in Appendices B and C, respectively. The lateral variations of the nozzle/afterbody ramp pressures of the exhaust flow are shown in these three appendices.

<u>Reynolds Number Effects</u>

A Reynolds number effect on the nozzle/afterbody ramp pressure distributions was minimal (no significant changes in pressure distribution at different test Reynolds numbers). The Reynolds number tested were 2 million and 4 million based on model length. The Reynolds number comparison plots for the assumed NPR schedule are presented in Appendix D. The ramp centerline pressure coefficient distributions were compared when a test configuration match was obtained. Only a limited number of test points were obtained at a Reynolds number of 2 million for the supersonic Mach numbers. As stated in Reference 12, a Reynolds number variation of 7 million to 17 million based on model length, did not result in a Reynolds number effect.

Reference 12 configuration was a generic hypersonic vehicle with a 20 degree conically shaped afterbody, tested at Mach numbers of 0.6 to 1.4, with simulated exhaust flow (ambient temperature air). Data analyses for this investigation focuses on the Reynolds number of 4 million.

Pressure Drag Coefficient

The afterbody/nozzle pressure drag coefficient, CDP, was selected as the primary parameter to determine the effects of Mach number, cowl configuration, and nozzle pressure ratio on the afterbody ramp performance. Table 4 presents the CDP for the nozzle pressure ratios tested (including repeats). As stated in Chapter 3.0, the CDP coefficient was calculated from a pressure area integration of the centerline pressure distribution. As expected, the nozzle exhaust flow for all test conditions was overexpanded and resulted in pressure drag on the ramp.

The effects of Mach number on CDP are presented in Figures 8a-d (CDP versus NPR plots) for the BL, L, +5, and -5, cowl configurations, respectively. The pressure drag coefficients, for subsonic and supersonic conditions, are different in magnitudes and follow different trends. The subsonic Mach numbers produced larger pressure drag coefficients than the supersonic flow conditions. For the subsonic Mach numbers, the data are very similar and approximately equal in magnitudes (except for NPR=1.0). The data at the subsonic Mach numbers follow a trend of a steep increase in CDP with an increase in NPR. The CDP decreased

for Mach 0.8, high NPR condition (greater than 5.0) for all cowl configurations except for the baseline. The data at the supersonic Mach numbers follow a trend of a nearly constant (flat) or nearly linear decrease in CDP with increasing NPR (NPR greater than 5.0 for the baseline, Mach number 1.9 condition). However, the CDP for Mach 1.9 is approximately twice that of Mach 3.0 throughout.

The effects of the cowl configurations on CDP are presented in Figures 9a-d (CDP versus NPR plots) at Mach numbers of 0.6, 0.8, 1.9, and 3.0, respectively. Subsonically and supersonically, the CDP levels are similar, up to NPR levels of 2.0 and 5.0, respectively, but at greater NPR conditions, the CDP levels vary. The figures show that the +5 degree cowl configuration resulted in the lowest pressure drag for all Mach numbers. Supersonically, the BL cowl configuration had the highest pressure drag. At Mach 0.6 the -5 degree cowl configuration had the highest pressure drag, while at Mach 0.8 the higher pressure drag was the BL or the -5 degree cowl configurations, depending on the NPR. The effects of Mach number, cowl configuration, and nozzle pressure ratio on the afterbody ramp pressure distribution characteristics (and hence, the pressure drag coefficient characteristics) are presented in the following sections.

<u>Mach Number Effects</u>

The different characteristics of the subsonic and supersonic pressure drag coefficients resulted from the

different pressure distribution characteristics. The Mach number effects on the pressure coefficient distributions are presented in Figures 10a-e (C_p versus model station plots) at specific NPR for the baseline (BL) cowl configuration. In these figures the cross-sectional shape of the nozzle/afterbody is shown above the pressure coefficient data to show the relative position of the data with respect to the afterbody ramp. Data for the other cowl configurations are presented in Appendix E. Data for the subsonic conditions (Mach numbers 0.6 and 0.8), Figure 10a (NPR approximately equal to one, flow off), the (external) flow overexpands to the same negative C_p and the recompression begins at the same location. The data at Mach number 0.6 has a higher rate of recompression and compresses to a higher C_p, than for the Mach 0.8 condition. Data for the supersonic conditions, Mach numbers 1.9 and 3.0, the (external) flow overexpands to approximately one-half and one-quarter, respectively, of the C_p obtained subsonically. For these supersonic conditions the pressure distributions appear nearly flat. The Mach 1.9 recovers (recompresses to near ambient conditions) at the last probe location, while the Mach 3.0 condition does not recompress (flat pressure distribution).

For the NPR 3.0 and 5.0, Figures 10b and 10c show for the subsonic conditions that the exhaust overexpands to a much lower pressure (more negative) C_p. The Mach number 0.6 flow expands to a lower C_p than for Mach number 0.8, but

continues to have a higher rate of compression and compresses to a higher C_p. Figure 10c (NPR=5) shows the pressures starting to fluctuate on the afterbody ramp, with the nozzle exhaust flow having regions of compression and expansion. The effect is shown more clearly in the other cowl configurations (Appendix E). The pressure coefficients for the supersonic Mach numbers do not show these large changes in C_p with NPR. However, the Mach number 1.9 C_p distribution shows some recompression characteristics, but, the exhaust flow does not recover to ambient. The Mach 3.0 C_p distributions are nearly flat.

For Figures 10d and 10e, nozzle pressure ratios of 7.0 and 12, respectively, the pressure distribution characteristics for these supersonic Mach numbers are similar the supersonic pressure distributions above. For the Mach number 1.9 pressure distributions, both figures show an initial compression of the exhaust flow downstream of the throat. The exhaust flow then expands (to a lower pressure than that initially encountered) and then recompresses, but not to ambient. The pressure distribution for the Mach number 3.0 condition (Figure 10e) shows the compression downstream of the throat, the reexpansion, and then the recompression. These (subsonic and supersonic) Mach number characteristics are shown more clearly in the Appendix E, for the other cowl configurations.

The above pressure distribution characteristics determine the pressure drag characteristics shown in the CDP

plots. These characteristics of the lower pressures and corresponding higher CDP for the subsonic Mach numbers, and the higher pressures and corresponding lower CDP of the supersonic Mach numbers. Stated in Reference 13, the effect of flow separation is an increase of the thrust above that of an overexpanded condition that the flow does not separate, but continues the expansion to lower pressures. The nozzle exhaust flow for the supersonic Mach numbers appears to separate so the flow does not continue to expand to lower pressures, while the characteristic of the subsonic Mach numbers of the flow significantly overexpanding to low pressures and resulting in the higher CDP.

Schlieren photographs are presented in Figure 11a-d, for the baseline (BL) cowl at the assumed NPR schedule. Pictures for the other cowl configurations are presented in Appendix F. For the subsonic Mach numbers (Figures 11a and 11b) the nozzle exhaust flow overexpansion regions (light regions), the compression regions (dark regions), and the plume boundary can be seen. The schlieren photos for the supersonic Mach numbers are presented in Figures 11c and 11d, for Mach numbers 1.9 and 3.0, respectively. The plume shock (external exhaust shock), the plume flow boundary, and the shocks in the jet plume flow can be seen. The expanding nozzle exhaust plume turns the supersonic external flow which forms a shock. The oblique shock angles from vary 45 to 35 degrees, for the Mach 1.9 and 3.0, respectively. This angle changes considerably with cowl and NPR (see Appendix F).

The nozzle exhaust (plume) overexpands and shocks are formed in the exhaust flow. Exhaust flow expanding from the model side at the cowl exit can be observed in the photos. Figure 12 is a diagram of the overexpanded nozzle exhaust flow at supersonic Mach numbers.

The nozzle exhaust flow and the interactions with the external flow are different for subsonic and supersonic conditions. As discussed in Reference 14, for the subsonic flow conditions, the nozzle plume boundary is a constant pressure boundary, and after the exhaust flow overexpands it reflects off the boundary as compression waves (the waves reflecting off the boundary are reflected in the opposite sense), and results in the fluctuating underexpansions and overexpansions that occur as the pressure attempts to reach to ambient. At supersonic speeds, the pressure is no longer constant, as the plume shock increases the local pressure. The exhaust flow overexpands and the expansion waves interact with the plume boundary which helps turn the exhaust flow in the free-stream direction (14:3). The exhaust flow will adjust to (near) ambient conditions very quickly, normally within one shock cell (14:3). For the tested nozzle/afterbody configuration, the nozzle exhaust flow overexpands and then the supersonic flow is turned by the afterbody ramp and by the separation (bubble) near the throat. A shock forms and causes the recompression downstream of the throat. This recompression is shown in the nozzle cowl and NPR effects plots (below).

Nozzle Cowl Effects

The nozzle cowl configuration effects are presented in Figures 13a-d for the assumed NPR schedule and the respective Mach numbers. The other NPR nozzle cowl effects plots, for the Mach numbers and NPR ranges tested, are presented in Appendix G (with similar trends). The Mach number of 0.6 (NPR = 2.0) data are shown in Figure 13a, all pressure distributions for the cowl configurations were similar, hence, similar CDP values (Figure 9a). In Figure 13b, the Mach number of 0.8 (NPR = 3.0) data, the cowl configurations produced different initial expansion and compression characteristics of the exhaust flow, hence, different CDP values. The +5 cowl configuration had nearly the lowest initial pressure but the highest rate of compression followed by the L cowl configuration (the lowest initial pressure). The other two cowl configurations have similar (more gradual) compressions, with the BL cowl at the highest initial pressure and recovering to the higher pressures. From the Mach 0.8 CDP plot (Figure 9b), the highest to lowest drags are the -5, L, BL, and +5 cowl configurations, respectively.

The supersonic Mach numbers pressure distributions presented in Figures 13c and d (NPR of 7.0 and 16.0), for Mach numbers 1.9 and 3.0, respectively, clearly shows the characteristics of the pressure rise downstream of the nozzle throat. For the Mach 1.9 condition, this exhaust flow initial compression (highest to lowest pressures

obtained) for the cowl configurations are +5, L, -5, and BL. The flow then expands and recompresses. The recompression characteristics varied for the cowl configurations (nearly in the reverse order of the initial compression). From the Mach 1.9 CDP plot (Figure 9c), the highest to lowest drags for the cowl configurations are BL, -5, L, and +5, respectively.

For the Mach 3.0 condition, the initial compression (highest to lowest pressure) for the cowl configurations are, +5, L, and BL. The exhaust flow expansion characteristics are similar and result in nearly the same (negative) C_p, and appears to separate without any recompression. The CDP are in the reverse order of the initial compression (Figure 9d).

Nozzle NPR Effects

The NPR effects, for the baseline (BL) cowl configuration are presented in Figure 14a-d, for Mach numbers 0.6, 0.8, 1.9, and 3.0, respectively. The other cowl configurations are presented in Appendix H. The subsonic Mach number characteristics of the lower pressure (more overexpansion) for the increasing nozzle pressure ratios are clearly shown in Figures 14a and b, for the Mach numbers 0.6 and 0.8 conditions, respectively. The supersonic Mach number characteristics of the higher pressures of the initial compression for the increasing nozzle pressure ratios are clearly presented in Figures 14c and d, for Mach numbers 1.9 and 3.0 conditions, respectively.

5.0 Conclusions and Recommendations

Conclusions

The low speed performance of the tested generic hypersonic nozzle/afterbody was poor at the low speed, off-design conditions. The nozzle/afterbody exhaust flow was overexpanded for all tested configurations and conditions, and resulted in pressure drag (thrust loss).

The nozzle exhaust flow pressure distributions were symmetric about the centerline of the nozzle.

There was not a Reynolds number effect for the Reynolds numbers tested.

The flow characteristics were different for the subsonic and supersonic conditions. The supersonic Mach numbers performance was better (lower pressure drag) than the subsonic conditions. The subsonic pressure drag coefficients increased with increasing nozzle pressure ratios, while the supersonic pressure drag coefficients were constant or decreased with increasing nozzle pressure ratios.

The +5 degree cowl (straight, 0.5 inch. cowl angled 5 degrees toward the nozzle centerline) produced the lowest drag while the BL (baseline, no cowl) or -5 cowl (straight, 0.5 inch. cowl angled 5 degrees away from the nozzle centerline) produced the most drag (depending on NPR and Mach number).

The overexpansion (low pressure) region of the ramp for the subsonic Mach number conditions increased with

increasing NPR, while for the supersonic Mach number conditions the low pressure region decreased with increasing NPR.

The exhaust flow for the supersonic Mach number conditions appeared separated over portions of the ramp.

The performance characteristics of the nozzle are geometry dependent and may be the result of the severe convergent ramp and the sharp corner at the throat.

Recommendations

The testing of a more contoured ramp may improve the low speed, off-design, performance characteristics of a hypersonic nozzle/afterbody. The flow characteristics may be very geometry dependent, and the severe turn and sharp corner at the throat may be responsible for the low performance.

Because the performance is so poor, there is a need to test drag reduction devices (e.g., more variable geometry, mass addition, etc.), which may improve performance at these low speed, off-design conditions.

The nozzle exhaust flow should be measured (in-stream), using intrusive (pitot probes) and nonintrusive (laser velocimetry) methods.

A balance should be used to measure the nozzle/afterbody forces to obtain both nozzle thrust and drag, and represent the aeropropulsive characteristics of the nozzle/afterbody combination.

There is a need to examine the effects of a more representative exhaust products: the high temperature and the (variable) ratio of specific heats.

A comparison of the ramp test data with numerical methods should be done. This comparison could be used to calibrate/validate the numerical code, which then could be used as a nozzle/afterbody design tool.

References

1. Williams, R. M., "National Aero-Space Plane: Technology for America's Future," Aerospace America, Vol. 24, No. 11, November 1986, pp. 18-22.

2. Jones, R. A. and Huber, P.W., "Airframe-Integrated Propulsion System for Hypersonic Cruise Vehicles," Recent Advances in Structures for Hypersonic Flight, NASA CR 2065 Part 1, September 1978.

3. Small, W. J., Weidner, J. P., and Johnston, P. J., Scramjet Nozzle Design and Analysis as Applied to a Highly Integrated Hypersonic Research Airplane, NASA TN D-8334, November 1976.

4. Anderson, G. Y., Bencze, D. P., and Sanders, B. W., "Ground Tests Confirm the Promise of Hypersonic Propulsion," Aerospace America., Vol. 25, No. 9, September 1977, pp. 38-42.

5. Curran, E. T. and Stull, F.D., "The Potential Performance of the Supersonic Combustion Ramjet Engine," ASD-TDR-63-336, May 1963.

6. Cubbage, James M. and Mercer, Charles E. Investigation of Effect of Propulsion System Installation and Operation On Airbreathing Hypersonic Airplane At Mach 0.3 to 1.2, NASA TN D-8503, July 1977.

7. Edwards, T., "The Effect of Exhaust Plume/Afterbody Interaction on Installed Scramjet Performance," AIAA 89-0032, January 1989.

8. Bowers, D. l. AND Tamplin, G. "Throttle-Dependent Forces," Thrust and Drag: Its Prediction and Verification, edited by E.E. Covert et al., Vol. 98, AIAA, Inc., 1985, pp. 207-280.

9. Clark, G. F., "Trisonic Gasdynamics Facility User's Manual," AFWAL-TM-82-176-FIMM, April 1982.

10. Gwuton. R. W., "TGF Instrumentation Manual," Unpublished Internal Document, AFWAL/FIMM, 1982.

11. Walters, M. H., Turbojet Ramjet Propulsion System For All-Body Hypersonic Aircraft, NASA TN D-5993, January 1971.

12. Novak, C. J. and Cornelius, K. C., "Investigations of Low-Speed Nozzle/Afterbody Performance for a Generic Hypersonic Configuration," AIAA 88-0196, January 1988.

13. Sutton, G. P. and Ross D. M., Rocket Propulsion Elements, 4th edition, John Wiley & Sons, 1976, p. 71.

14. Hsu, A. T. and Liou, M.S., "A Computational Analysis of Under-Expanded Jets in the Hypersonic Regine," AIAA 88-4361, 1988.

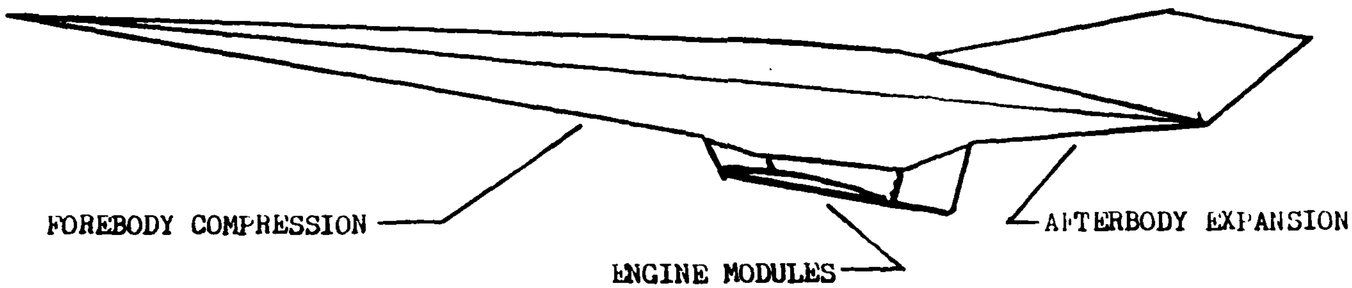

Figure 1. Schematic Representation of an Integrated Hypersonic Propulsion System

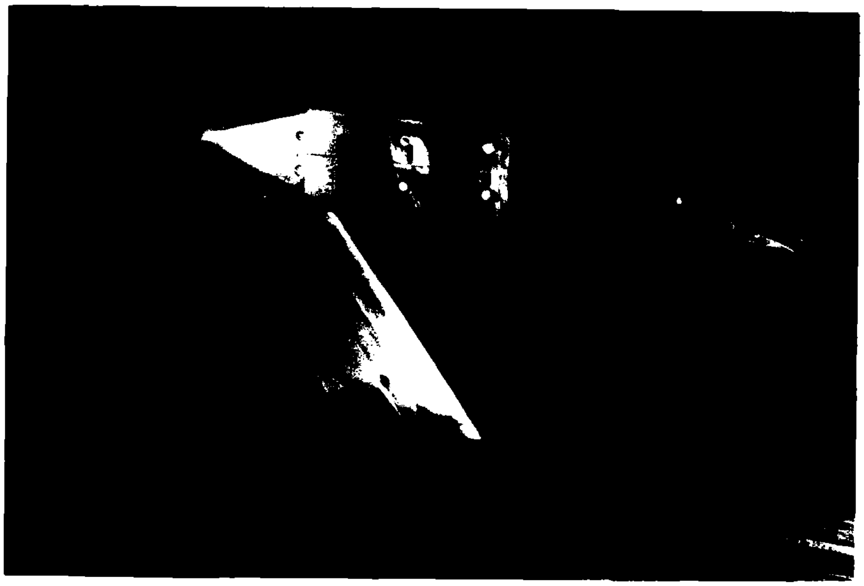

Figure 2. Hypersonic Nozzle/Afterbody Model Installed in the TGF

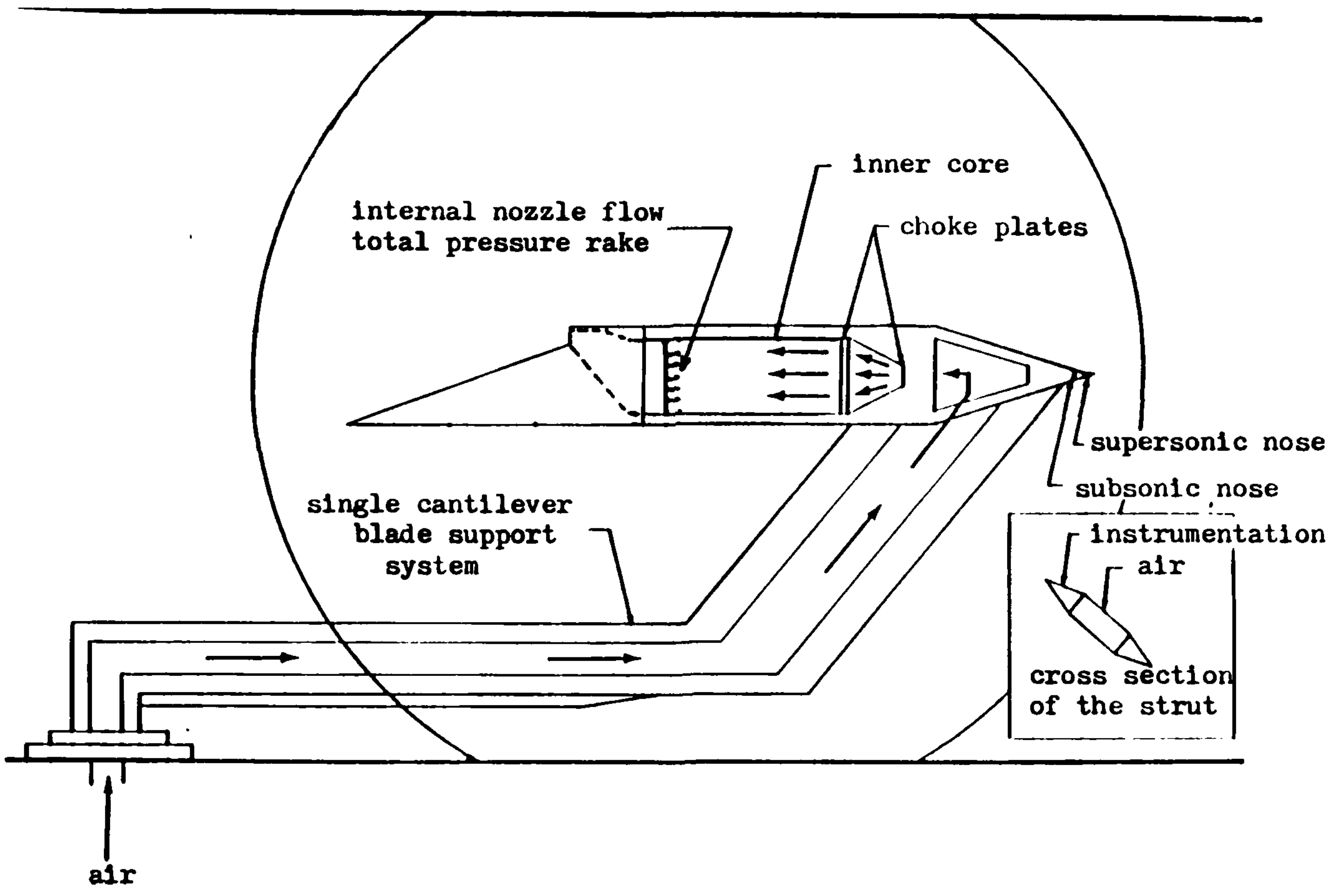

Figure 3. Diagram of the Hypersonic Nozzle/Afterbody Model and Support Strut

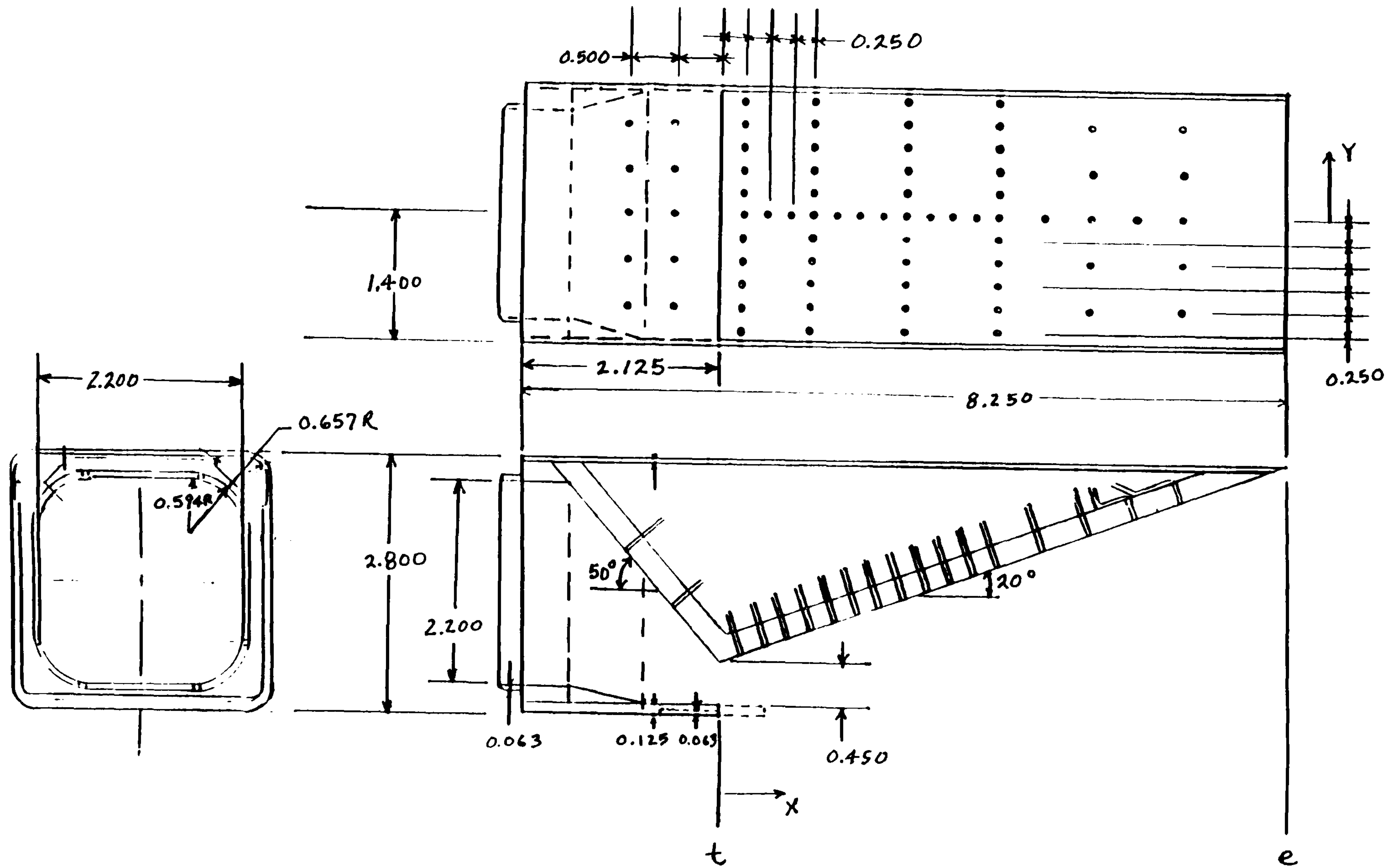

Figure 4. Hypersonic Nozzle/Afterbody Including Dimensions and Pressure Tap Locations

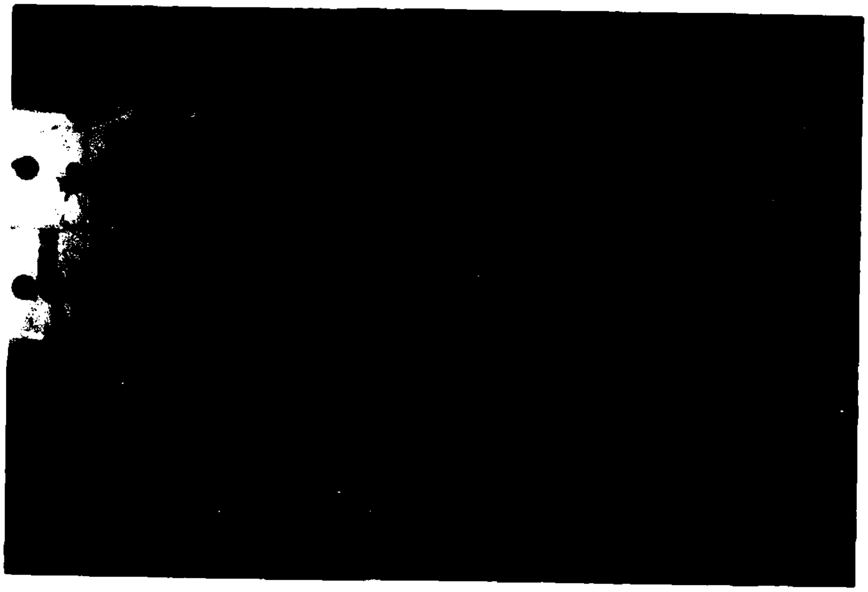

Figure 5a. Baseline (BL) Cowl Configuration

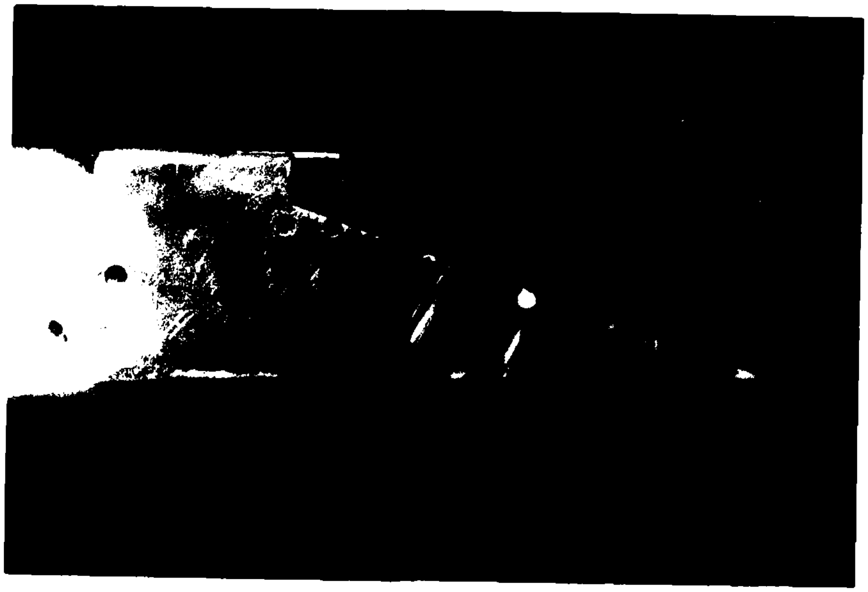

Figure 5b. Long (L) Cowl Configuration

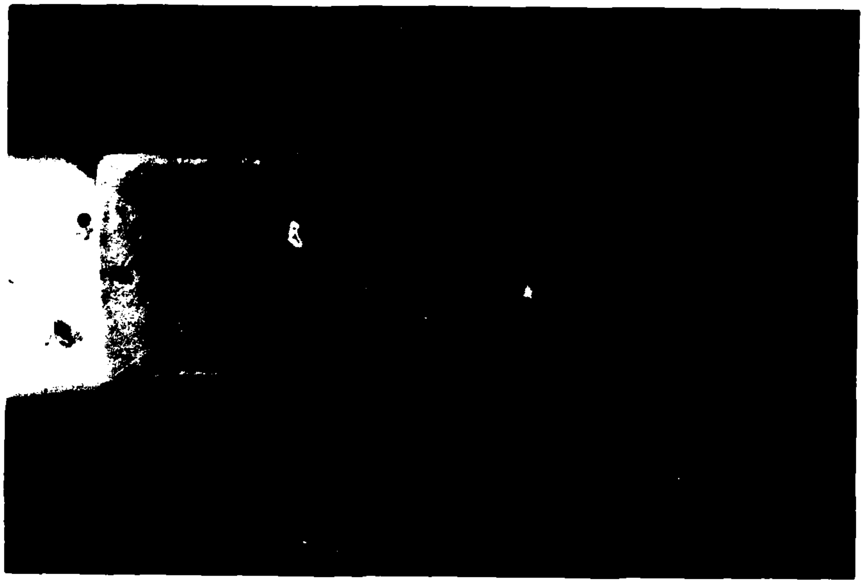

Figure 5c. Positive 5 Degree (+5) Cowl Configuration

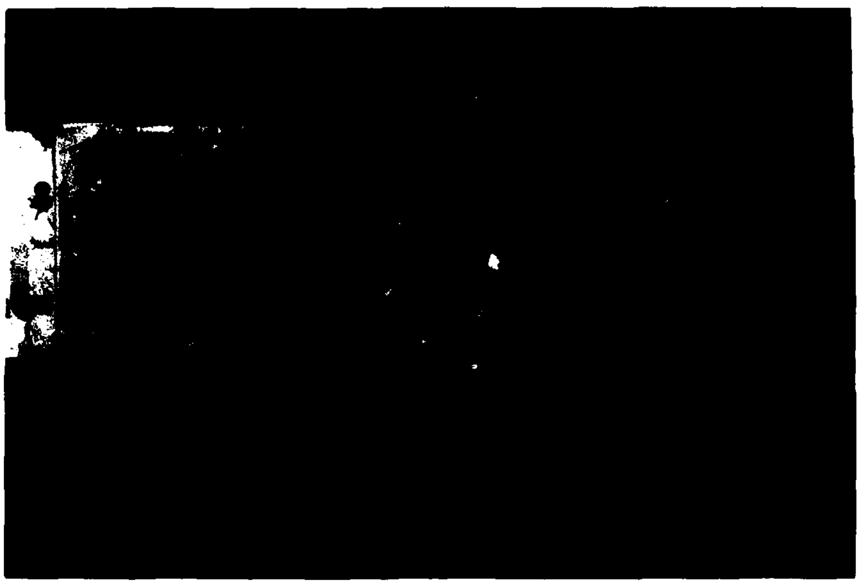

Figure 5d. Negative 5 Degree (-5) Cowl Configuration

Table 1a. Ramp Static Pressure Tap Locations, Model Installed Left Hand Side

MODEL X	MODEL Y: CENTER	-0.25	-0.50	-0.75	-1.00	-1.25
-1.000	75		77		79	
-0.500	76		78		80	
0.250	10	26	30	36	40	46
0.500	11					
0.750	12					
1.000	13	27	31	37	41	47
1.250	14					
1.500	15					
1.750	16					
2.000	17	28	32	38	42	48
2.250	18					
2.500	19					
2.750	20					
3.000	21	29	33	39	43	49
3.500	22					
4.000	23		34		44	
4.500	24					
5.000	25		35		45	

Table 1b. Ramp Static Pressure Tap Locations, Model Installed Right Hand Side

MODEL X	MODEL Y: CENTER	0.25	0.50	0.75	1.00	1.25
-1.000	75		77		79	
-0.500	76		78		80	
0.250	10	50	53	59	62	68
0.500	11					
0.750	12					
1.000	13	51	54	60	63	69
1.250	14					
1.500	15					
1.750	16					
2.000	17	52	55	61	64	70
2.250	18					
2.500	19					
2.750	20					
3.000	21		56		65	
3.500	22					
4.000	23		57		66	
4.500	24					
5.000	25		58		67	

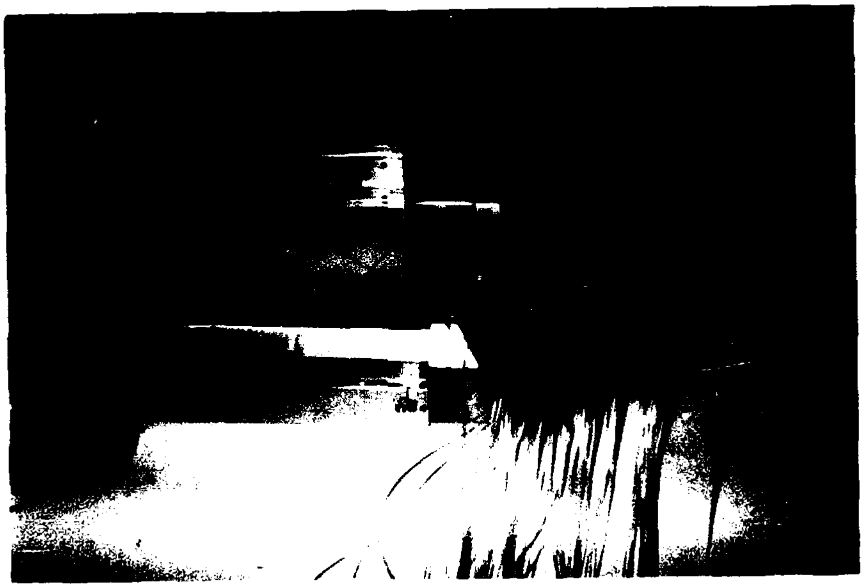

Figure 6. Nozzle/Afterbody Ramp Pressure Instrumentation Tubing

Table 2. Pressure Measurement Uncertainty

Item	*Reference	MAX Error (psf)	MAX Value Calibrated (psf)	% Error MAX Value
Pto	Po	0.9	445.5	0.20
Po	**VAC	1.7	1392.2	0.12
Pi	Po	2.1	363.5	0.57
Ptn	Po	31.0	7183.0	0.43

*: Does Not Include Error in Reference Quanity
**: VAC - Vacuum Reference

Table 3. Test Matrix Showing Test Point Numbers (TPN)

MACH = 0.6

NPR	BL (PN=11)	L (PN=12)	+5 (PN=13)	-5 (PN=14)
OFF	240	267	322,333	345,351
2	241	268	319	346
3	242,246	269,273,295	320,321,330	347,350
4	243	271	331	348
5	244	272,296	332	349

MACH = 0.8

NPR	BL (PN=11)	L (PN=12)	+5 (PN=13)	-5 (PN=14)
OFF	253	287	312	366
2	254	289,294	313	365
3	255,259	288	314,318	358,364
4	256	290	315	359
5	257	291	316	360,361
6	258	292	—	363
7	—	293	—	—

MACH = 1.9

NPR	BL (PN=11)	L (PN=12)	+5 (PN=13)	-5 (PN=14)
OFF	152	156	—	124
1	151,153,154	157	169	123
3	150	158	170	122
5	149	159	171	115
7	148	160	172	116
9	—	161	—	117
12	147	162	173	118
16	—	—	—	119
20	—	—	—	120

MACH = 3.0

NPR	BL (PN=11)	L (PN=12)	+5 (PN=13)	-5 (PN=14)
OFF	176	205	190	—
1	177,188	206	191	—
3	178,182	207	192,193,202	—
5	179	208	194,201	—
7	180	209,213	195	—
9	181	210	196,197	—
12	183	211	198	—
16	184	212	199,200	—
20	186	—	—	—
24	187	—	—	—

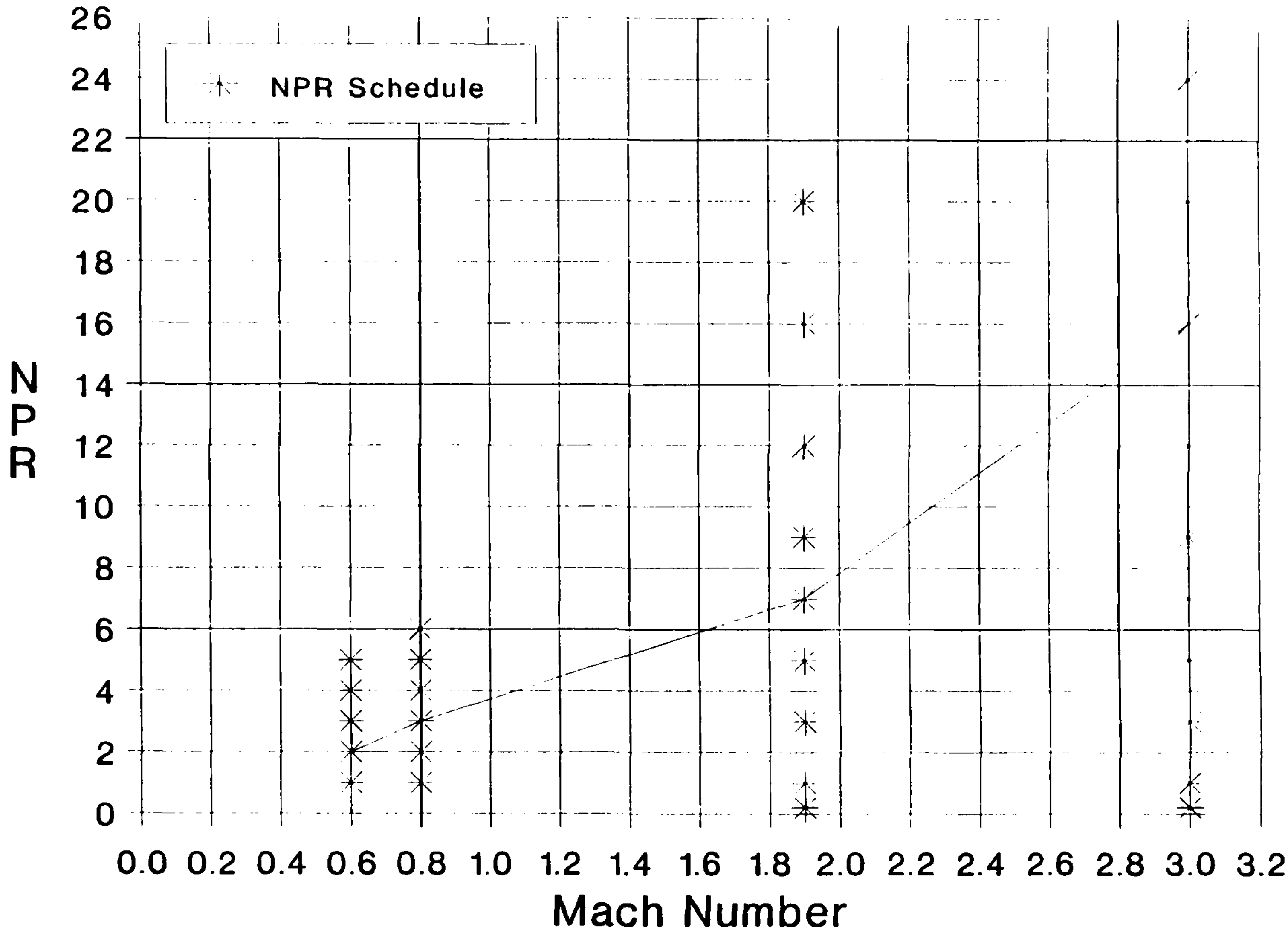

Figure 7. Nozzle Pressure Ratios (NPR) Test Ranges for each Mach Number and Assumed NPR Schedule

Table 4. Pressure Drag Coefficient (CDP) Data

TPN	PN	M	NPR	Re	P_o	Q_o	CDP
115.00	14.000	1.8900	4.9385	0.40032E+07	173.63	434.15	0.11698
116.00	14.000	1.8894	7.0515	0.39708E+07	172.83	431.89	0.11585
117.00	14.000	1.8891	9.0315	0.39674E+07	172.39	430.63	0.11324
118.00	14.000	1.8893	12.026	0.39830E+07	173.18	432.74	0.10250
119.00	14.000	1.8894	15.975	0.39833E+07	173.27	432.97	0.64534E-01
120.00	14.000	1.8890	20.180	0.39748E+07	172.88	431.84	0.45628E-01
122.00	14.000	1.9073	3.1182	0.39201E+07	167.35	426.14	0.11910
123.00	14.000	1.9077	1.0006	0.39208E+07	167.12	425.76	0.11087
124.00	14.000	1.9078	0.23744	0.39486E+07	167.72	427.31	0.72502E-01
147.00	11.000	1.8992	12.121	0.40686E+07	169.78	428.66	0.14483
148.00	11.000	1.8993	7.0714	0.40400E+07	169.67	428.43	0.14253
149.00	11.000	1.8990	4.9991	0.39711E+07	169.61	428.16	0.12083
150.00	11.000	1.8988	2.9872	0.39784E+07	170.31	429.83	0.11480
151.00	11.000	1.8987	0.96161	0.39482E+07	170.60	430.51	0.99404E-01
152.00	11.000	1.8981	0.29275	0.39463E+07	170.38	429.68	0.97952E-01
156.00	12.000	1.9039	0.24610	0.38272E+07	168.78	428.28	0.72256E-01
157.00	12.000	1.9041	0.99975	0.38385E+07	169.19	429.38	0.10802
158.00	12.000	1.9039	3.0170	0.38439E+07	168.93	428.63	0.11440
159.00	12.000	1.9033	4.9734	0.40270E+07	168.69	427.74	0.11399
160.00	12.000	1.9026	7.1597	0.39066E+07	168.58	427.19	0.11627
161.00	12.000	1.9018	9.0726	0.39501E+07	169.00	427.89	0.10498
162.00	12.000	1.9014	12.249	0.39373E+07	169.01	427.71	0.89593E-01
169.00	13.000	1.9051	1.0152	0.38834E+07	168.80	428.87	0.10525
170.00	13.000	1.9050	3.0673	0.39577E+07	168.54	428.16	0.11475
171.00	13.000	1.9047	4.9763	0.40098E+07	168.53	427.98	0.11775
172.00	13.000	1.9049	7.0362	0.39321E+07	169.07	429.42	0.10816
173.00	13.000	1.9046	11.976	0.39435E+07	168.93	428.94	0.73240E-01
176.00	11.000	3.0063	0.36128	0.37767E+07	52.847	334.33	0.50696E-01
177.00	11.000	3.0048	0.82552	0.38852E+07	52.772	333.54	0.48621E-01
178.00	11.000	3.0047	3.1034	0.39893E+07	52.786	333.60	0.49491E-01
179.00	11.000	3.0020	5.0523	0.39534E+07	53.060	334.73	0.49130E-01
180.00	11.000	2.9990	6.9561	0.39280E+07	53.345	335.86	0.54317E-01
181.00	11.000	2.9948	8.9958	0.38980E+07	53.717	337.25	0.57880E-01
183.00	11.000	2.9904	12.185	0.39590E+07	54.129	338.84	0.57268E-01
184.00	11.000	2.9864	15.973	0.39604E+07	54.430	339.81	0.54581E-01
186.00	11.000	2.9780	20.255	0.39732E+07	55.076	341.92	0.47640E-01
187.00	11.000	2.9761	23.985	0.39976E+07	55.267	342.66	0.40356E-01
190.00	13.000	3.0111	0.27120	0.40904E+07	52.369	332.38	0.54105E-01
191.00	13.000	3.0110	1.2295	0.39837E+07	52.348	332.22	0.62724E-01
192.00	13.000	3.0122	3.0463	0.39303E+07	52.214	331.63	0.57655E-01
194.00	13.000	3.0113	5.1240	0.39056E+07	52.258	331.70	0.52598E-01
195.00	13.000	3.0099	7.0412	0.39182E+07	52.423	332.45	0.47752E-01
196.00	13.000	3.0101	9.1072	0.39203E+07	52.425	332.50	0.39907E-01
197.00	13.000	3.0091	9.0925	0.39167E+07	52.431	332.33	0.40423E-01
198.00	13.000	3.0089	12.000	0.39195E+07	52.501	332.72	0.30086E-01
199.00	13.000	3.0091	15.959	0.39215E+07	52.512	332.83	0.12284E-01
205.00	12.000	3.0166	0.34769	0.39576E+07	51.813	330.04	0.57043E-01
206.00	12.000	3.0165	1.2730	0.39380E+07	51.832	330.15	0.60195E-01
207.00	12.000	3.0175	2.9329	0.39187E+07	51.710	329.59	0.59340E-01
208.00	12.000	3.0174	5.0302	0.39040E+07	51.777	329.99	0.56044E-01
209.00	12.000	3.0176	7.0025	0.38963E+07	51.745	329.83	0.52026E-01
210.00	12.000	3.0173	9.0066	0.38852E+07	51.726	329.64	0.46145E-01
211.00	12.000	3.0174	12.006	0.38846E+07	51.765	329.90	0.38288E-01
212.00	12.000	3.0169	15.995	0.38791E+07	51.760	329.78	0.23160E-01
240.00	11.000	0.60196	0.90310	0.39847E+07	1001.8	254.10	0.61993E-01
241.00	11.000	0.60283	2.0167	0.39798E+07	1004.8	255.62	0.13136
242.00	11.000	0.60313	3.0851	0.39865E+07	1004.9	255.88	0.15040
243.00	11.000	0.60024	4.0249	0.39370E+07	1005.3	253.55	0.19589
244.00	11.000	0.60090	4.8908	0.39422E+07	1002.1	253.29	0.25132
253.00	11.000	0.80673	0.82424	0.39505E+07	699.65	318.74	0.10704
254.00	11.000	0.80365	2.0901	0.39416E+07	701.46	317.13	0.14218
255.00	11.000	0.80167	3.0905	0.39360E+07	702.99	316.26	0.15973
256.00	11.000	0.80158	4.0360	0.39416E+07	703.43	316.38	0.21593
257.00	11.000	0.80367	5.0730	0.39491E+07	702.72	317.72	0.24234
258.00	11.000	0.80571	6.0590	0.39449E+07	699.63	317.92	0.29482
267.00	12.000	0.60284	0.87860	0.42206E+07	1000.5	254.52	0.56627E-01
268.00	12.000	0.60607	2.1069	0.42301E+07	997.49	256.48	0.14060
269.00	12.000	0.60120	3.0350	0.42116E+07	1002.2	253.56	0.18290
271.00	12.000	0.60336	4.0481	0.42197E+07	1000.9	255.05	0.20198
272.00	12.000	0.60261	5.0011	0.42129E+07	1001.5	254.57	0.19436
287.00	12.000	0.80448	0.78135	0.39519E+07	698.71	316.54	0.95402E-01

Table 4. (Continued)

TPN	PN	M	NPR	Re	P_o	Q_o	CDP
288.00	12.000	0.80072	3.0278	0.39495E+07	701.96	315.05	0.17590
289.00	12.000	0.79799	1.9932	0.39601E+07	707.36	315.30	0.14521
290.00	12.000	0.80305	4.0968	0.39599E+07	701.07	316.48	0.19144
291.00	12.000	0.80308	4.9634	0.39525E+07	700.04	316.03	0.19426
292.00	12.000	0.80233	6.0316	0.39571E+07	702.01	316.34	0.12824
293.00	12.000	0.80153	7.0836	0.39577E+07	702.44	315.90	0.14446
312.00	13.000	0.80778	0.78886	0.39754E+07	698.58	319.08	0.11001
313.00	13.000	0.80209	2.0323	0.39800E+07	705.98	317.93	0.14134
314.00	13.000	0.80325	3.0763	0.39624E+07	701.87	317.00	0.14861
315.00	13.000	0.79711	4.0904	0.39454E+07	706.00	314.01	0.14330
316.00	13.000	0.79802	4.9760	0.39504E+07	704.95	314.25	0.16375
319.00	13.000	0.60742	2.0314	0.39848E+07	995.08	257.00	0.12960
320.00	13.000	0.60886	2.9798	0.39992E+07	997.41	258.83	0.13933
322.00	13.000	0.61037	0.89435	0.40122E+07	995.36	259.58	0.64563E-01
331.00	13.000	0.58601	3.9665	0.38917E+07	1015.9	244.21	0.16717
332.00	13.000	0.57516	4.7552	0.38325E+07	1021.5	236.55	0.18804
345.00	14.000	0.60461	0.86983	0.39899E+07	1000.7	256.08	0.48556E-01
346.00	14.000	0.60453	2.0065	0.39835E+07	1000.4	255.94	0.12938
347.00	14.000	0.60192	3.0044	0.39646E+07	1002.5	254.25	0.19732
348.00	14.000	0.58616	4.0486	0.38716E+07	1008.6	242.58	0.25619
349.00	14.000	0.59788	4.7248	0.39507E+07	1005.4	251.58	0.26700
358.00	14.000	0.82433	3.0740	0.40249E+07	690.54	328.46	0.20123
359.00	14.000	0.81309	4.0039	0.39804E+07	693.57	320.97	0.21311
360.00	14.000	0.80262	5.0137	0.39578E+07	702.74	316.89	0.26875
363.00	14.000	0.78977	6.0328	0.39154E+07	708.90	309.52	0.23778
365.00	14.000	0.81809	2.1021	0.39889E+07	689.99	323.25	0.16117
366.00	14.000	0.82305	0.75872	0.40094E+07	688.44	326.45	0.11656

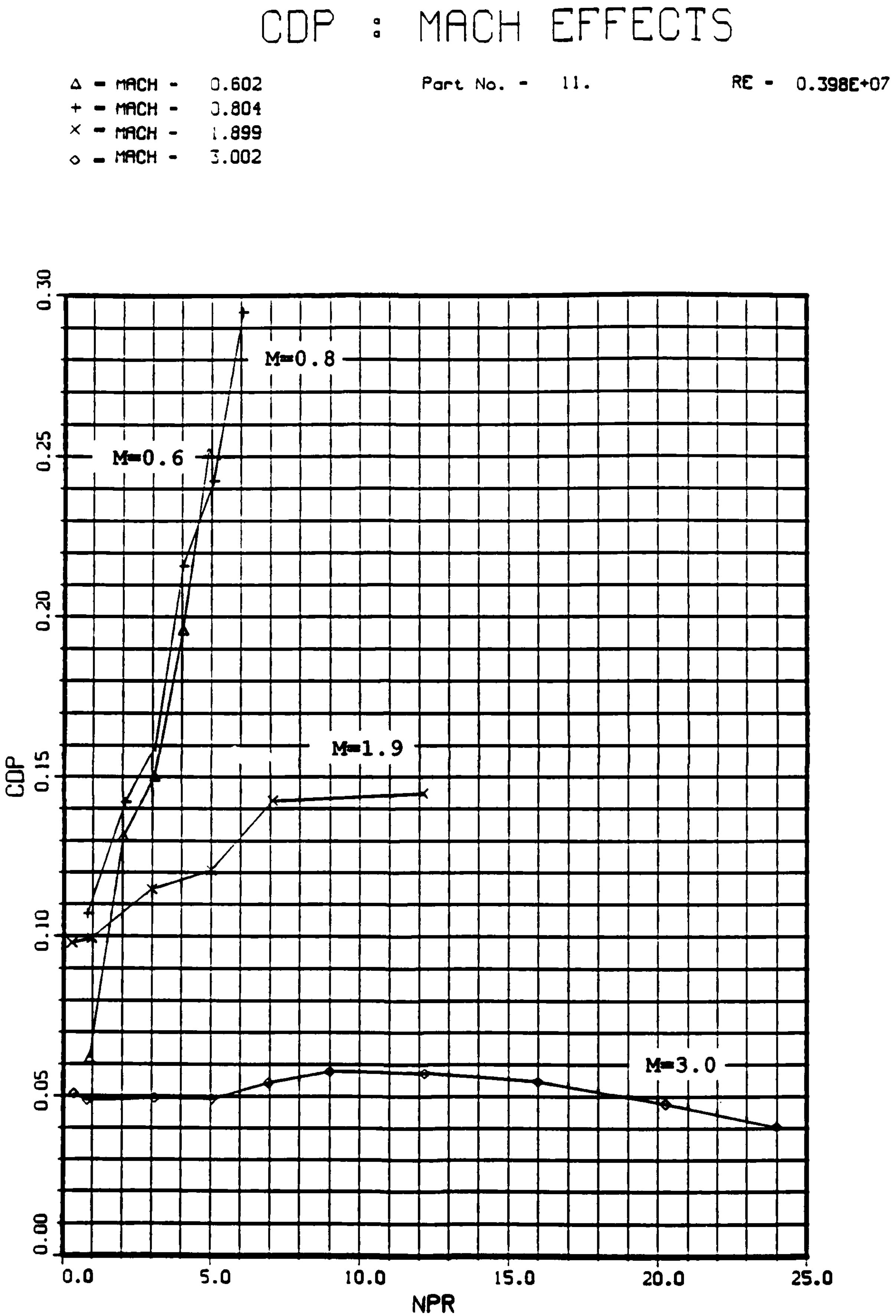

Figure 8a. Pressure Drag Coefficient, CDP vs NPR: Mach Effects, Baseline (BL) Cowl Configuration

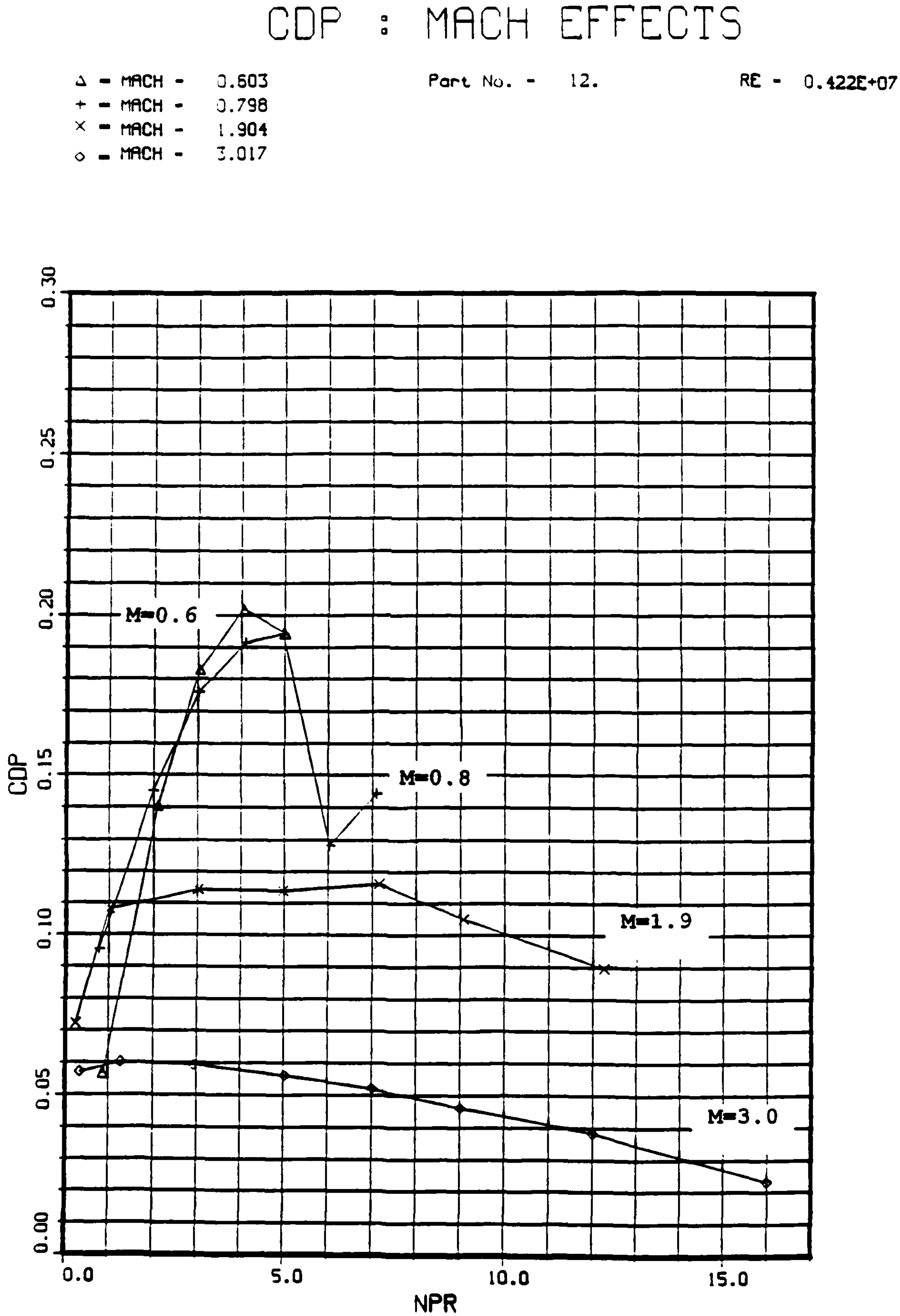

Figure 8b. Pressure Drag Coefficient, CDP vs NPR: Mach Effects, Long (L) Cowl Configuration

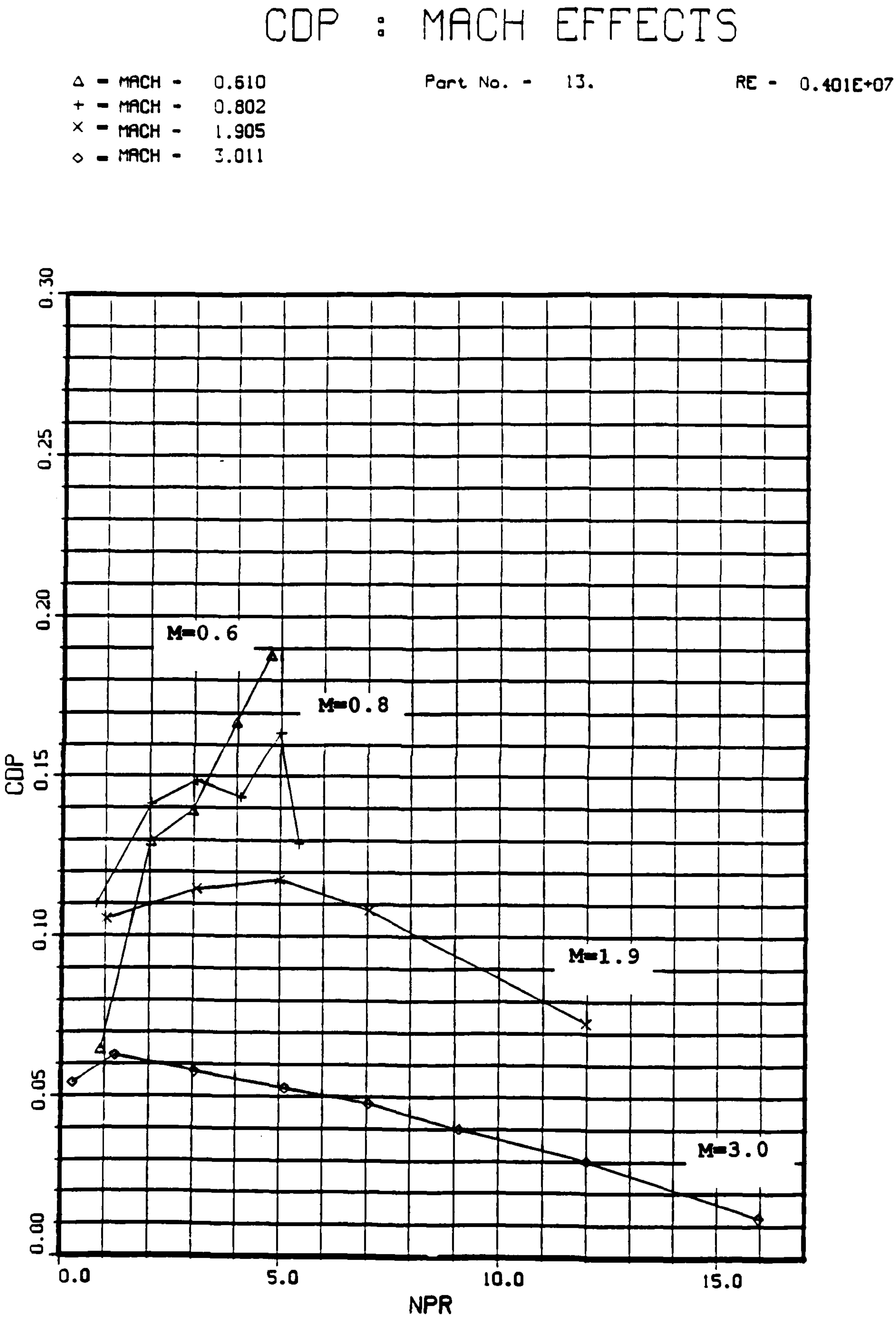

Figure 8c. Pressure Drag Coefficient, CDP vs NPR: Mach Effects, Positive (+5) Cowl Configuration

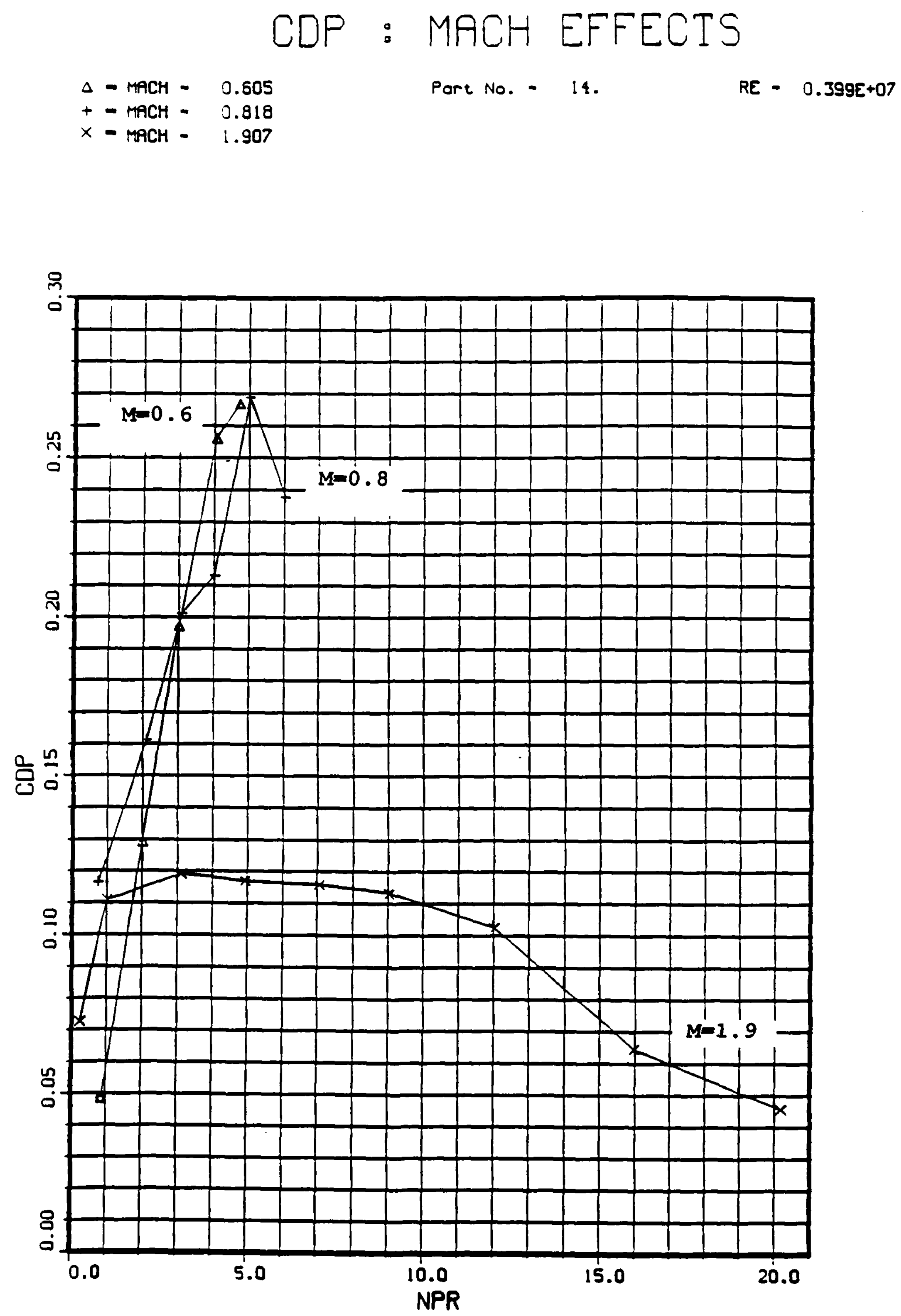

Figure 8d. Pressure Drag Coefficient, CDP vs NPR: Mach Effects, Negative (-5) Cowl configuration

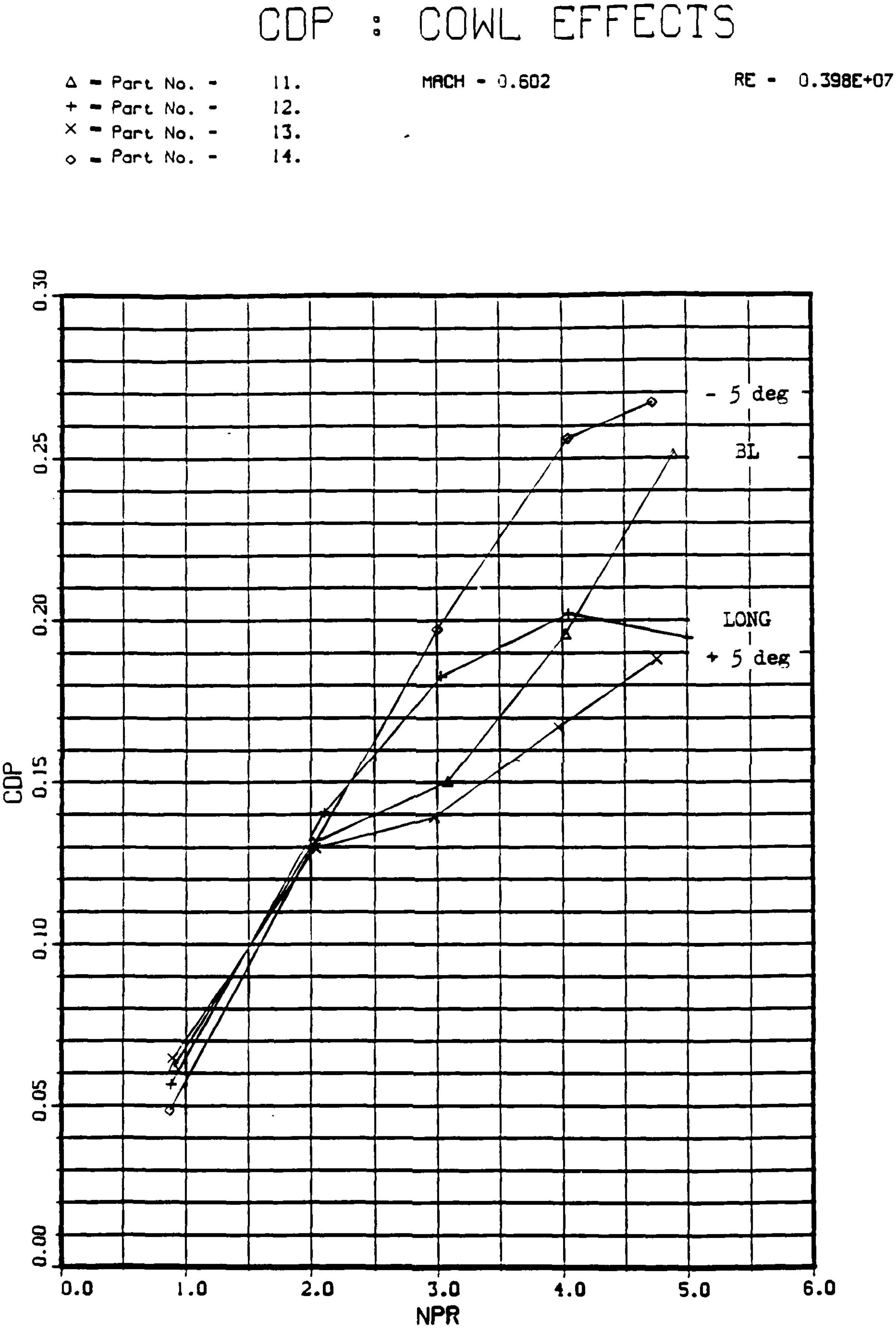

Figure 9a. Pressure Drag Coefficient, CDP vs NPR: Cowl Effects, Mach 0.6

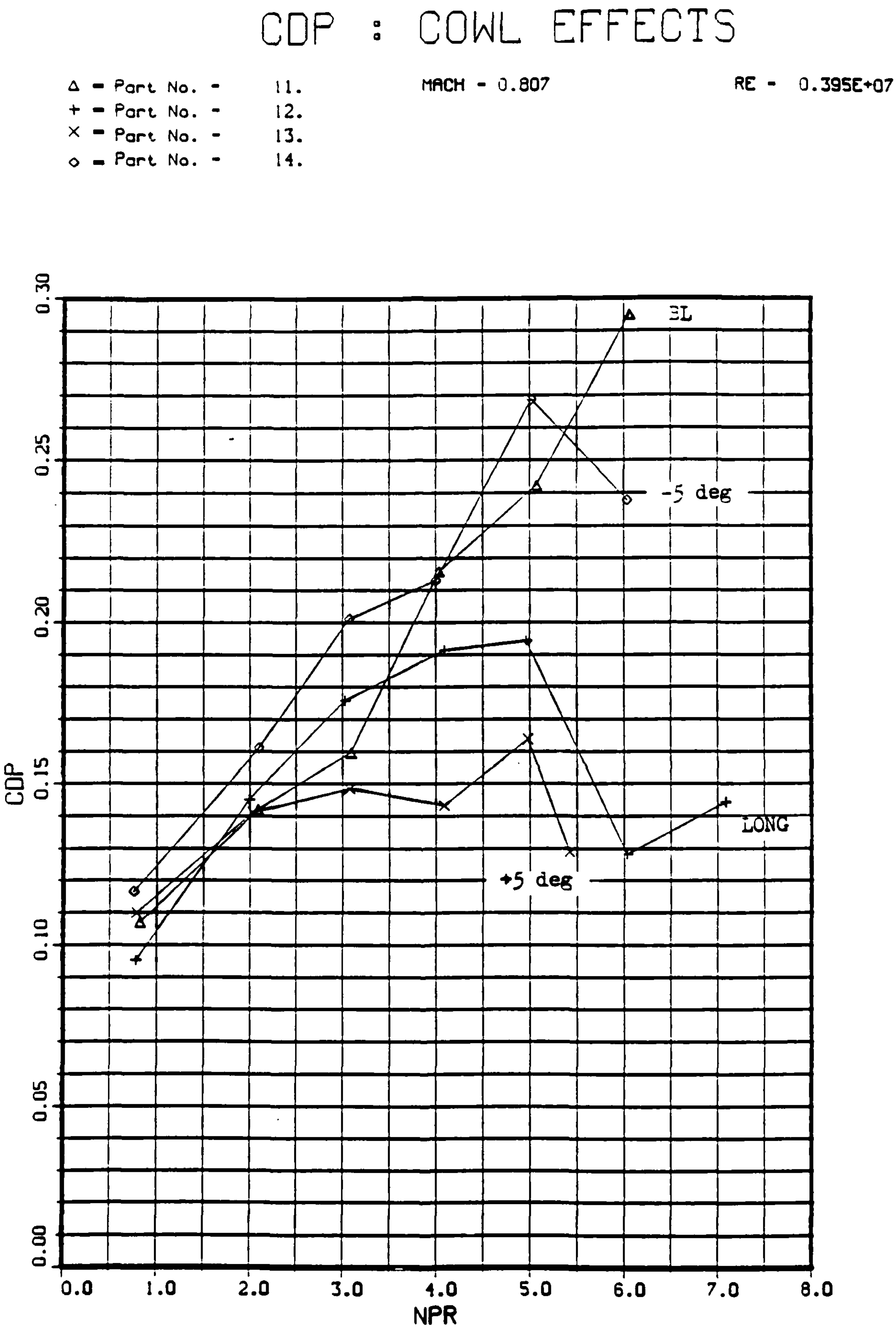

Figure 9b. Pressure Drag Coefficient, CDP vs NPR: Cowl Effects, Mach 0.8

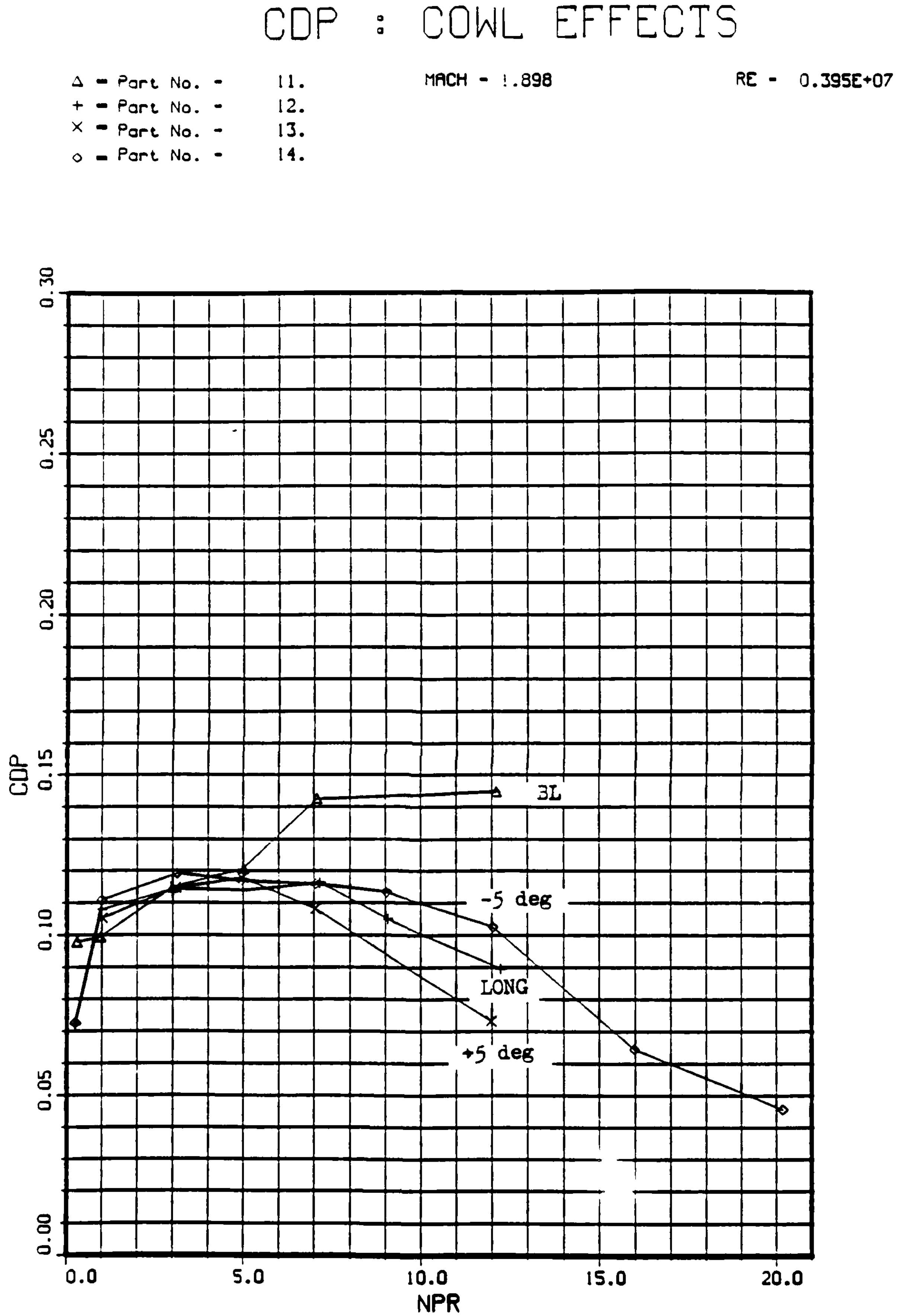

Figure 9c. Pressure Drag Coefficient, CDP vs NPR: Cowl Effects, Mach 1.9

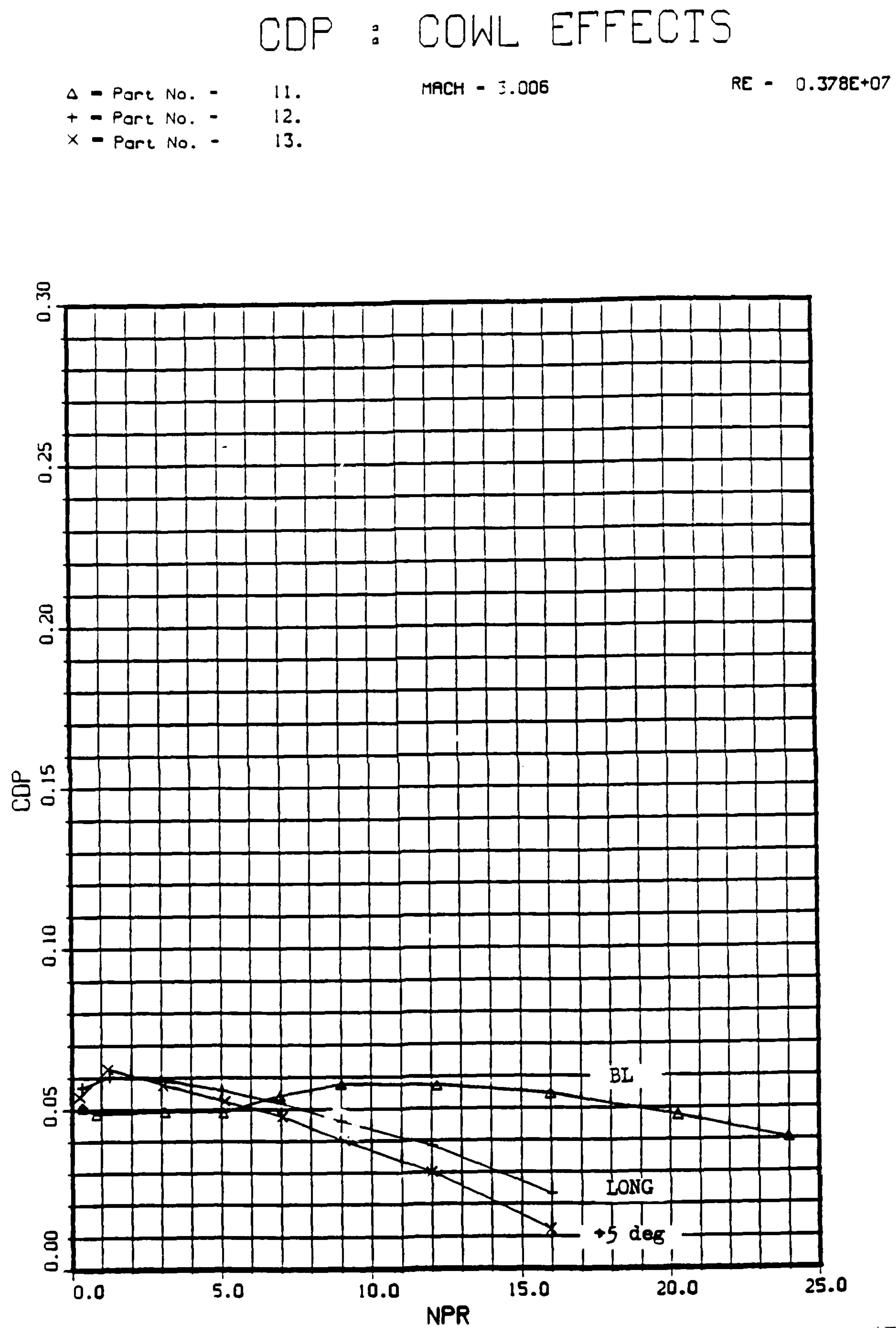

Figure 9d. Pressure Drag Coefficient, CDP vs NPR: Cowl Effects, Mach 3.0

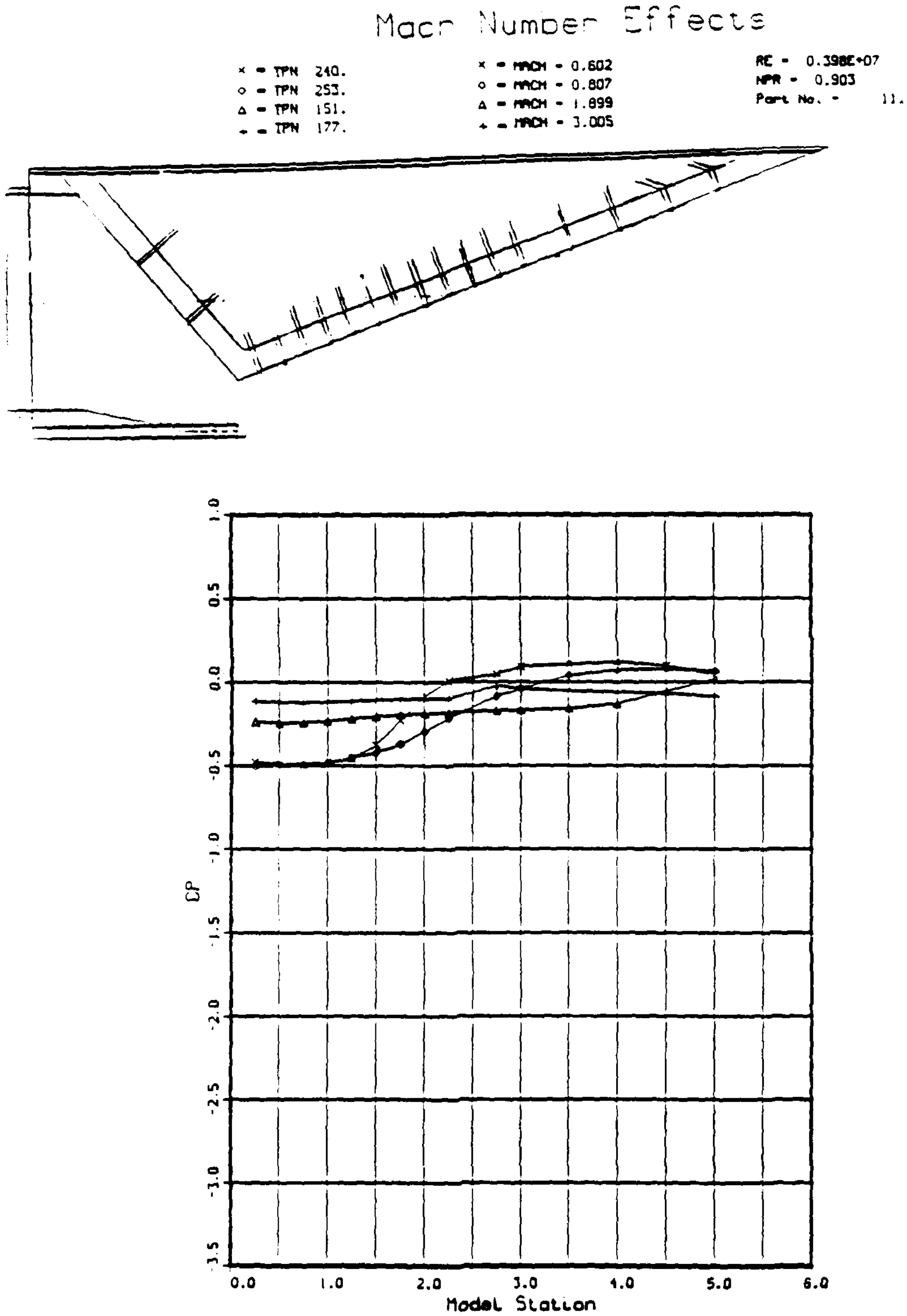

Figure 10a. Pressure Coefficient, C_p vs Model Station: Mach Number Effects, BL Cowl, NPR = 1.0

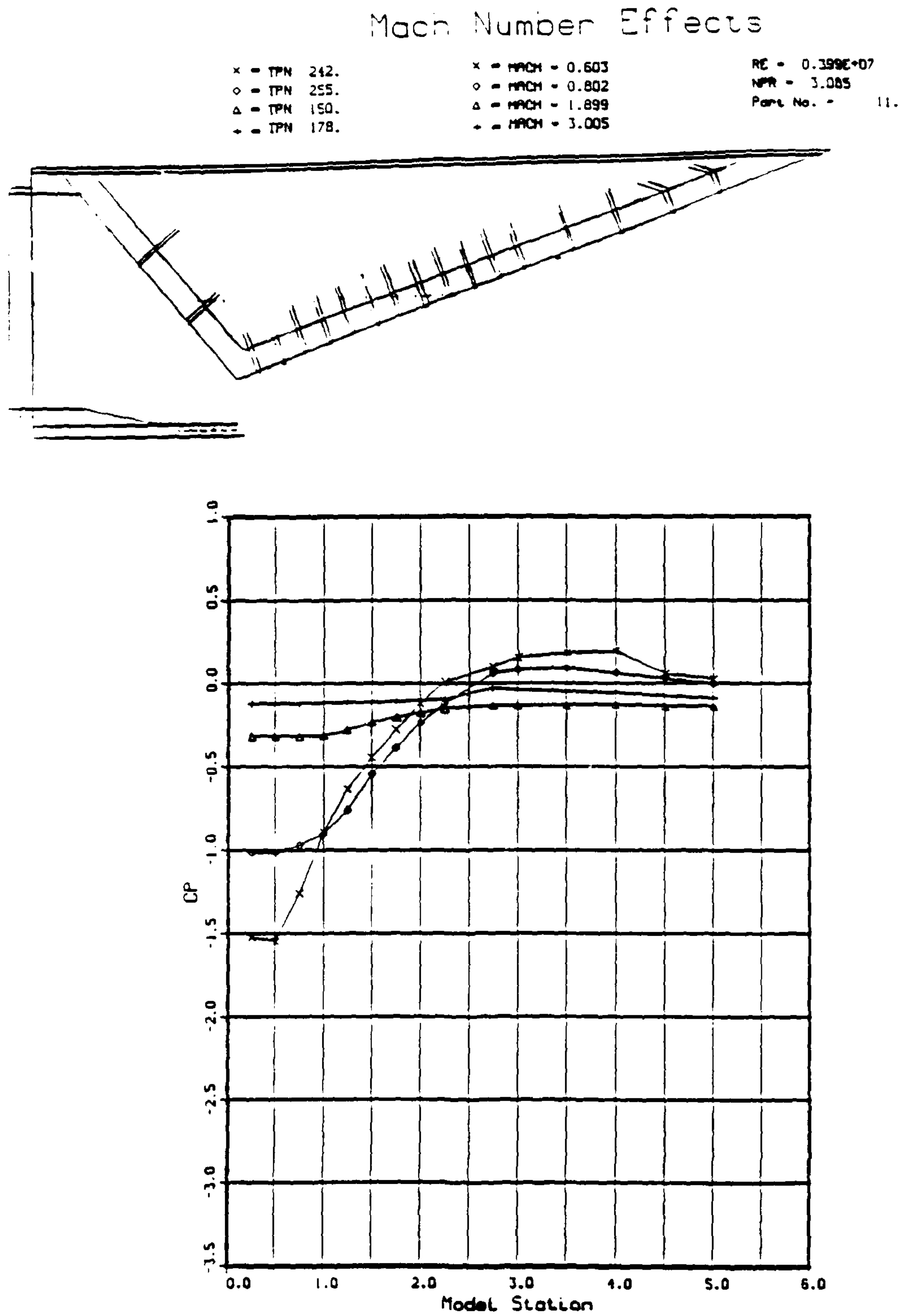

Figure 10b. Pressure Coefficient, C_p vs Model Station: Mach Number Effects, BL Cowl, NPR = 3.0

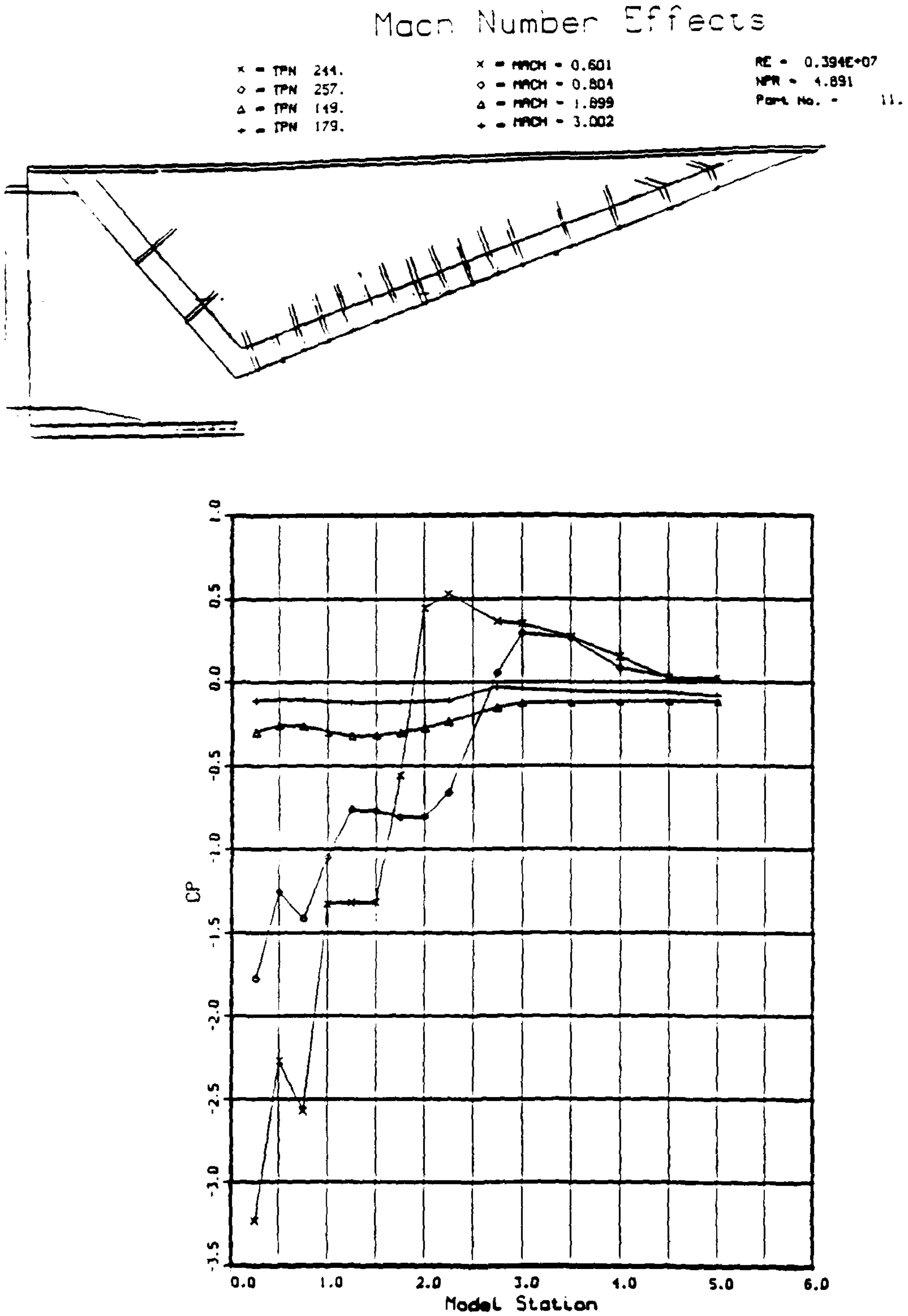

Figure 10c. Pressure Coefficient, C_p vs Model Station: Mach Number Effects, BL Cowl, NPR = 5.0

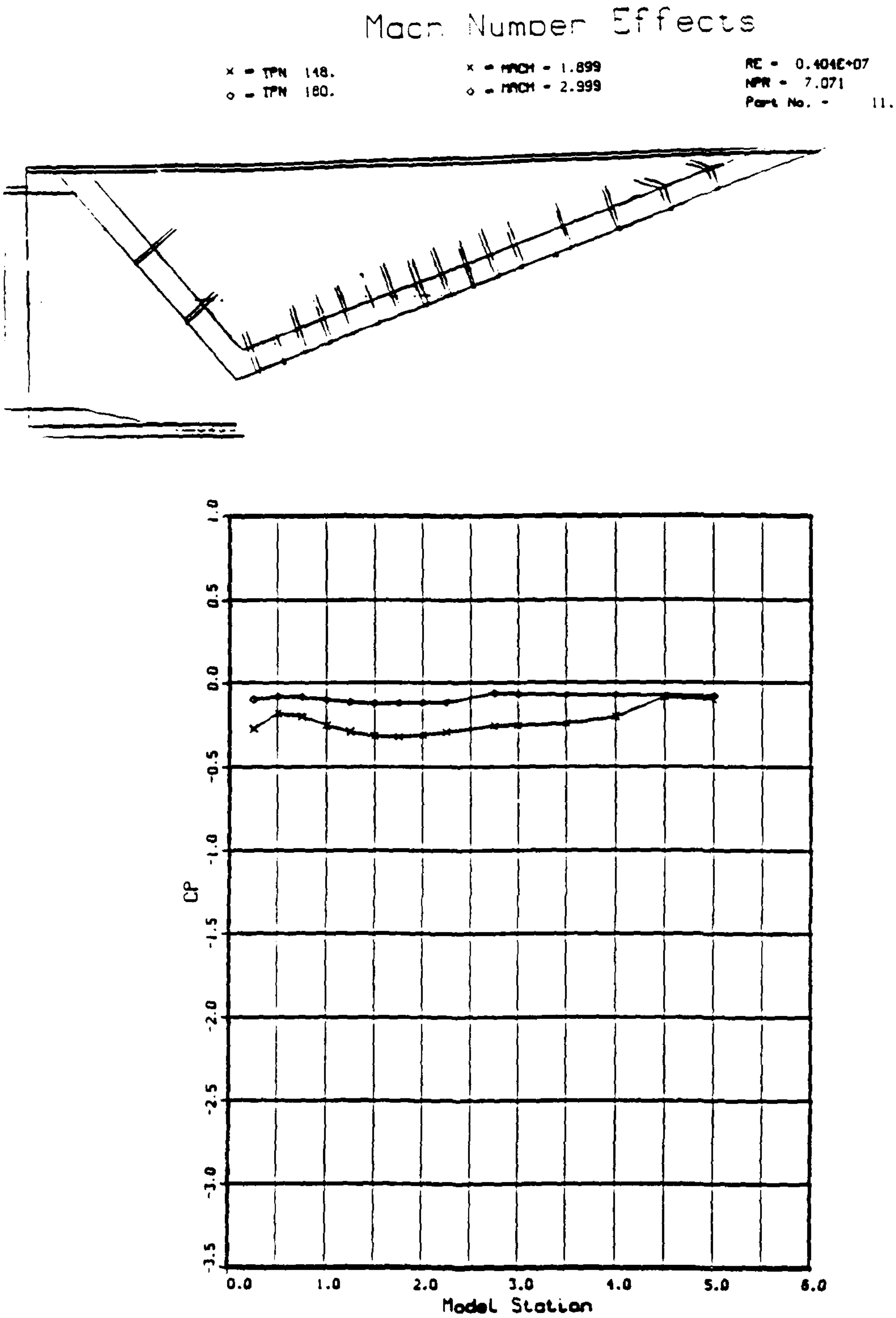

Figure 10d. Pressure Coefficient, C_p vs Model Station: Mach Number Effects, BL Cowl, NPR = 7.0

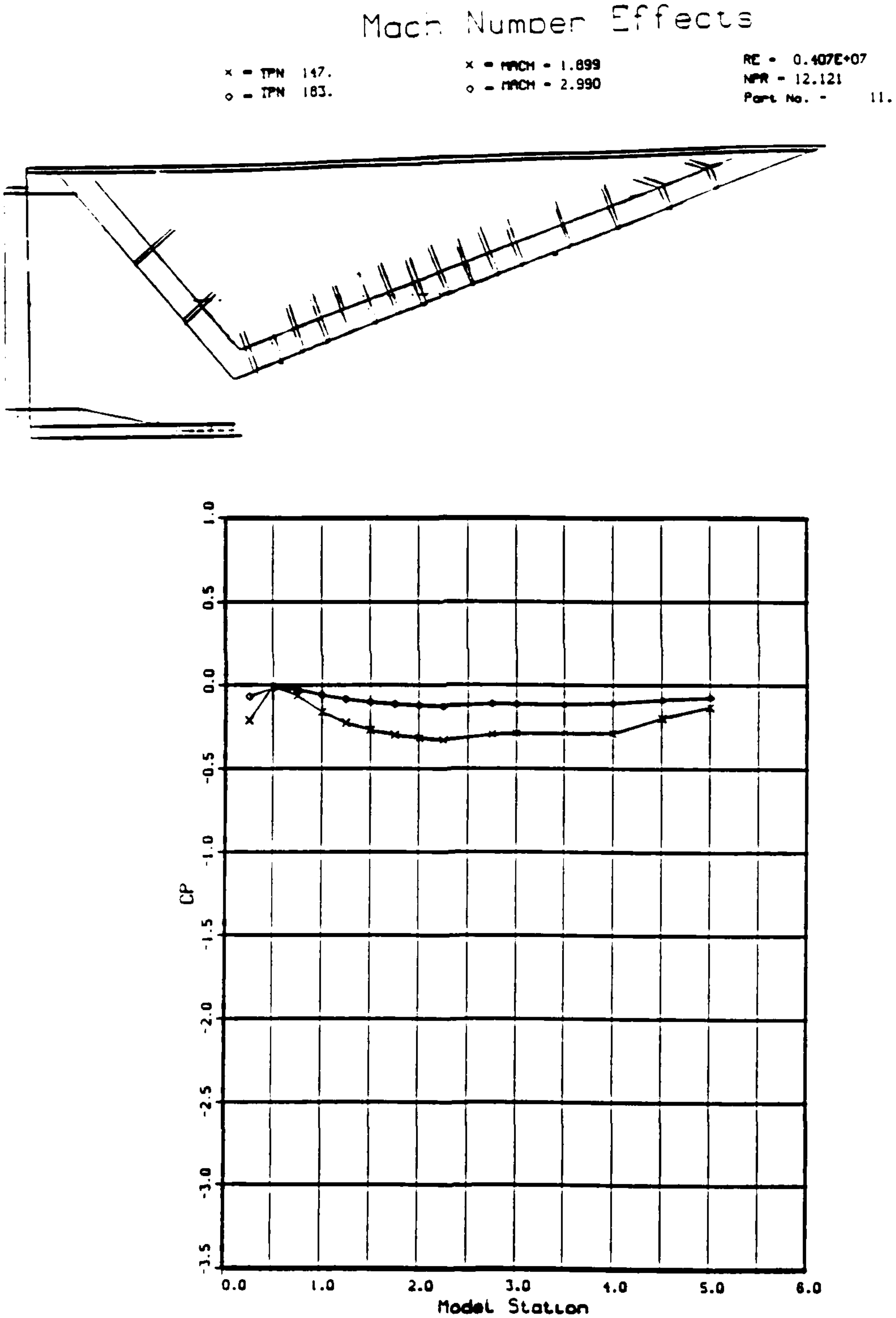

Figure 10e. Pressure Coefficient, C_p vs Model Station: Mach Number Effects, BL Cowl, NPR = 12.0

Figure 11a. Schlieren Photograph: Mach = 0.6, NPR = 2.0, BL Cowl

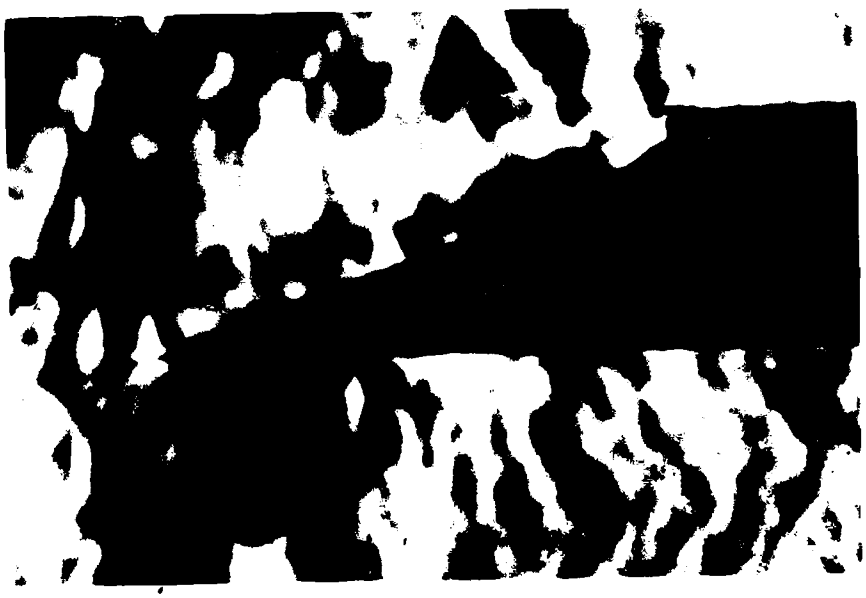

Figure 11b. Schlieren Photograph: Mach = 0.8, NPR = 3.0, BL Cowl

Figure 11c. Schlieren Photograph: Mach = 1.9, NPR = 7.0, BL Cowl

Figure 11d. Schlieren Photograph: Mach = 3.0, NPR = 16.0, BL Cowl

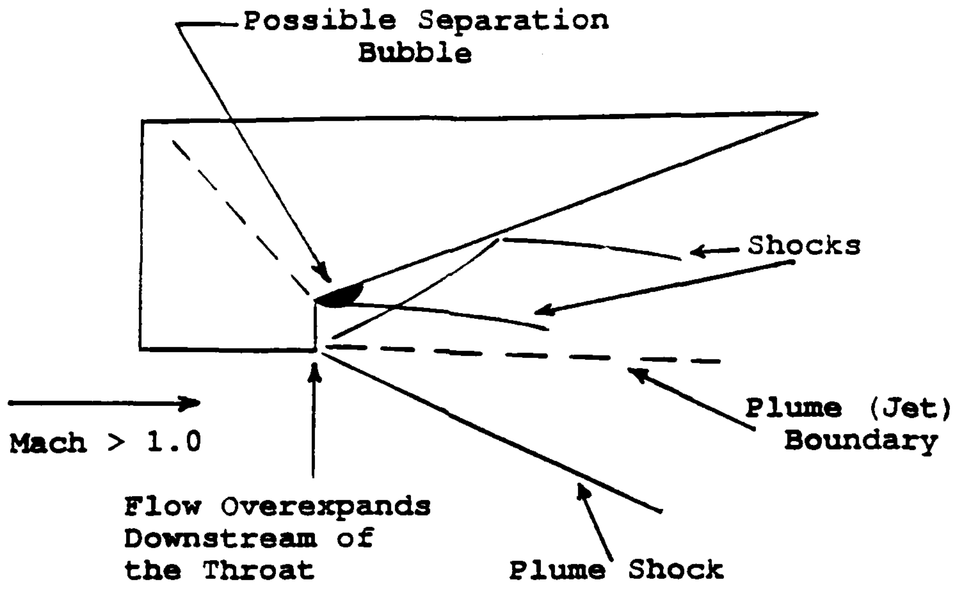

Figure 12. Schematic of an Overexpanded Exhaust at Supersonic Free-Stream Mach Numbers

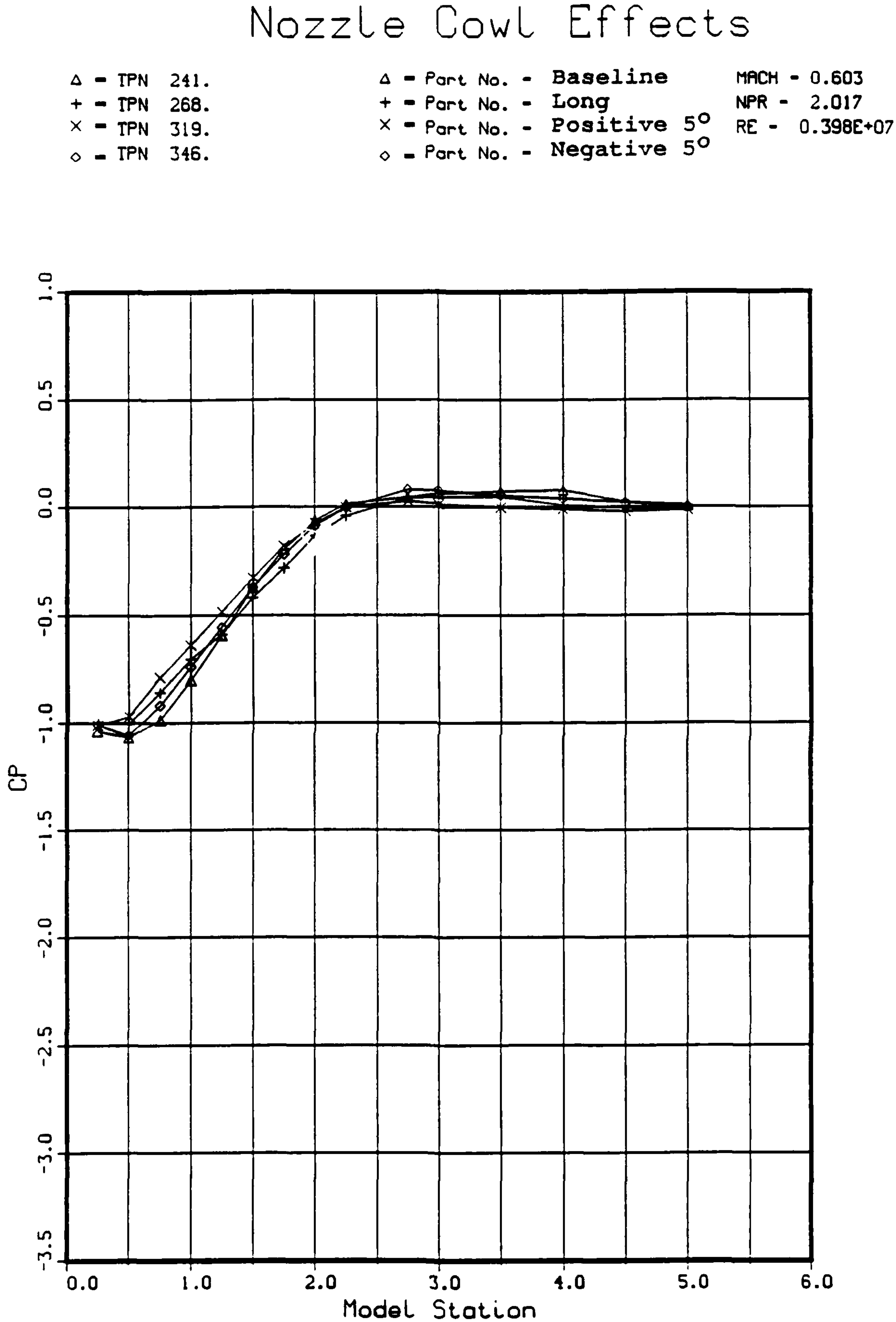

Figure 13a. **Pressure Coefficient, C_p vs Model Station: Nozzle Cowl Effects, Mach = 0.6, NPR = 2.0**

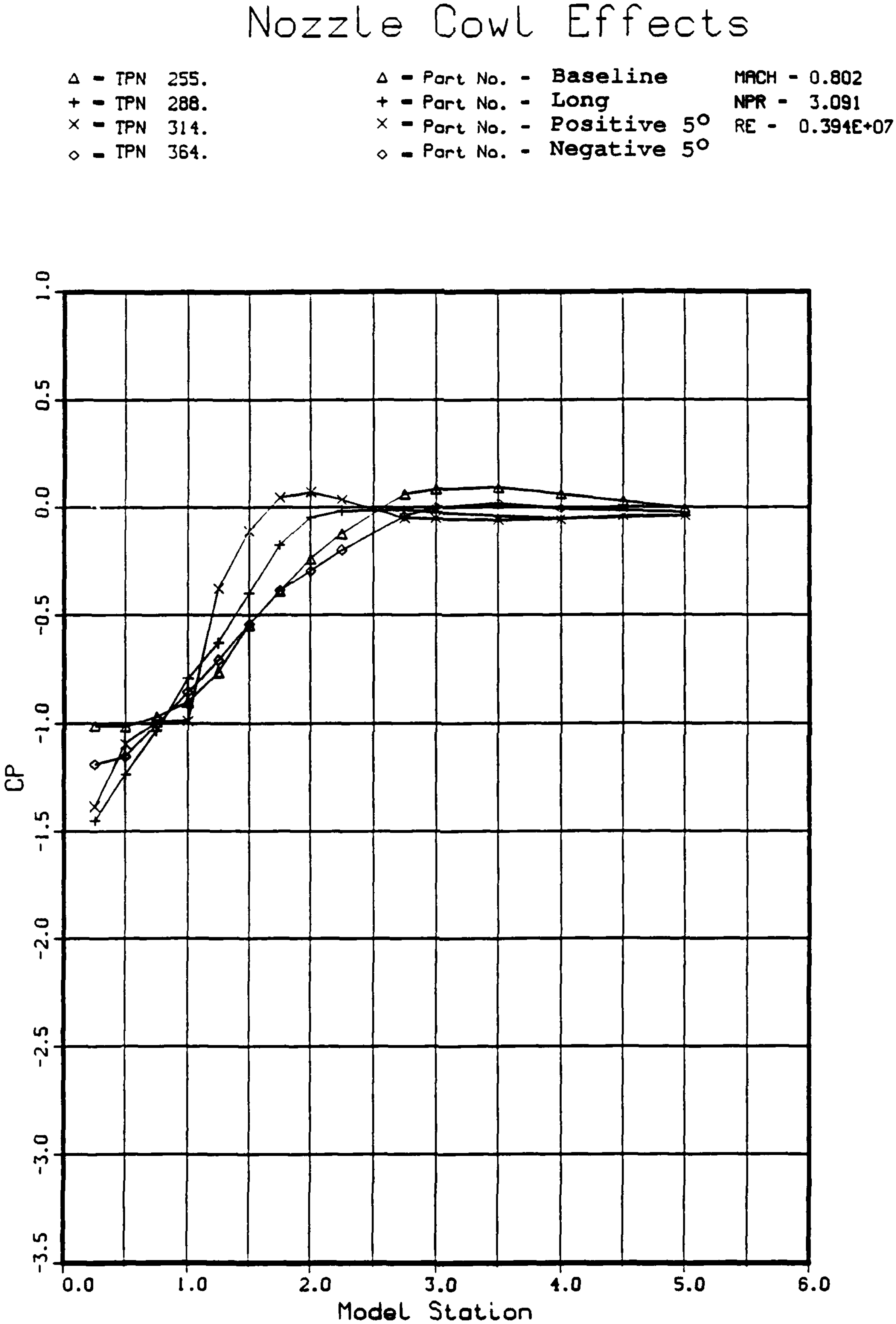

Figure 13b. Pressure Coefficient, C_p vs Model Station: Nozzle Cowl Effects, Mach = 0.8, NPR = 3.0

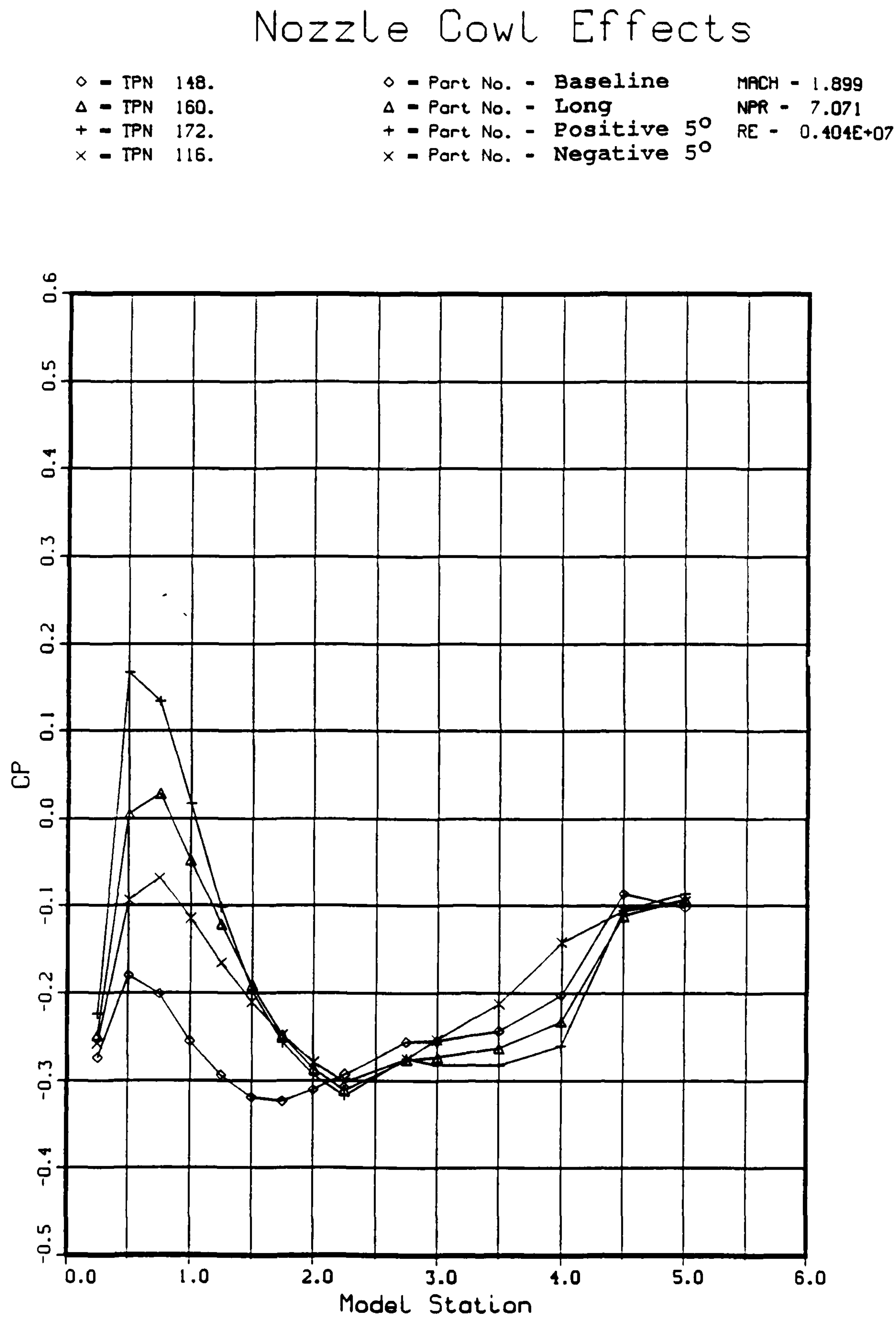

Figure 13c. Pressure Coefficient, C_p vs Model Station: Nozzle Cowl Effects, Mach = 1.9, NPR = 7.0

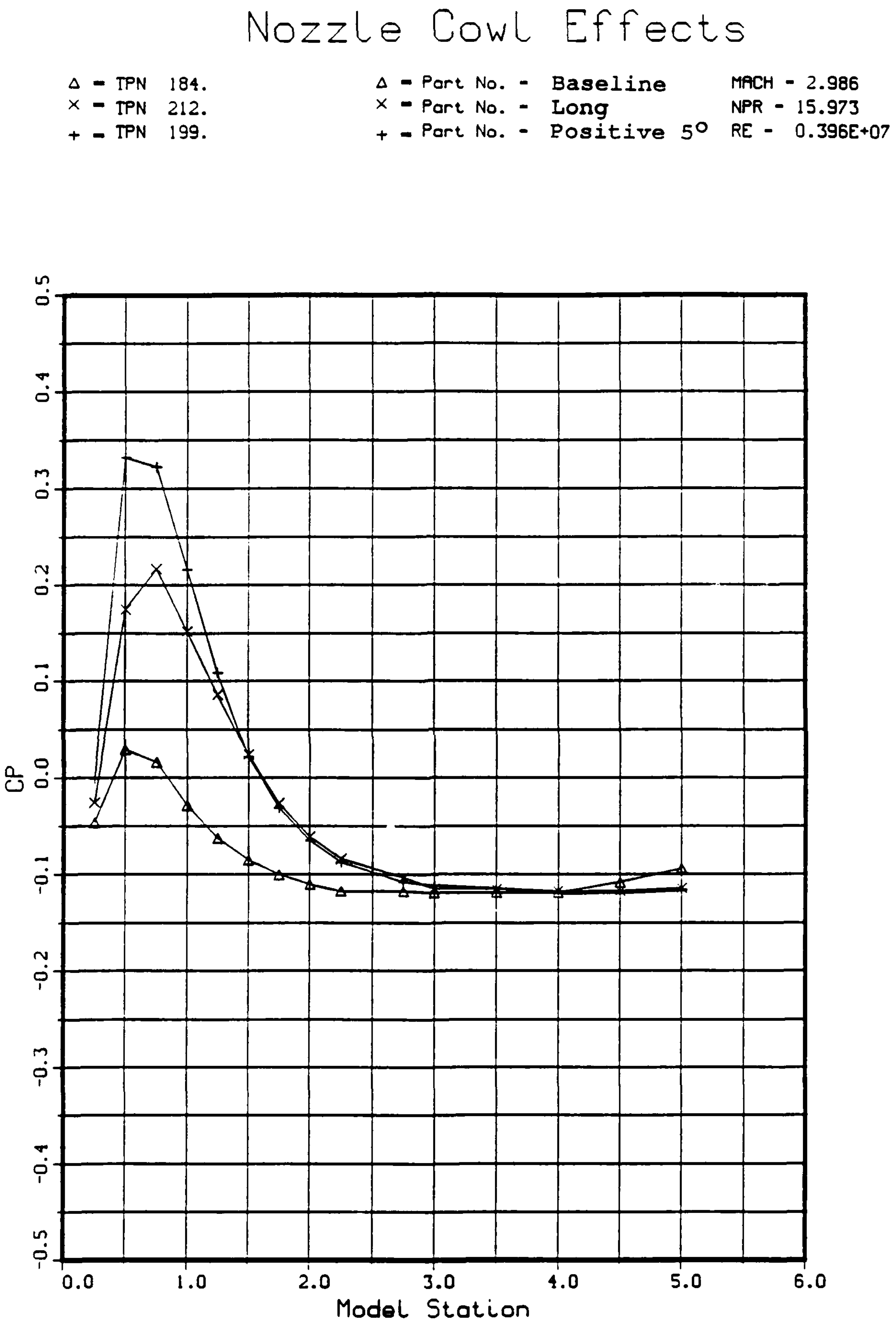

Figure 13d. Pressure Coefficient, C_p vs Model Station: Nozzle Cowl Effects, Mach = 3.0, NPR = 16.0

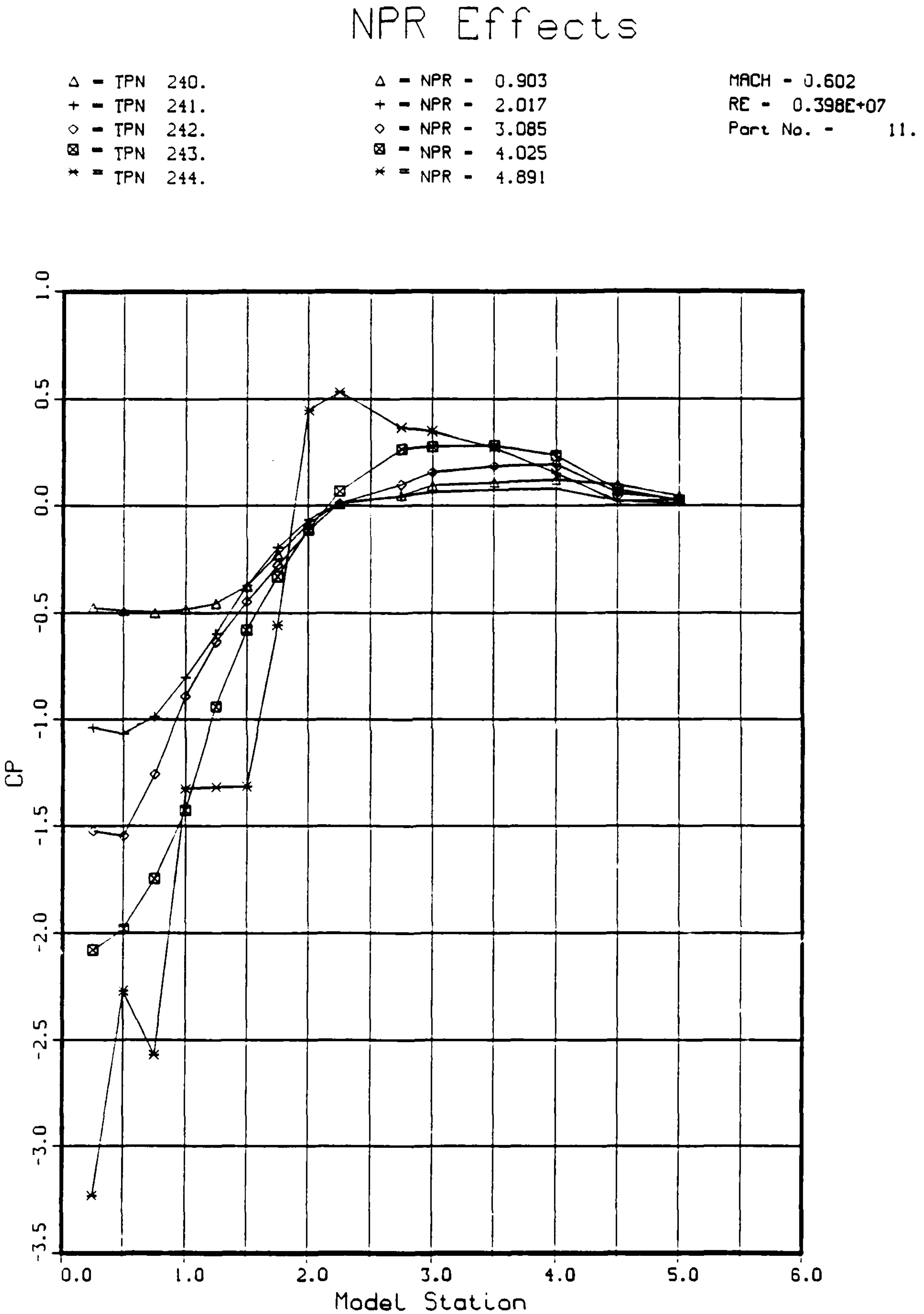

Figure 14a. Pressure Coefficient, C_p vs Model Station: NPR Effects, Mach = 0.6, BL Cowl

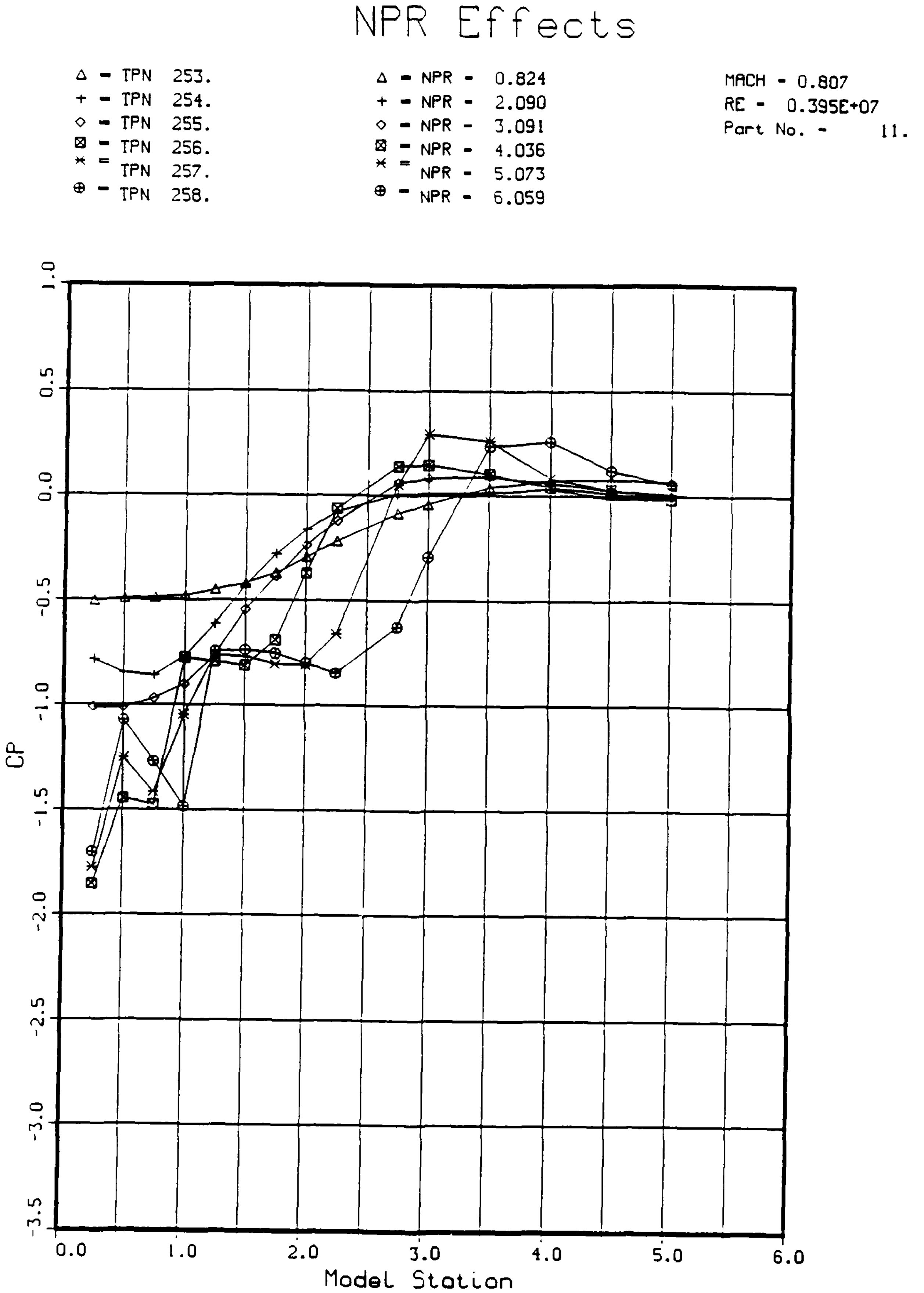

Figure 14b. Pressure Coefficient, C_p vs Model Station: NPR Effects, Mach = 0.8, BL Cowl

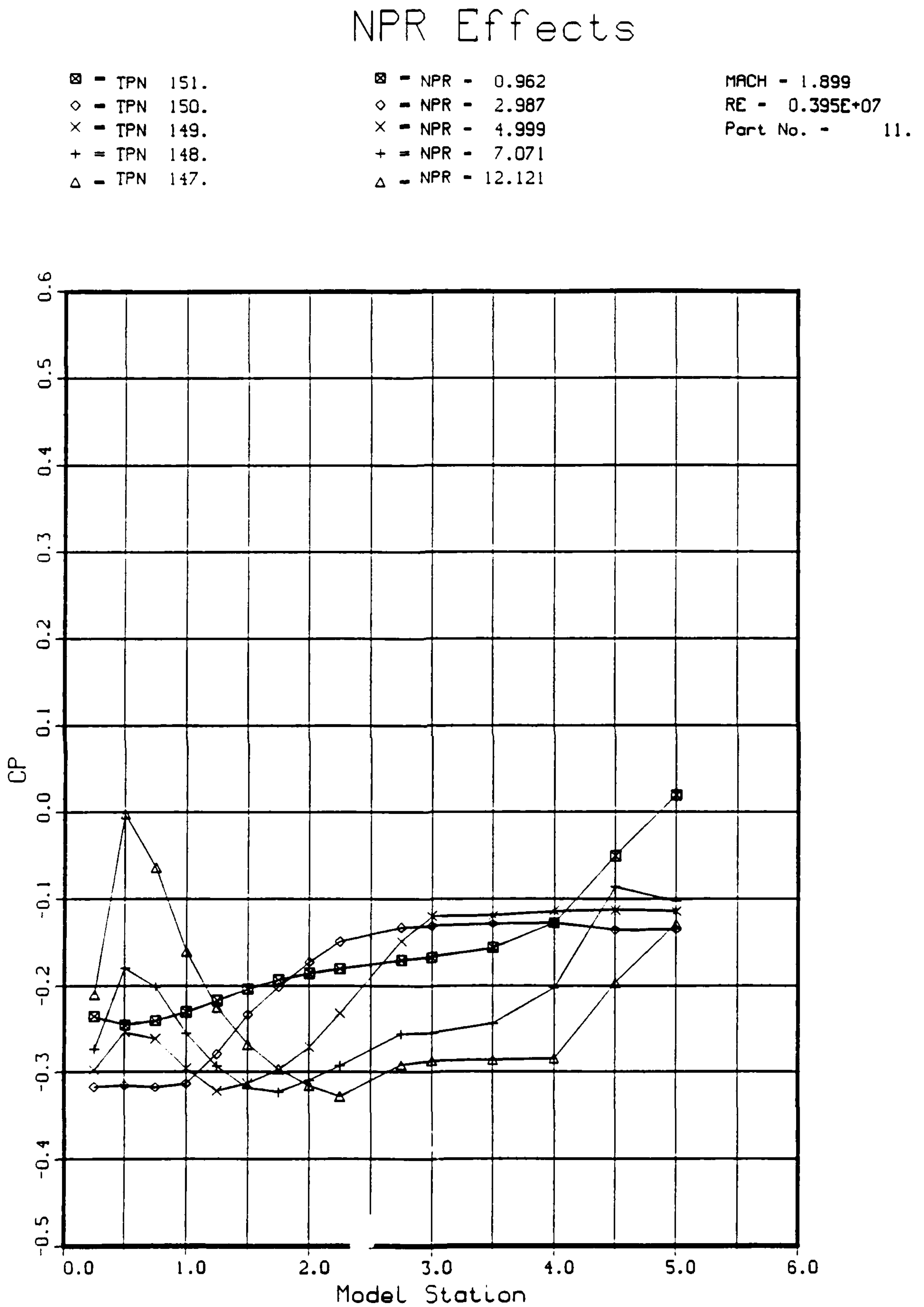

Figure 14c. Pressure Coefficient, C_p vs Model Station: NPR Effects, Mach = 1.9, BL Cowl

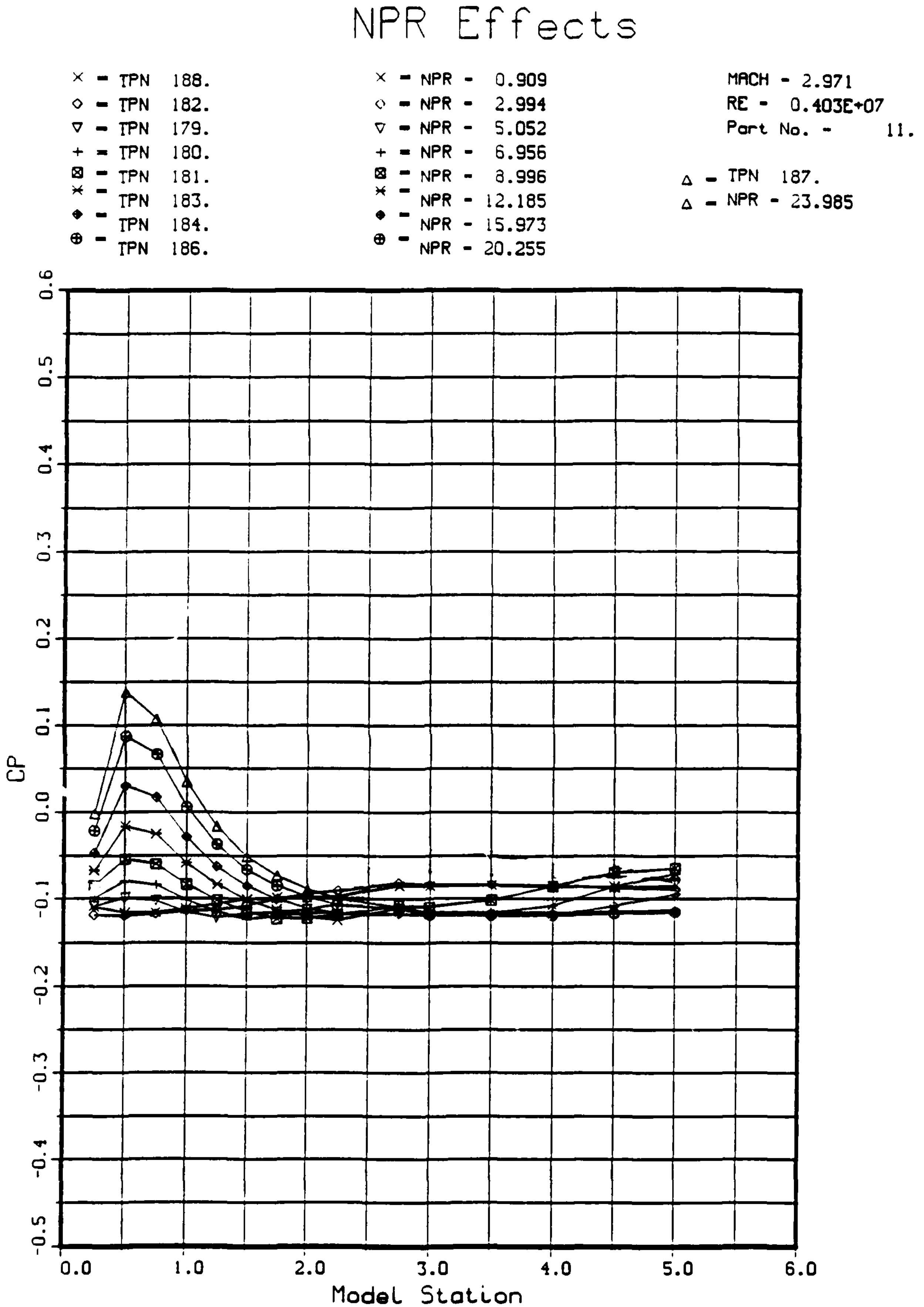

Figure 14d. Pressure Coefficient, C_p vs Model Station: NPR Effects, Mach = 3.0, BL Cowl

Appendix A: Pressure Coefficient (C_p) Contours

Contour pressure coefficients (C_p) plots representing the pressure distribution of the entire ramp are presented in Appendix A. Note, that for the 0.6 Mach number, baseline (BL) and -5 degree (-5) cowls, there is a lower pressure region on the left side downstream of the throat, but not for the other cowl configurations. The BL and -5, with higher expansion ratios (unlimited expansion with the BL) allow the flow to expand quicker and the flow, near critical, is distorted and may not be filling the cowl exit evenly. But, the flow for the rest of the ramp for this case is mostly symmetric. This NPR schedule for the tested Mach numbers 0.6, 0.8, 1.9, and 3.0, is 2.0, 3.0, 7.0, and 16.0, respectively. This schedule is representative of a generic flight path. The flow was very symmetric about the centerline of the nozzle ramp (left to right side comparison) for most of the conditions tested.

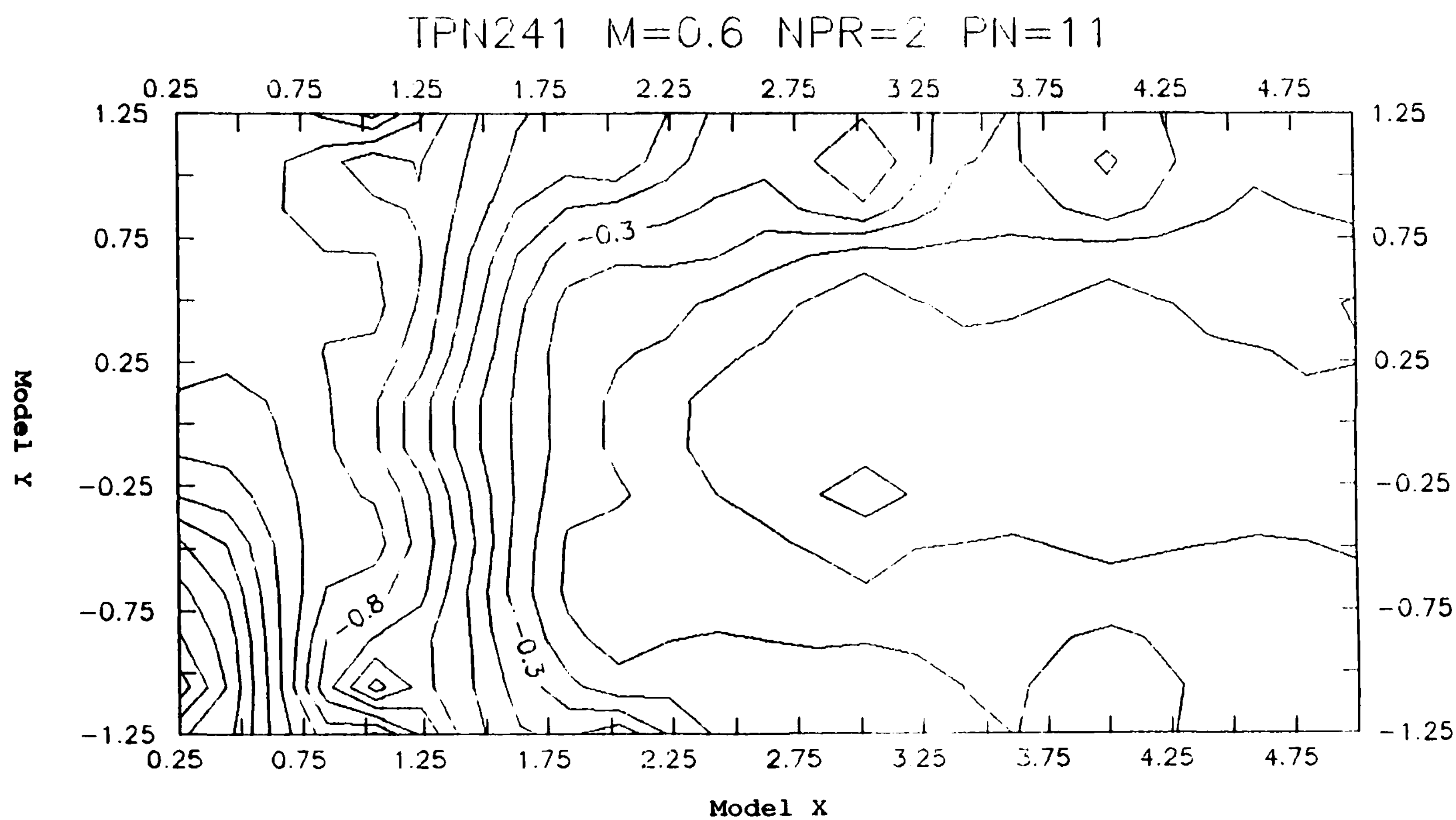

Figure A1. Pressure Coefficient (C_p) Contours: Mach 0.6, NPR = 2.0, BL_{Cowl}

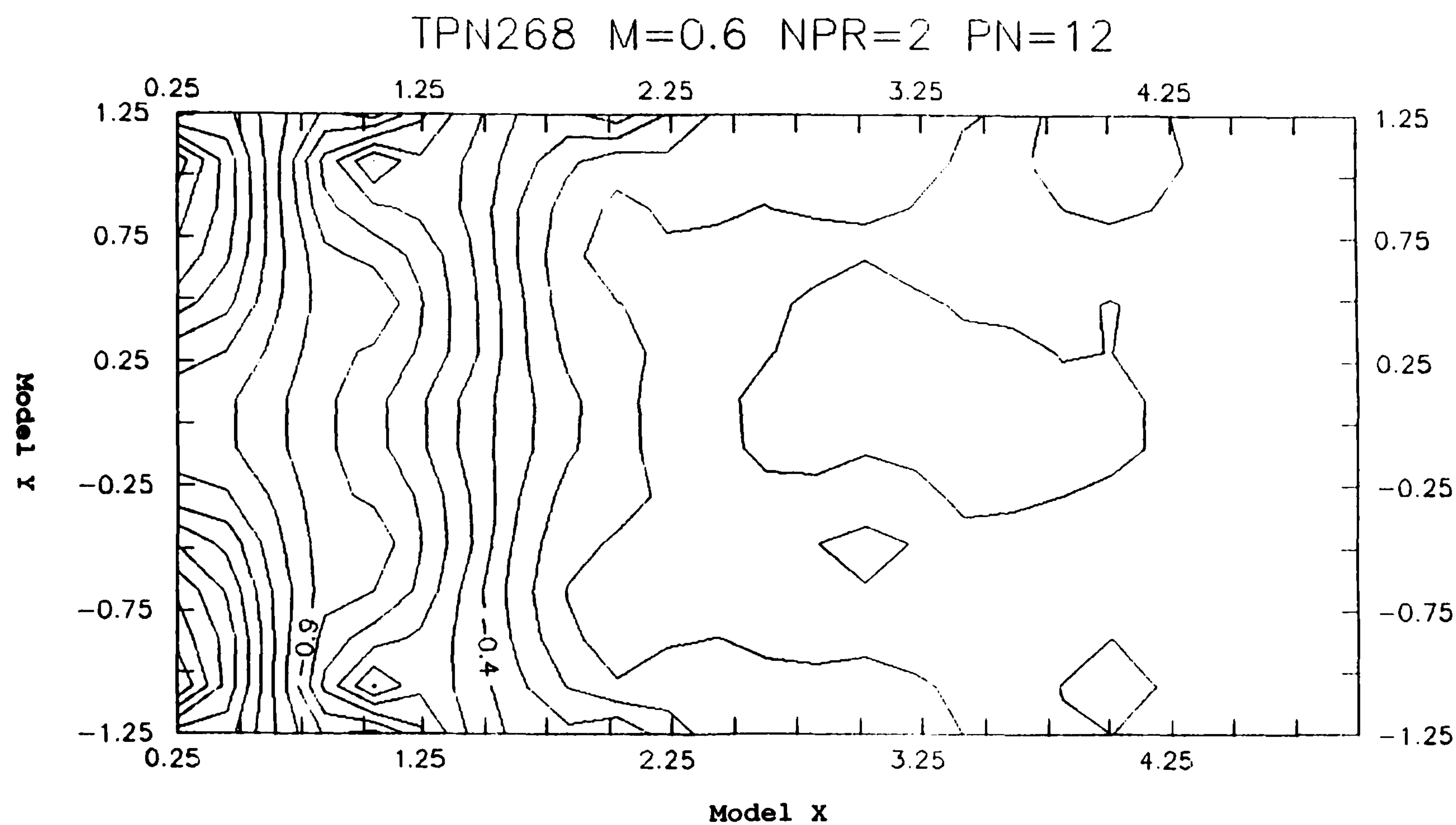

Figure A2. Pressure Coefficient (C_p) Contours: Mach 0.6, NPR = 2.0, L_{Cowl}

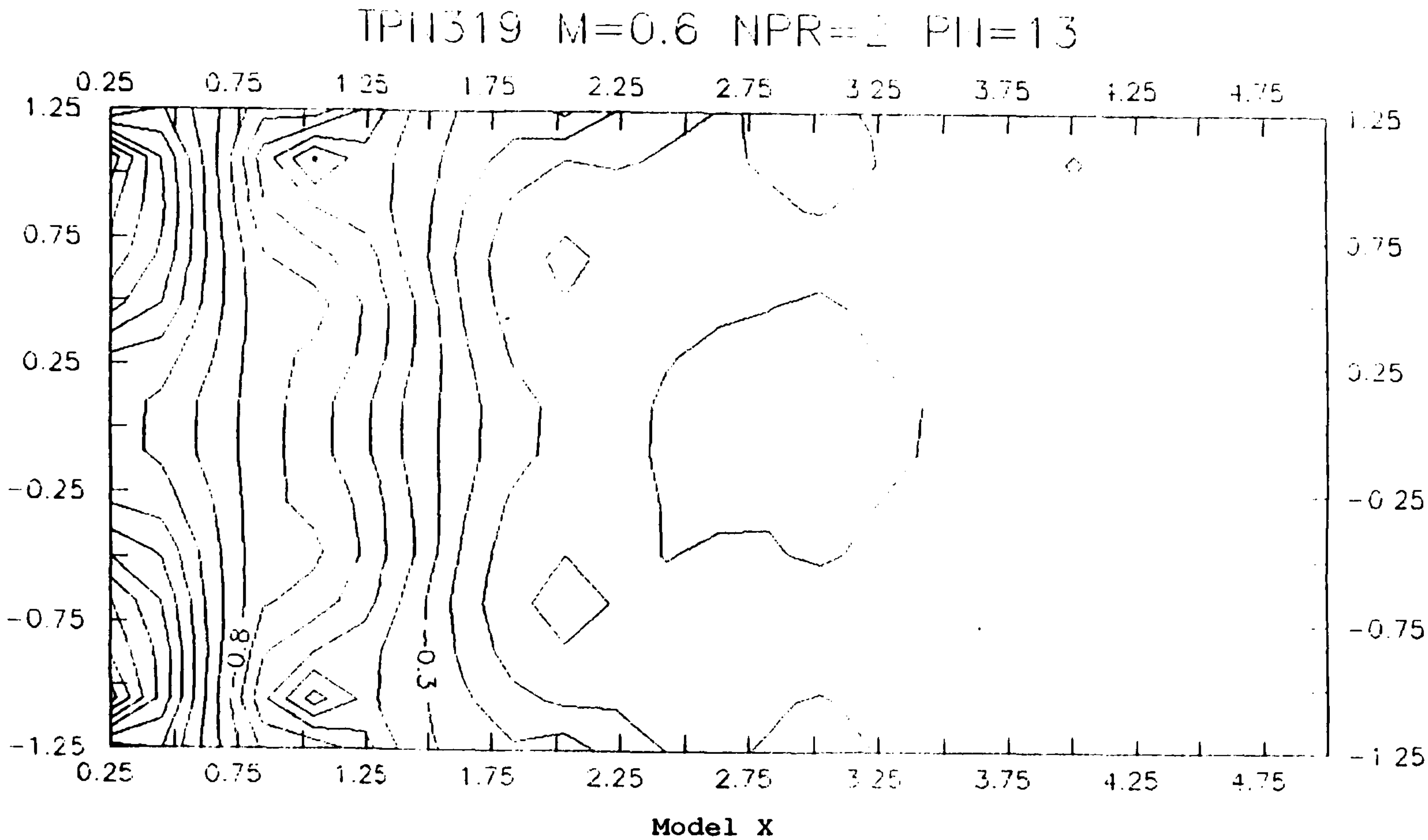

Figure A3. Pressure Coefficient (C_p) Contours: Mach 0.6, NPR = 2.0, +5 Cowl

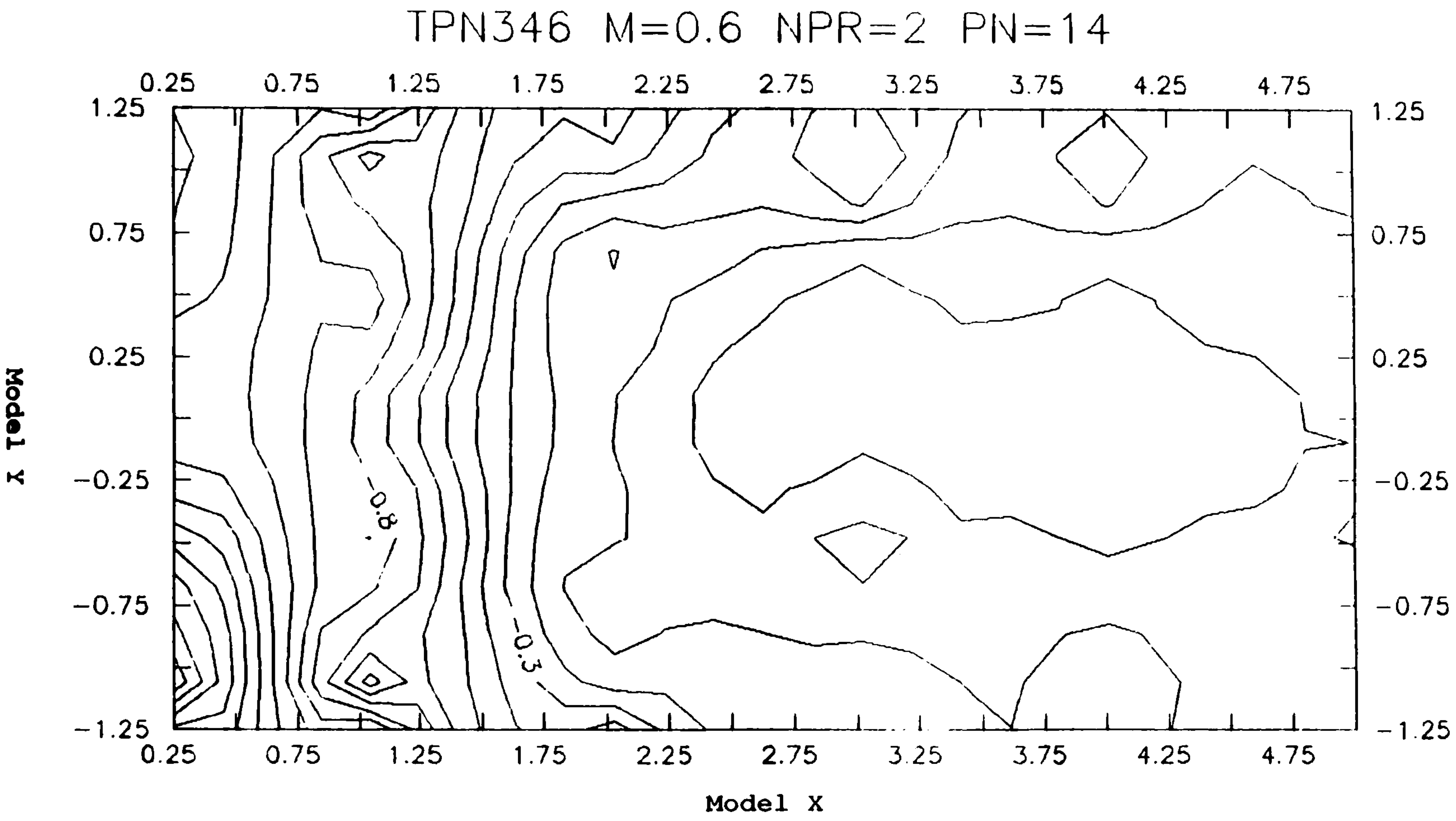

Figure A4. Pressure Coefficient (C_p) Contours: Mach 0.6, NPR = 2.0, -5 Cowl

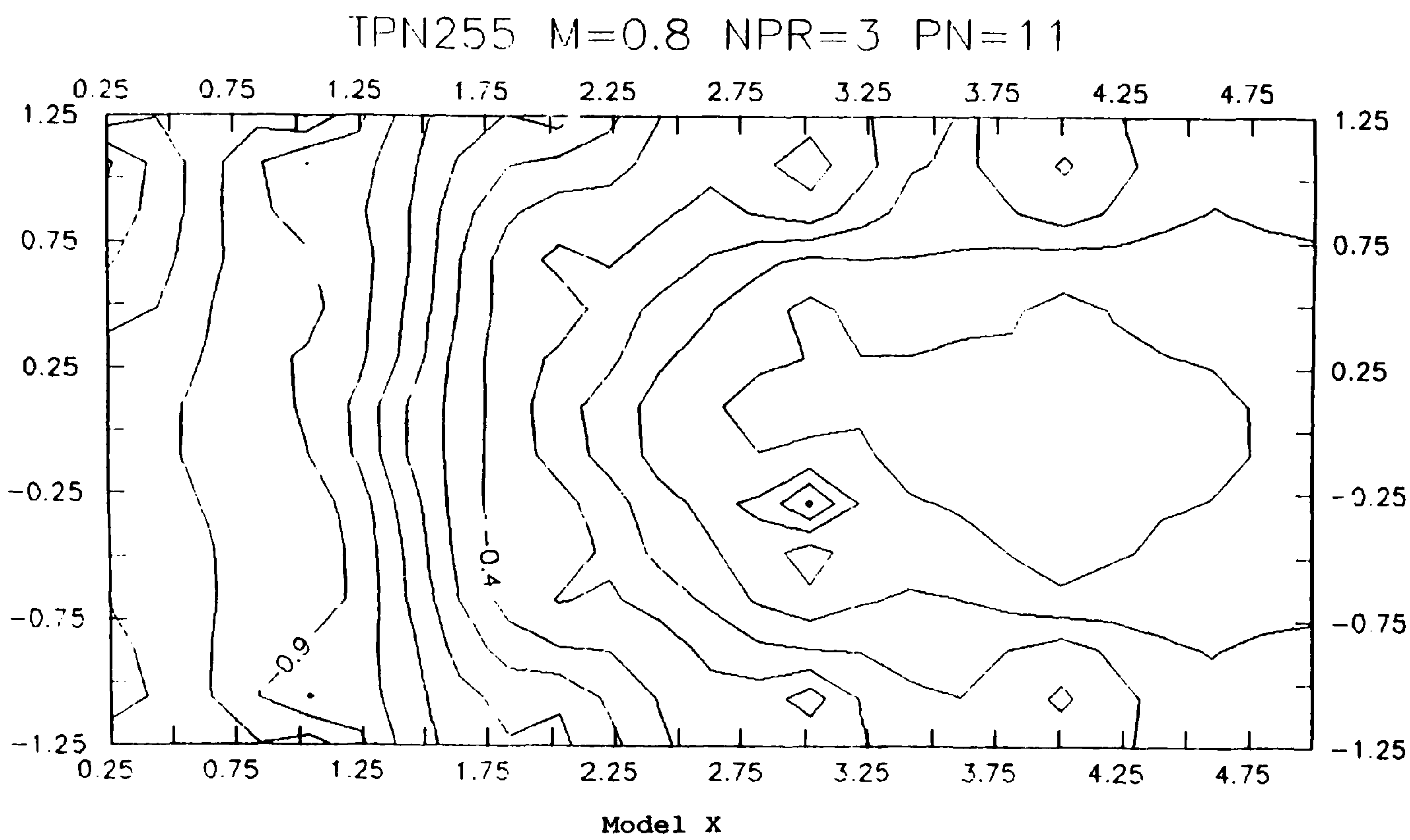

Figure A5. Pressure Coefficient (C_p) Contours: Mach 0.8, NPR = 3.0, BL Cowl

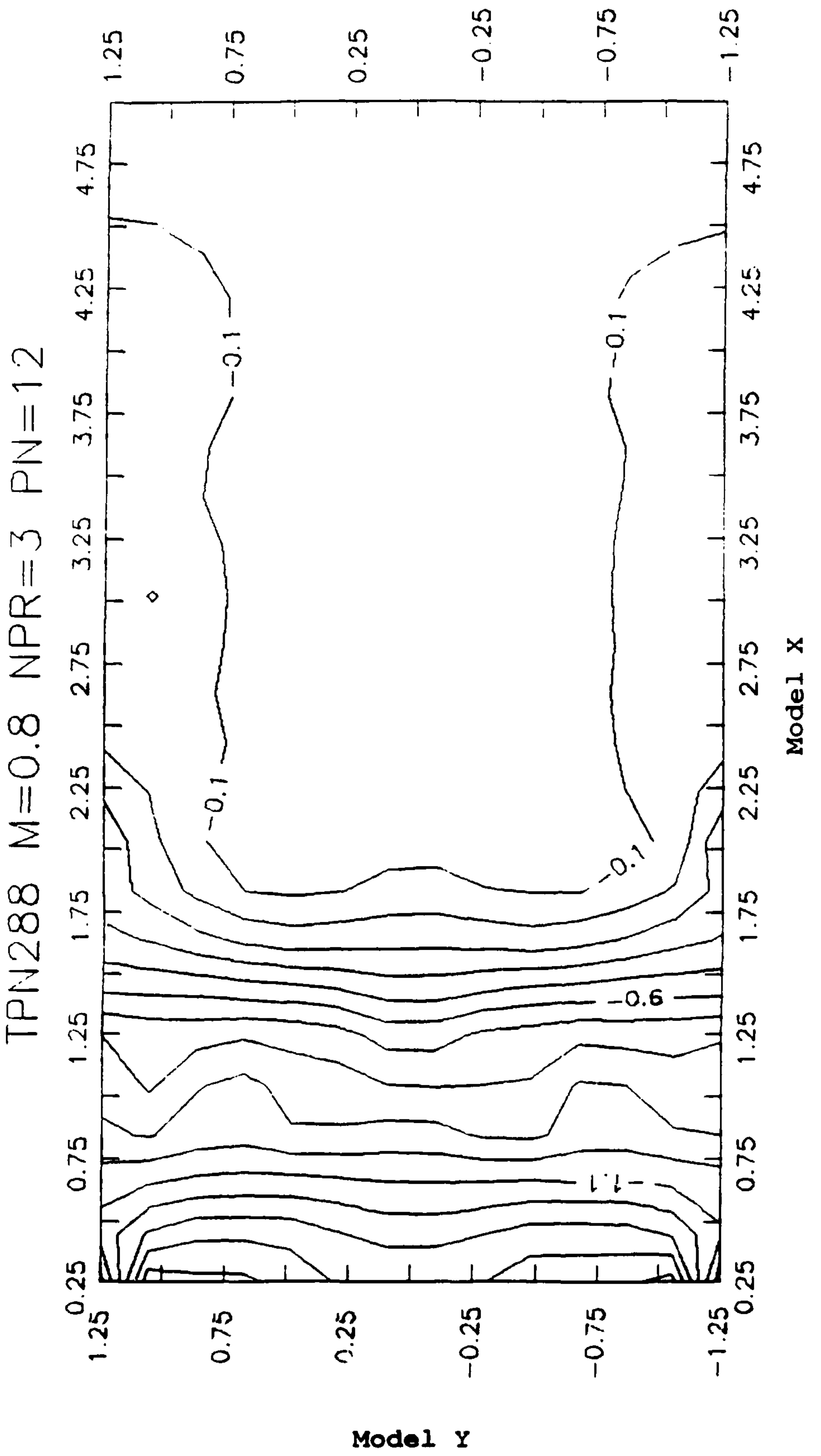

Figure A6. Pressure Coefficient (C_p) Contours: Mach 0.8, NPR = 3.0, L_{Cowl}

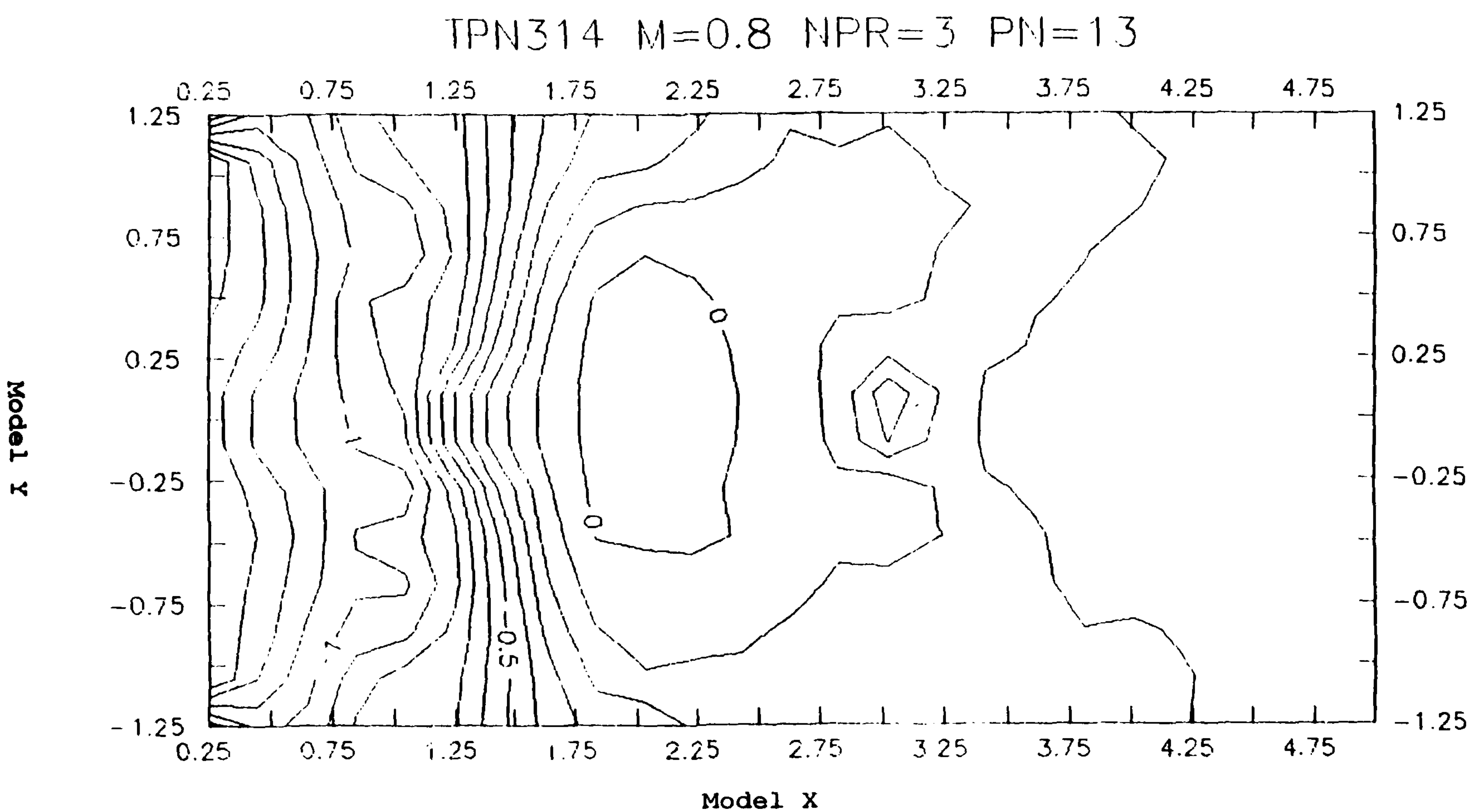

Figure A7. Pressure Coefficient (C_p) Contours: Mach 0.8, NPR = 3.0, +5 Cowl

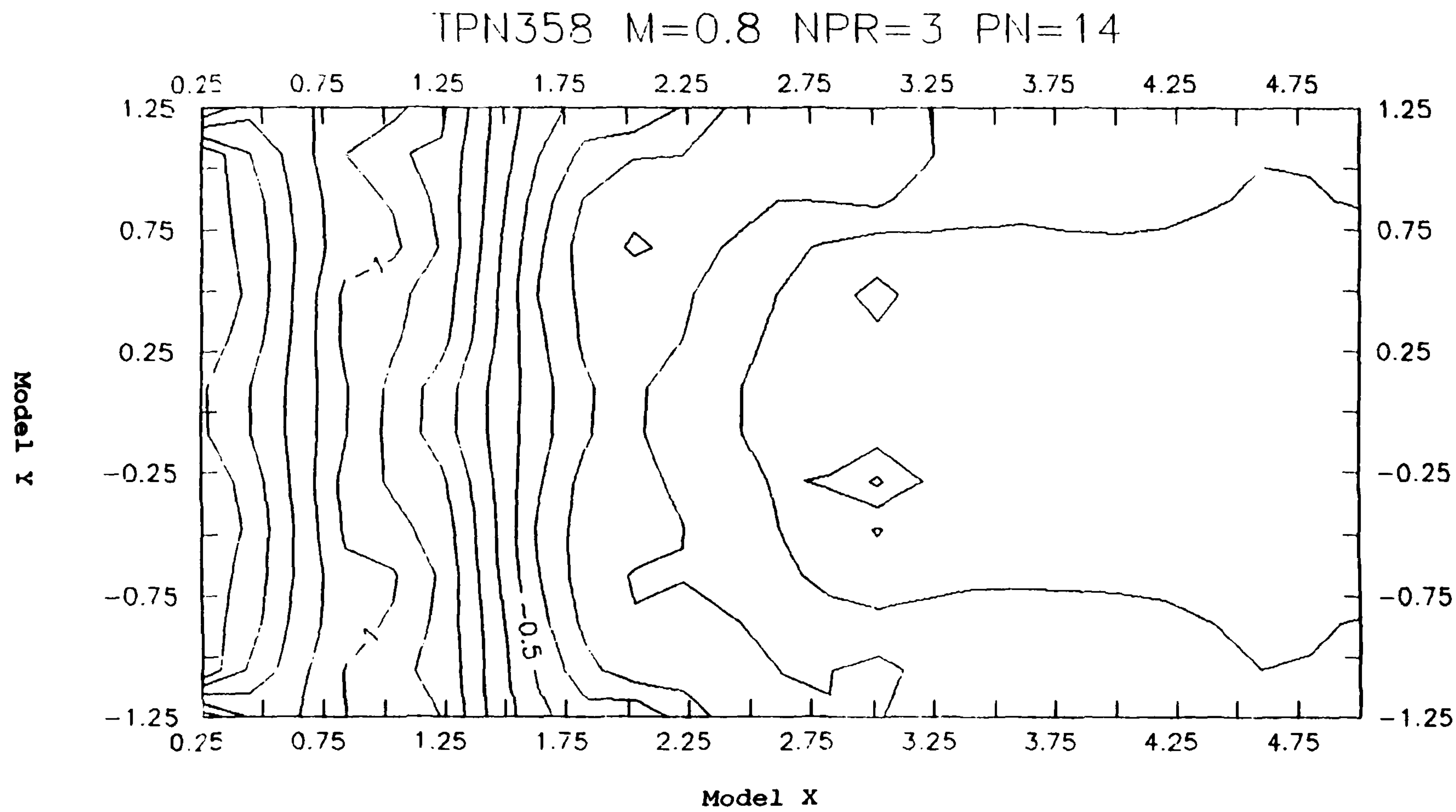

Figure A8. Pressure Coefficient (C_p) Contours: Mach 0.8, NPR = 3.0, -5 Cowl

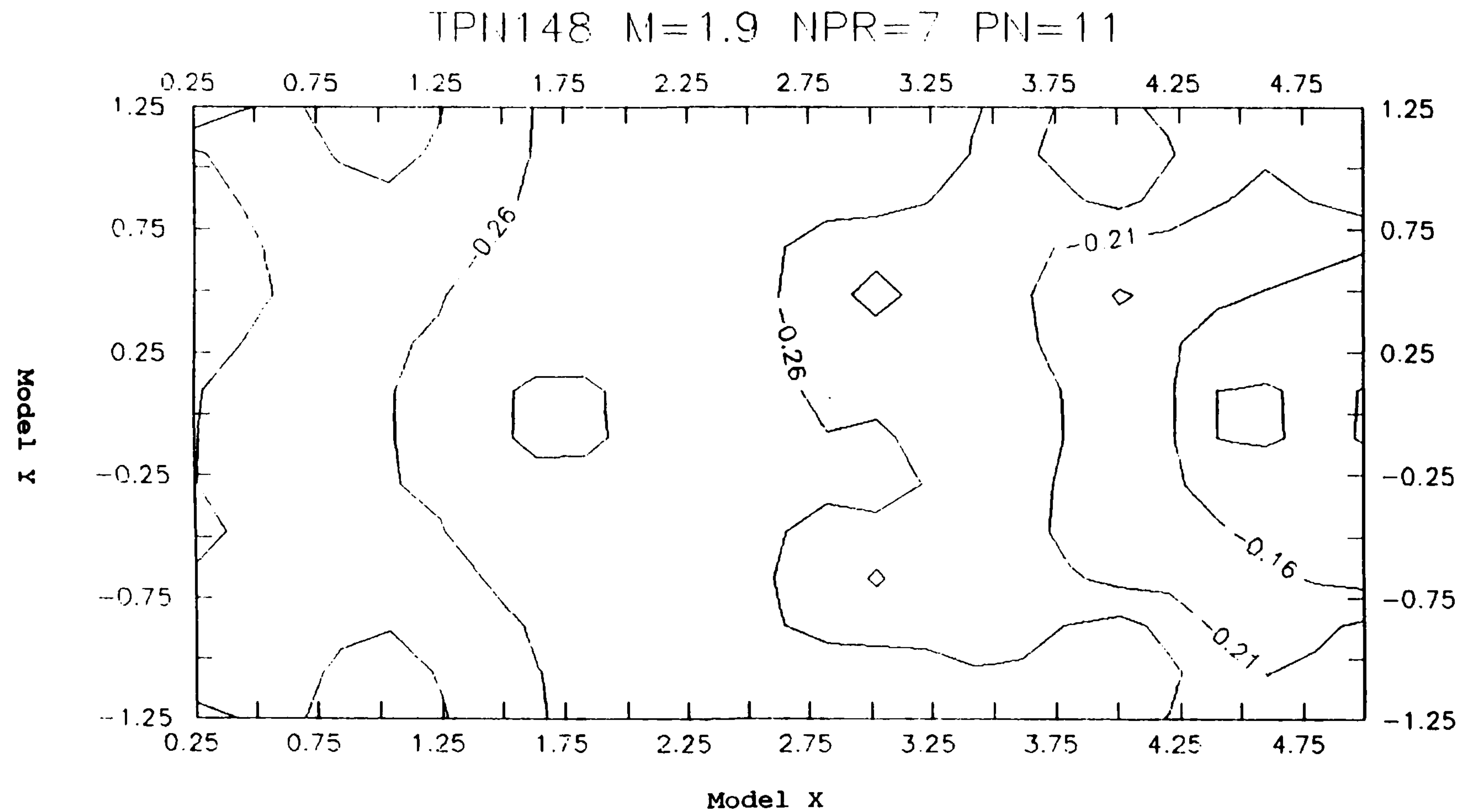

Figure A9. Pressure Coefficient (C_p) Contours: Mach 1.9, NPR = 7.0, BL Cowl

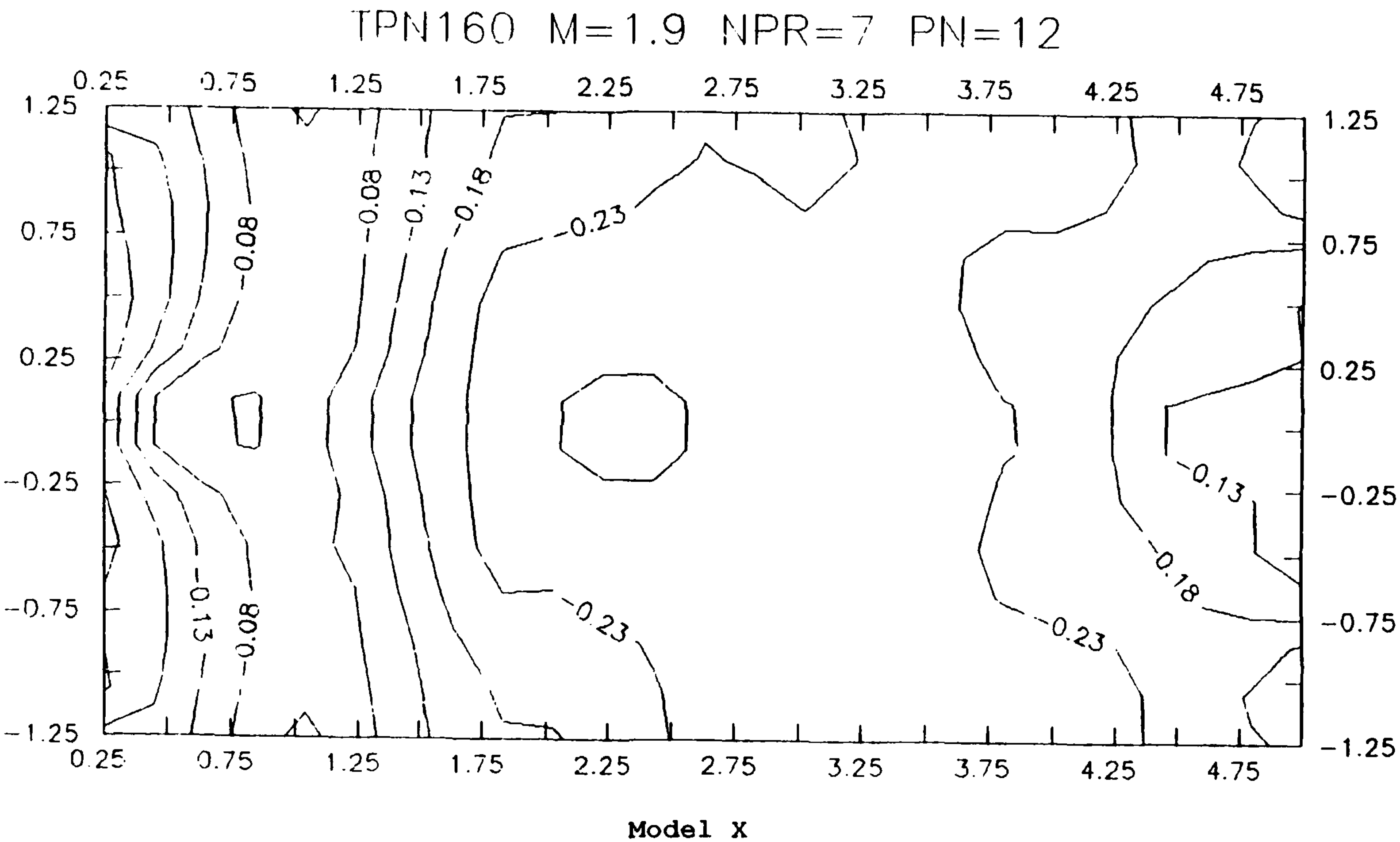

Figure A10. Pressure Coefficient (C_p) Contours: Mach 1.9, NPR = 7.0, L_{Cowl}

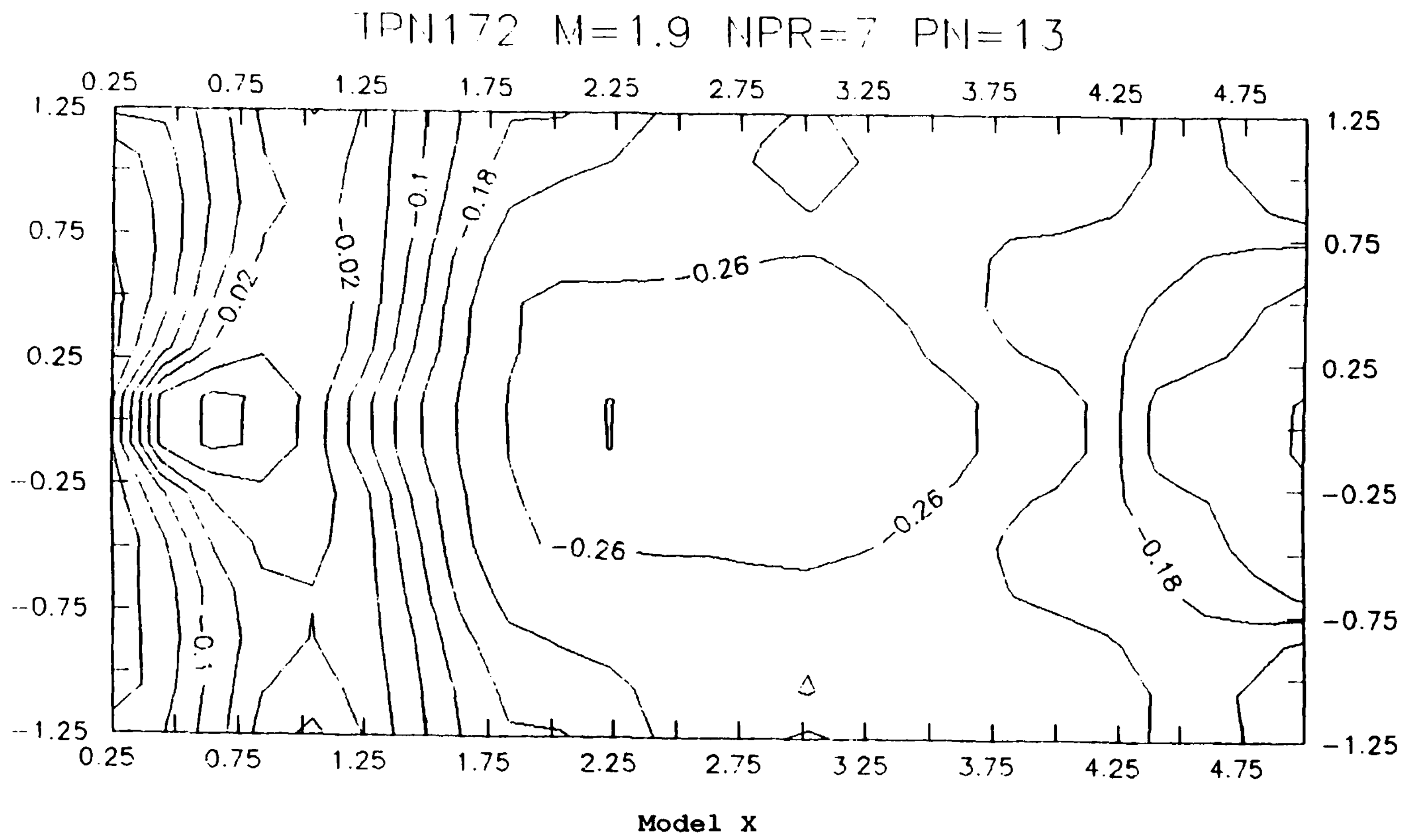

Figure A11. Pressure Coefficient (C_p) Contours: Mach 1.9, NPR = 7.0, +5 Cowl

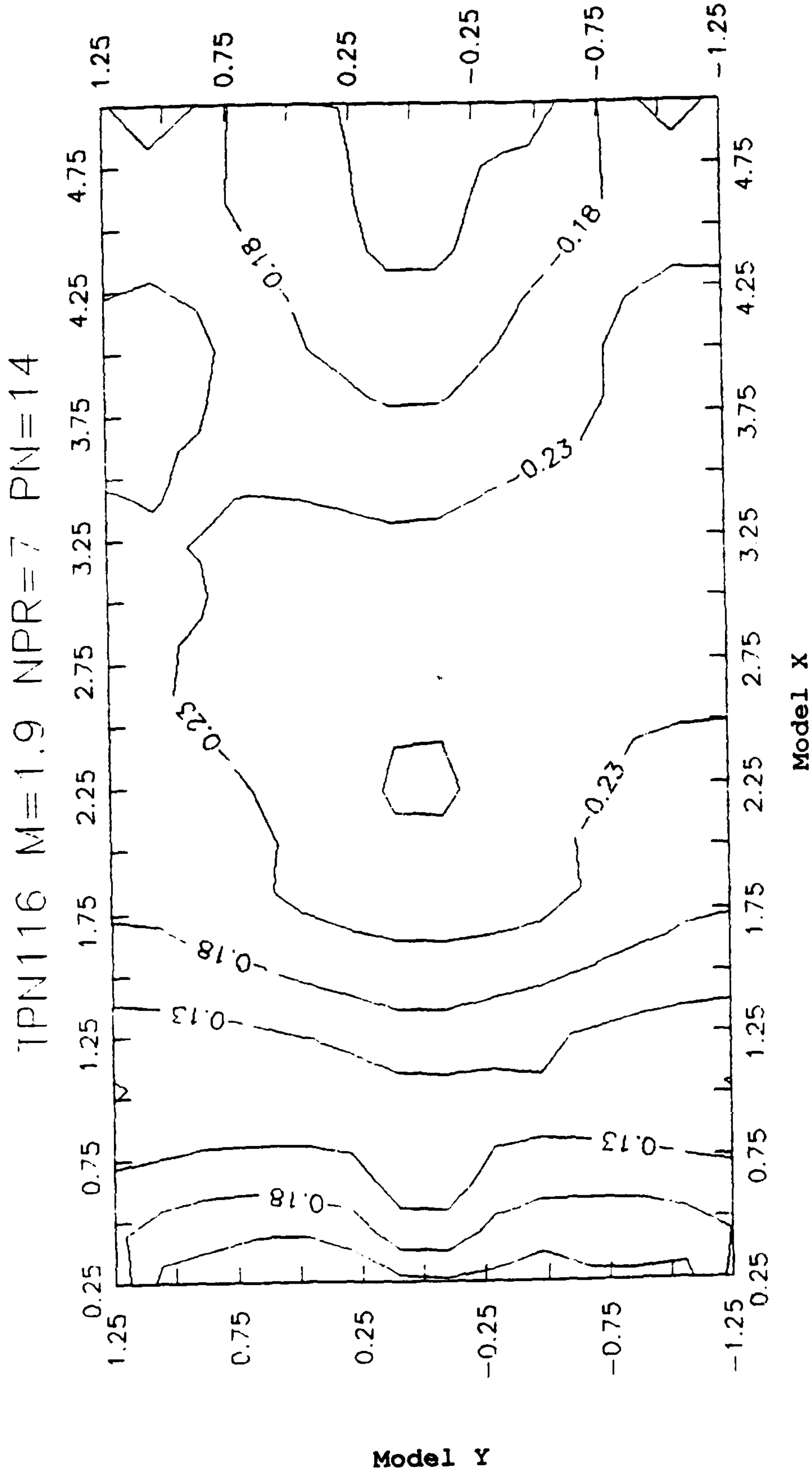

Figure A12. Pressure Coefficient (C_p) Contours: Mach 1.9, NPR = 7.0, -5 Cowl

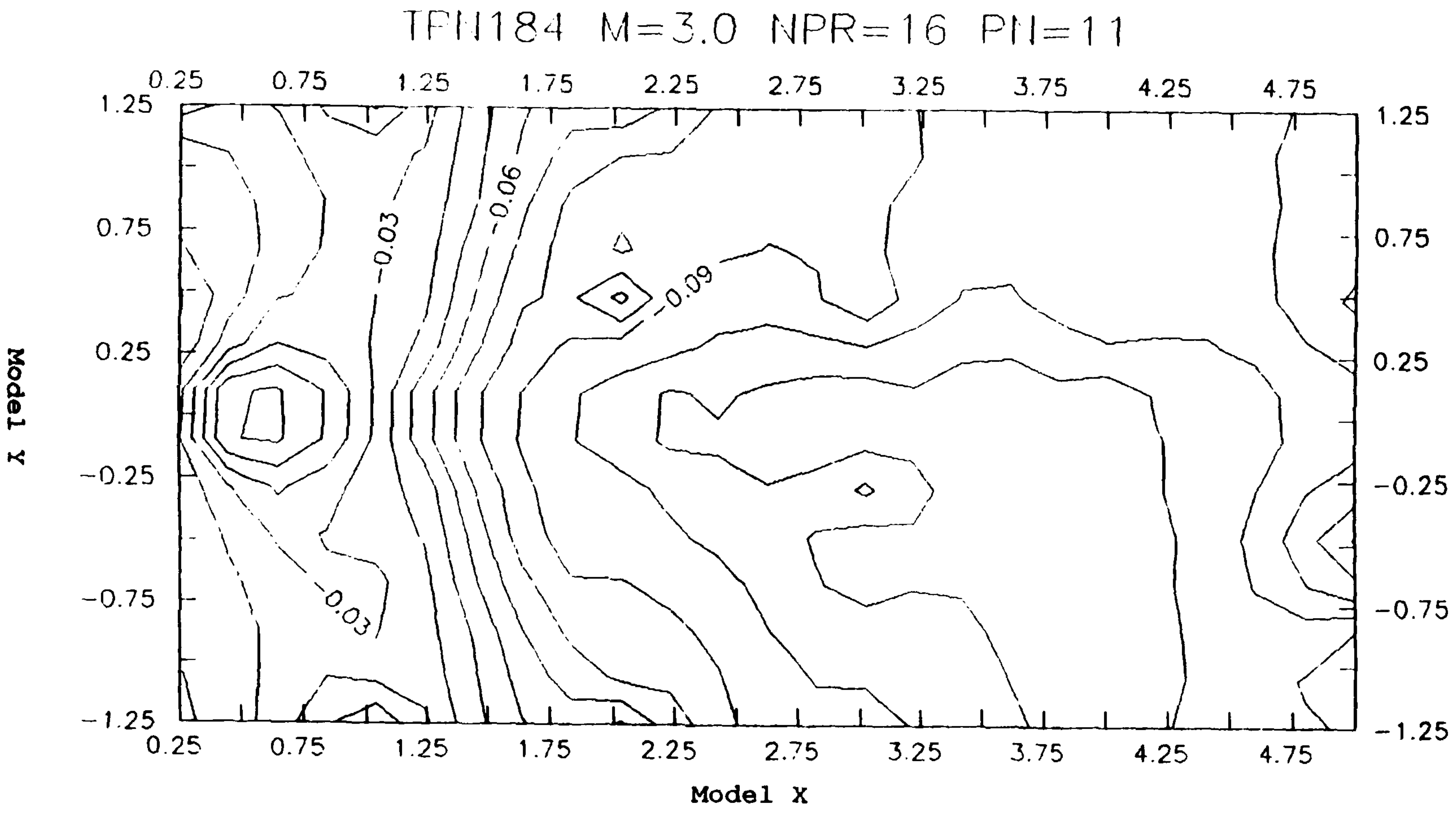

Figure A13. Pressure Coefficient (C_p) Contours:
Mach 3.0, NPR = 16.0, BL Cowl

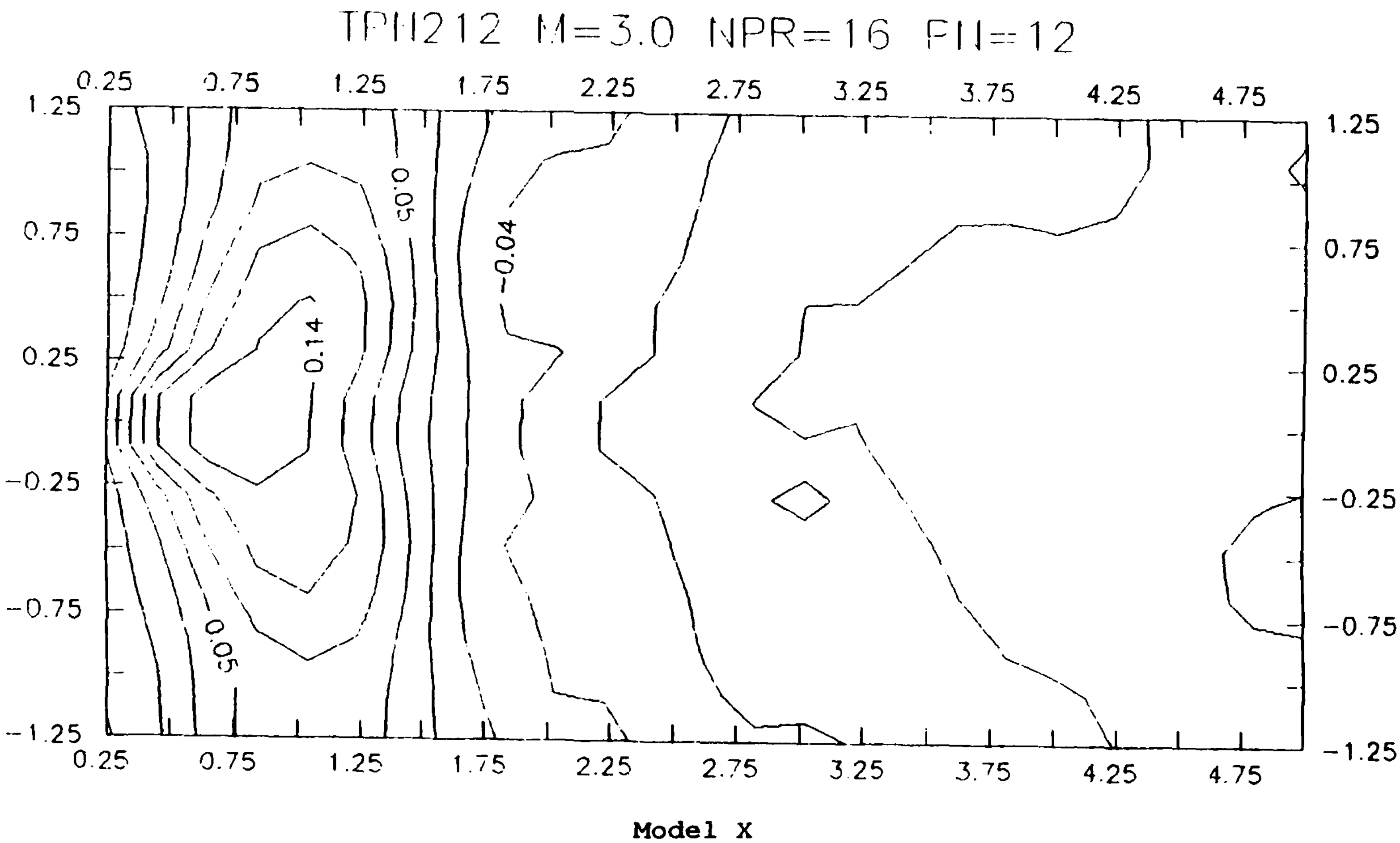

Figure A14. Pressure Coefficient (C_p) Contours: Mach 3.0, NPR = 16.0, L Cowl

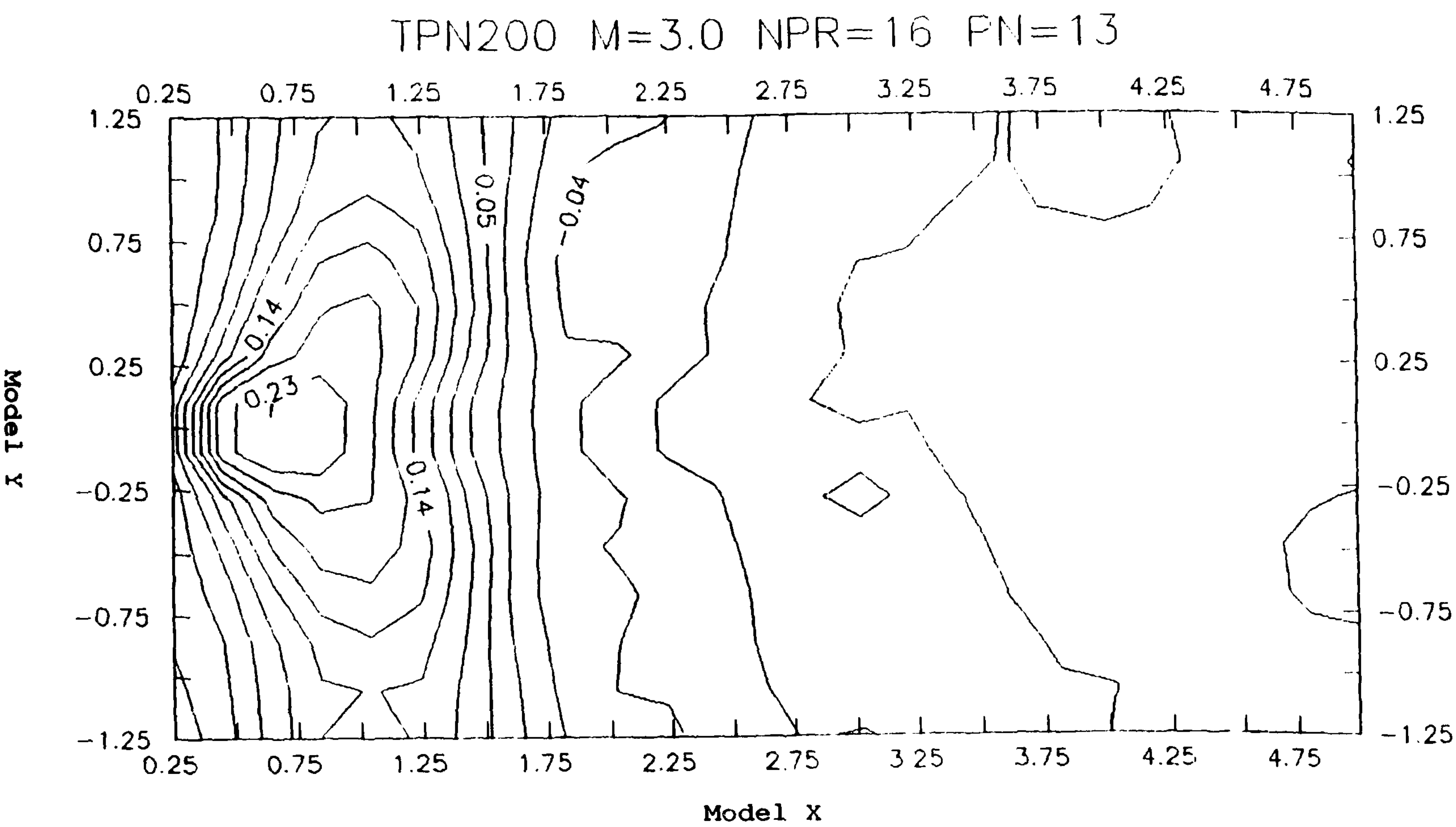

Figure A15. Pressure Coefficient (C_p) Contours:
Mach 3.0, NPR = 16.0, +5 Cowl

Appendix B: Surface Pressure Coefficient,

C_p vs Model Station

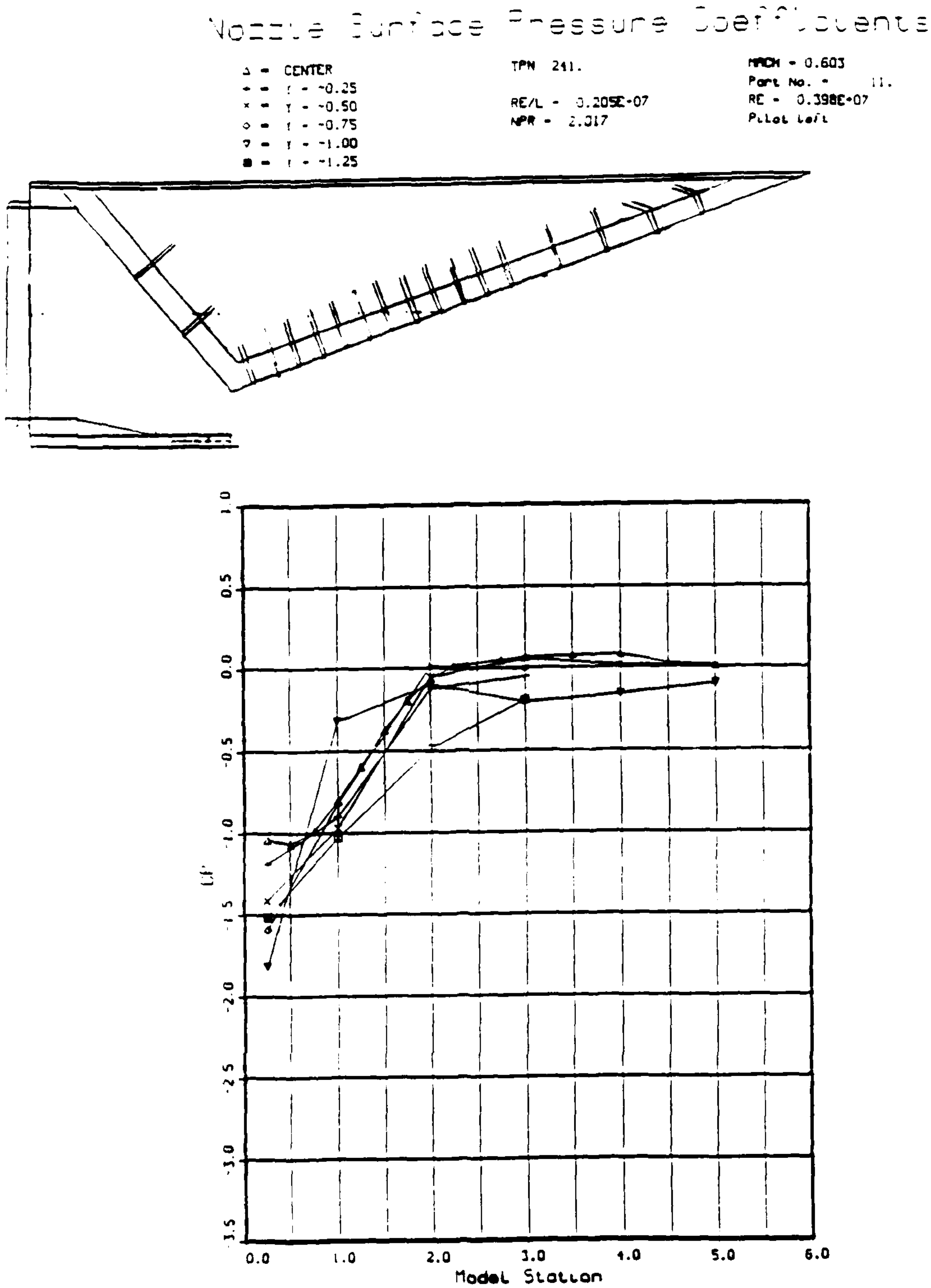

Figure B1. Surface Pressure Coefficients, C_p vs Model Station: Mach 0.6, NPR = 2.0, BL Cowl

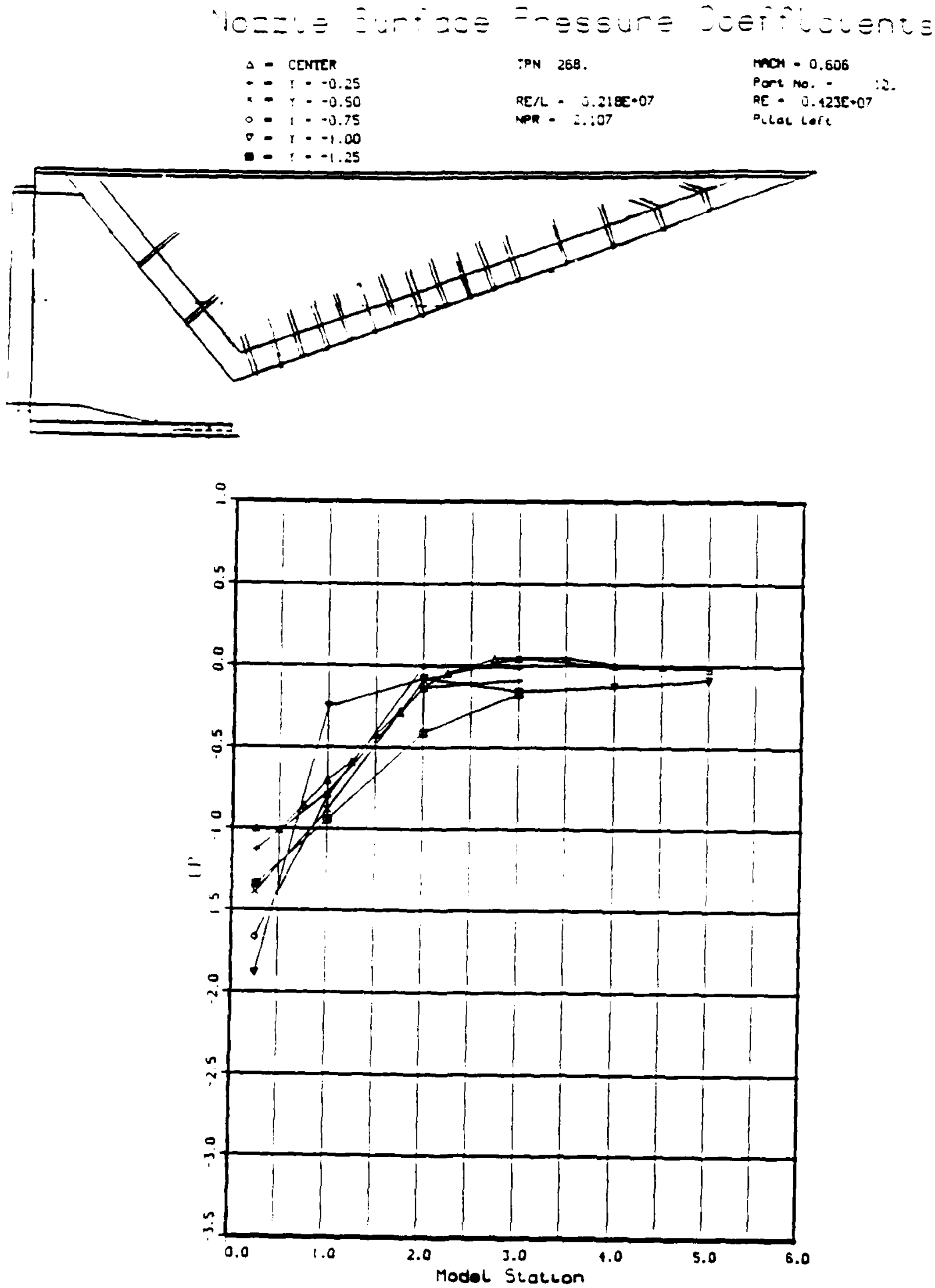

Figure B2. Surface Pressure Coefficients, C_p vs Model Station: Mach 0.6, NPR = 2.0, L Cowl

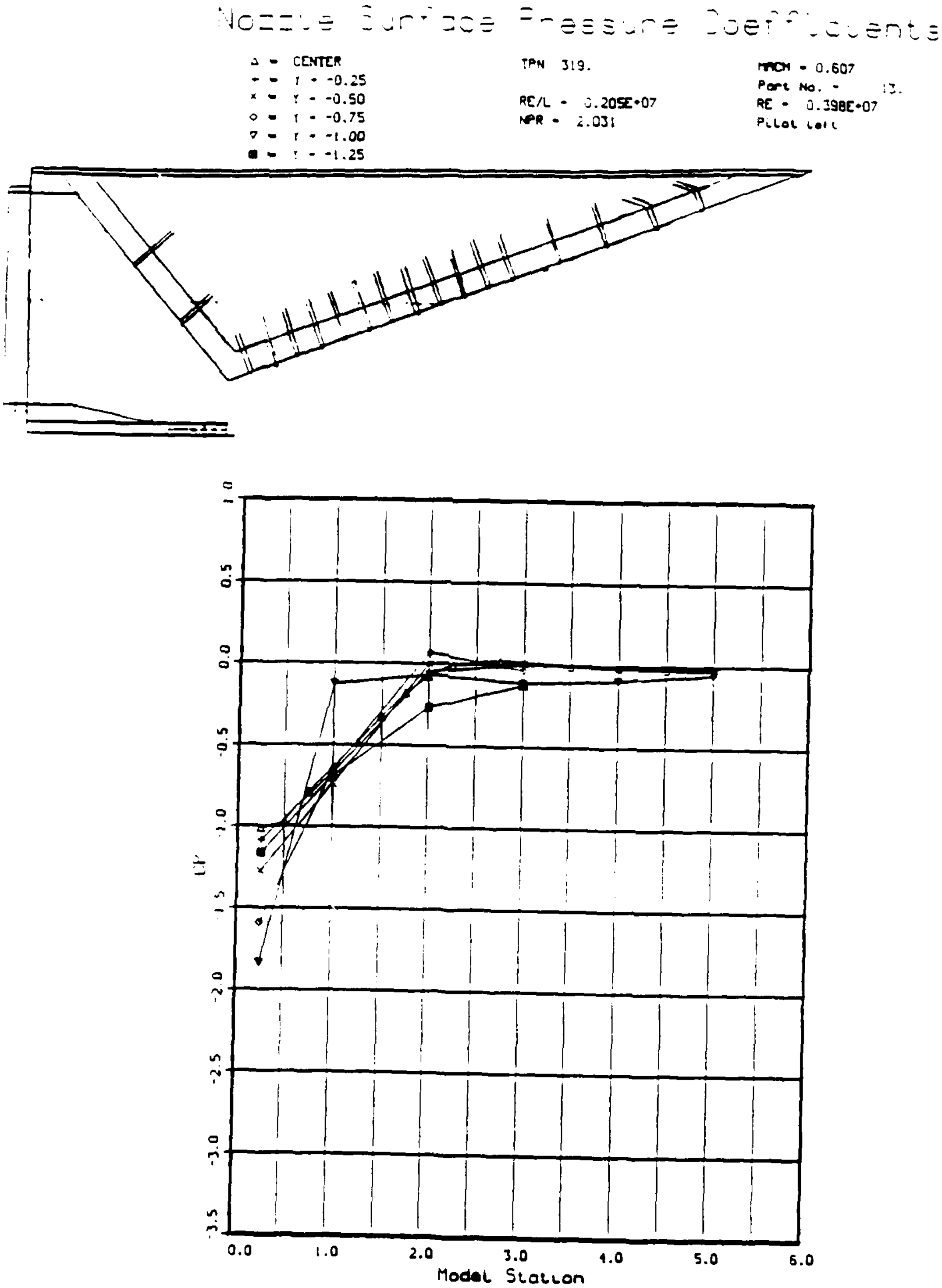

Figure B3. Surface Pressure Coefficients, C_p vs Model Station: Mach 0.6, NPR = 2.0, +5 Cowl

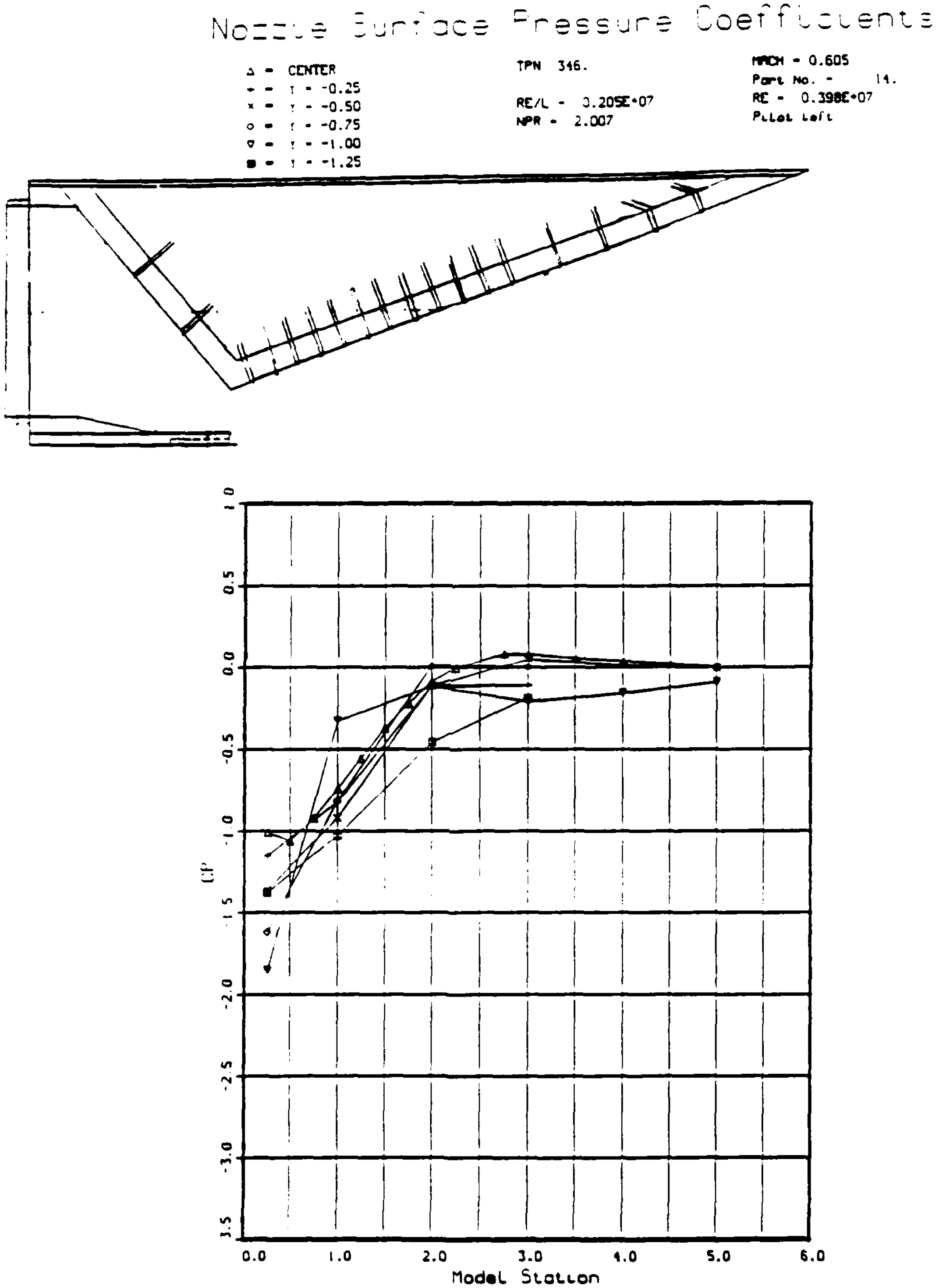

Figure B4. Surface Pressure Coefficients, C_p vs Model Station: Mach 0.6, NPR = 2.0, -5 Cowl

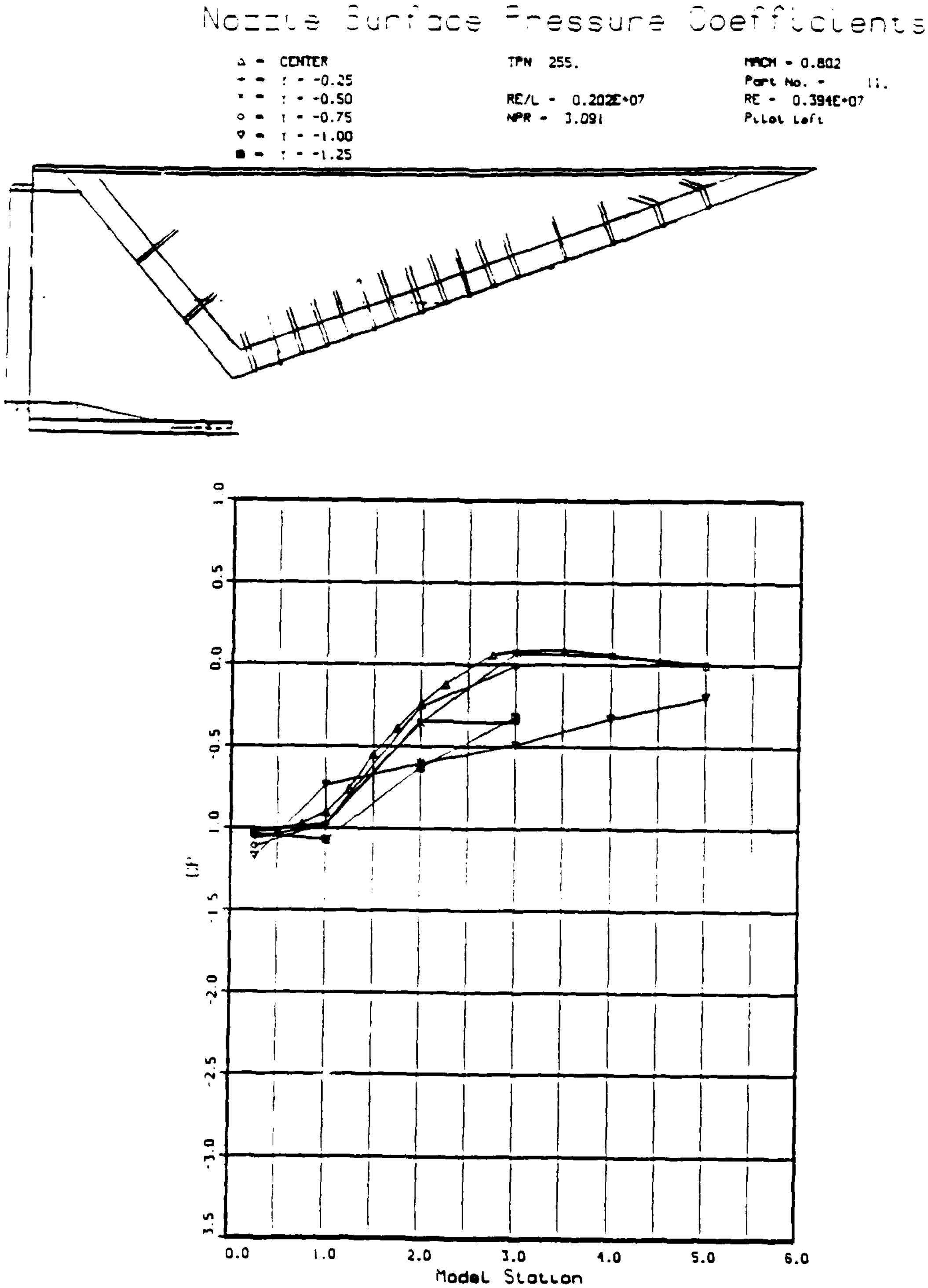

Figure B5. Surface Pressure Coefficients, C_p vs Model Station: Mach 0.8, NPR = 3.0, BL Cowl

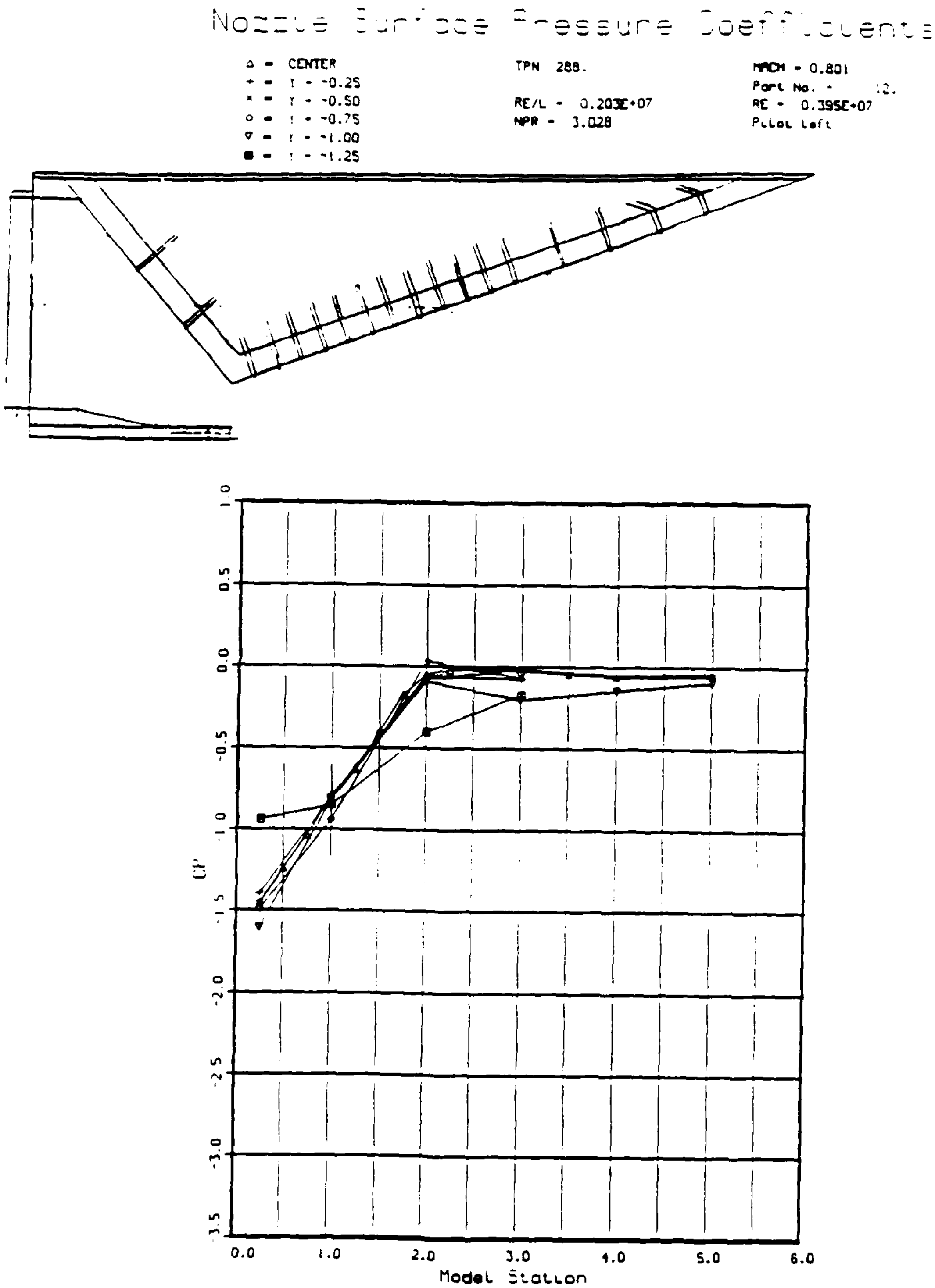

Figure B6. Surface Pressure Coefficients, C_p vs Model Station: Mach 0.8, NPR = 3.0, L Cowl

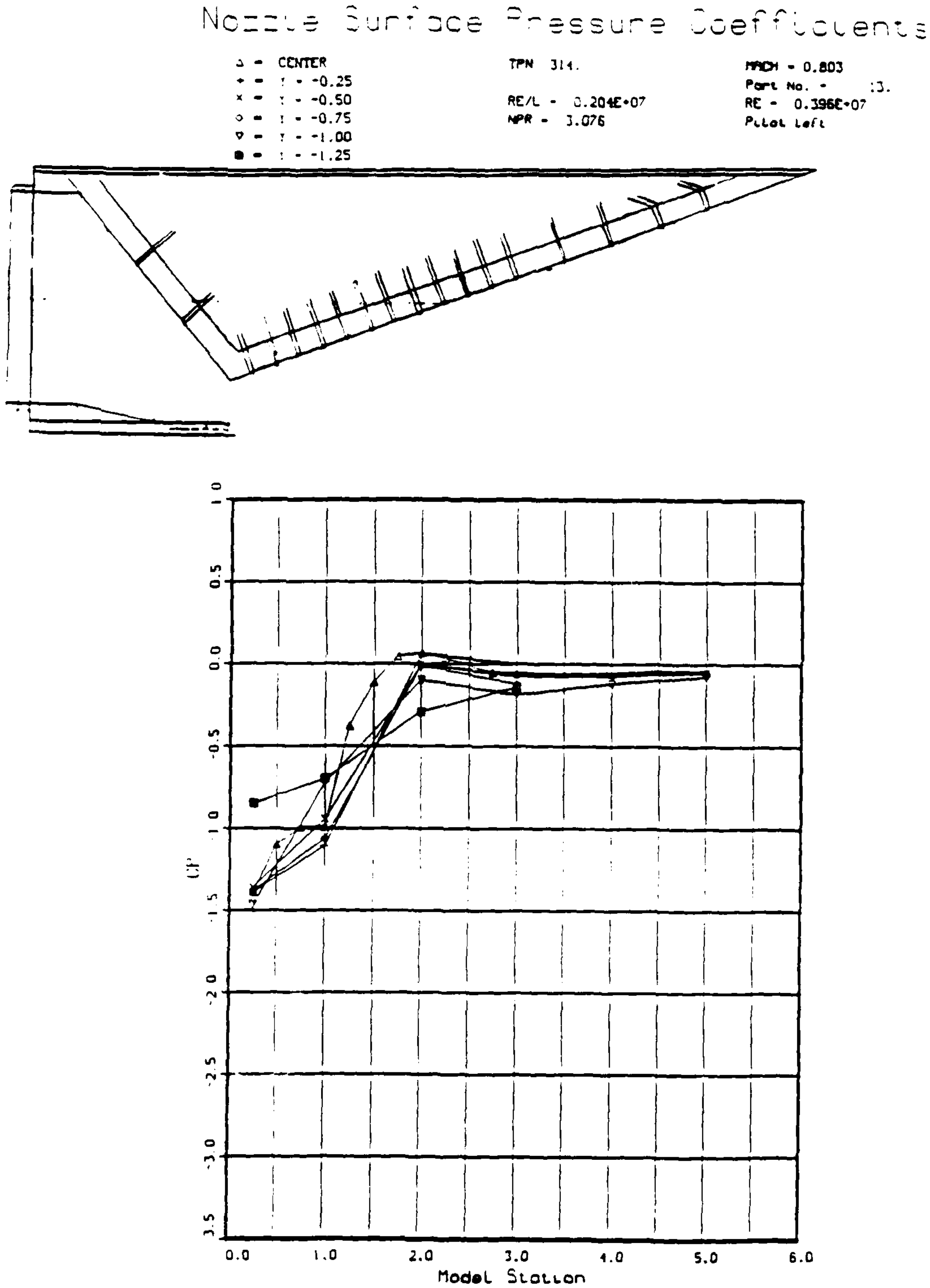

Figure B7. Surface Pressure Coefficients, C_p vs Model Station: Mach 0.8, NPR = 3.0, +5 Cowl

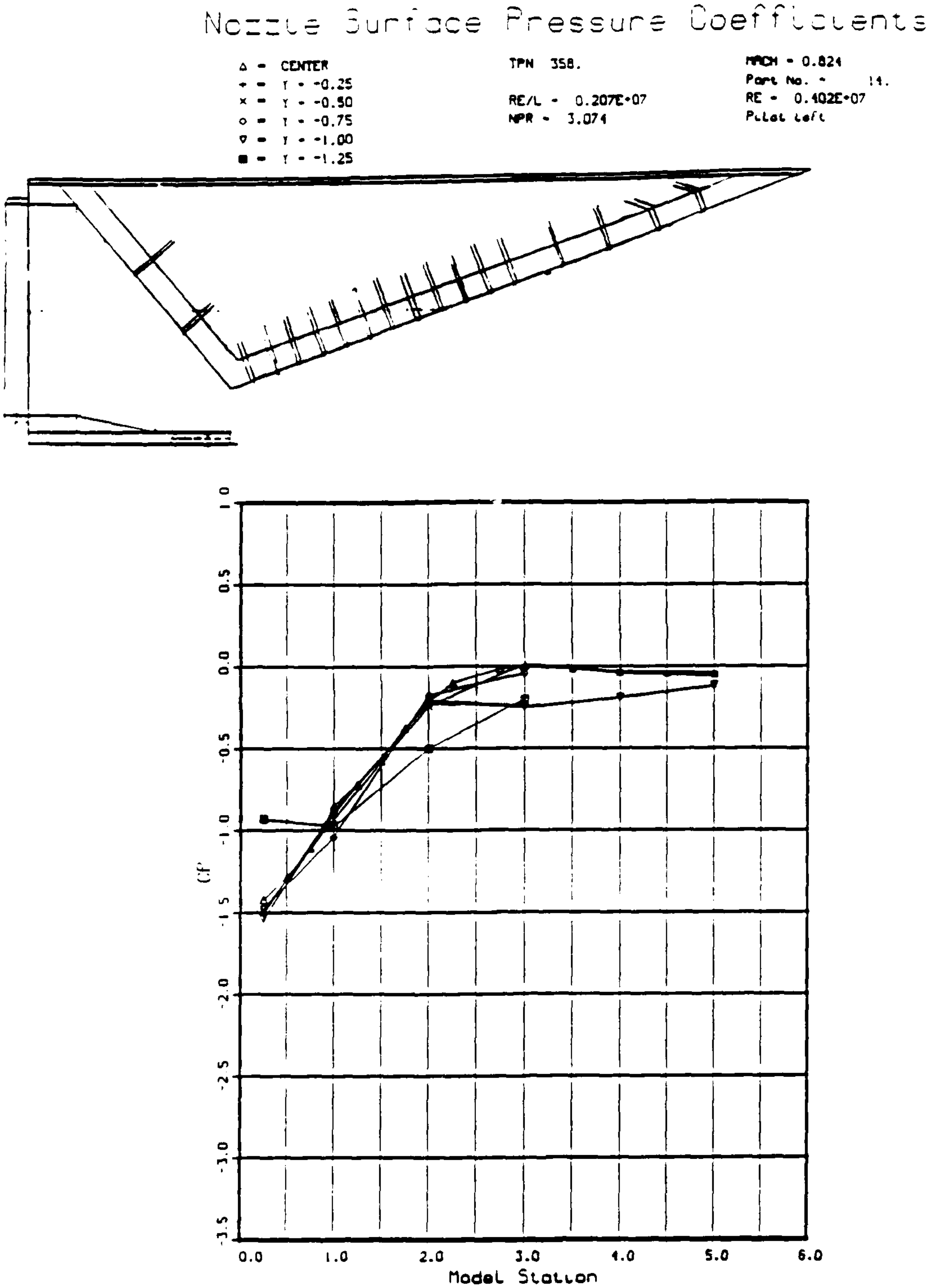

Figure B8. Surface Pressure Coefficients, C_p vs Model Station: Mach 0.8, NPR = 3.0, -5 Cowl

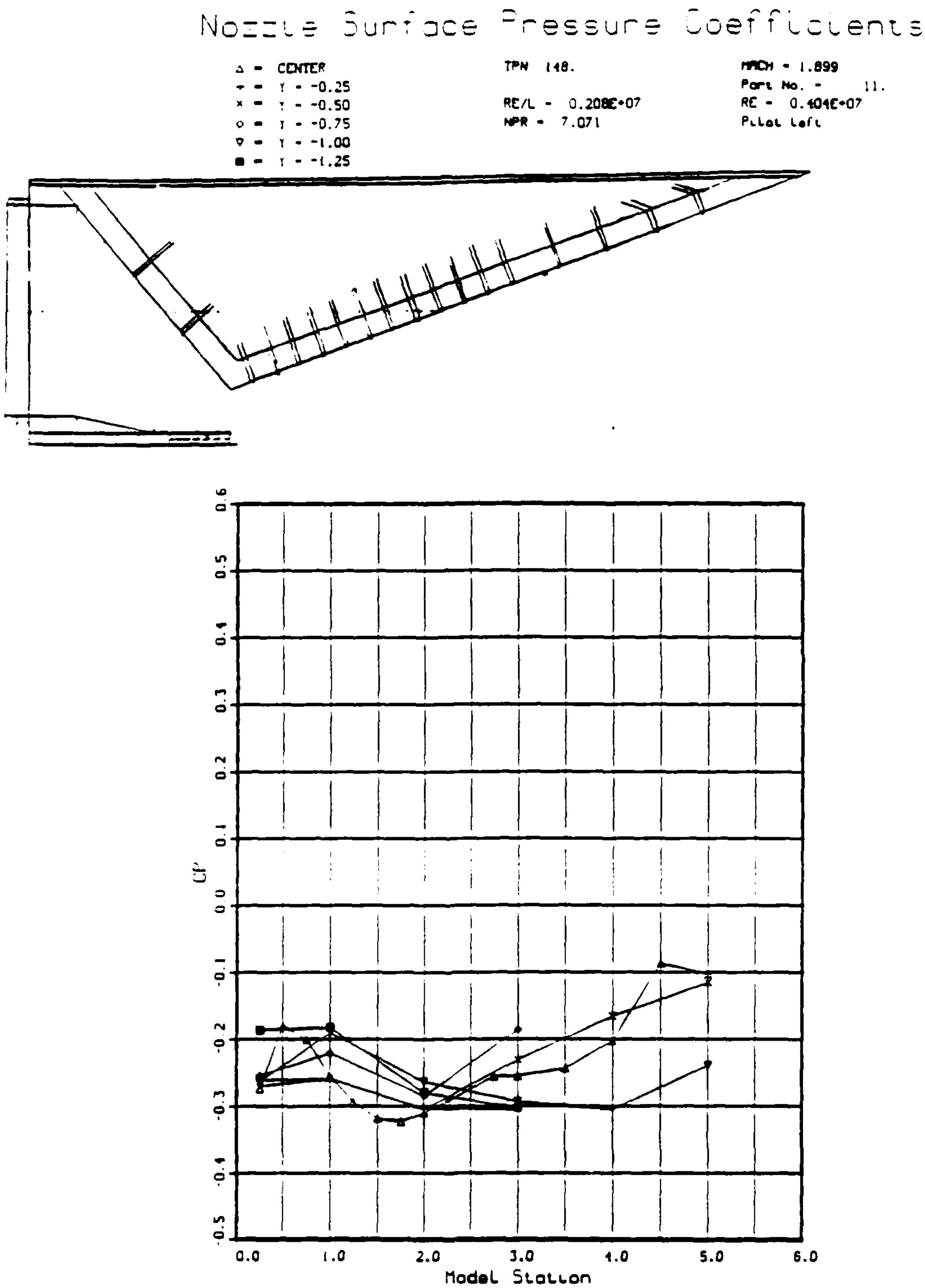

Figure B9. Surface Pressure Coefficients, C_p vs Model Station: Mach 1.9, NPR = 7.0, BL Cowl

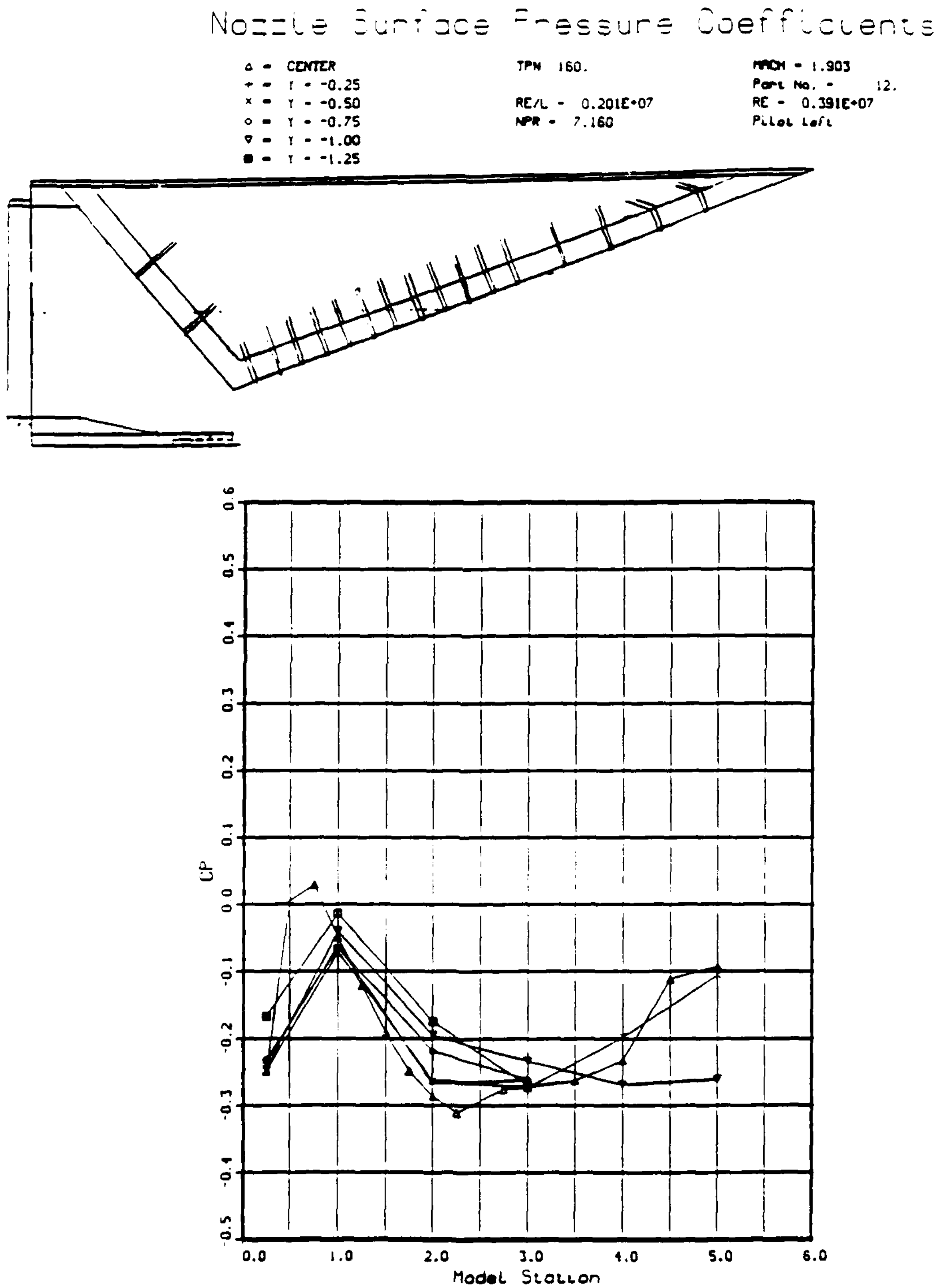

Figure B10. Surface Pressure Coefficients, C_p vs Model Station: Mach 1.9, NPR = 7.0, L Cowl

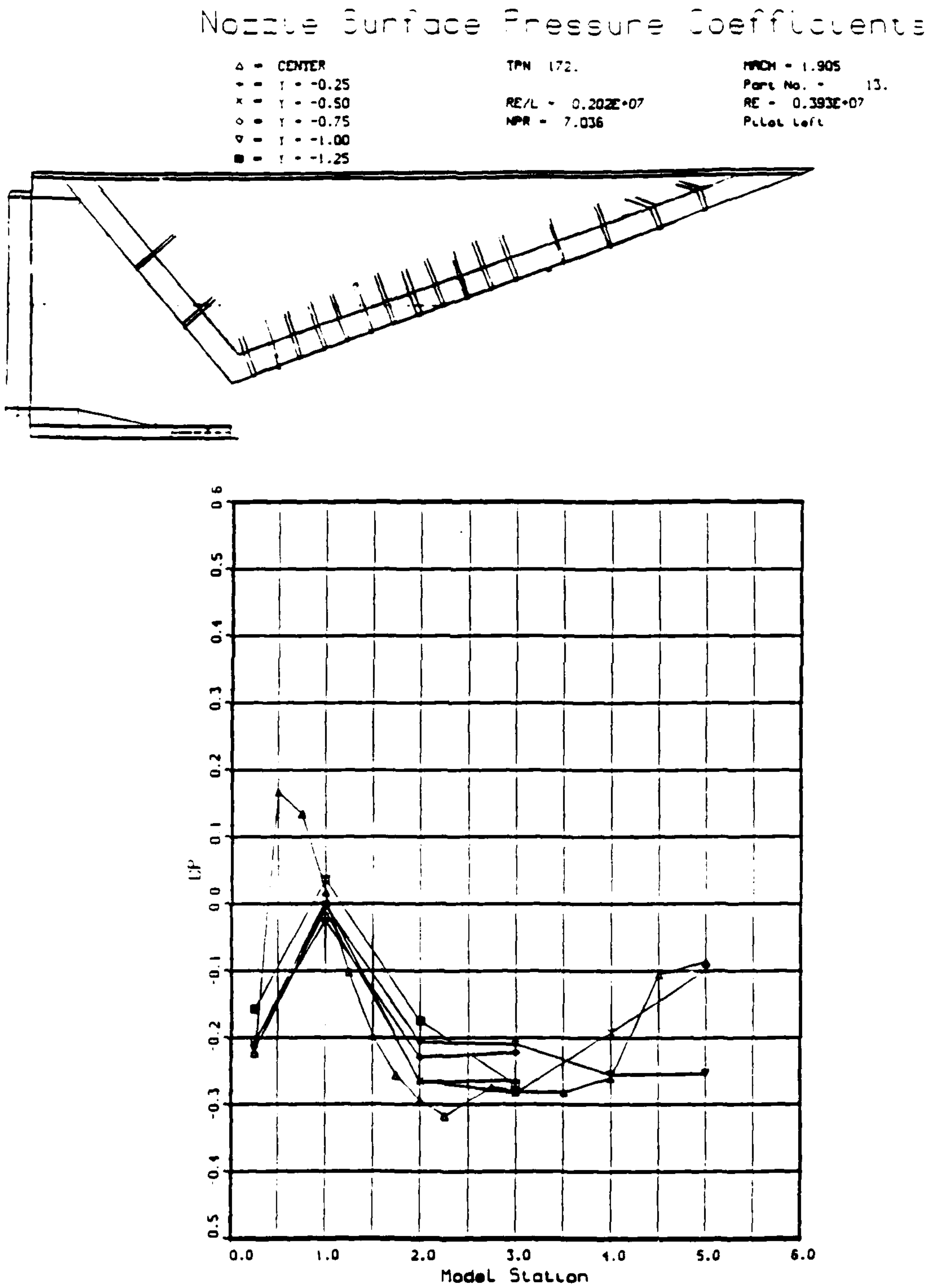

Figure B11. Surface Pressure Coefficients, C_p vs Model Station: Mach 1.9, NPR = 7.0, +5 Cowl

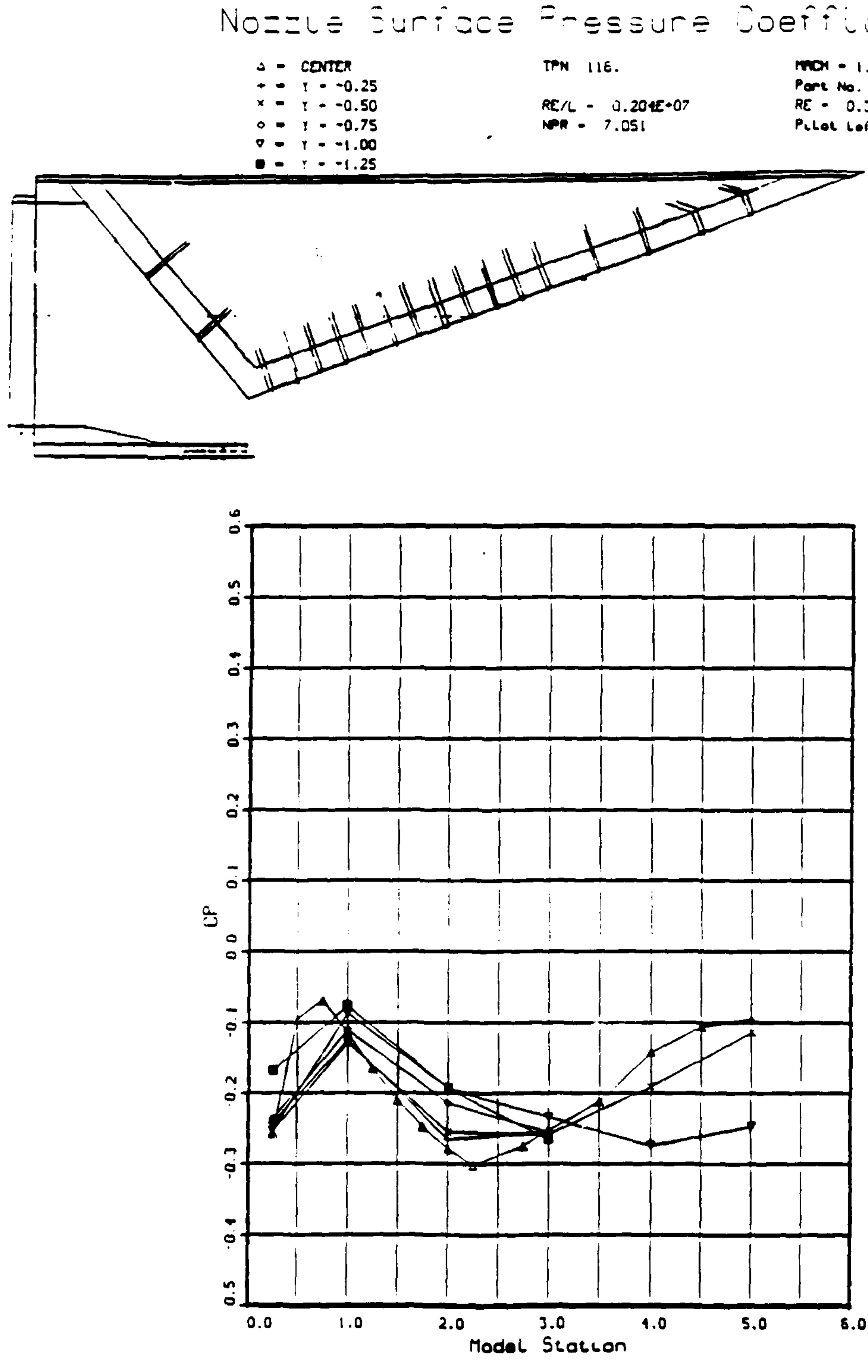

Figure B12. Surface Pressure Coefficients, C_p vs Model Station: Mach 1.9, NPR = 2.0, -5 Cowl

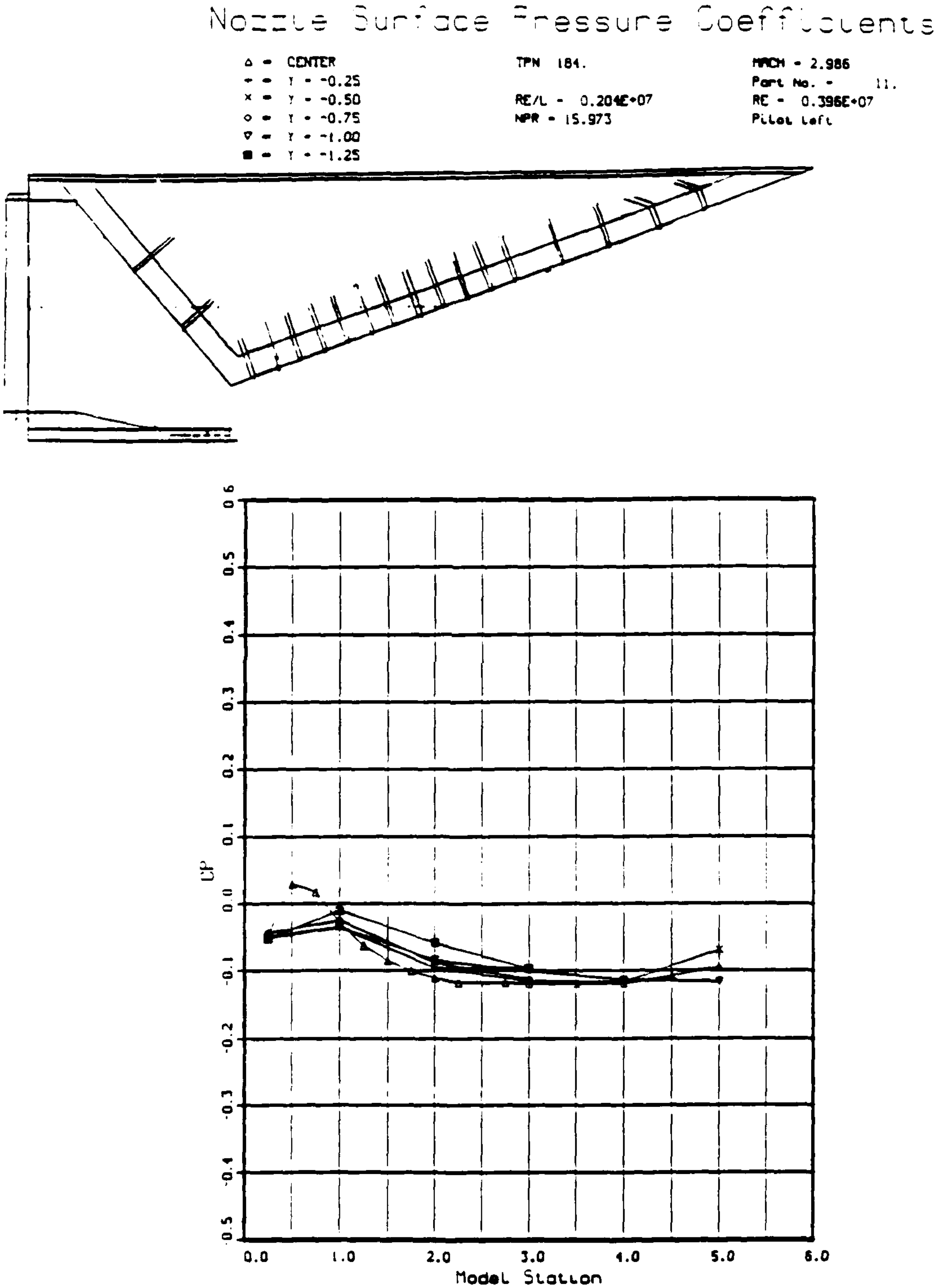

Figure B13. Surface Pressure Coefficients, C_p vs Model Station: Mach 3.0, NPR = 16.0, BL Cowl

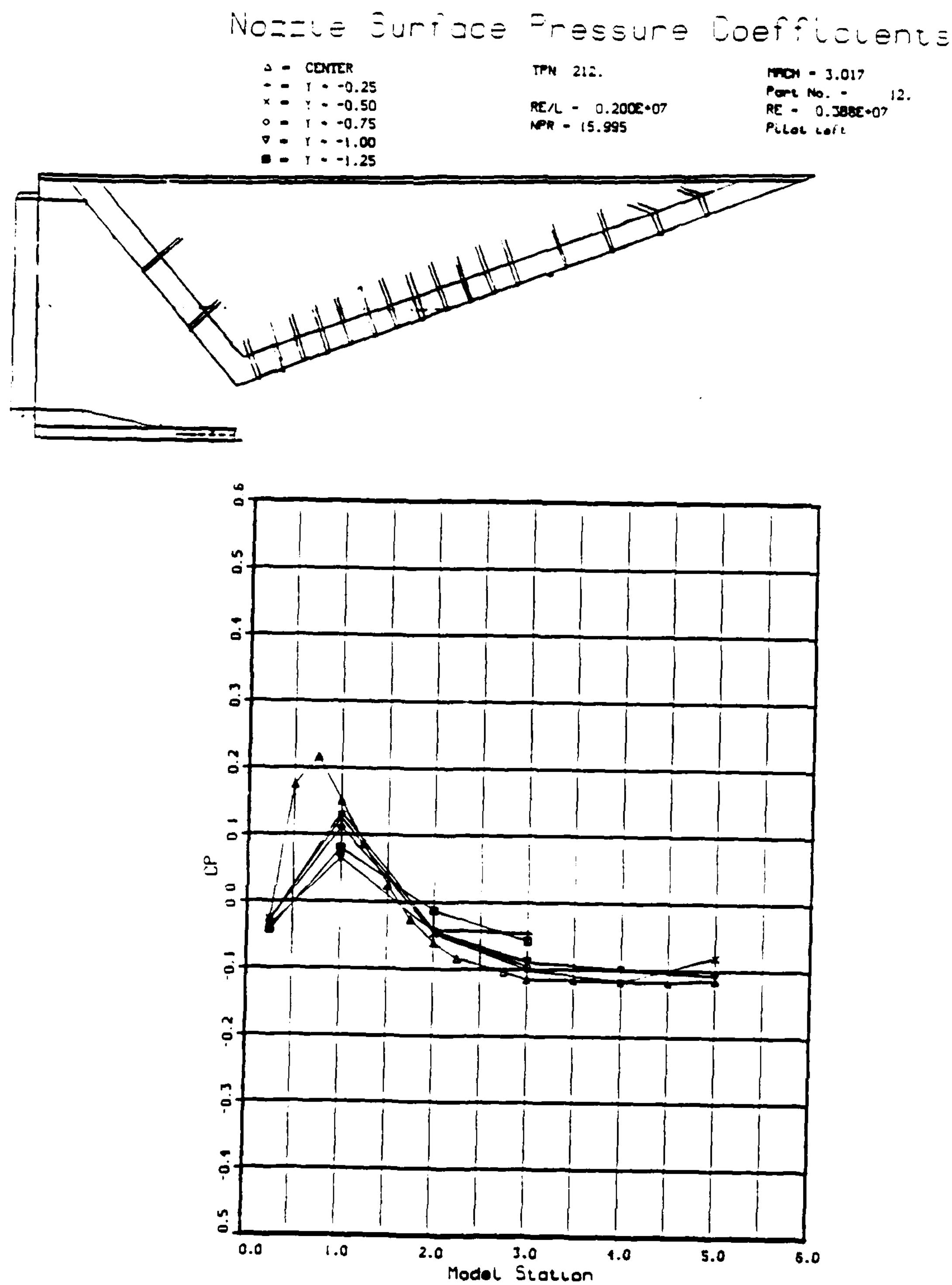

Figure B14. Surface Pressure Coefficients, C_p vs Model Station: Mach 3.0, NPR = 16.0, L Cowl

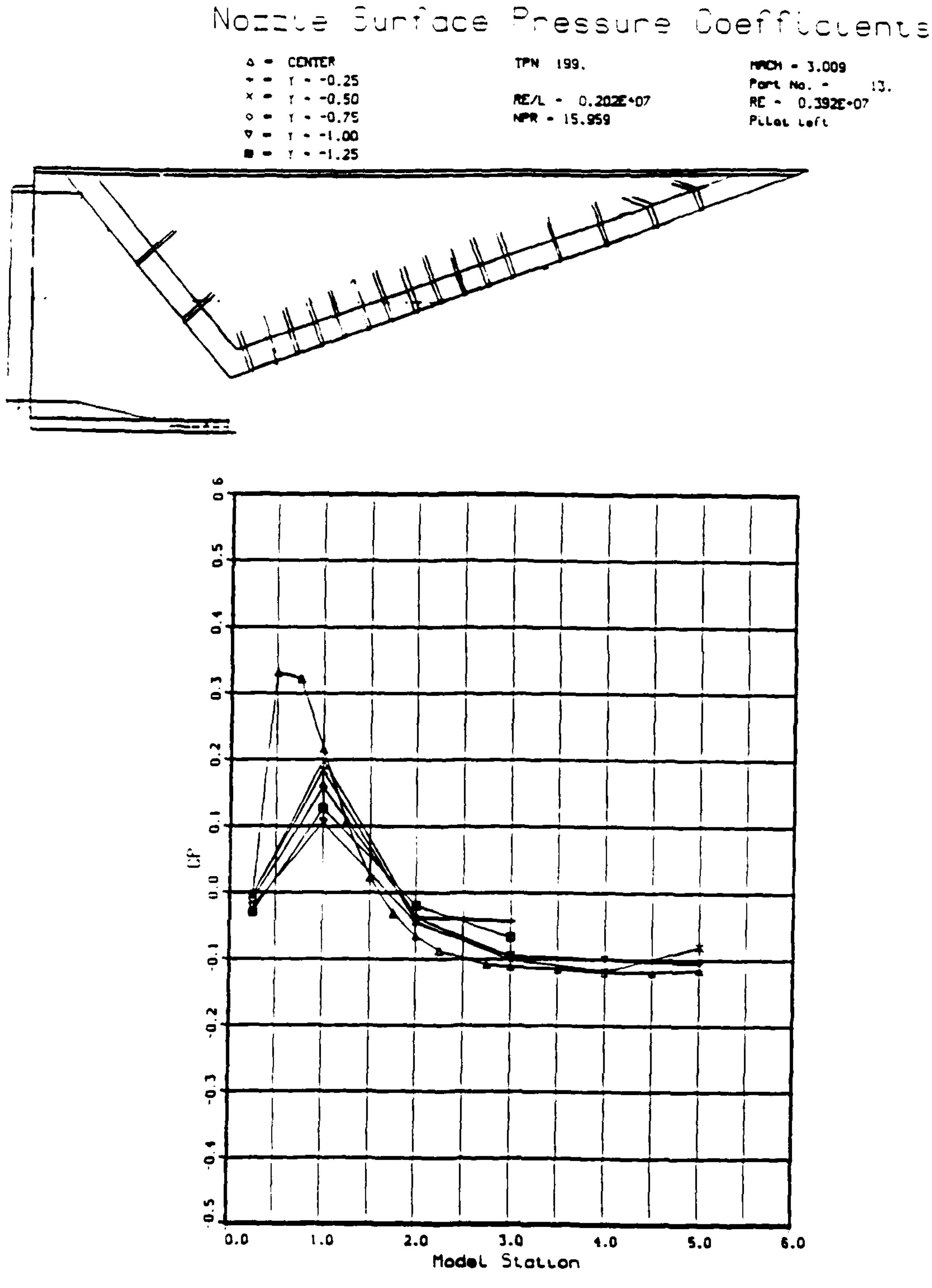

Figure B15. Surface Pressure Coefficients, C_p vs Model Station: Mach 3.0, NPR = 16.0, +5 Cowl

Appendix C: Surface Pressure Ratio, P_i/P_{Tn} vs Model Station

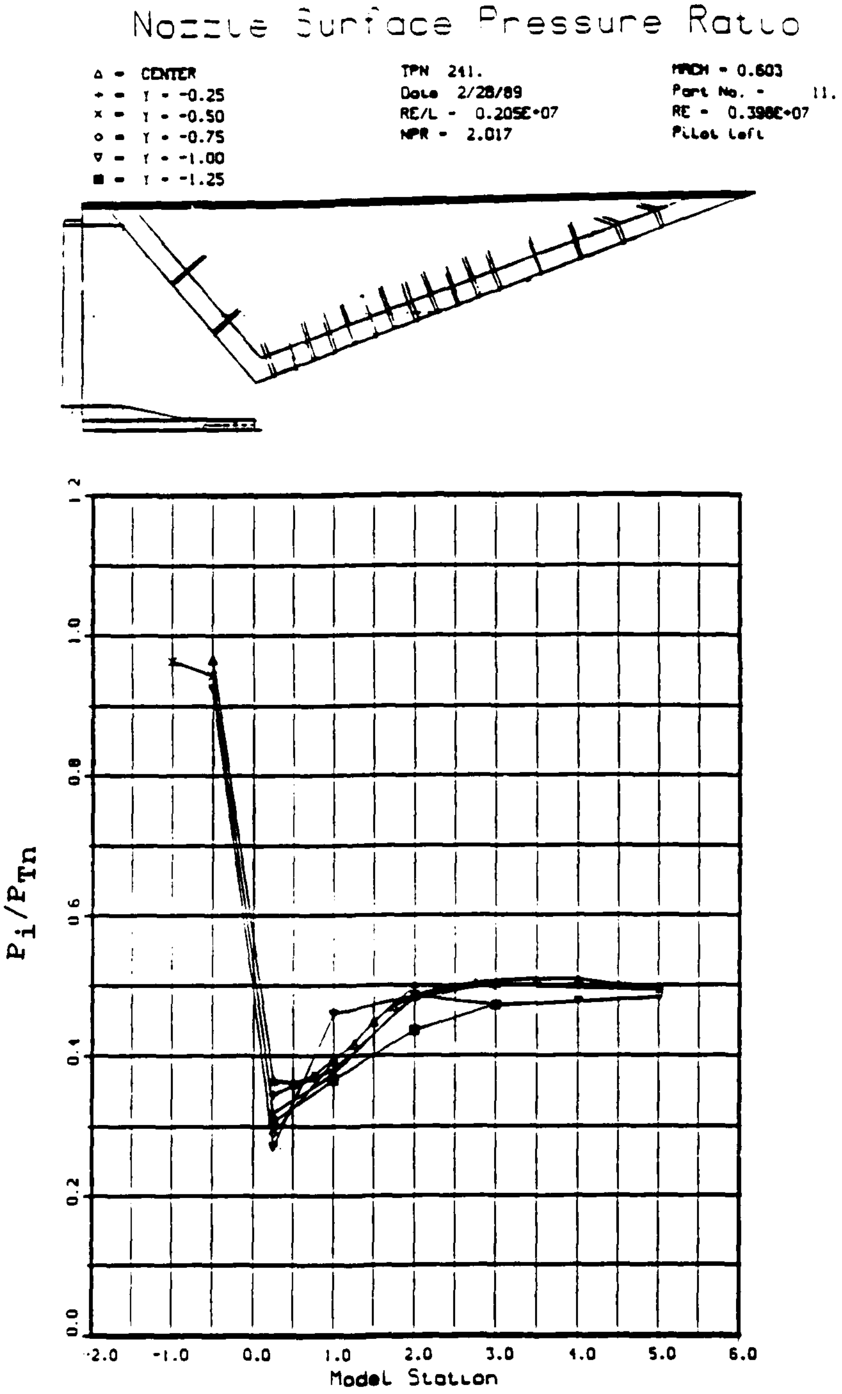

Figure C1. Surface Pressure Ratio, P_i/P_{Tn} vs Model Station: Mach 0.6, NPR = 2.0, BL Cowl

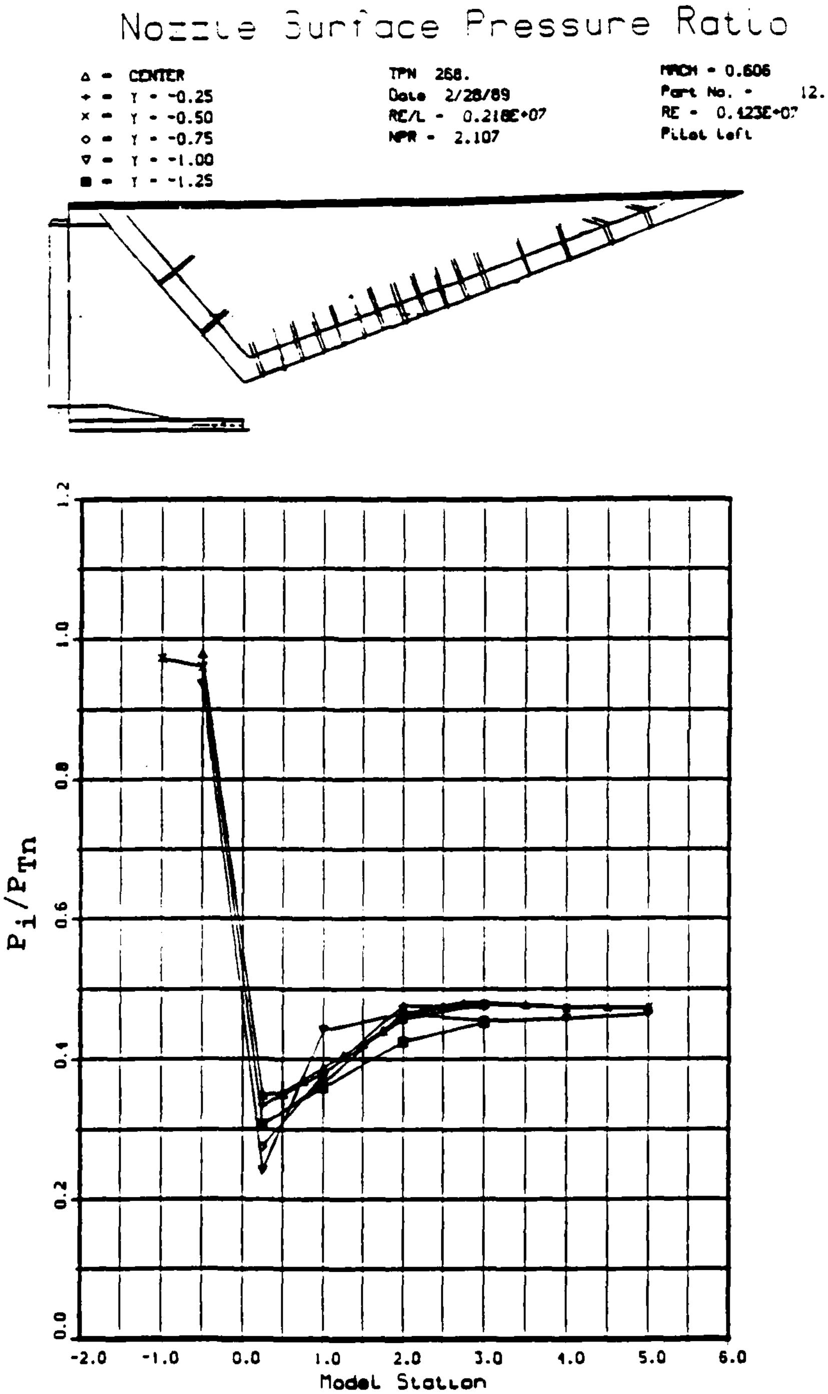

Figure C2. Surface Pressure Ratio, P_i/P_{Tn} vs Model Station: Mach 0.6, NPR = 2.0, L Cowl

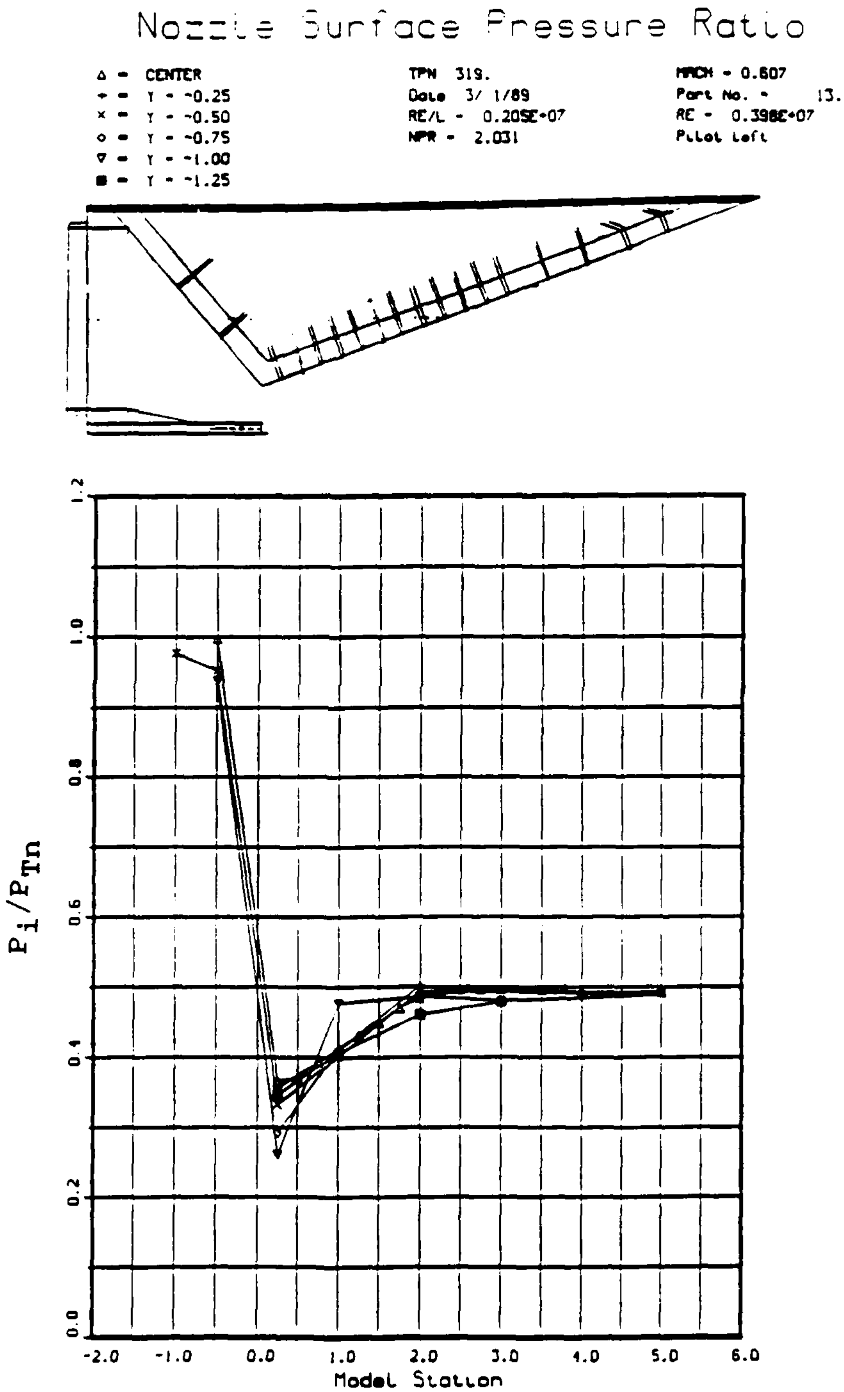

Figure C3. Surface Pressure Ratio, P_i/P_{Tn} vs Model Station: Mach 0.6, NPR = 2.0, +5 Cowl

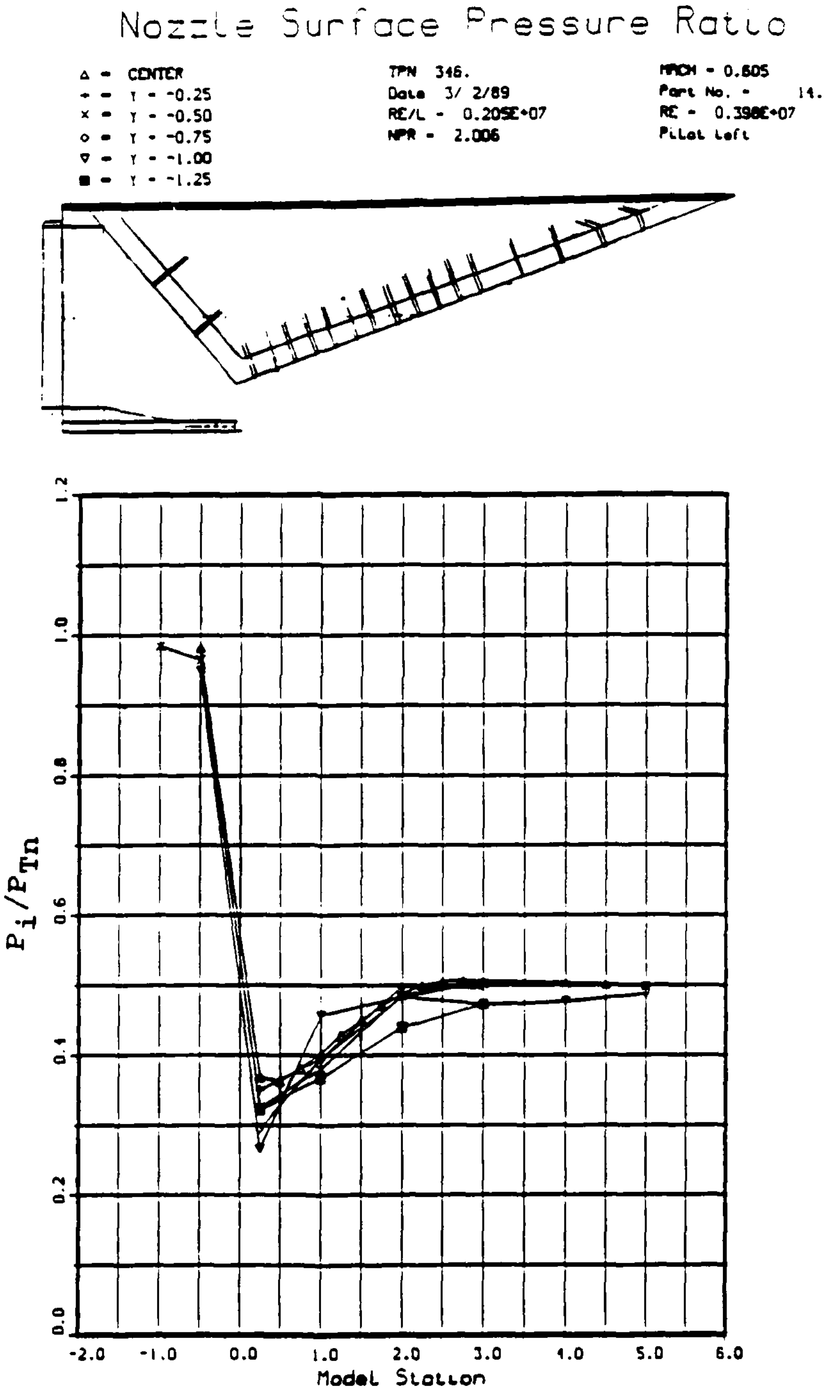

Figure C4. Surface Pressure Ratio, P_i/P_{Tn} vs Model Station: Mach 0.6, NPR = 2.0, -5 Cowl

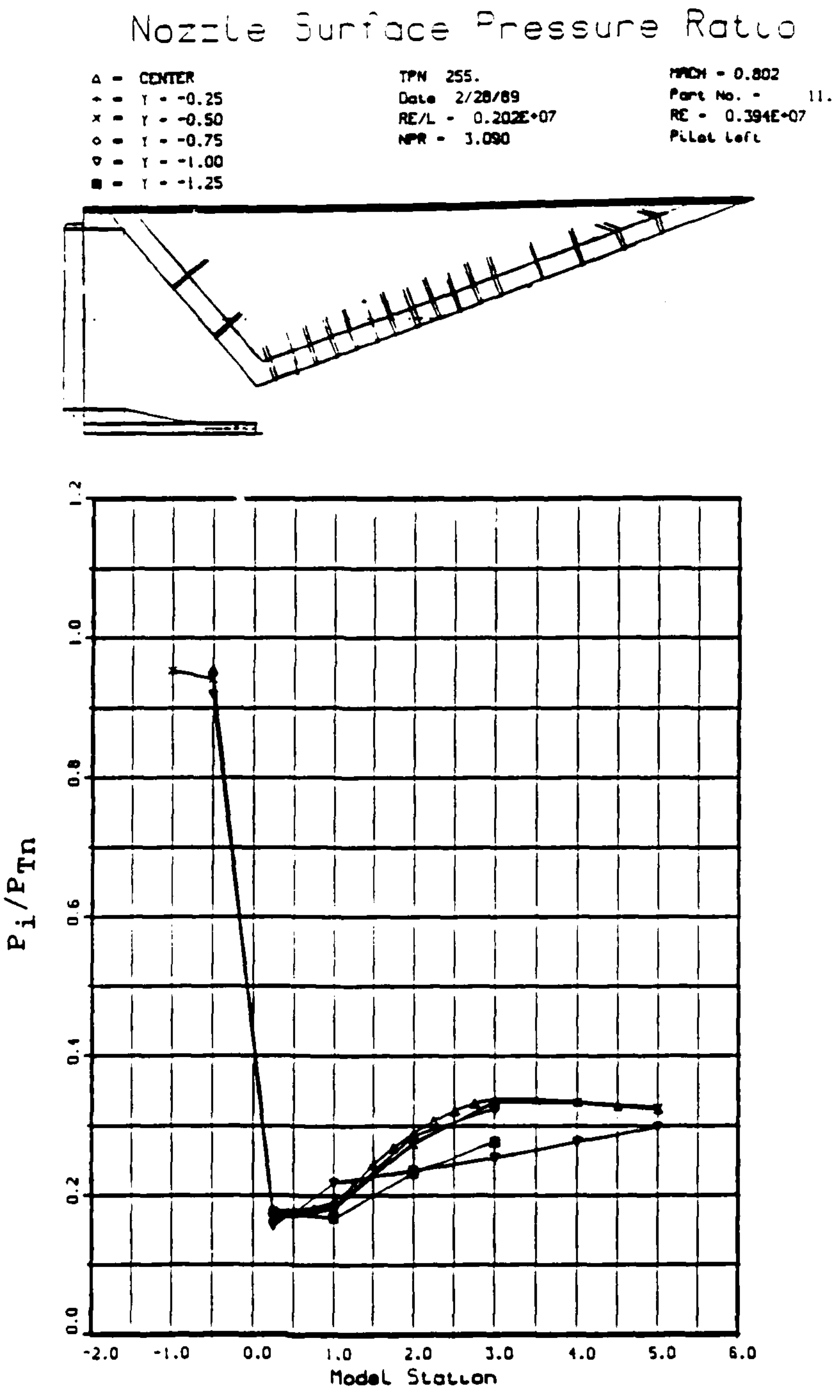

Figure C5. Surface Pressure Ratio, P_i/P_{Tn} vs Model Station: Mach 0.8, NPR = 3.0, BL Cowl

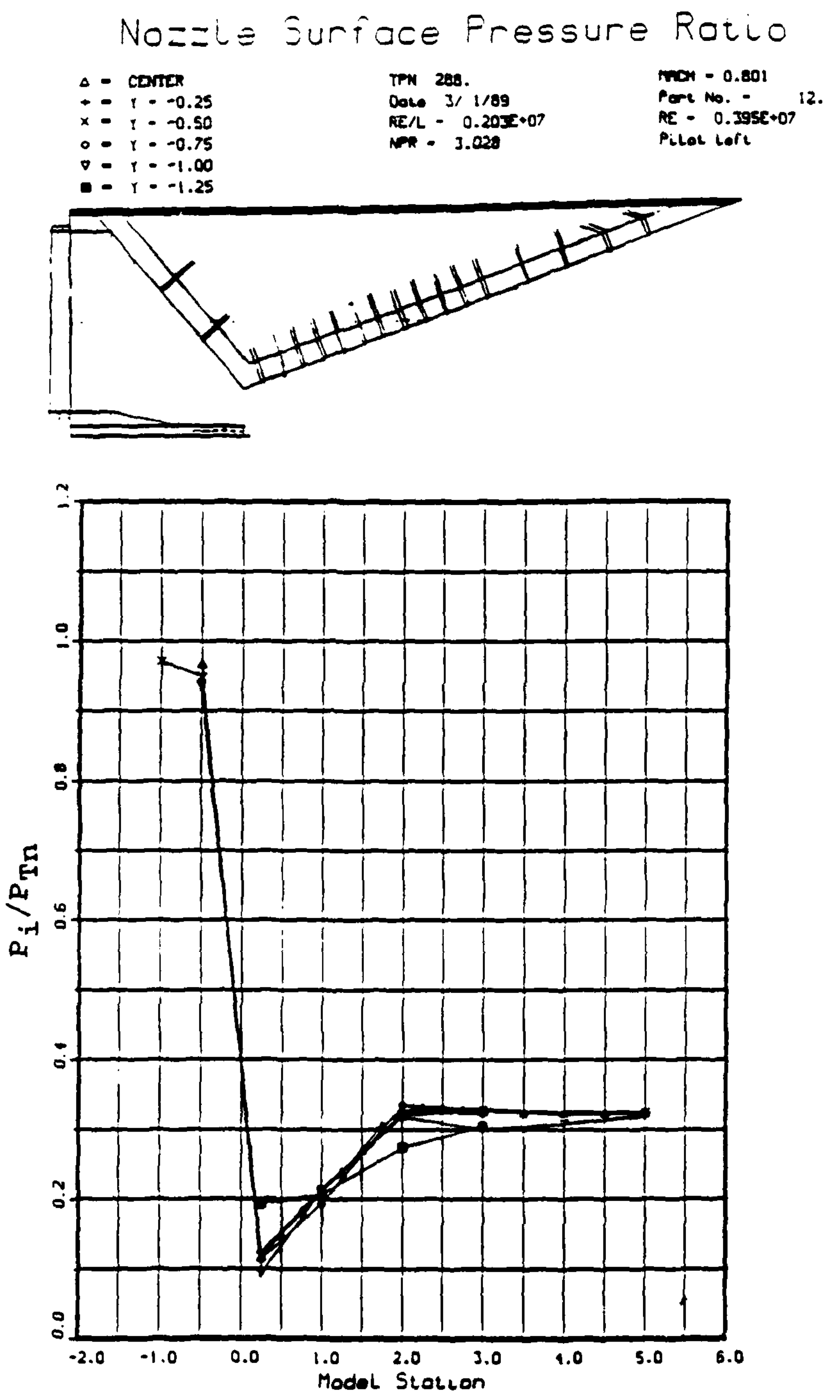

Figure C6. Surface Pressure Ratio, P_i/P_{Tn} vs Model Station: Mach 0.8, NPR = 3.0, L Cowl

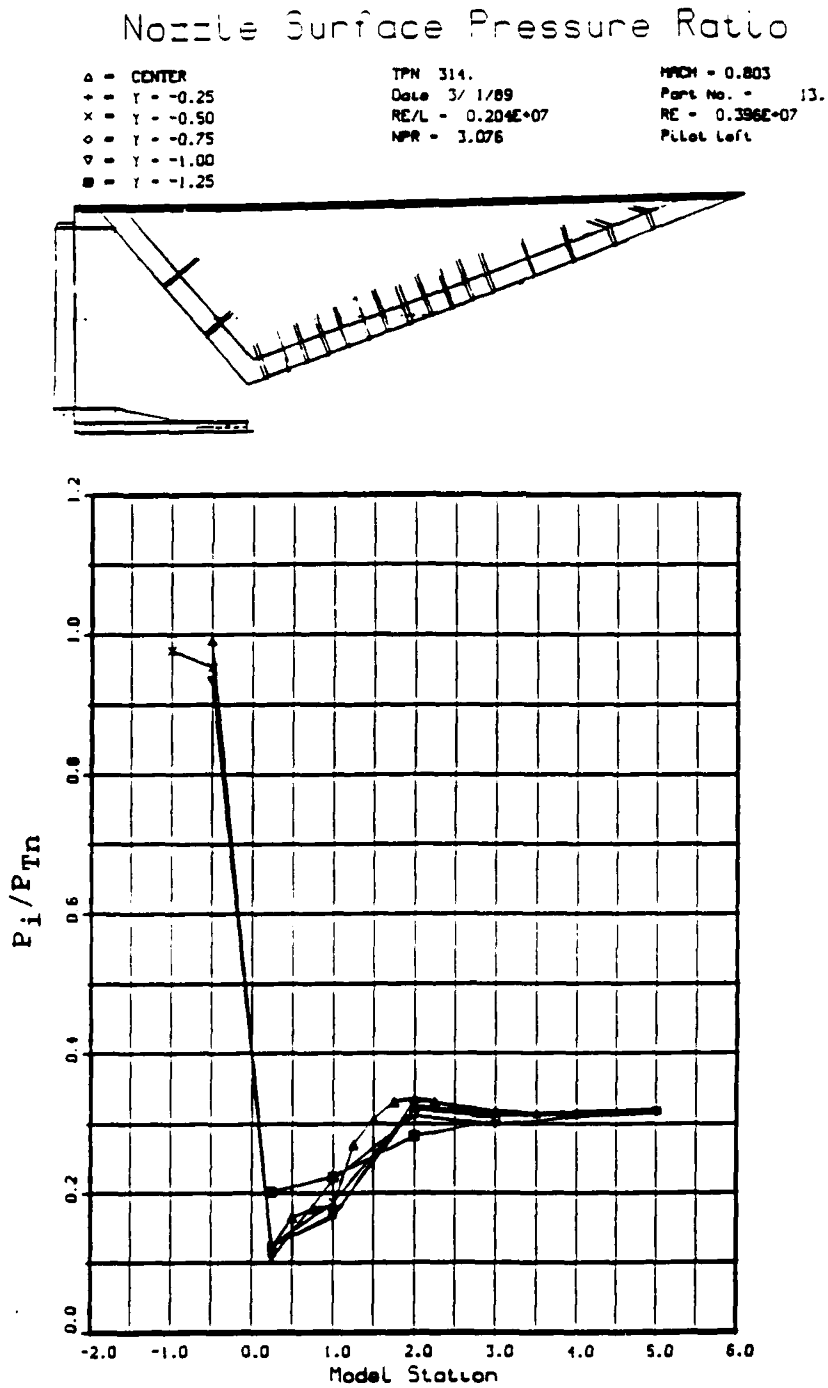

Figure C7. Surface Pressure Ratio, P_i/P_{Tn} vs Model Station: Mach 0.8, NPR = 3.0, +5 Cowl

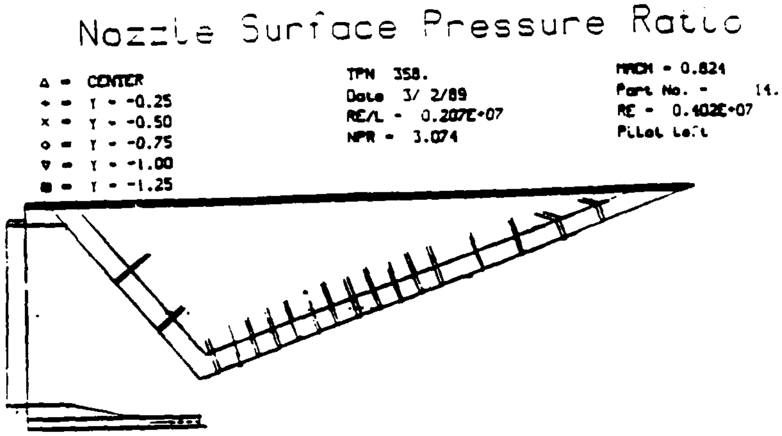

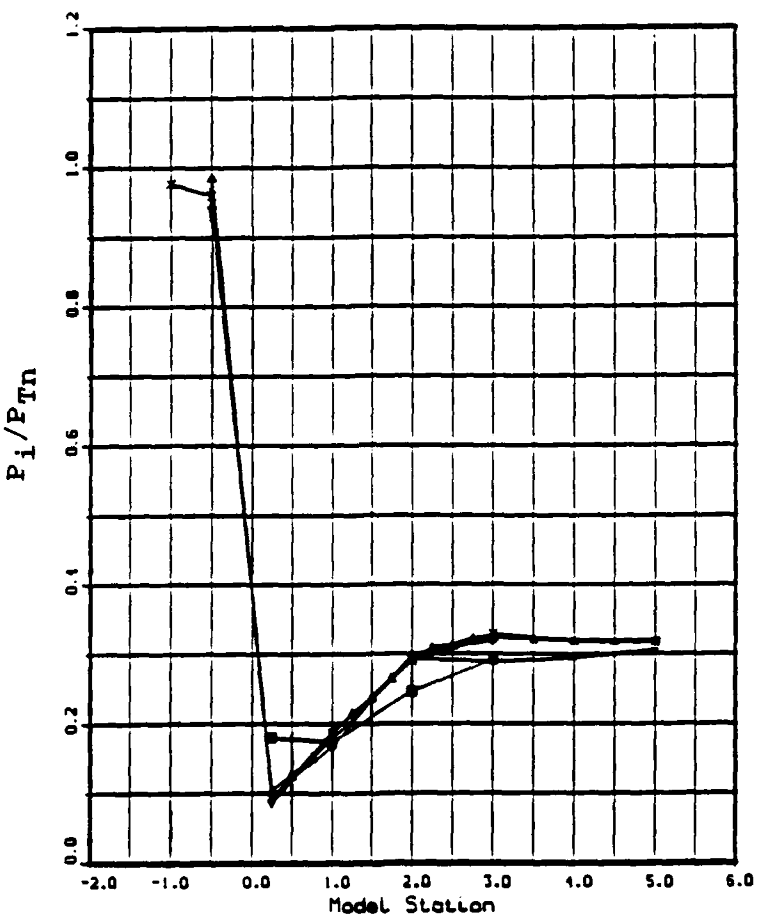

Figure C8. Surface Pressure Ratio, P_i/P_{Tn} vs Model Station: Mach 0.8, NPR = 3.0, -5 Cowl

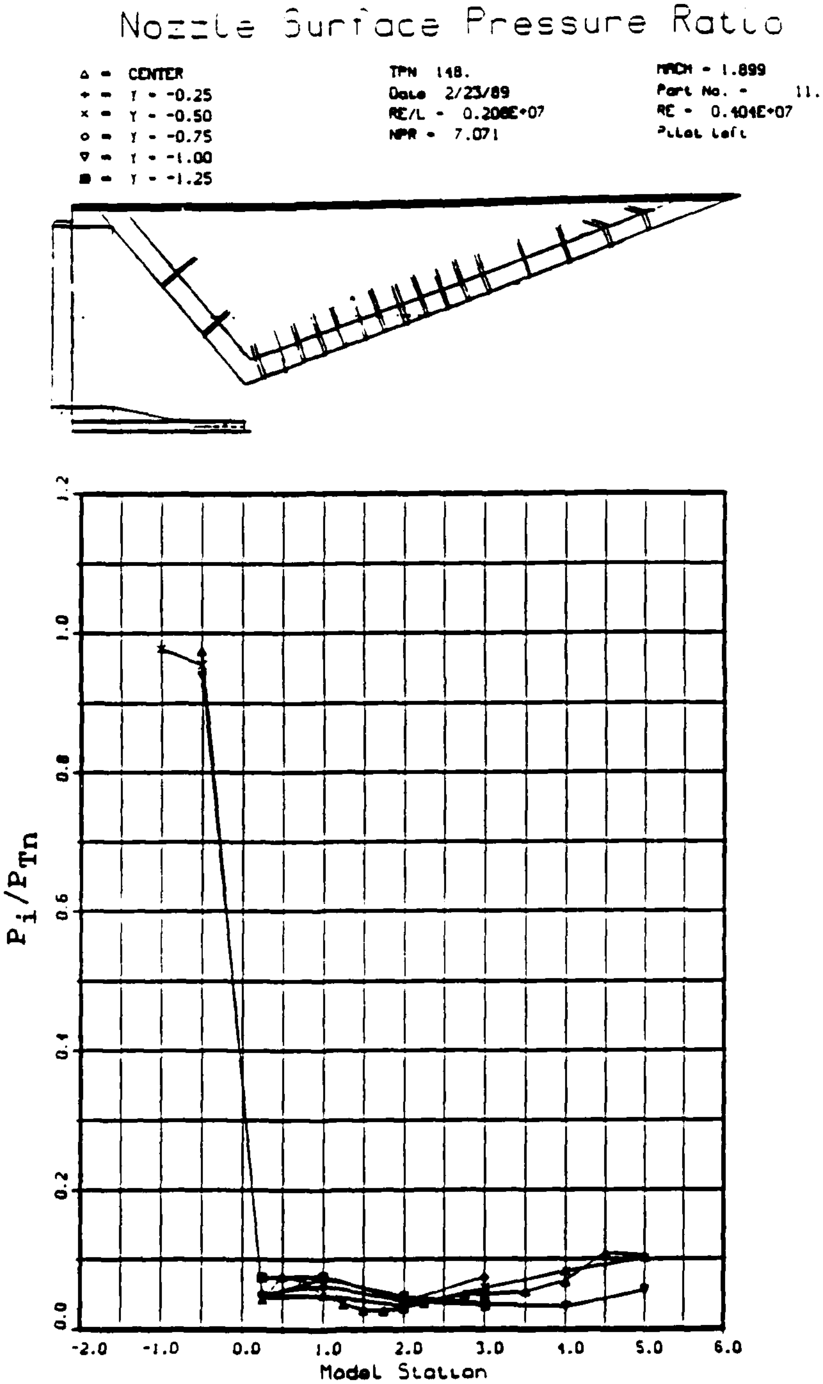

Figure C9. Surface Pressure Ratio, P_i/P_{Tn} vs Model Station: Mach 1.9, NPR = 7.0, BL Cowl

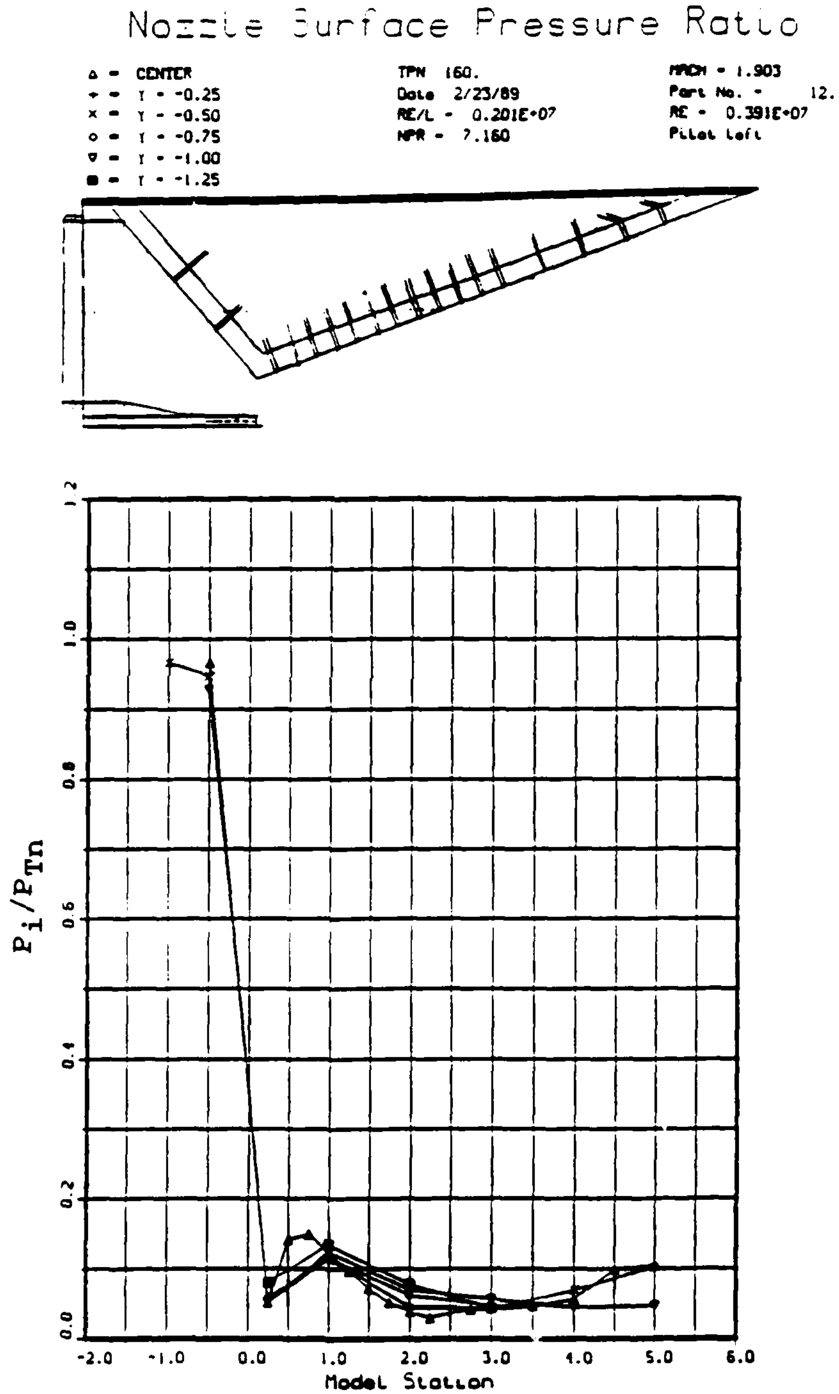

Figure 10. Surface Pressure Ratio, P_i/P_{Tn} vs Model Station: Mach 1.9, NPR = 7.0, L Cowl

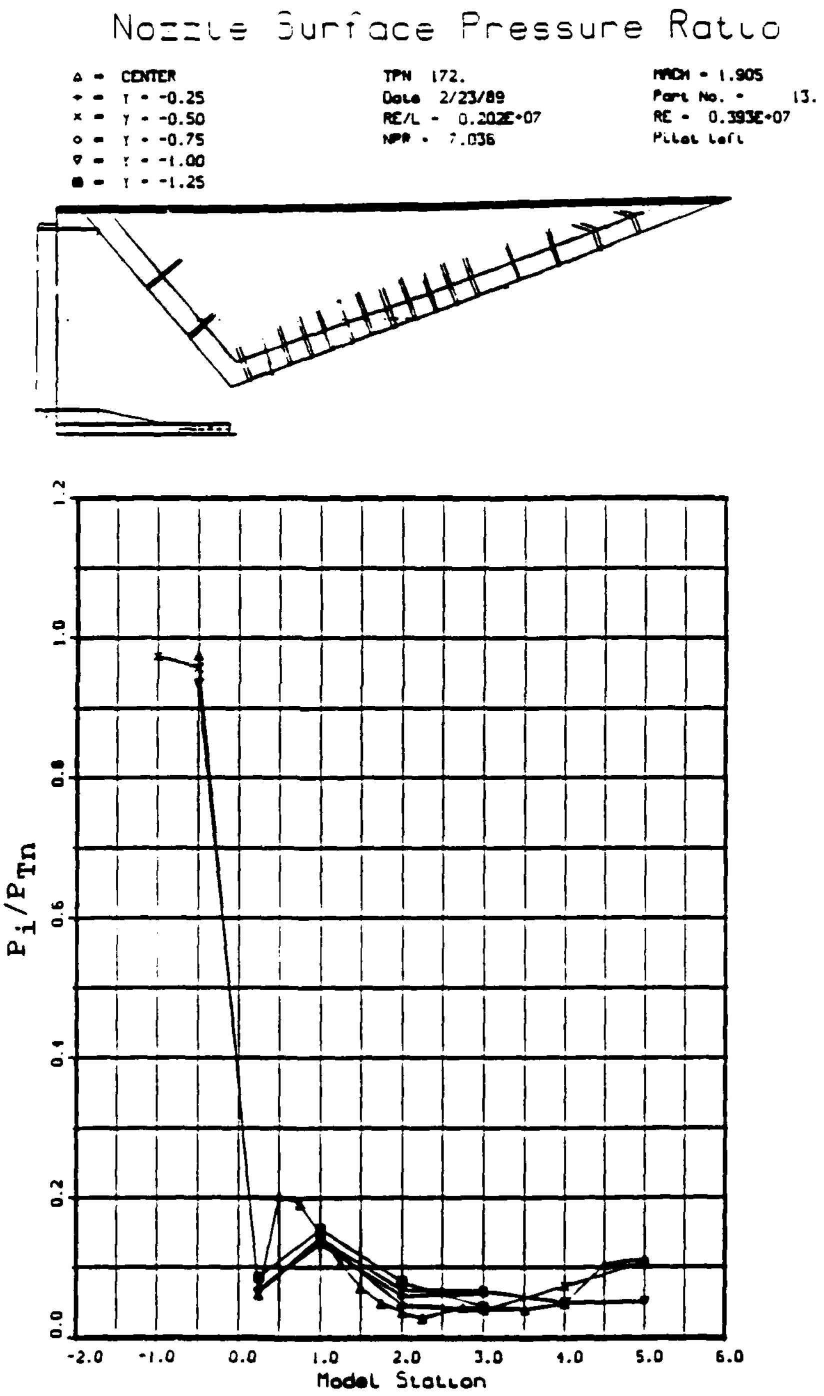

Figure C11. Surface Pressure Ratio, P_i/P_{Tn} vs Model Station: Mach 1.9, NPR = 7.0, +5 Cowl

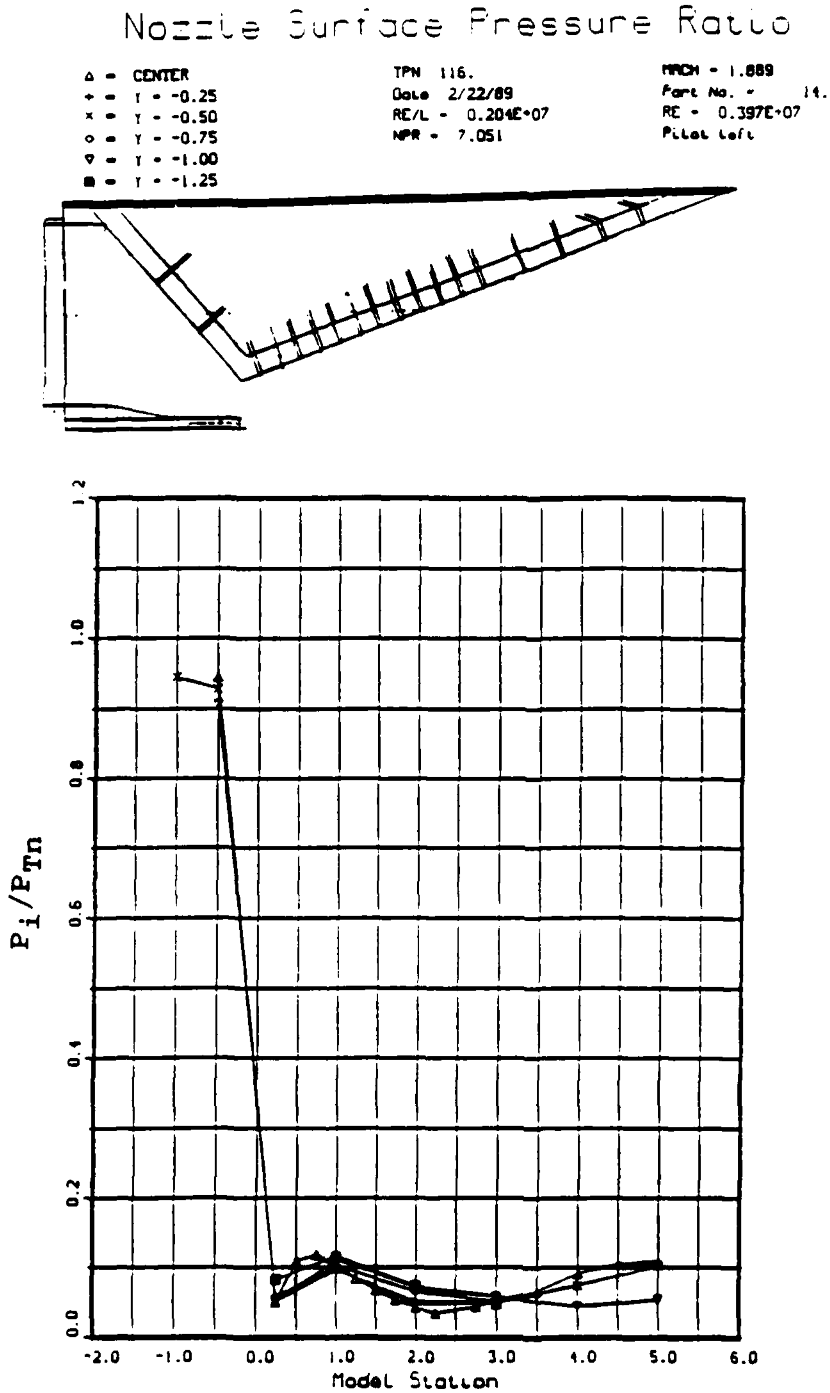

Figure C12. Surface Pressure Ratio, P_i/P_{Tn} vs Model Station: Mach 1.9, NPR = 2.0, -5 Cowl

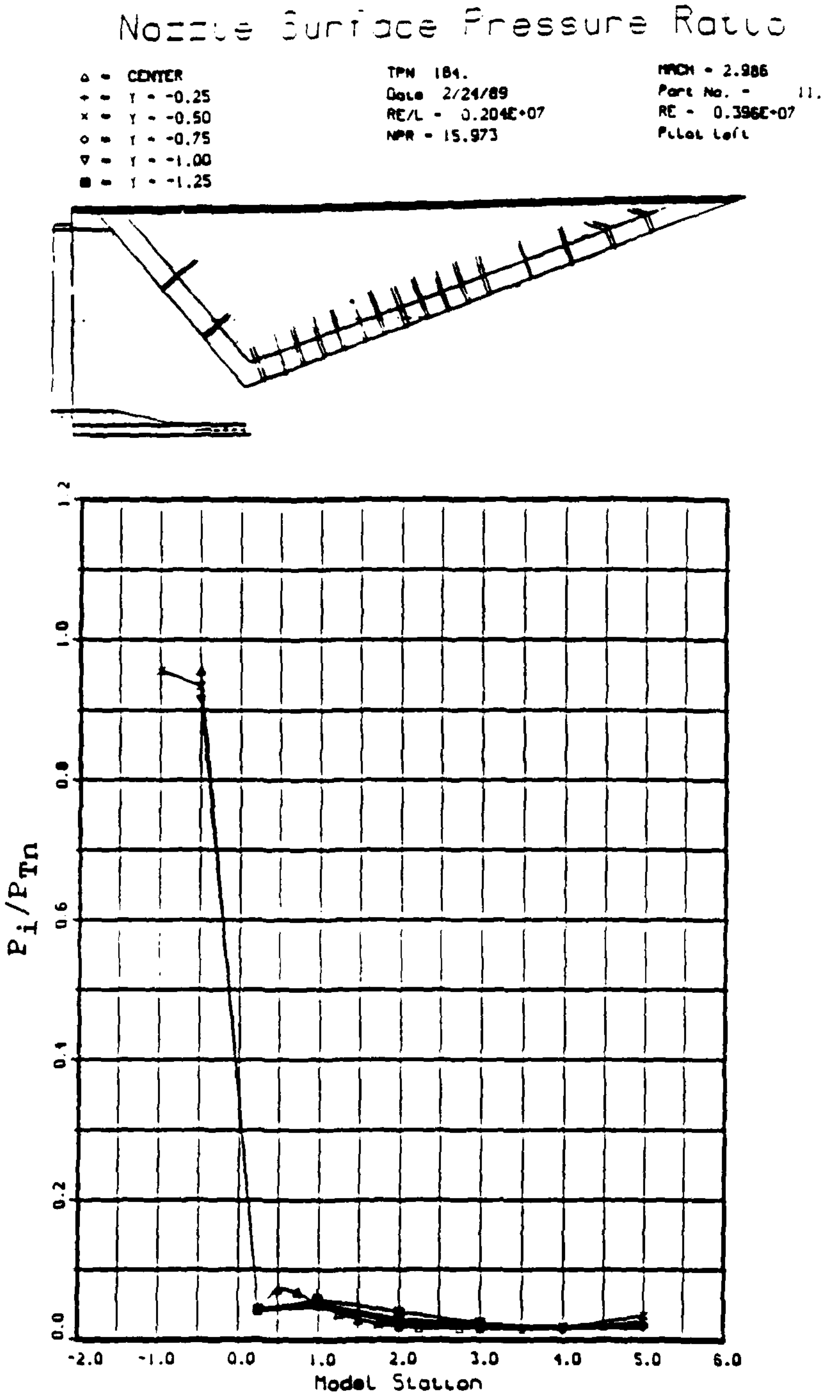

Figure C13. Surface Pressure Ratio, P_i/P_{Tn} vs Model Station: Mach 3.0, NPR = 16.0, BL Cowl

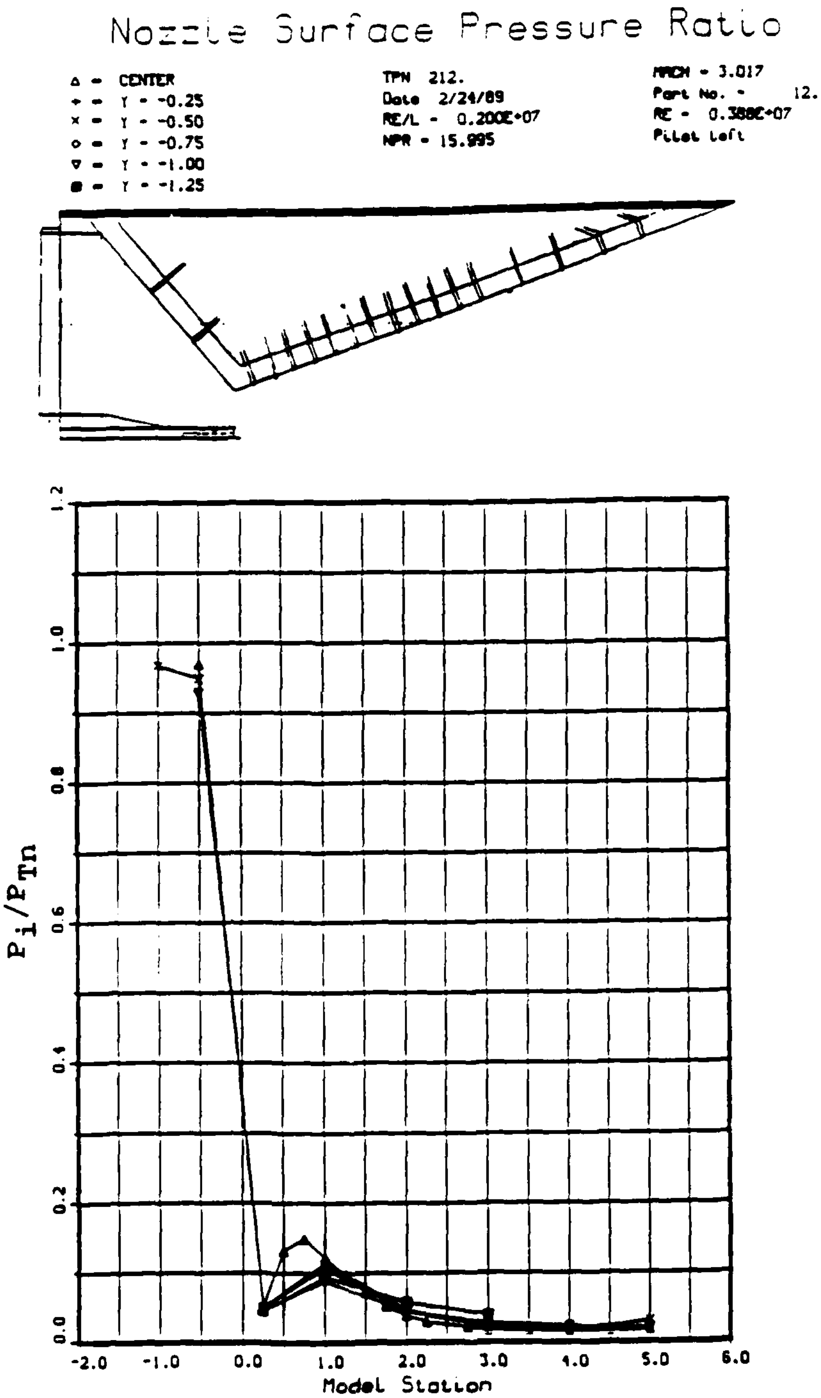

Figure C14. Surface Pressure Ratio, P_i/P_{Tn} vs Model Station: Mach 3.0, NPR = 16.0, L Cowl

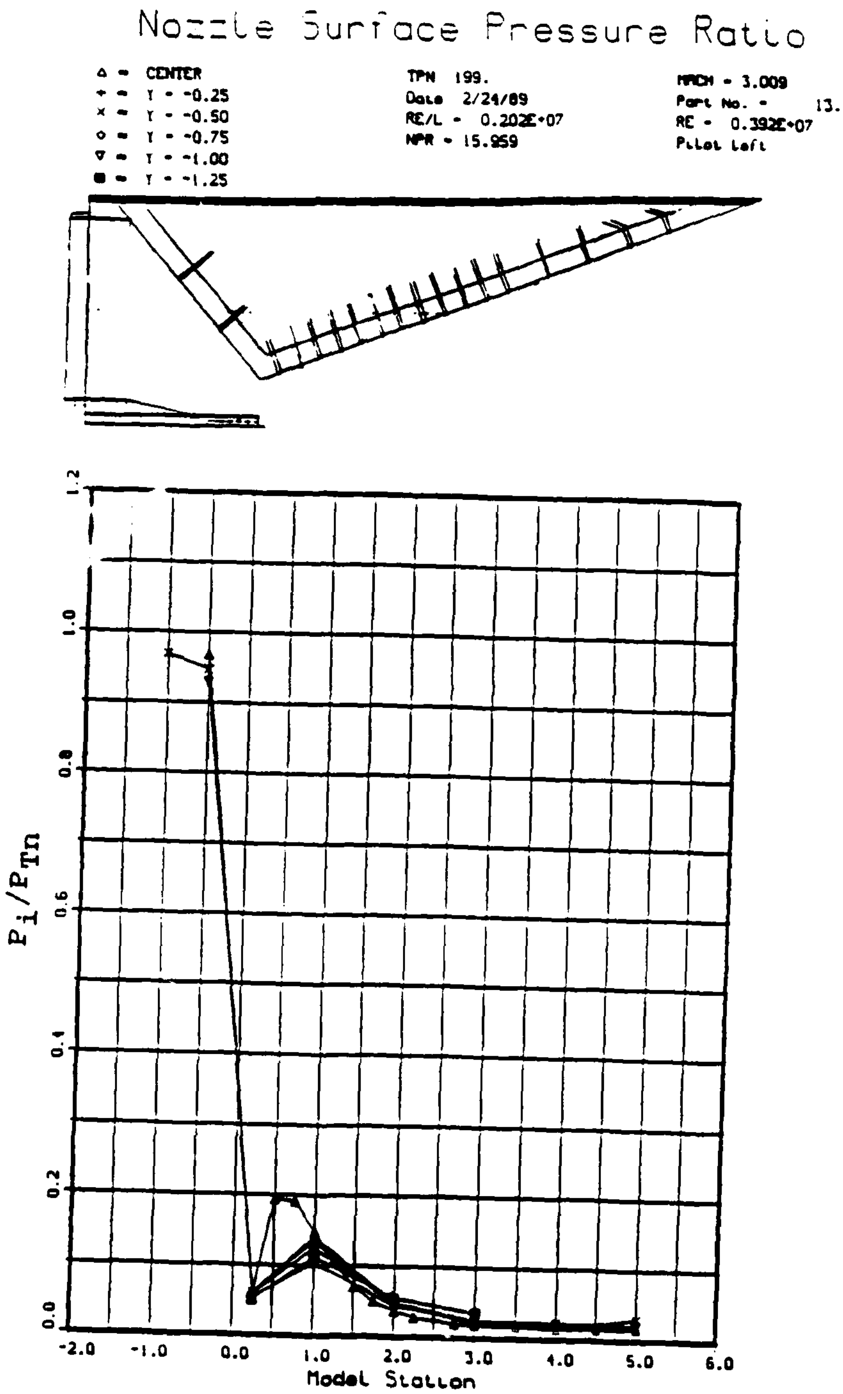

Figure C15. Surface Pressure Ratio, P_i/P_{Tn} vs Model Station: Mach 3.0, NPR = 16.0, +5 Cowl

Appendix D: Reynolds Number Effects,

C_p vs Model Station

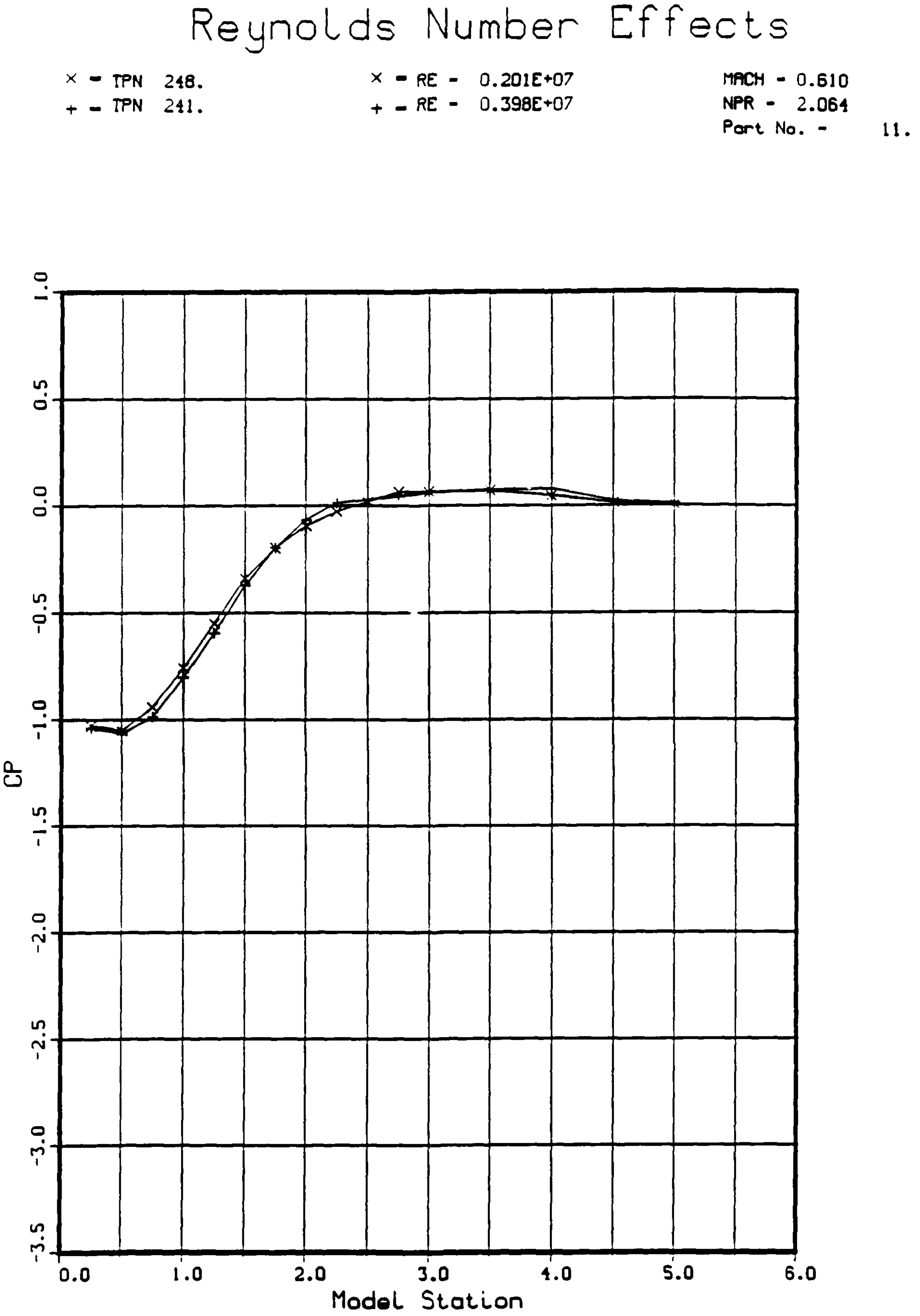

Figure D1. Reynolds Number Effects, C_p vs Model Station: Mach 0.6, NPR = 2.0, BL Cowl

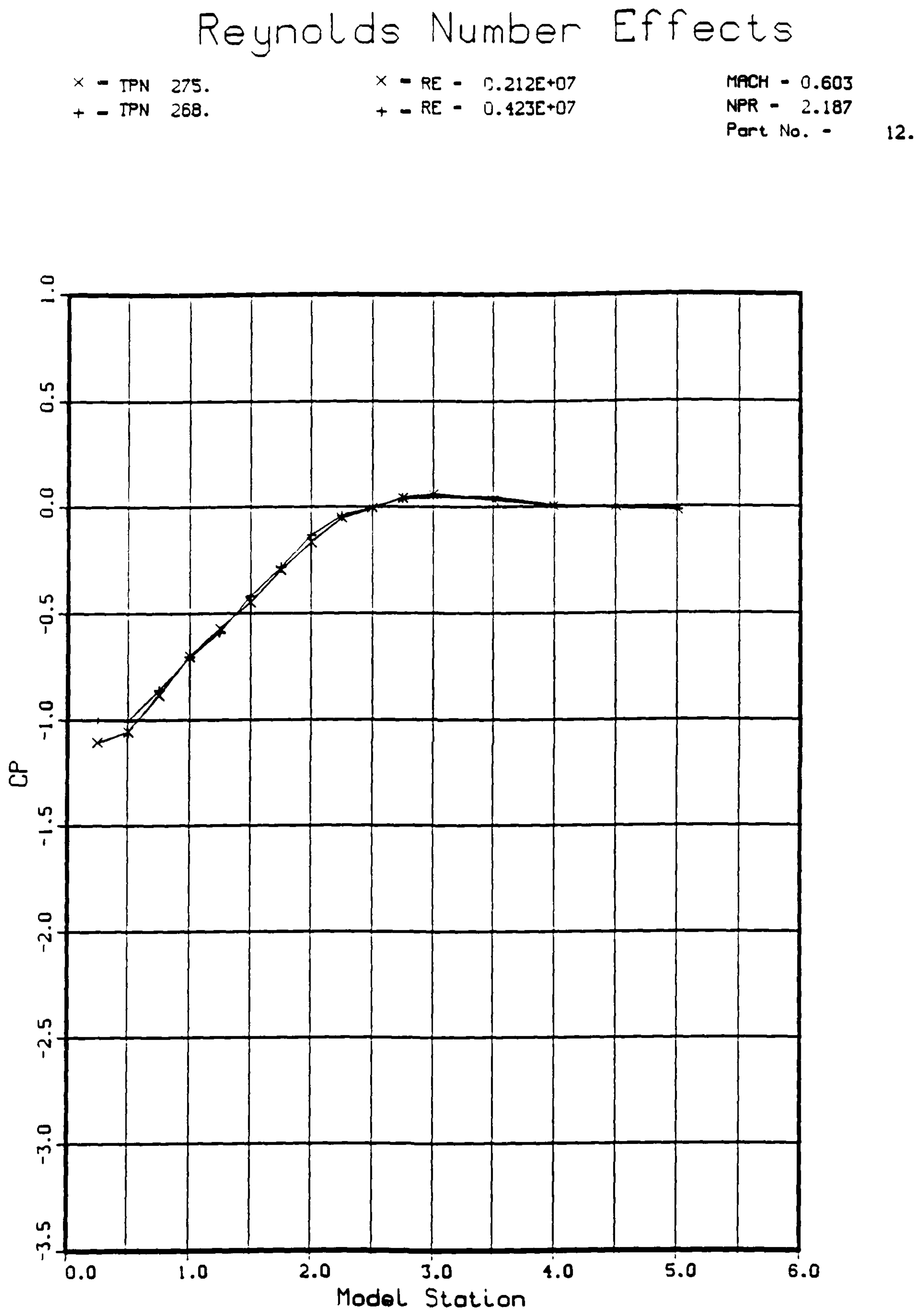

Figure D2. Reynolds Number Effects, C_p vs Model Station: Mach 0.6, NPR = 2.0, L Cowl

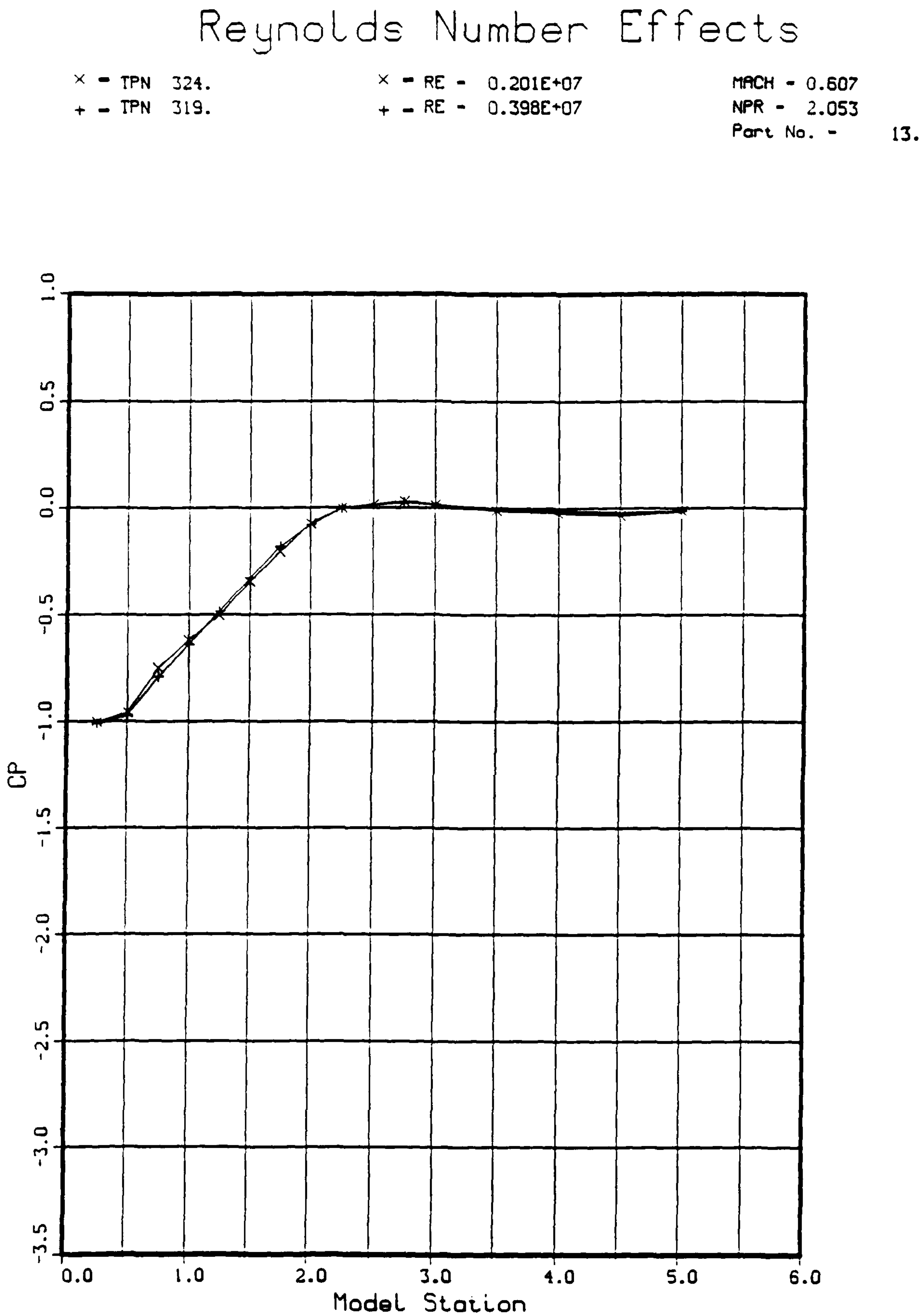

Figure D3. Reynolds Number Effects, C_p vs Model Station: Mach 0.6, NPR = 2.0, +5 Cowl

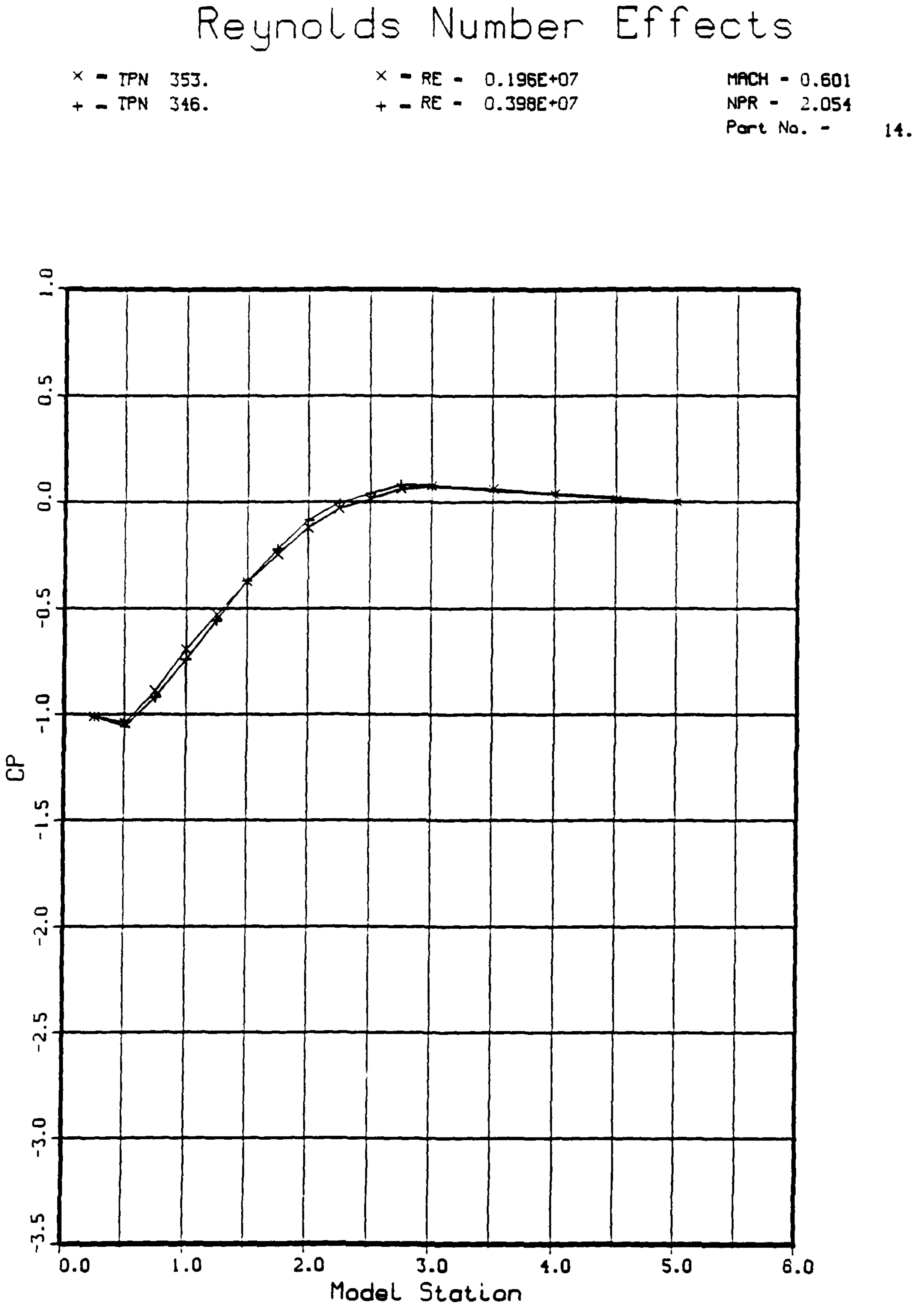

Figure D4. Reynolds Number Effects, C_p vs Model Station: Mach 0.6, NPR = 2.0, -5 Cowl

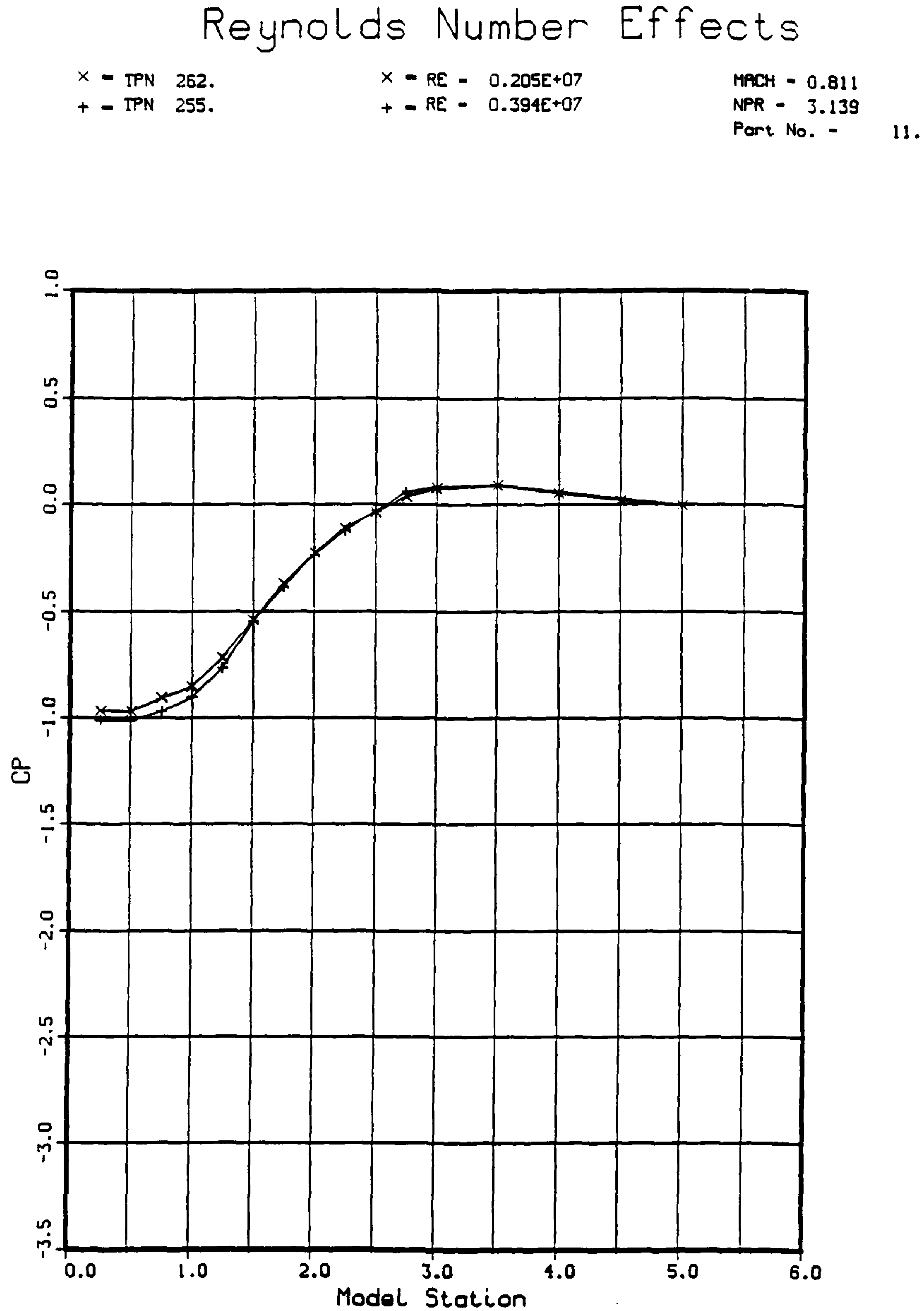

Figure D5. Reynolds Number Effects, C_p vs Model Station: Mach 0.8, NPR = 3.0, BL Cowl

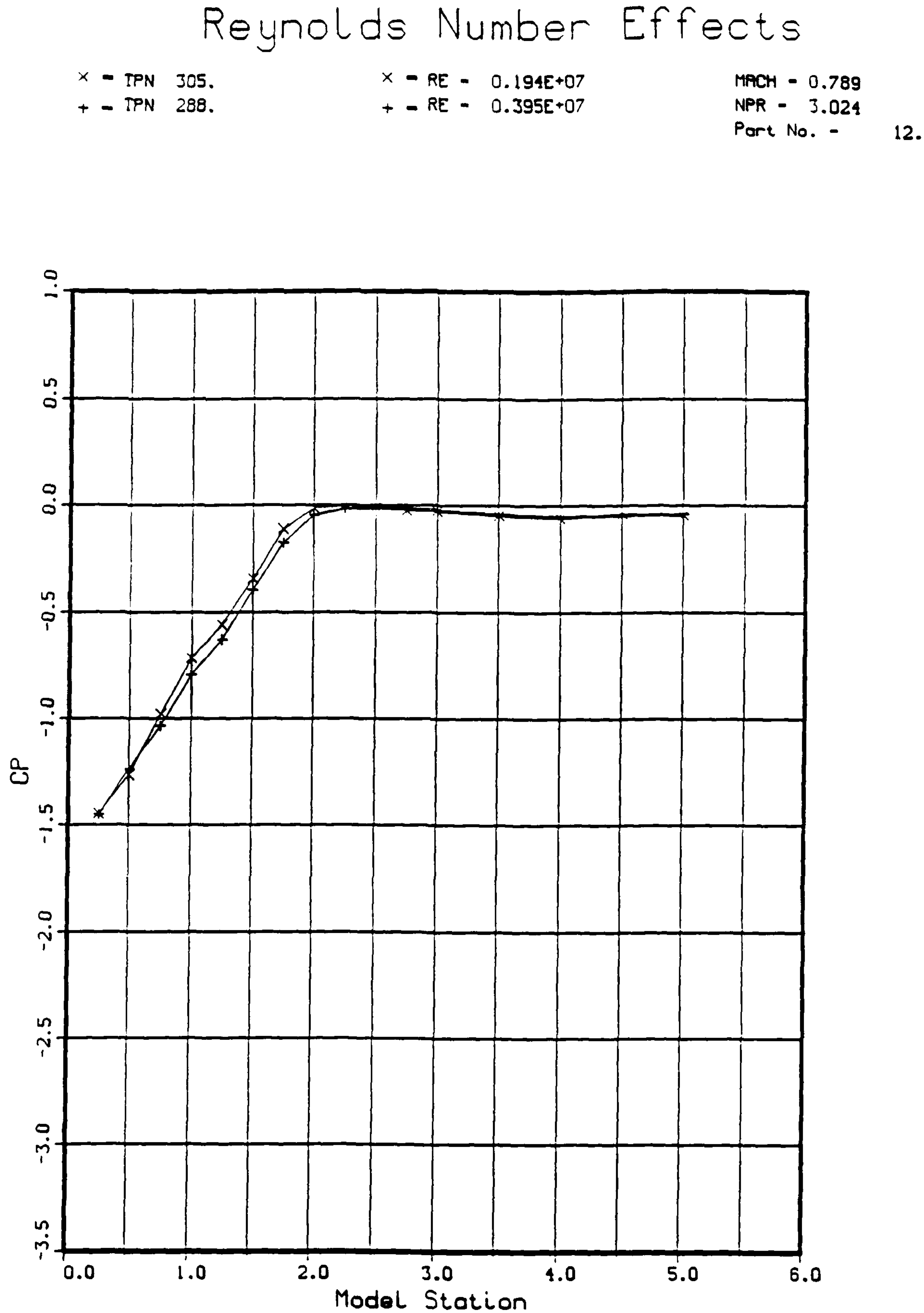

Figure D6. Reynolds Number Effects, C_p vs Model Station: Mach 0.8, NPR = 3.0, L Cowl

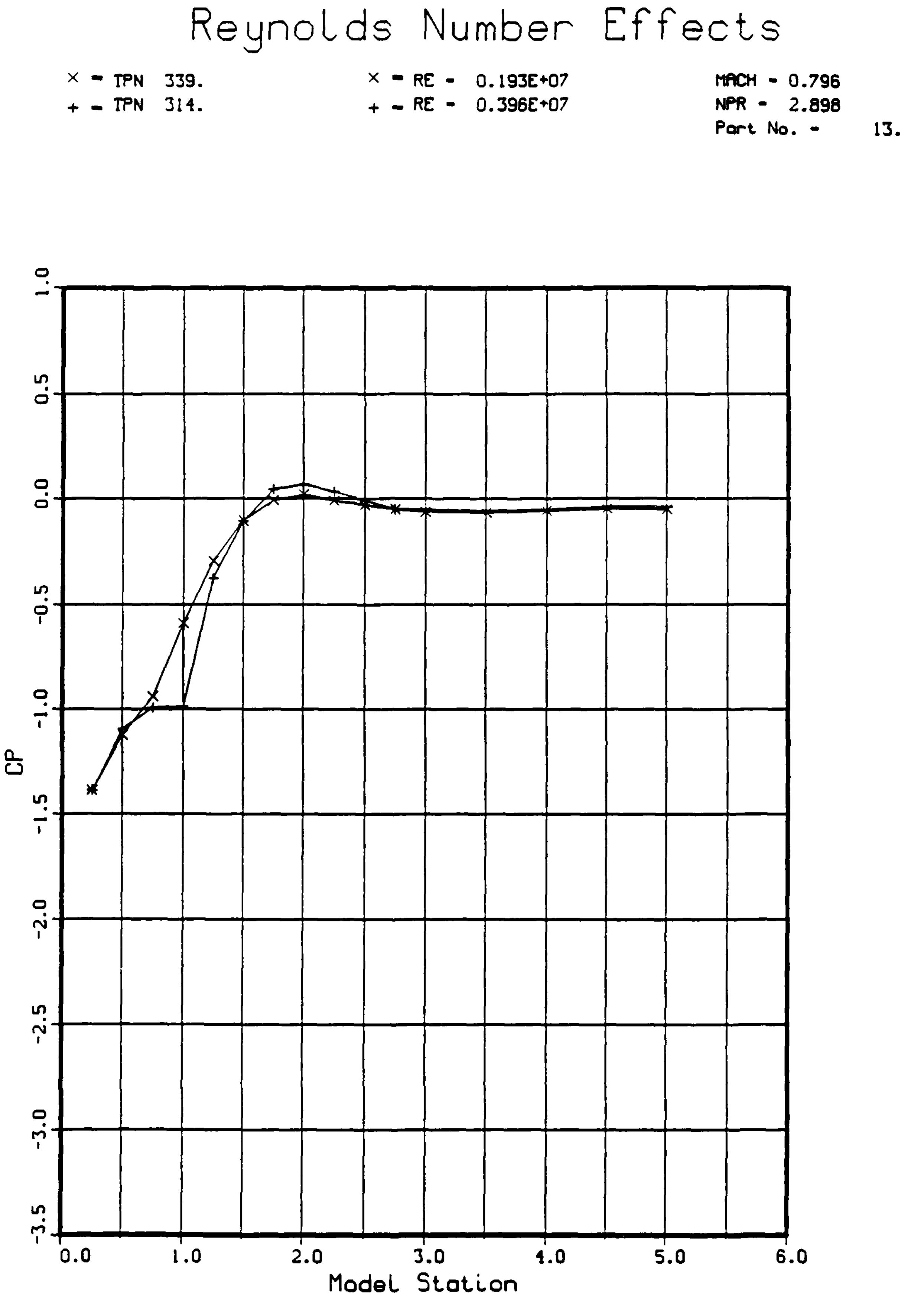

Figure D7. Reynolds Number Effects, C_p vs Model Station: Mach 0.8, NPR = 3.0, +5 Cowl

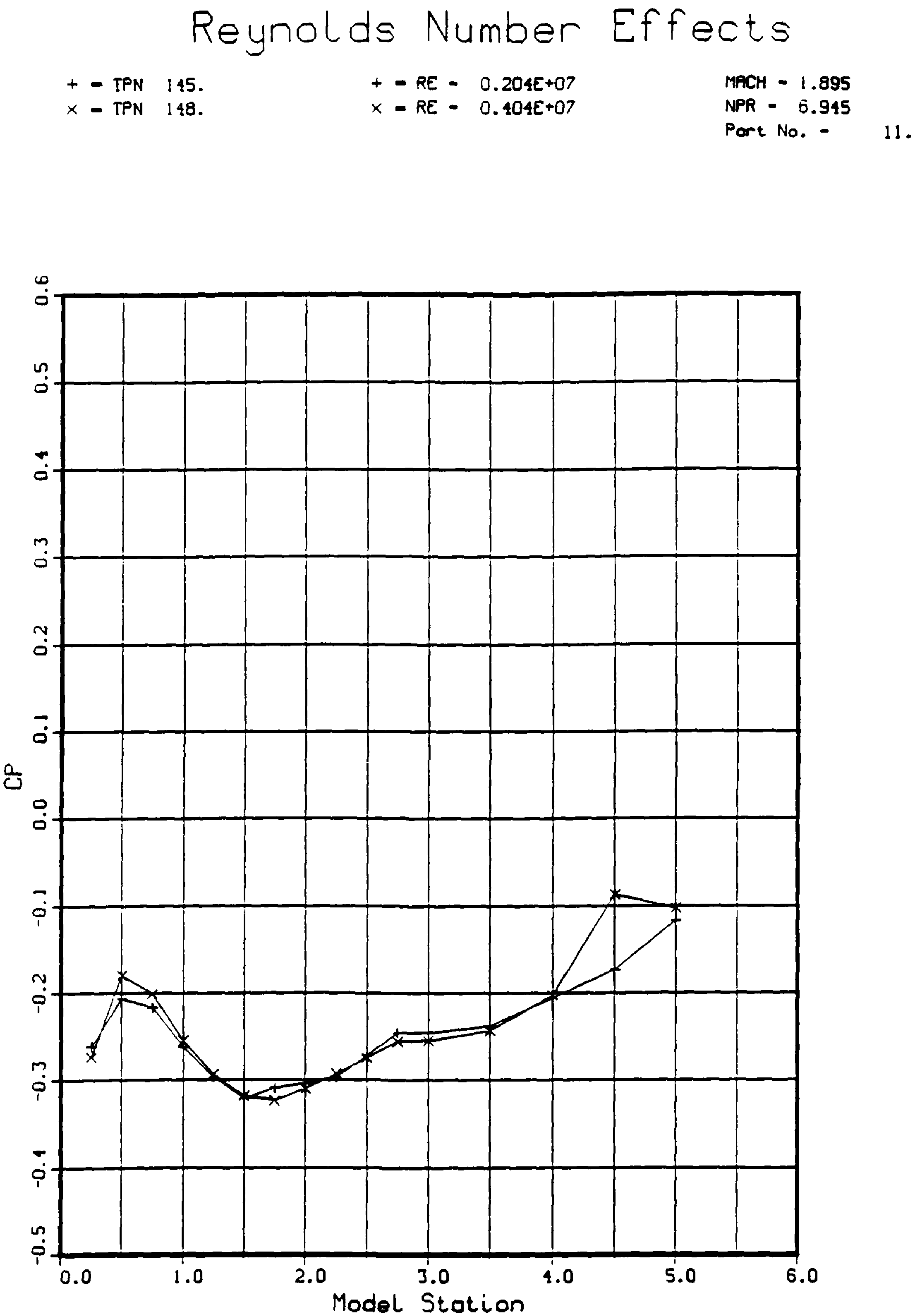

Figure D8. Reynolds Number Effects, C_p vs Model Station: Mach 1.9, NPR = 7.0, BL Cowl

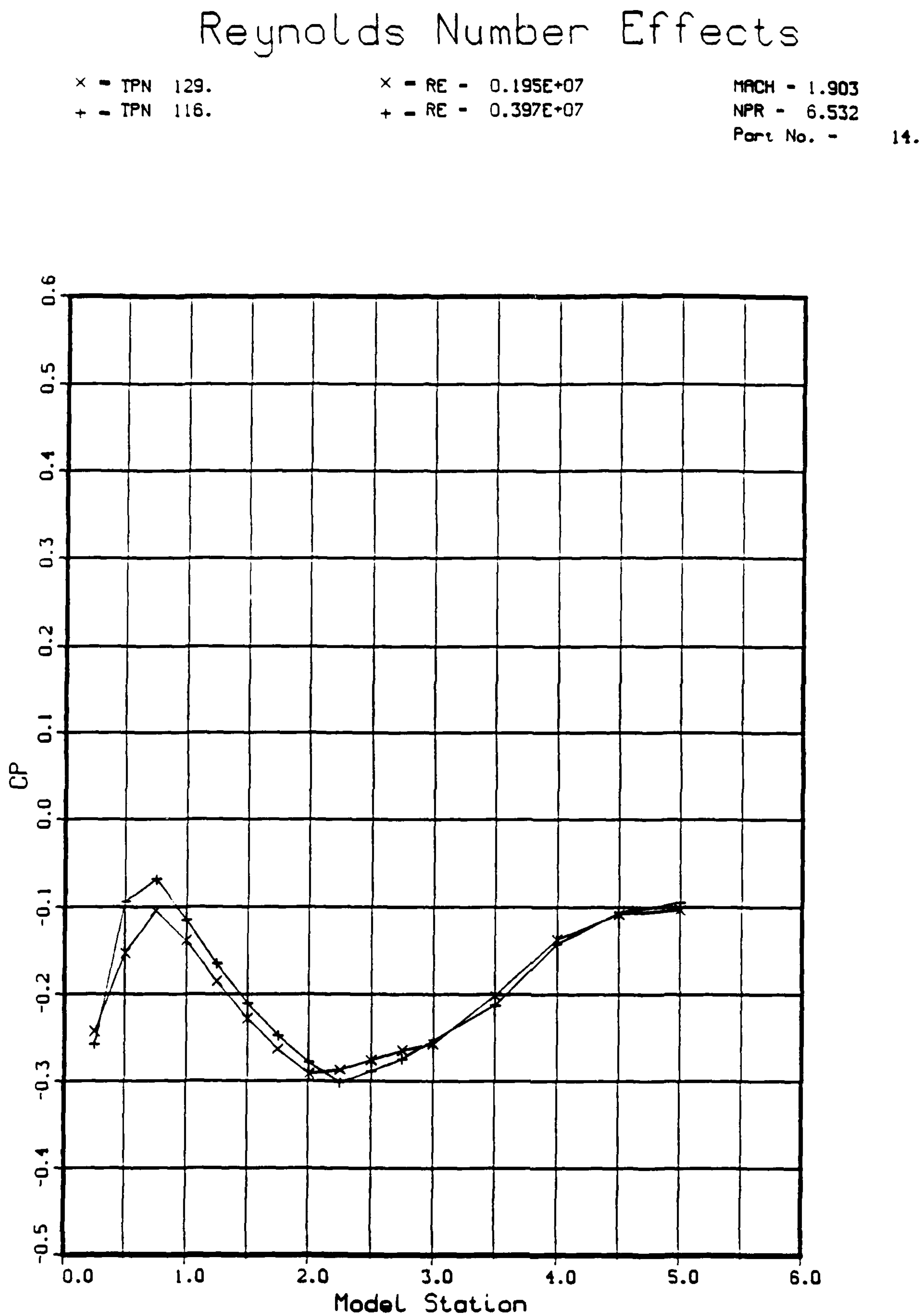

Figure D9. Reynolds Number Effects, C_p vs Model Station: Mach 1.9, NPR = 7.0, -5 Cowl

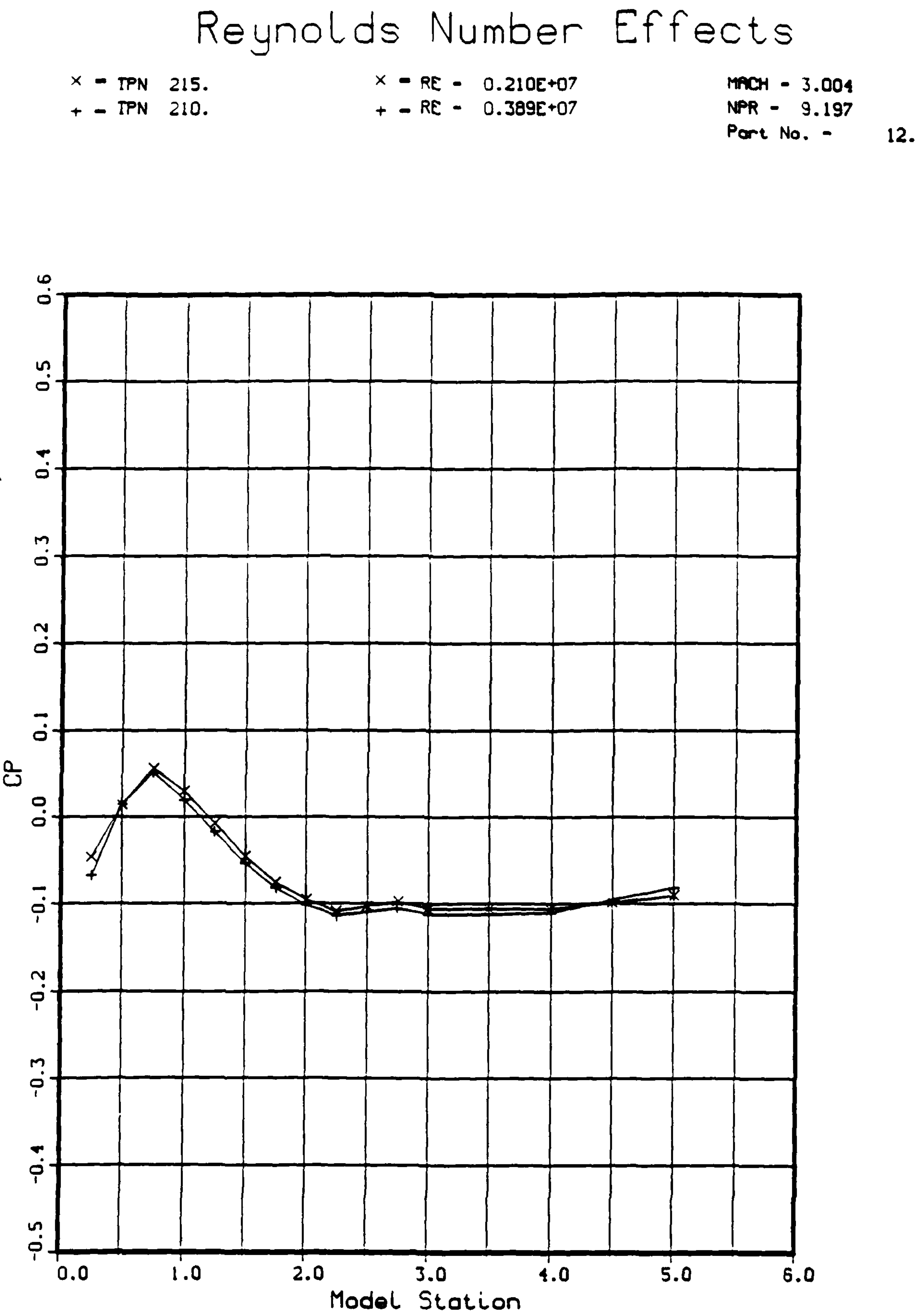

Figure D10. Reynolds Number Effects, C_p vs Model Station: Mach 3.0, NPR = 9.0, L Cowl

Appendix E: Pressure Coefficients, C_p vs Model Station: Mach Effects

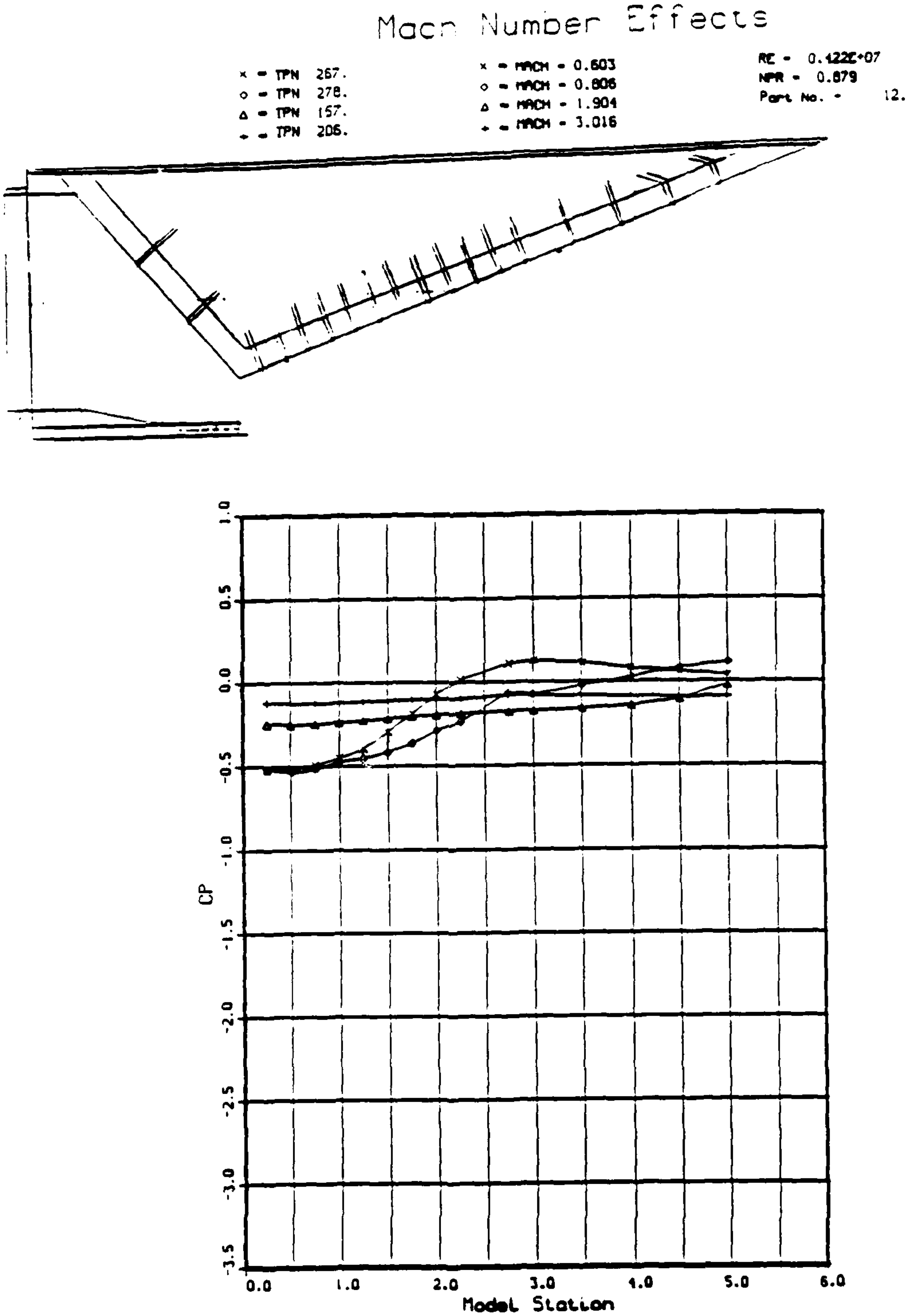

Figure E1. Pressure Coefficients, C_p vs Model Station, Mach Effect: NPR = 1.0, L Cowl

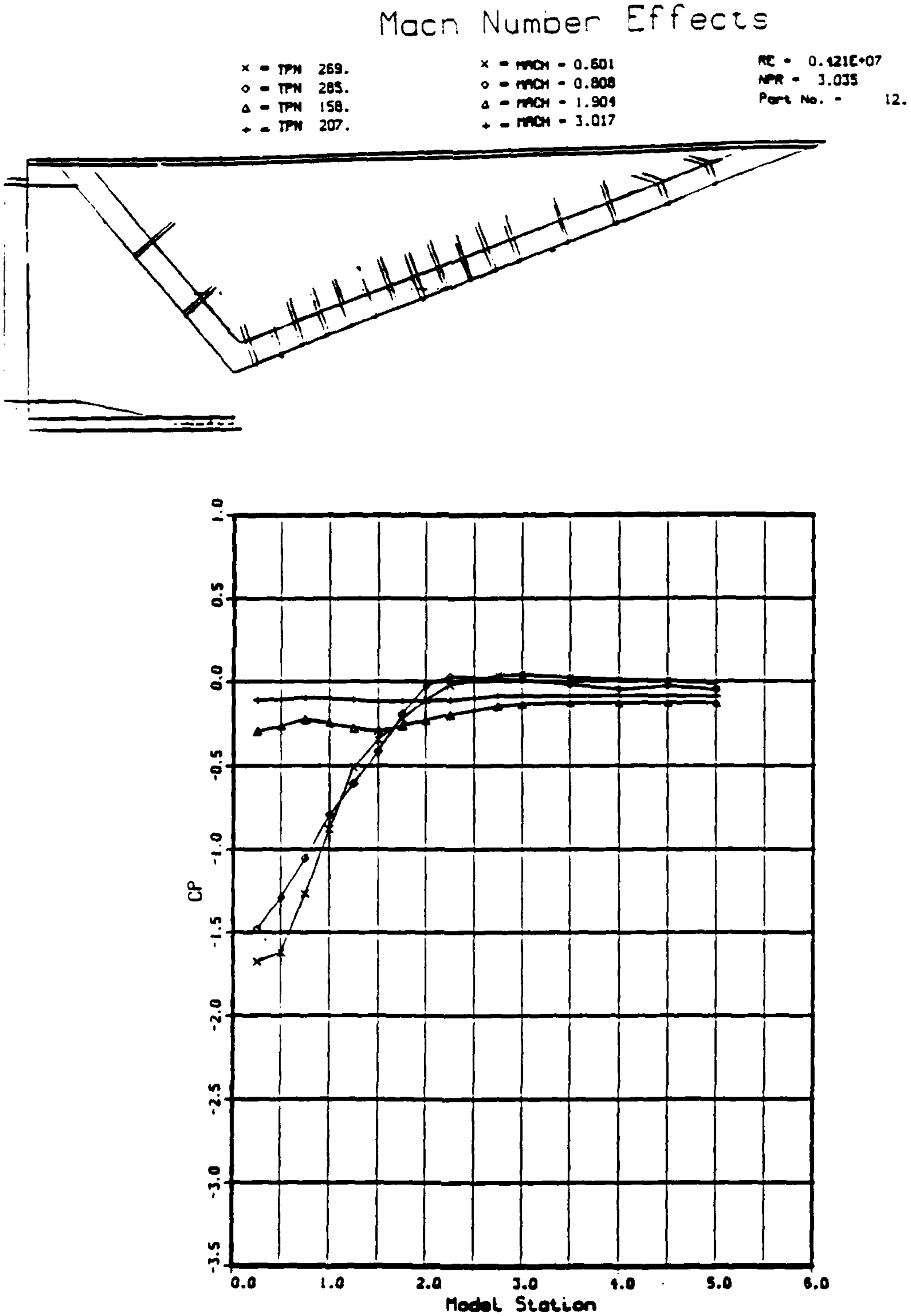

Figure E2. Pressure Coefficients, C_p vs Model Station, Mach Effect: NPR = 3.0, L Cowl

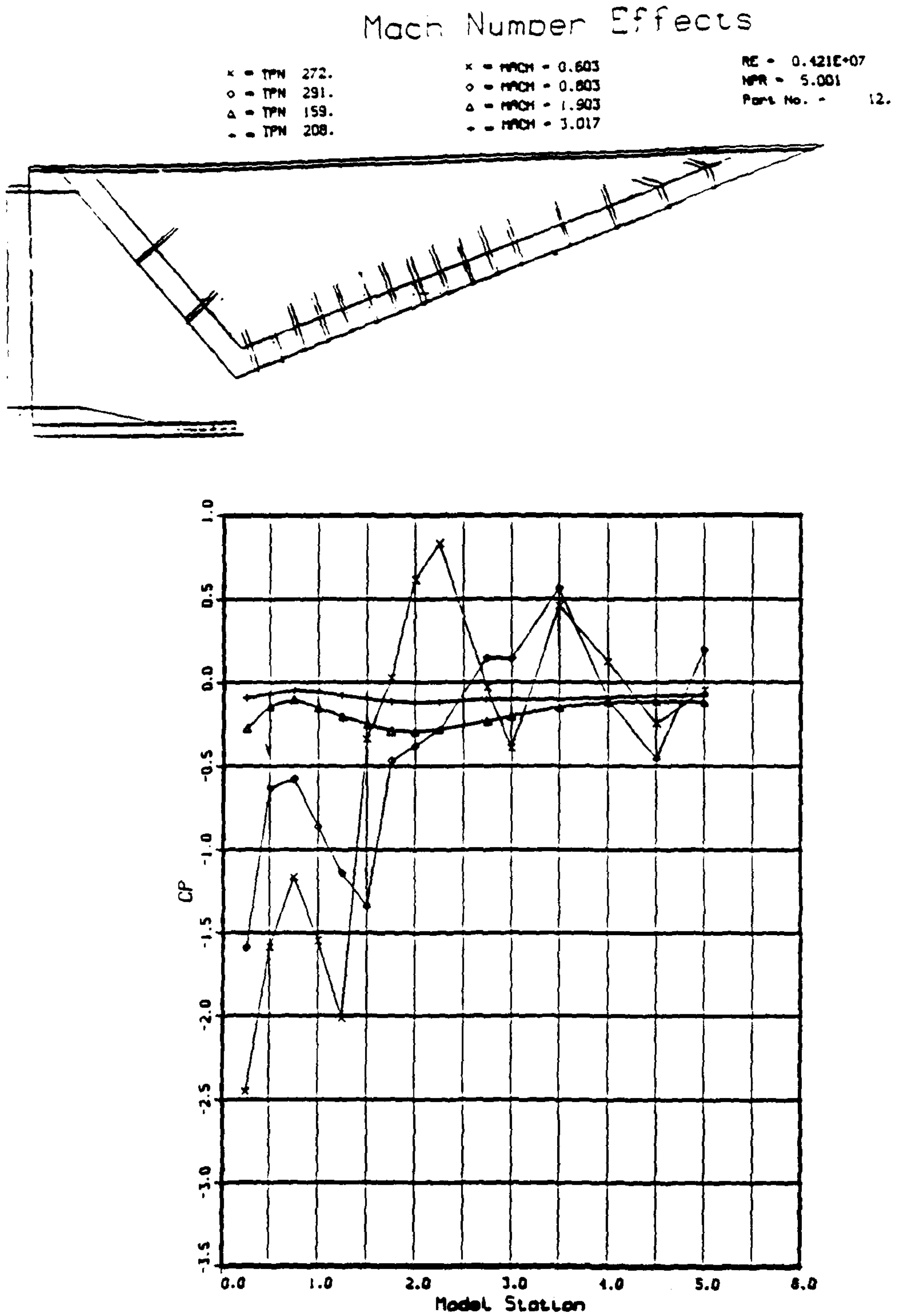

Figure E3. Pressure Coefficients, C_p vs Model Station, Mach Effect: NPR = 5.0, L Cowl

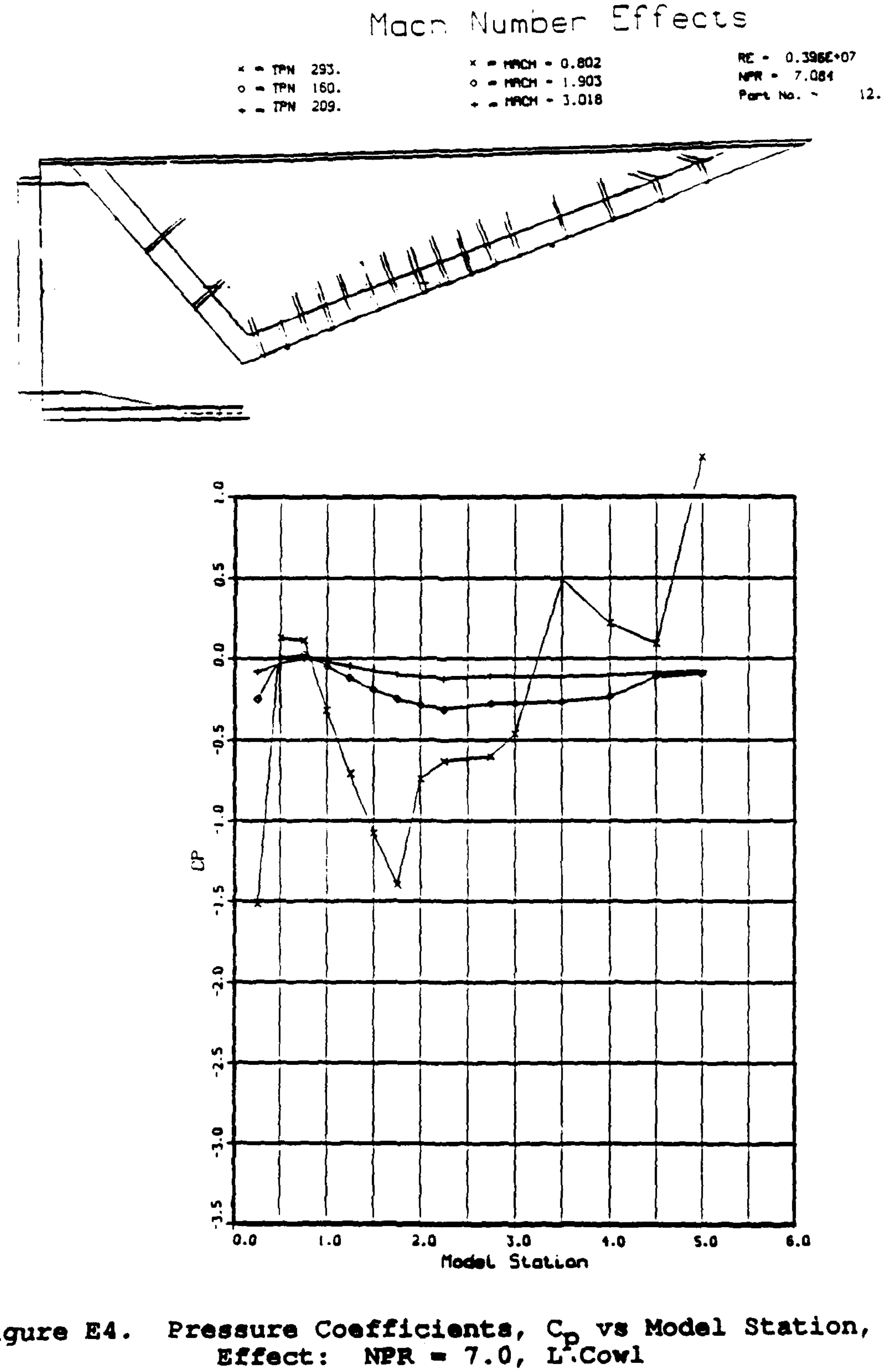

Figure E4. Pressure Coefficients, C_p vs Model Station, Mach Effect: NPR = 7.0, L.Cowl

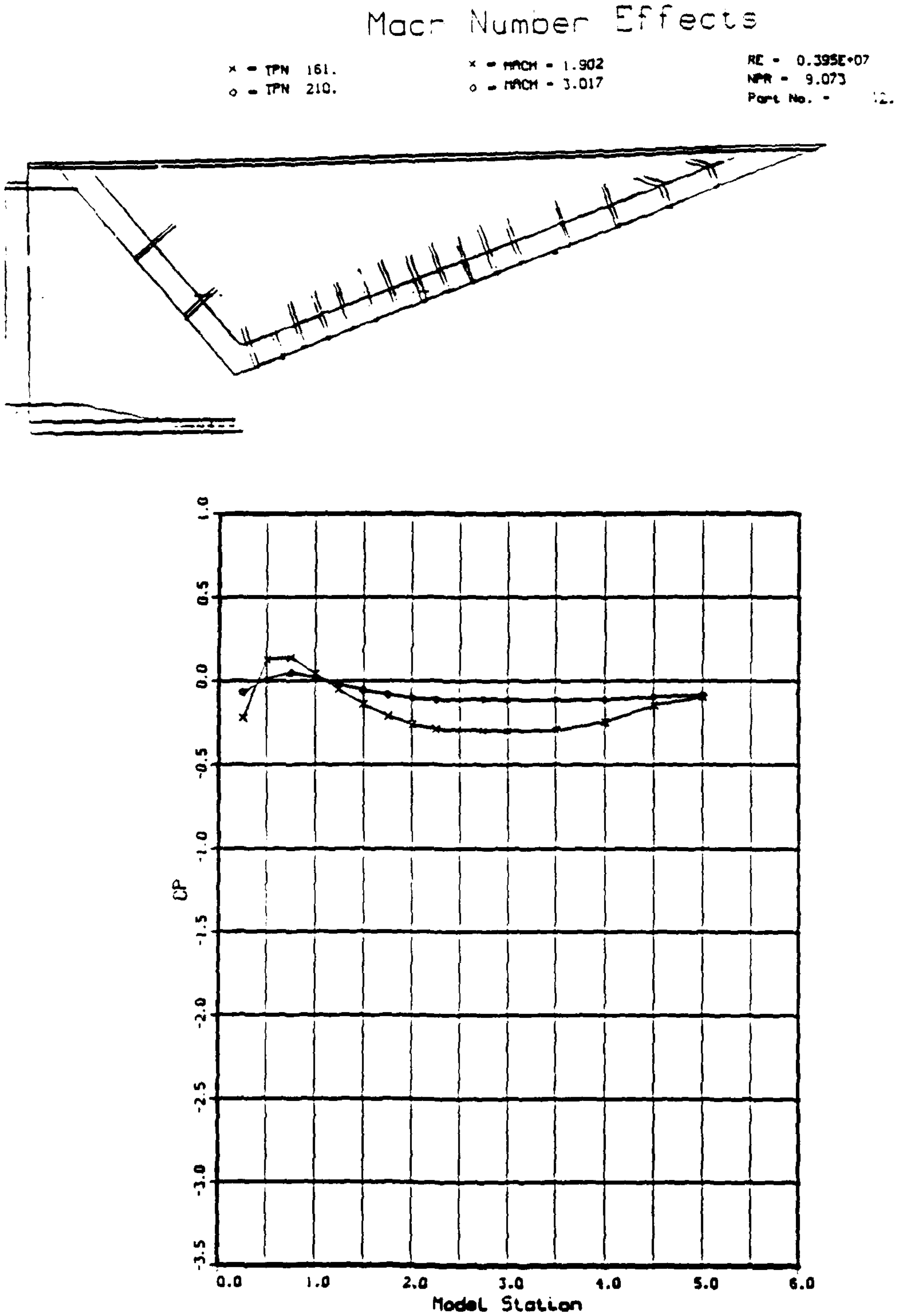

Figure E5. Pressure Coefficients, C_p vs Model Station, Mach Effect: NPR = 9.0, L Cowl

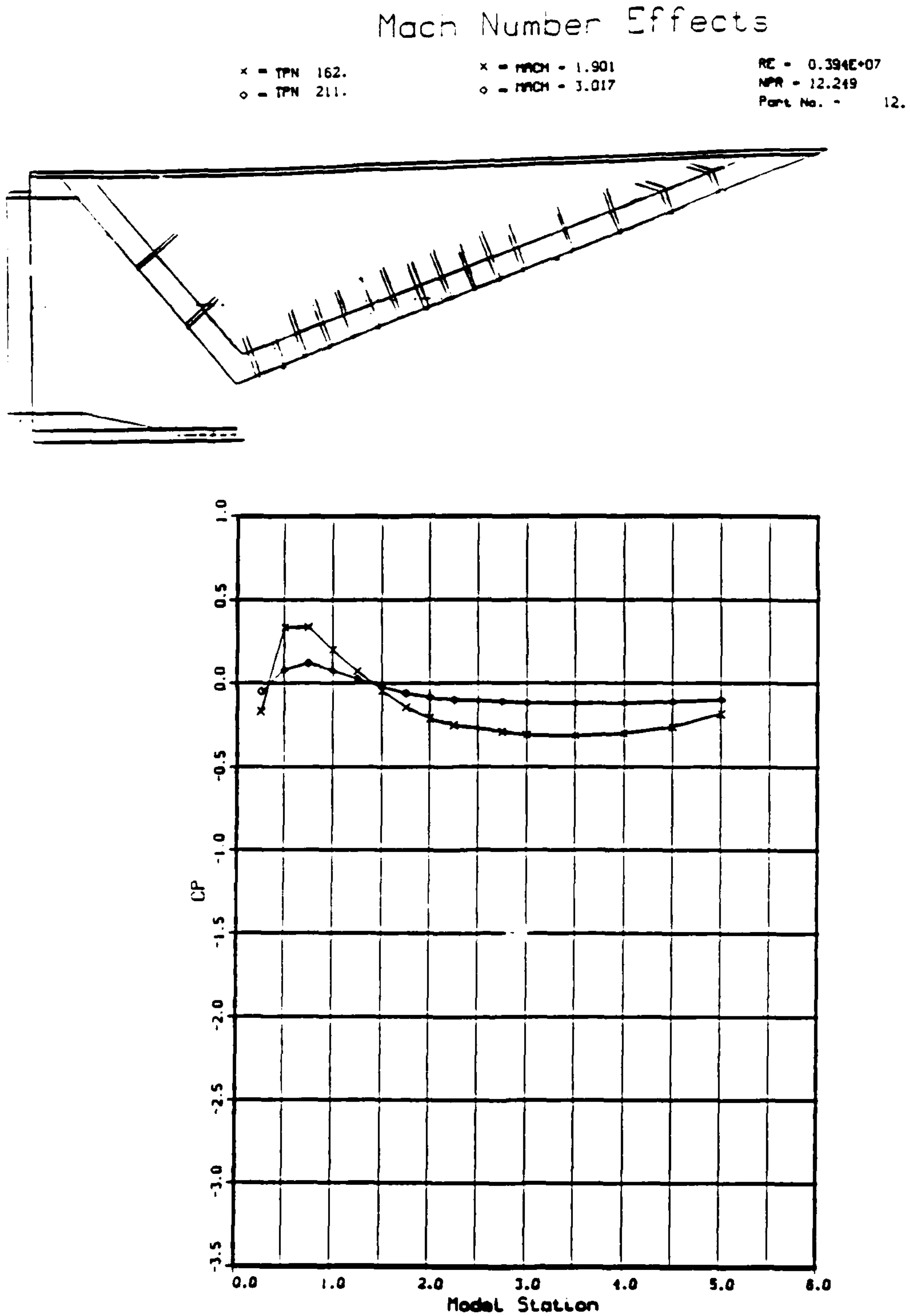

Figure E6. Pressure Coefficients, C_p vs Model Station, Mach Effect: NPR = 12.0, L Cowl

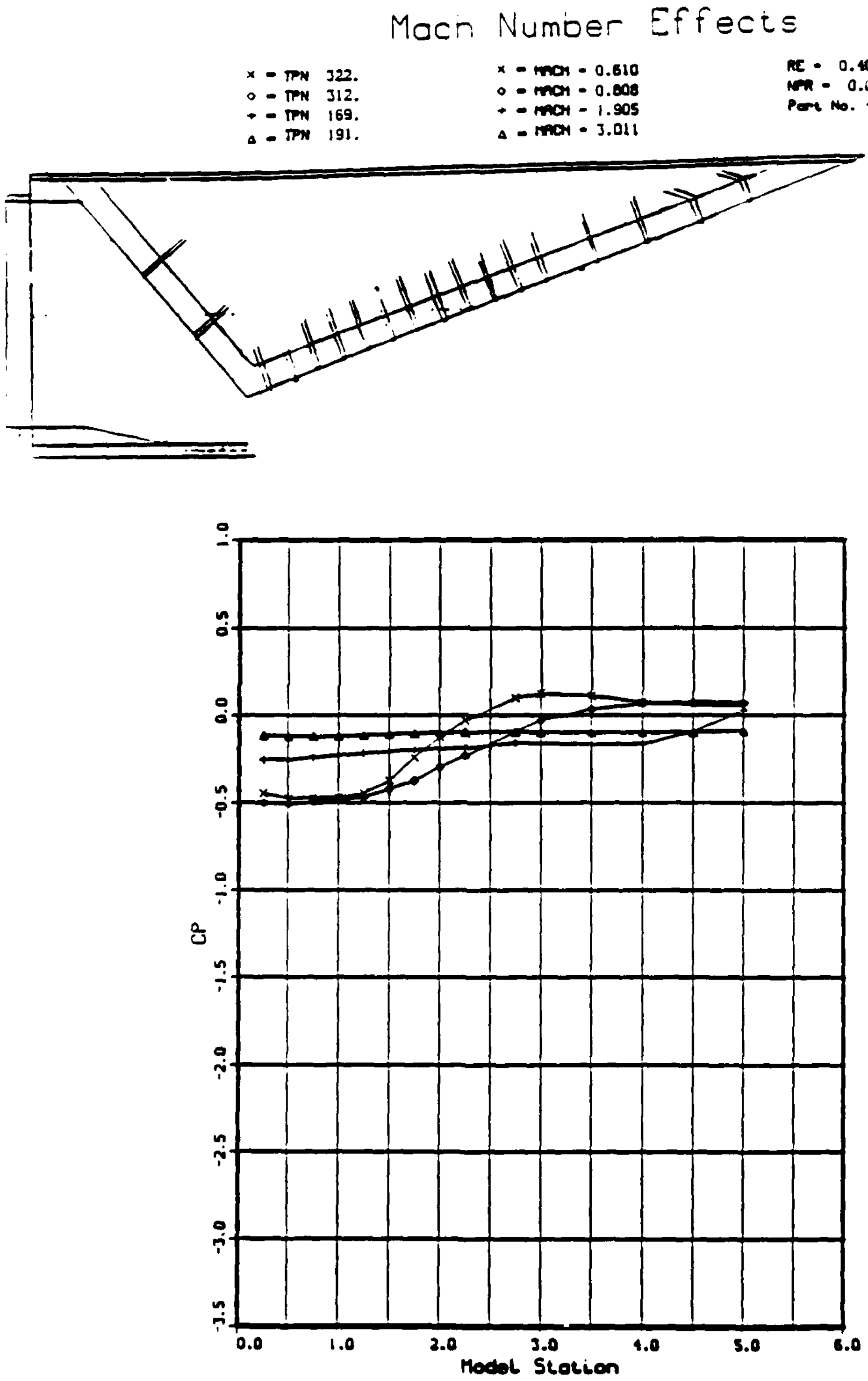

Figure E7. Pressure Coefficients, C_p vs Model Station, Mach Effect: NPR = 1.0, +5 Cowl

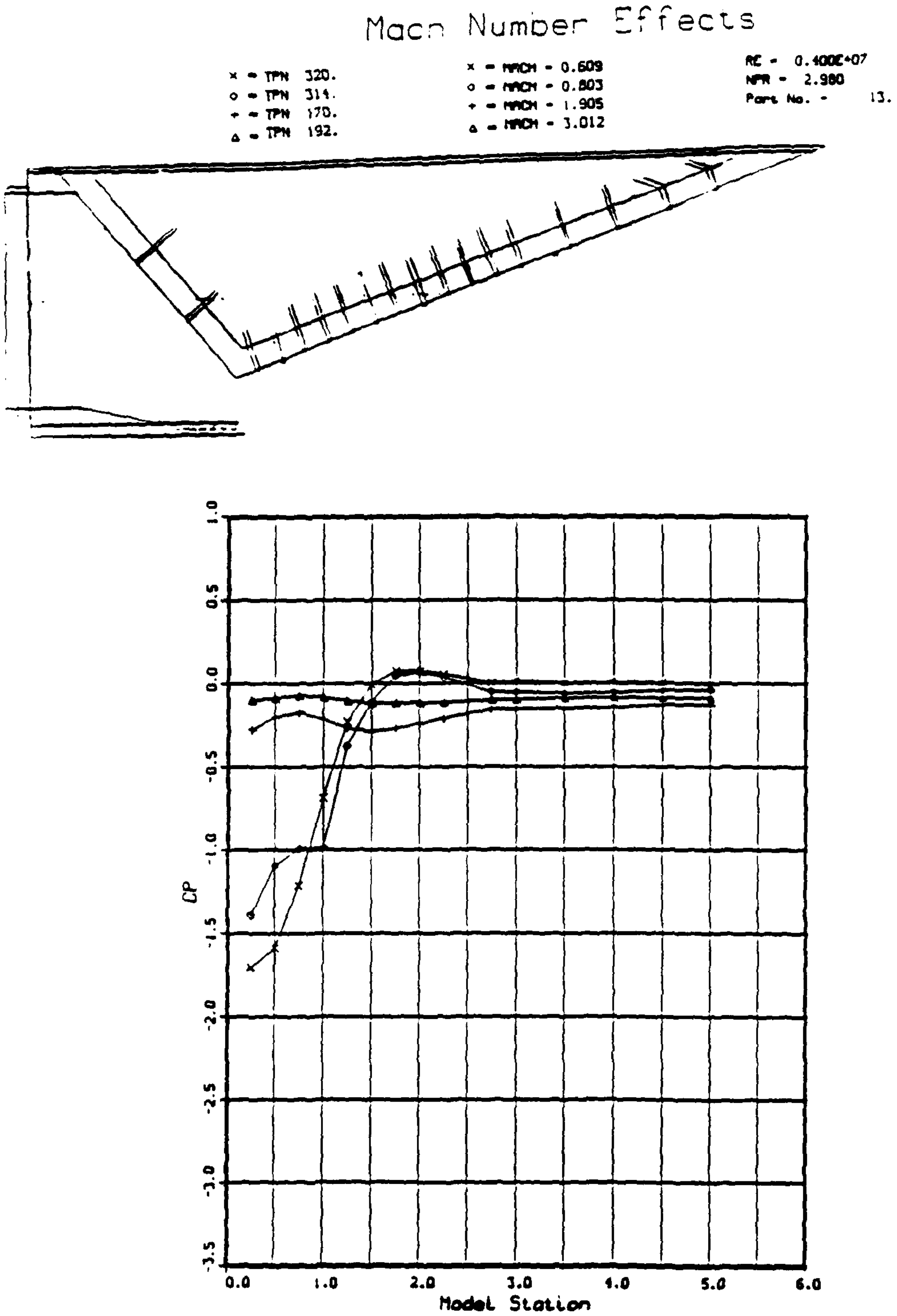

Figure E8. Pressure Coefficients, C_p vs Model Station, Mach Effect: NPR = 3.0, +5. Cowl

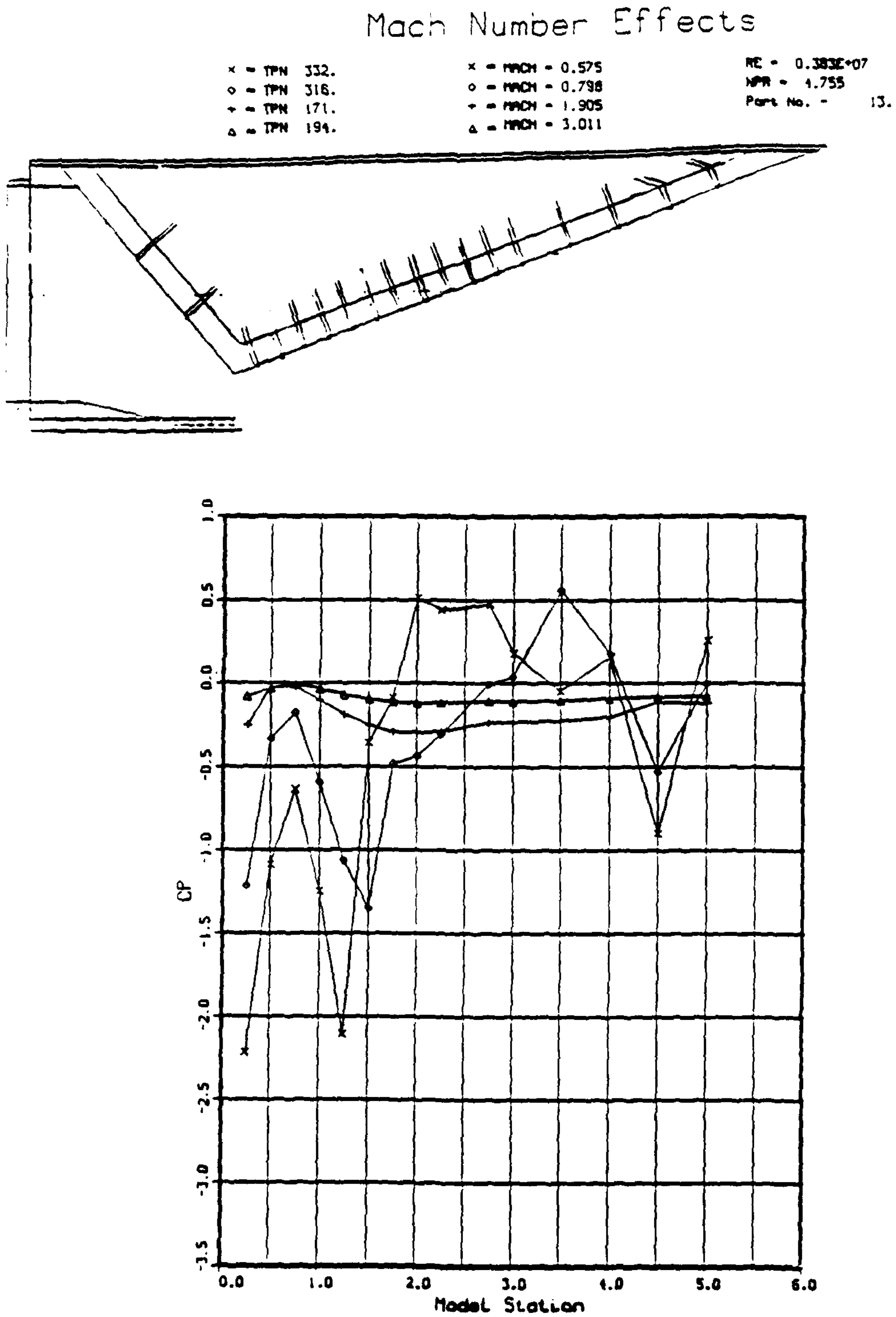

Figure E9. Pressure Coefficients, C_p vs Model Station, Mach Effect: NPR = 5.0, +5 Cowl

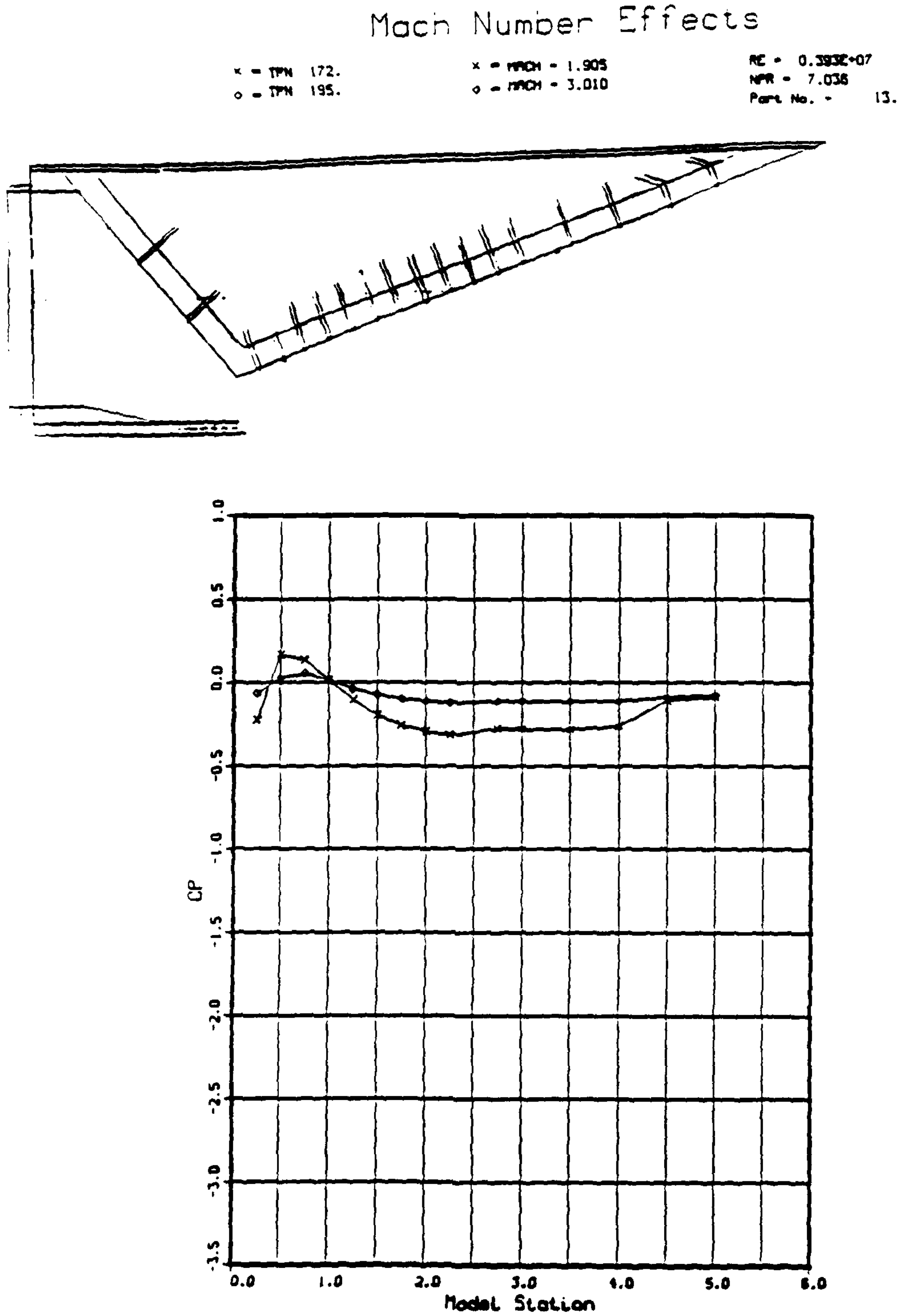

Figure E10. Pressure Coefficients, C_p vs Model Station, Mach Effect: NPR = 7.0, +5 Cowl

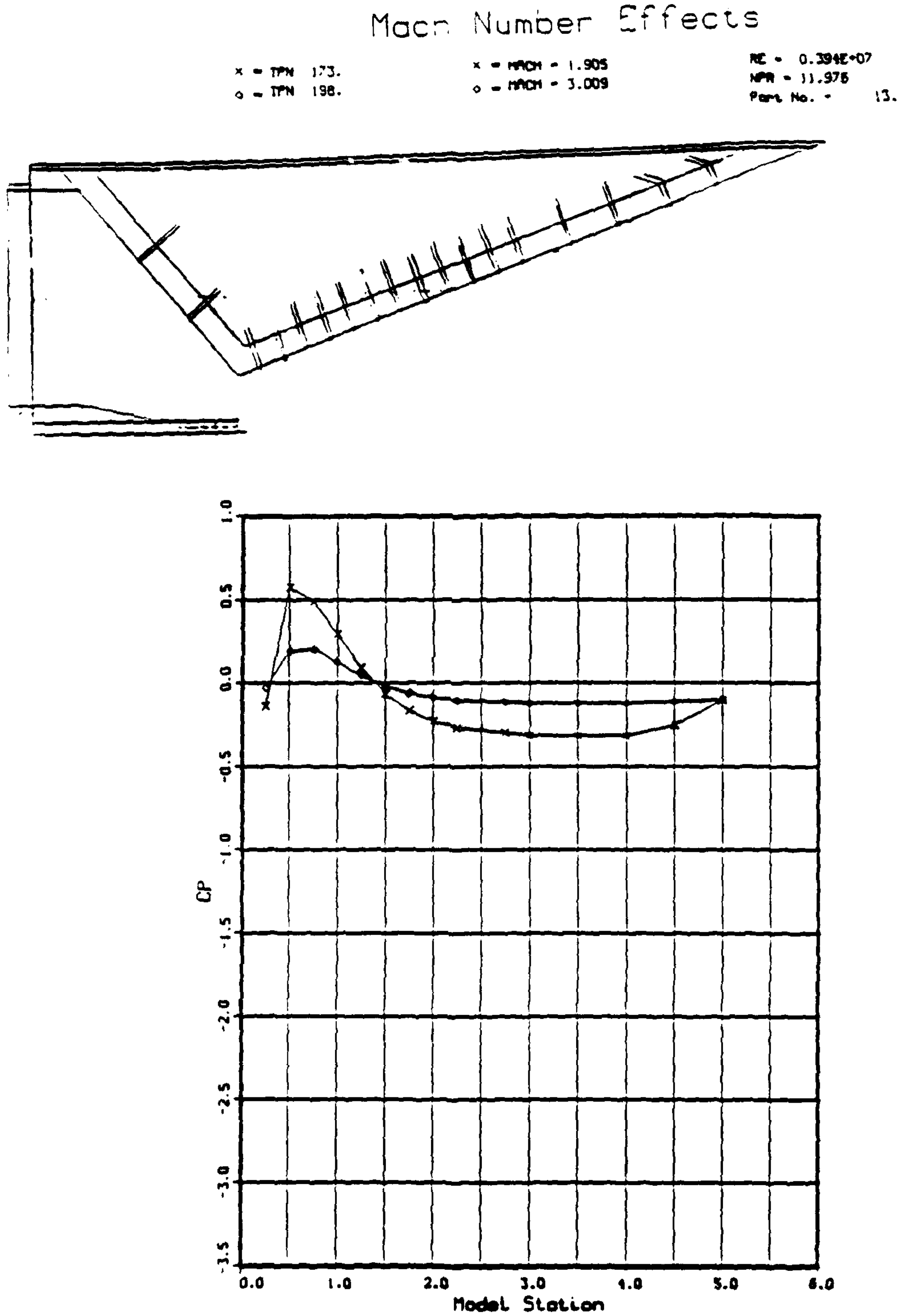

Figure E11. Pressure Coefficients, C_p vs Model Station, Mach Effect: NPR = 12.0, +5 Cowl

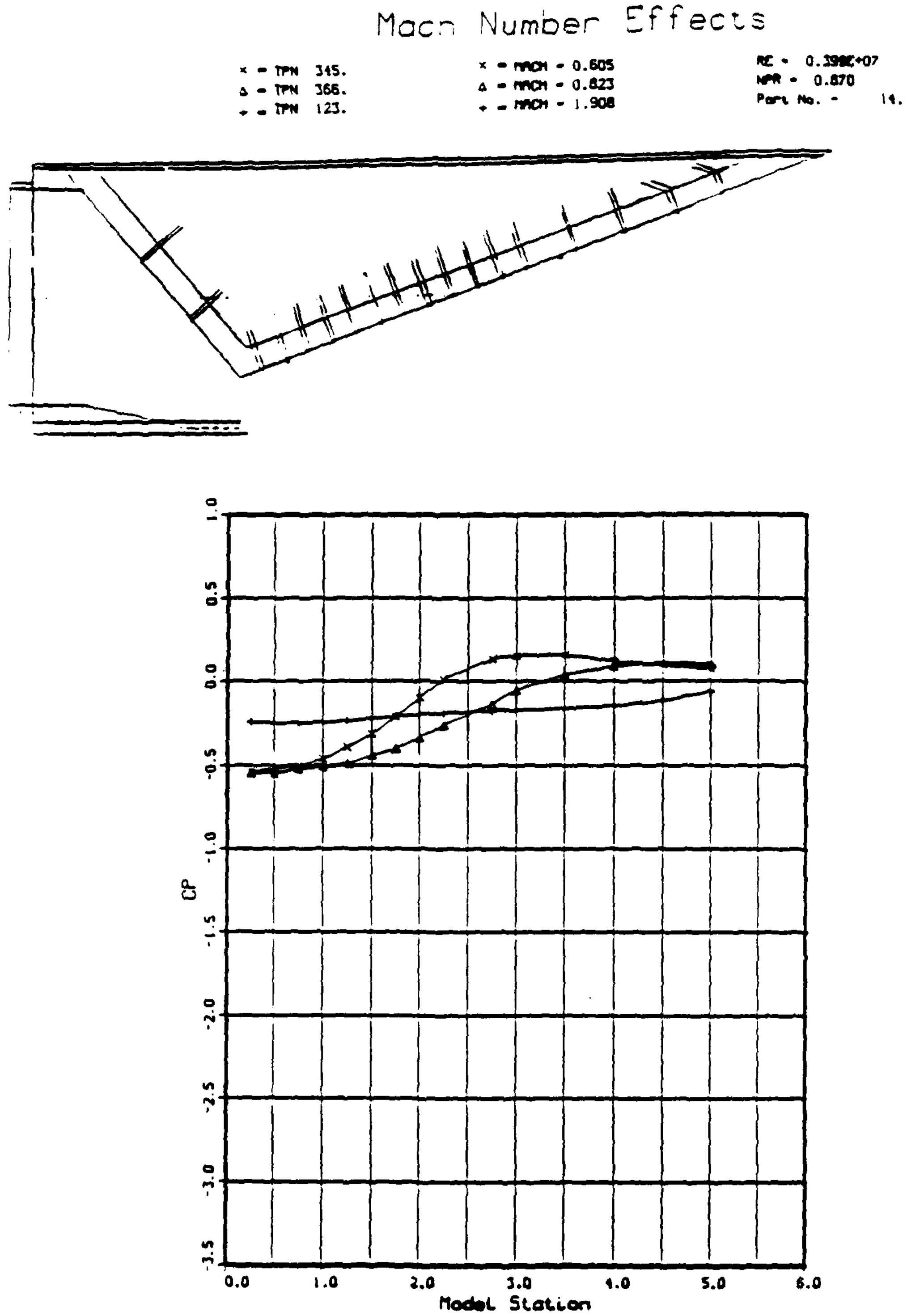

Figure E12. Pressure Coefficients, C_p vs Model Station, Mach Effect: NPR = 1.0, -5 Cowl

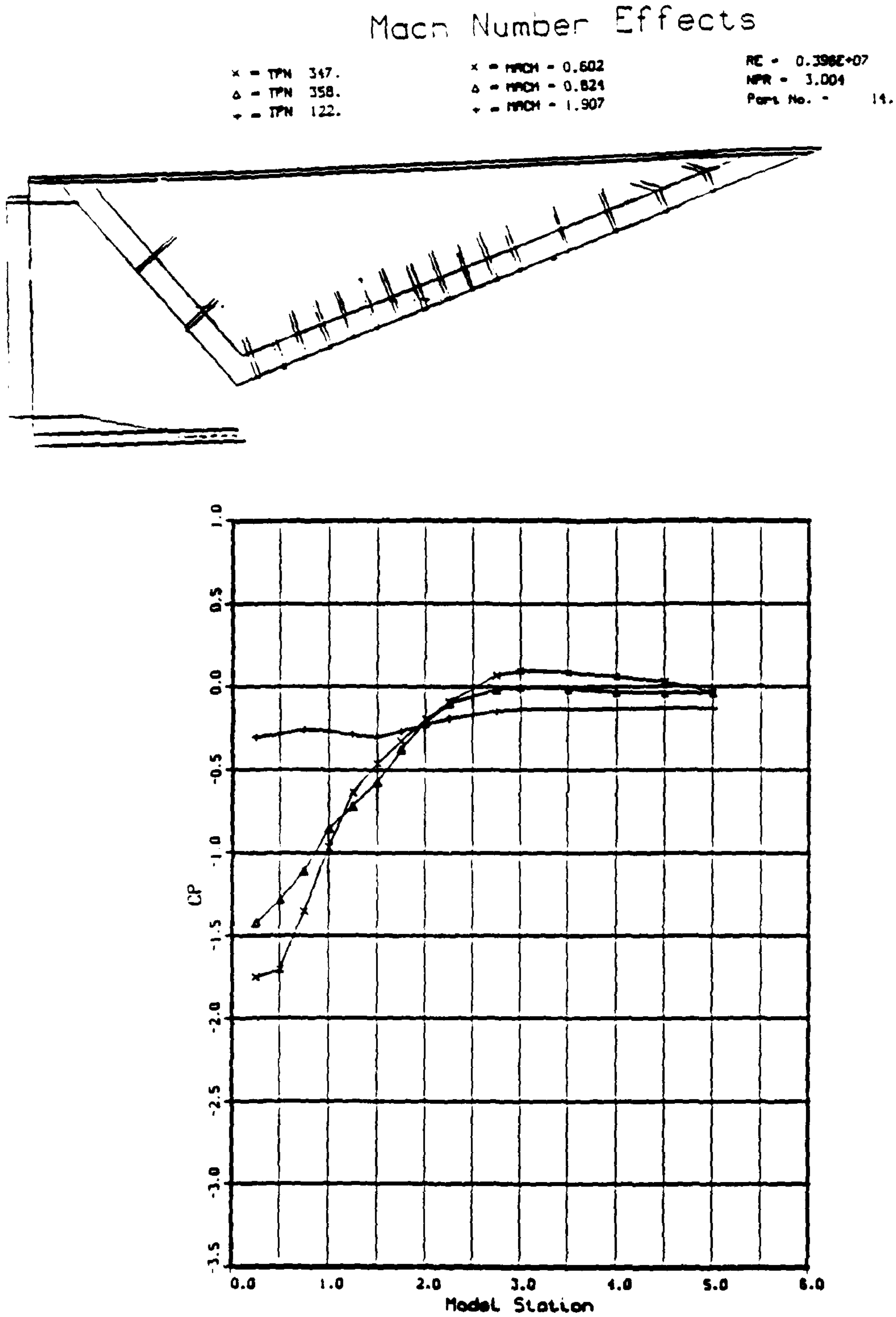

Figure E13. Pressure Coefficients, C_p vs Model Station, Mach Effect: NPR = 3.0, -5 Cowl

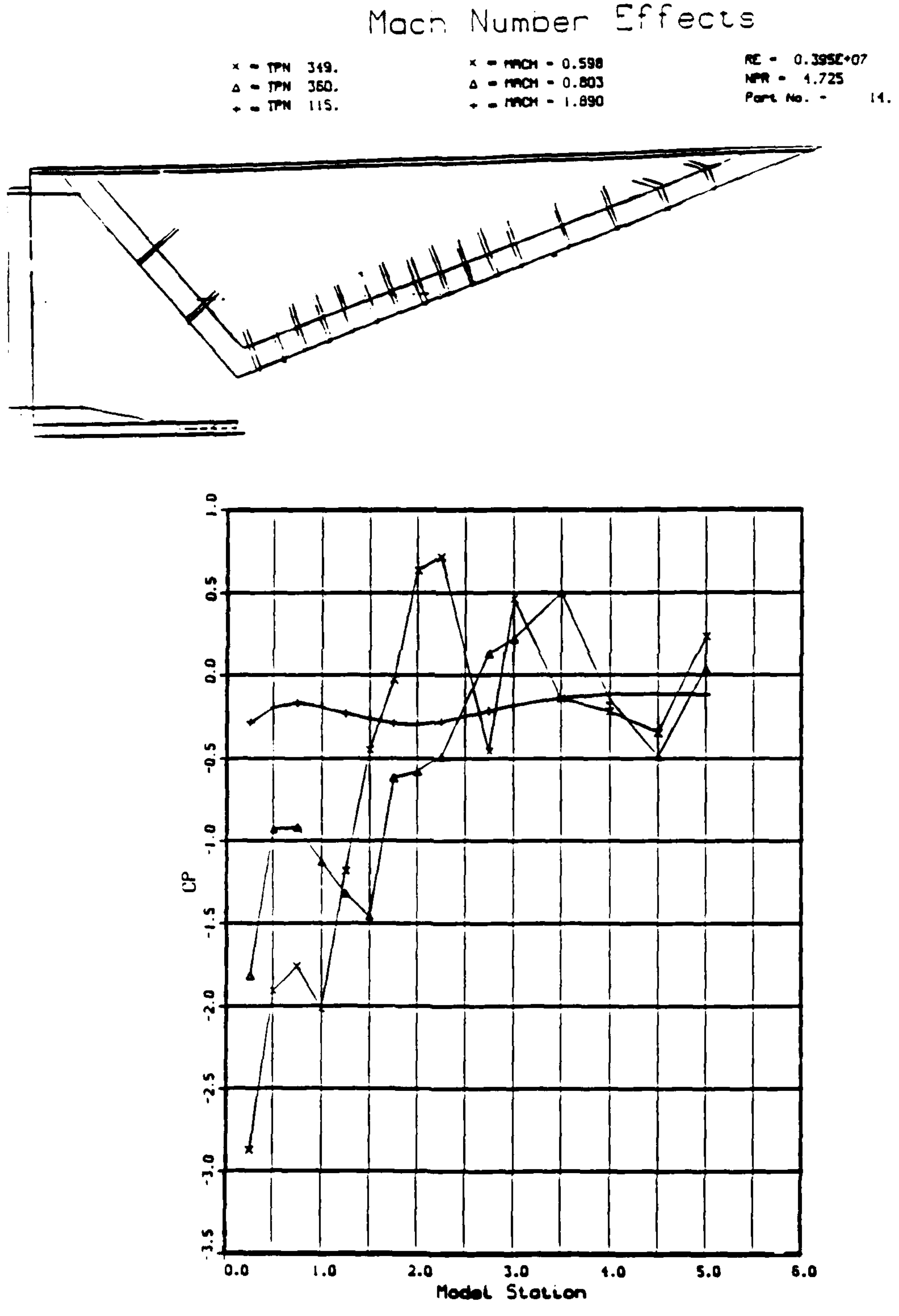

Figure E14. Pressure Coefficients, C_p vs Model Station, Mach Effect: NPR = 5.0, -5 Cowl

Appendix F: Schlieren Photographs

Figure F1. Schlieren: Mach 0.6, NPR = 2.0, L Cowl

Figure F2. Schlieren: Mach 0.6, NPR = 2.0, +5 Cowl

Figure F3. Schlieren: Mach 0.6, NPR = 2.0, -5 Cowl

Figure F4. Schlieren: Mach 0.8, NPR = 3.0, L Cowl

Figure F5. Schlieren: Mach 0.8, NPR = 3.0, +5 Cowl

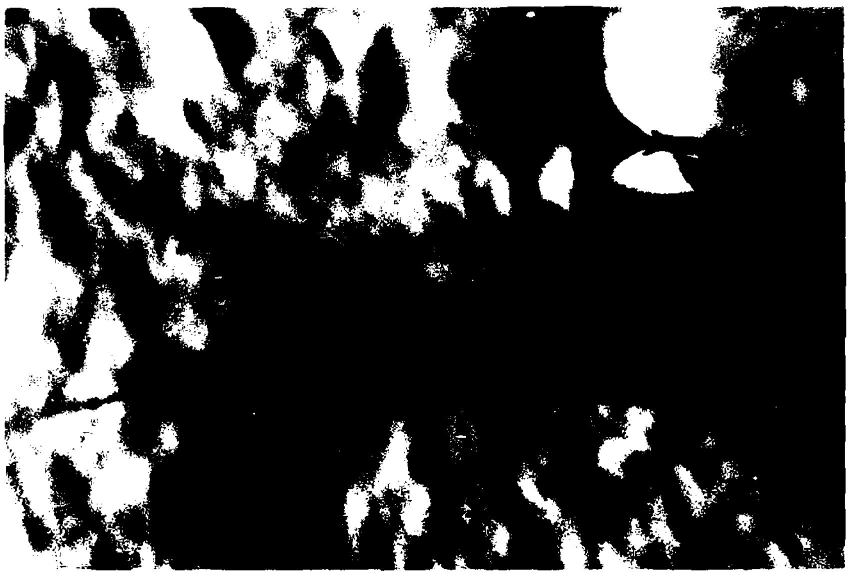

Figure F6. Schlieren: Mach 0.8, NPR = 3.0, -5 Cowl

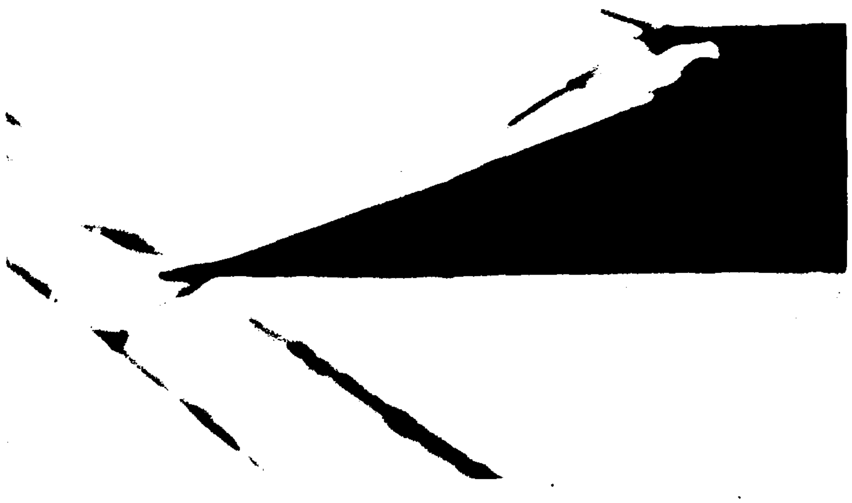

Figure F7. Schlieren: Mach 1.9, NPR = 7.0, L Cowl

Figure F8. Schlieren: Mach 1.9, NPR = 7.0, +5 Cowl

Figure F9. Schlieren: Mach 1.9, NPR = 7.0, -5 Cowl

Figure F10. Schlieren: Mach 3.0, NPR = 16.0, L Cowl

Figure F11. Schlieren: Mach 3.0, NPR = 16.0, +5 Cowl

Appendix G: Pressure Coefficients, C_p vs Model Station: Cowl Effects

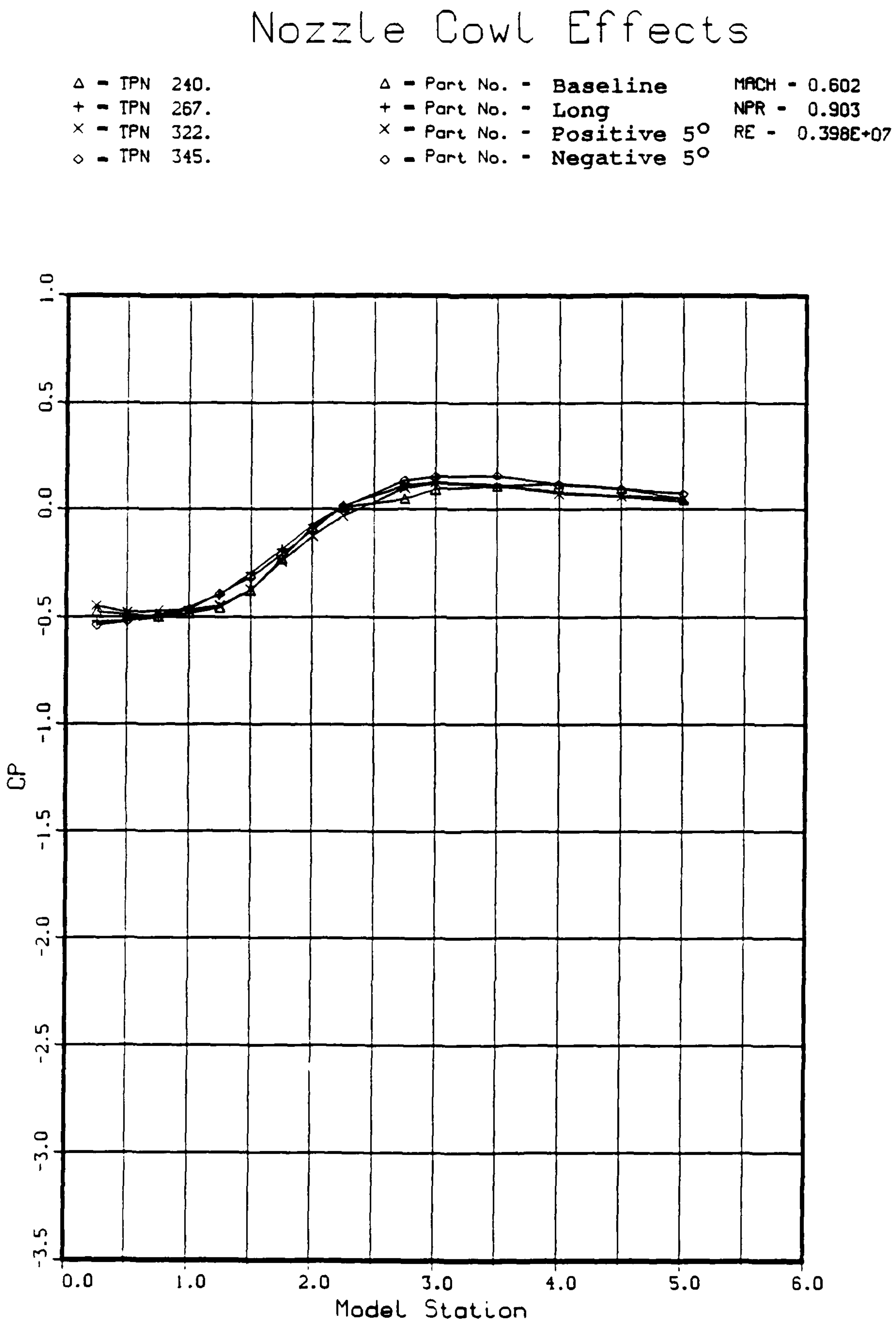

Figure G1. Pressure Coefficients, C_p vs Model Station, Nozzle Cowl Effects: Mach 0.6, NPR = 1.0

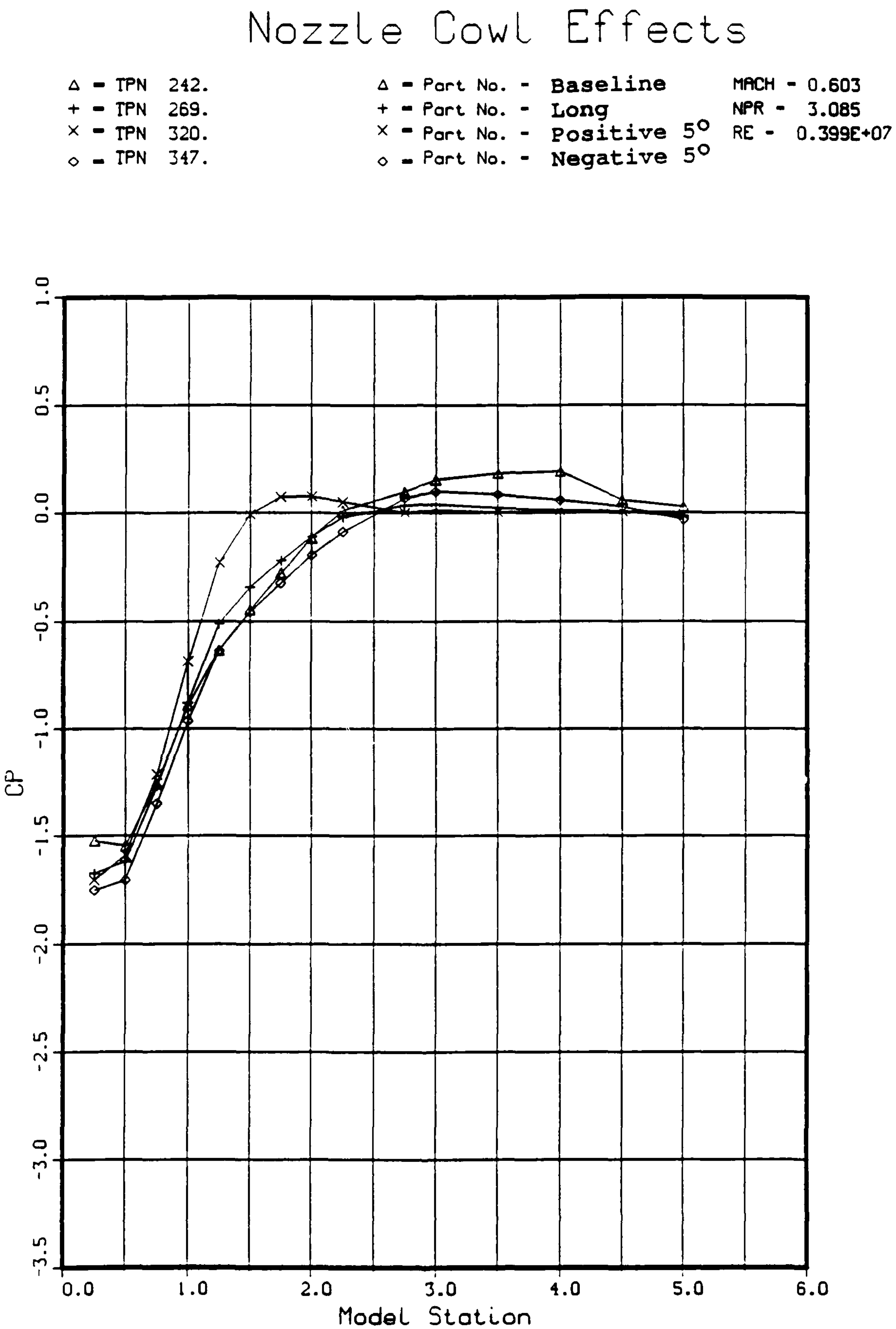

Figure G2. Pressure Coefficients, C_p vs Model Station, Nozzle Cowl Effects: Mach 0.6, NPR = 3.0

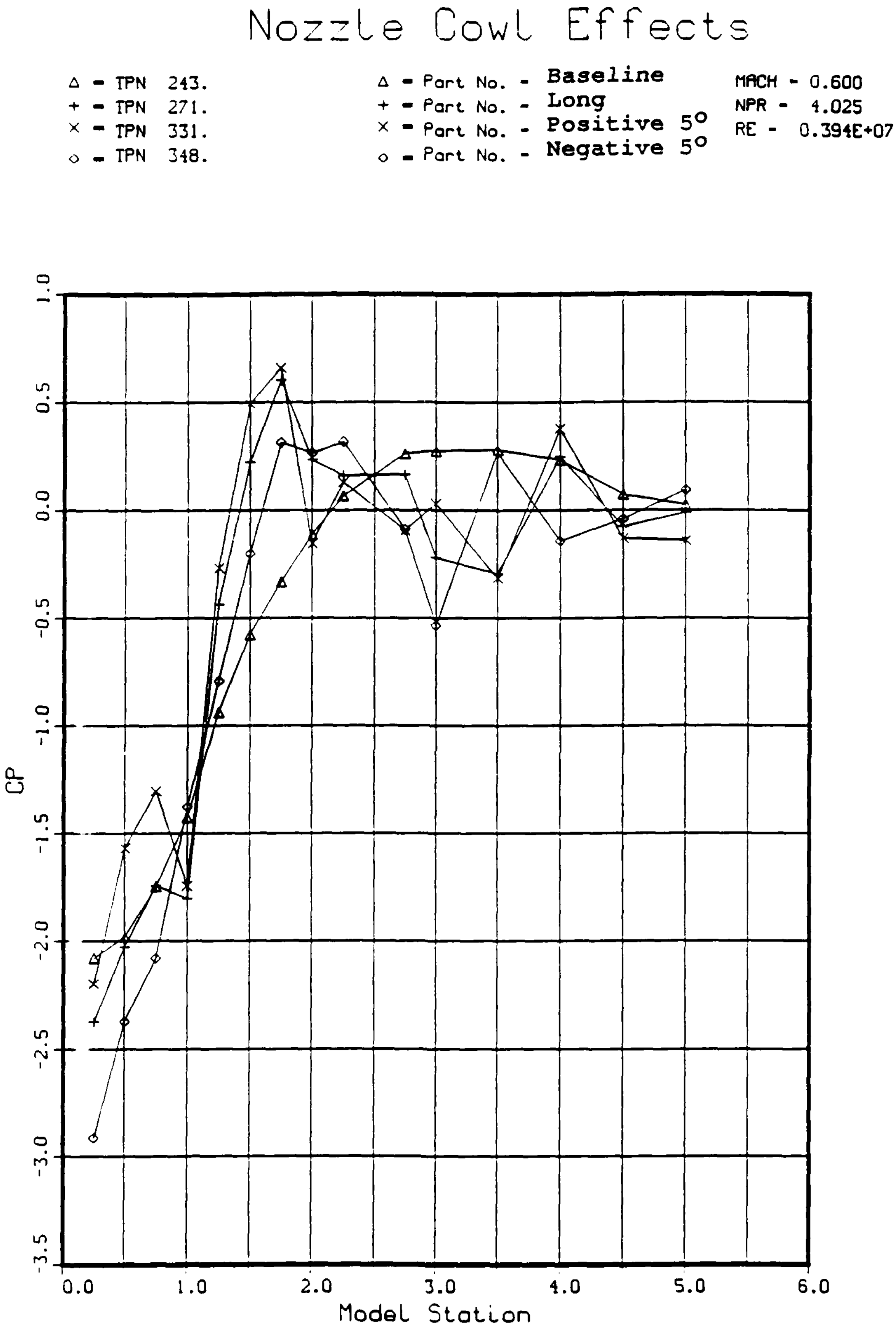

Figure G3. Pressure Coefficients, C_p vs Model Station, Nozzle Cowl Effects: Mach 0.6, NPR = 4.0

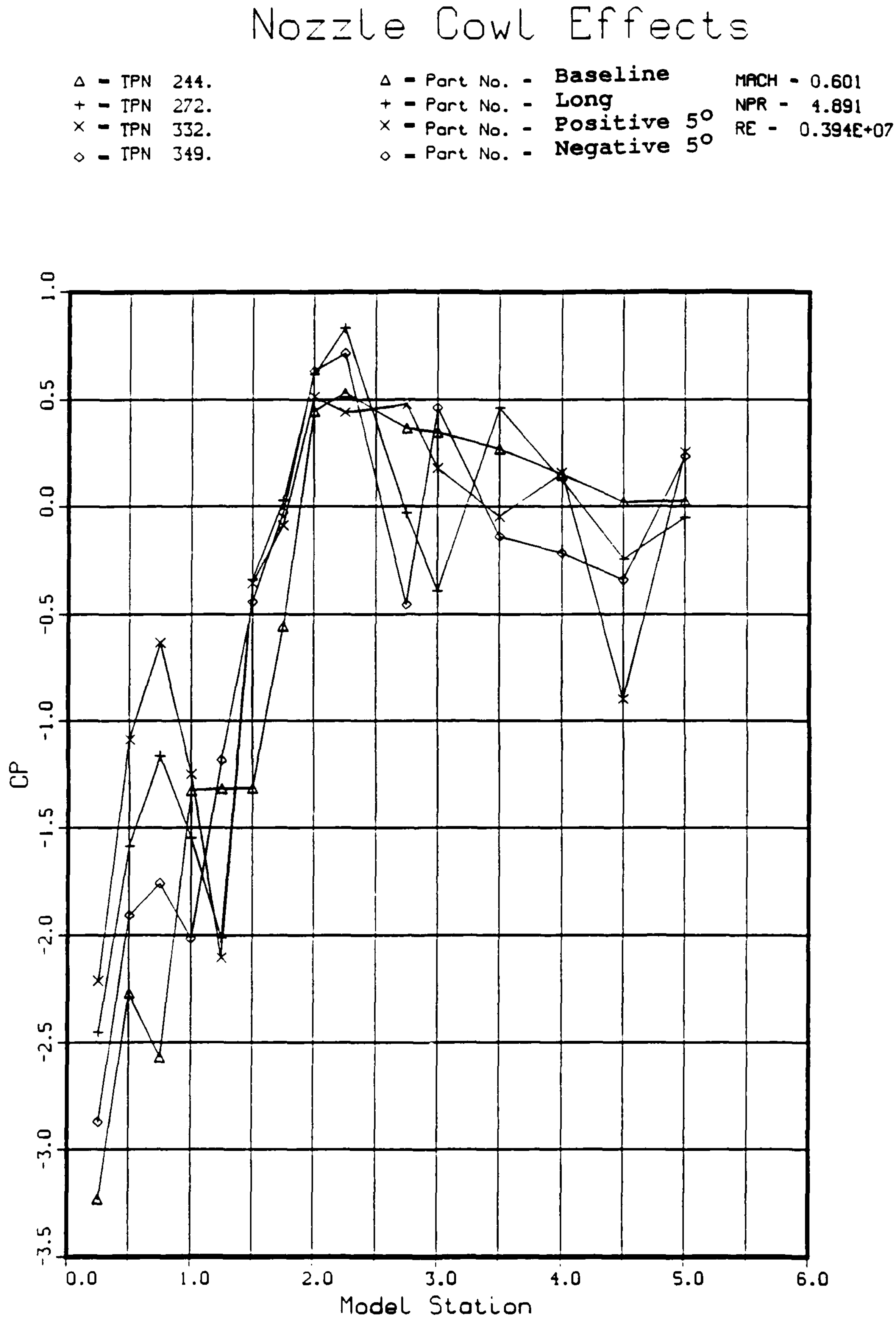

Figure G4. Pressure Coefficients, C_p vs Model Station, Nozzle Cowl Effects: Mach 0.6, NPR = 5.0

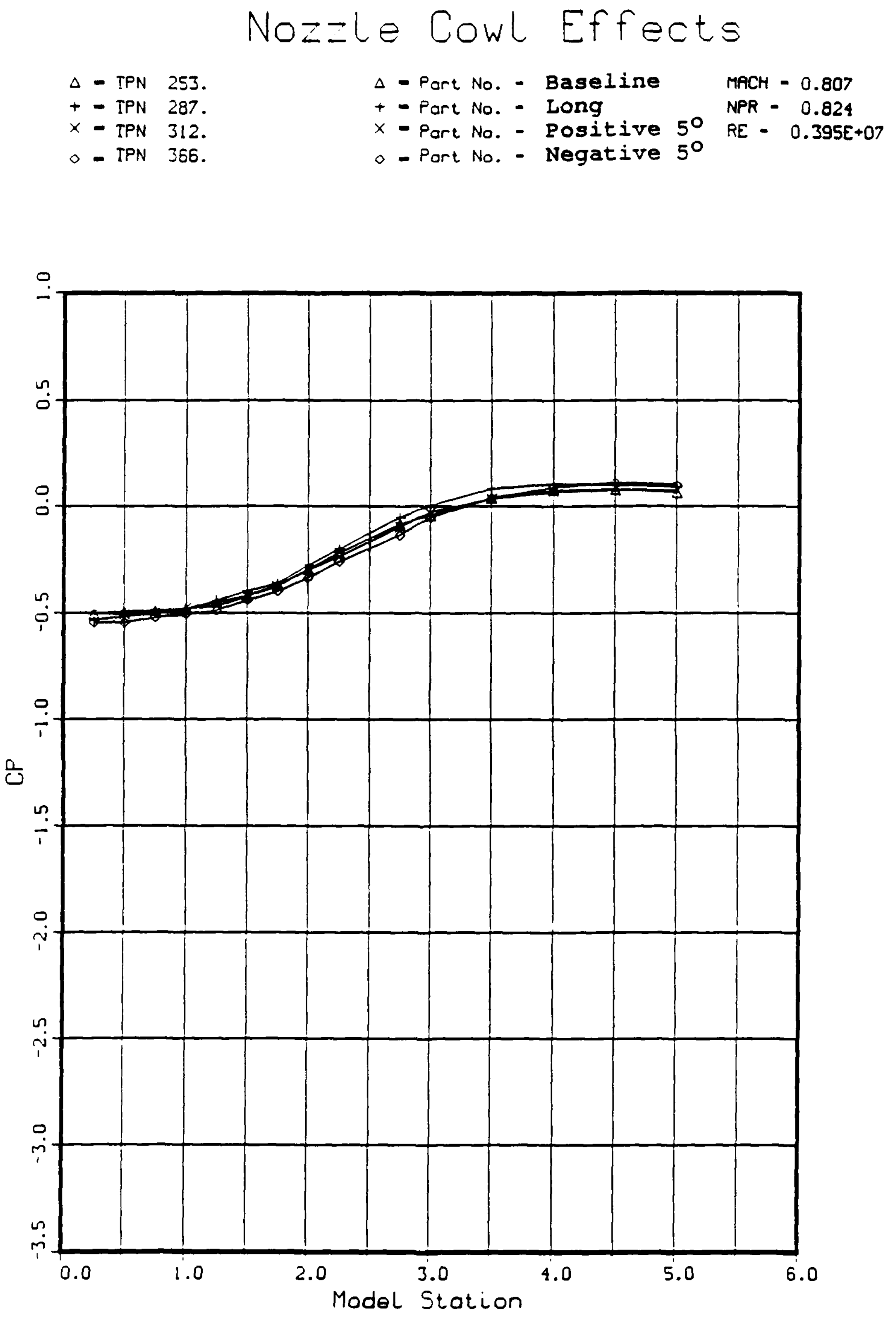

Figure G5. Pressure Coefficients, C_p vs Model Station, Nozzle Cowl Effects: Mach 0.8, NPR = 1.0

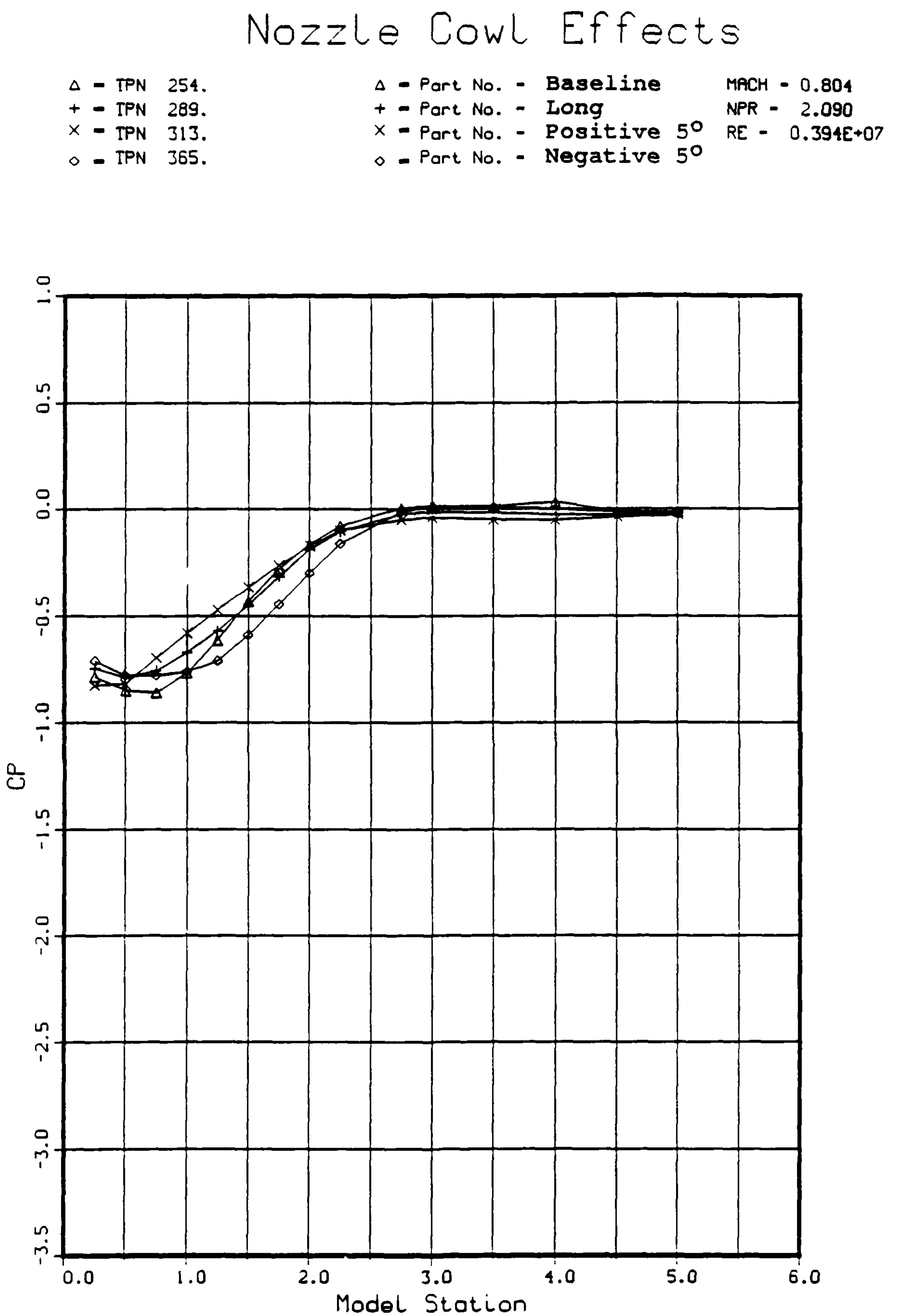

Figure G6. Pressure Coefficients, C_p vs Model Station, Nozzle Cowl Effects: Mach 0.8, NPR = 2.0

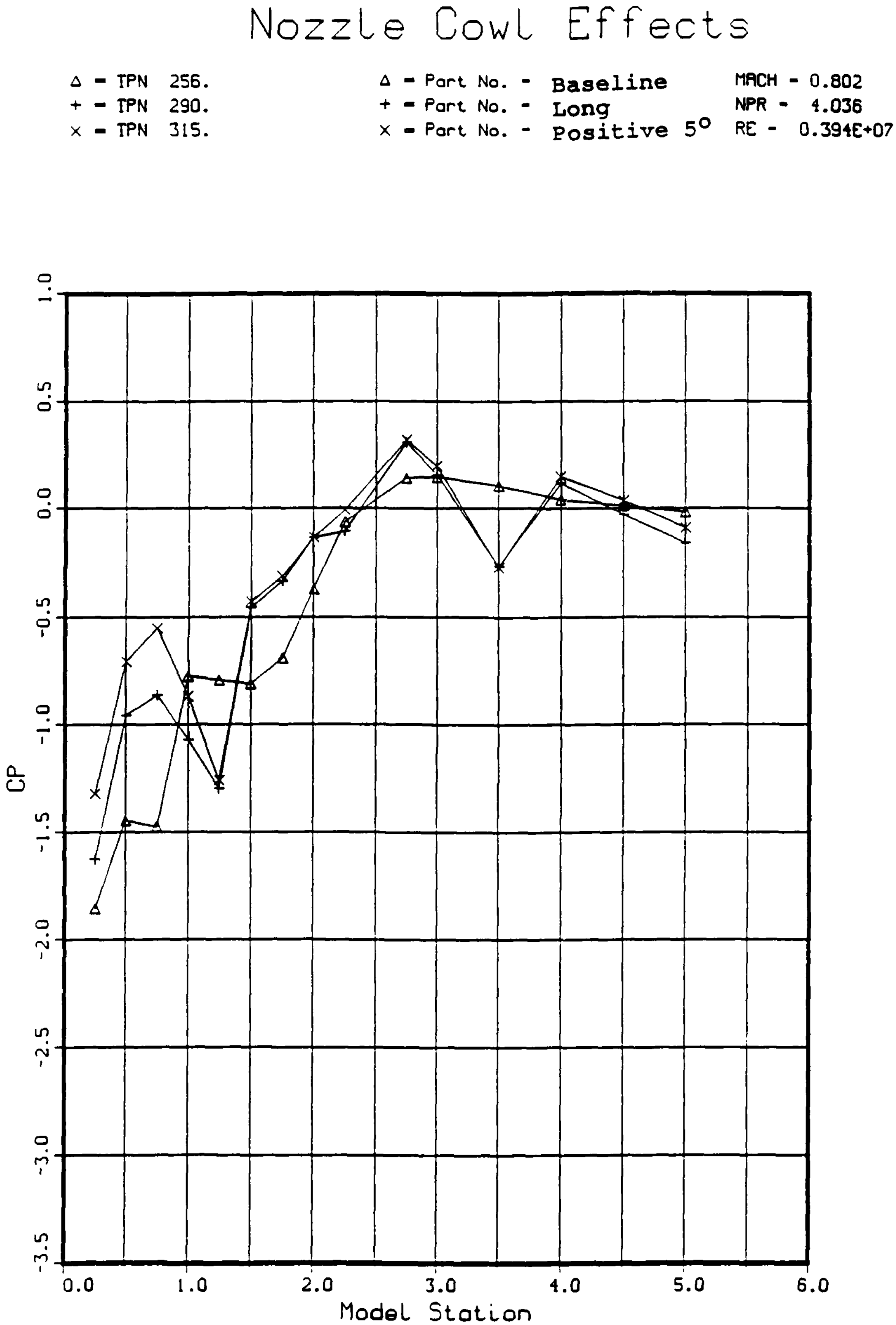

Figure G7. Pressure Coefficients, C_p vs Model Station, Nozzle Cowl Effects: Mach 0.8, NPR = 4.0

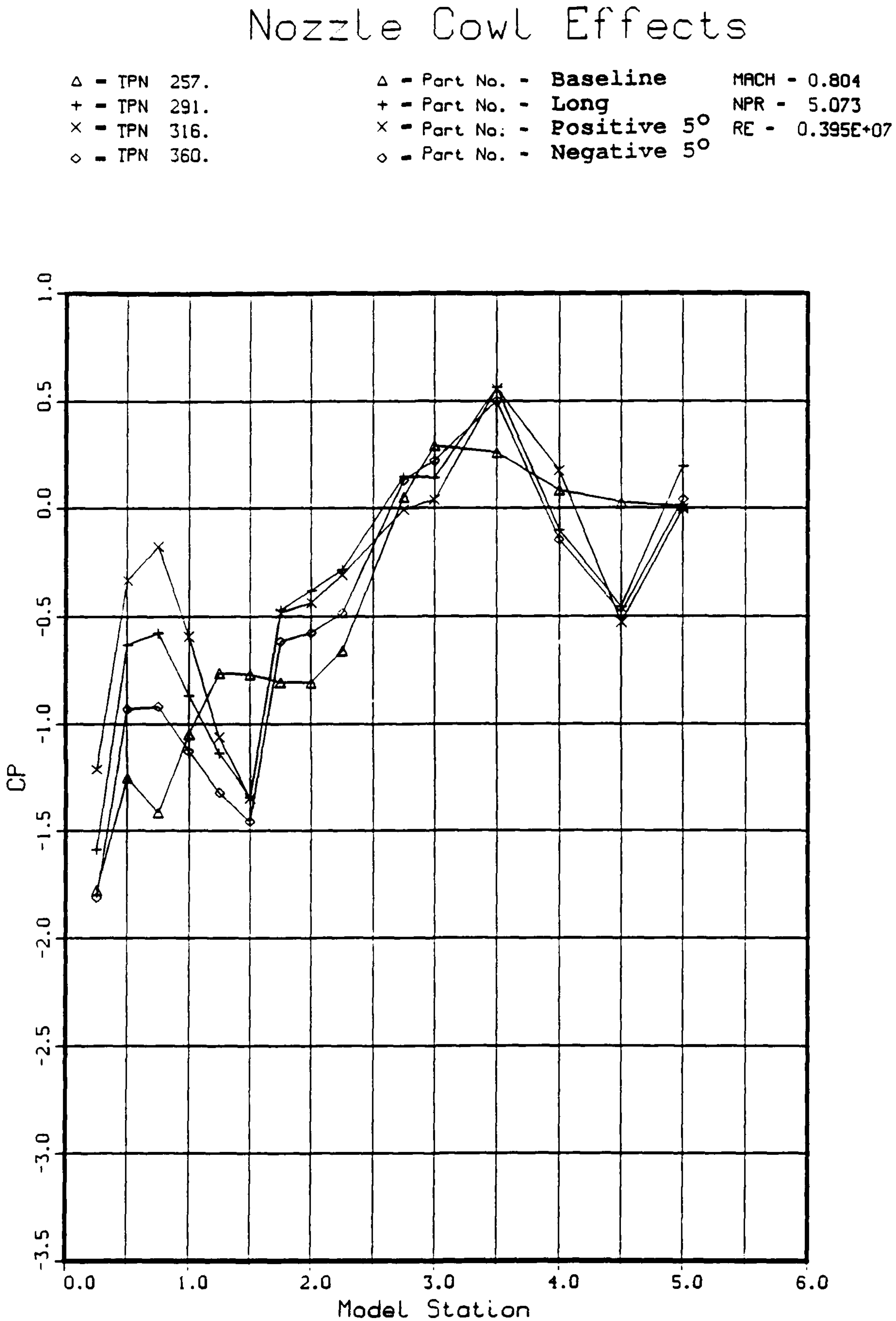

Figure G8. Pressure Coefficients, C_p vs Model Station, Nozzle Cowl Effects: Mach 0.8, NPR = 5.0

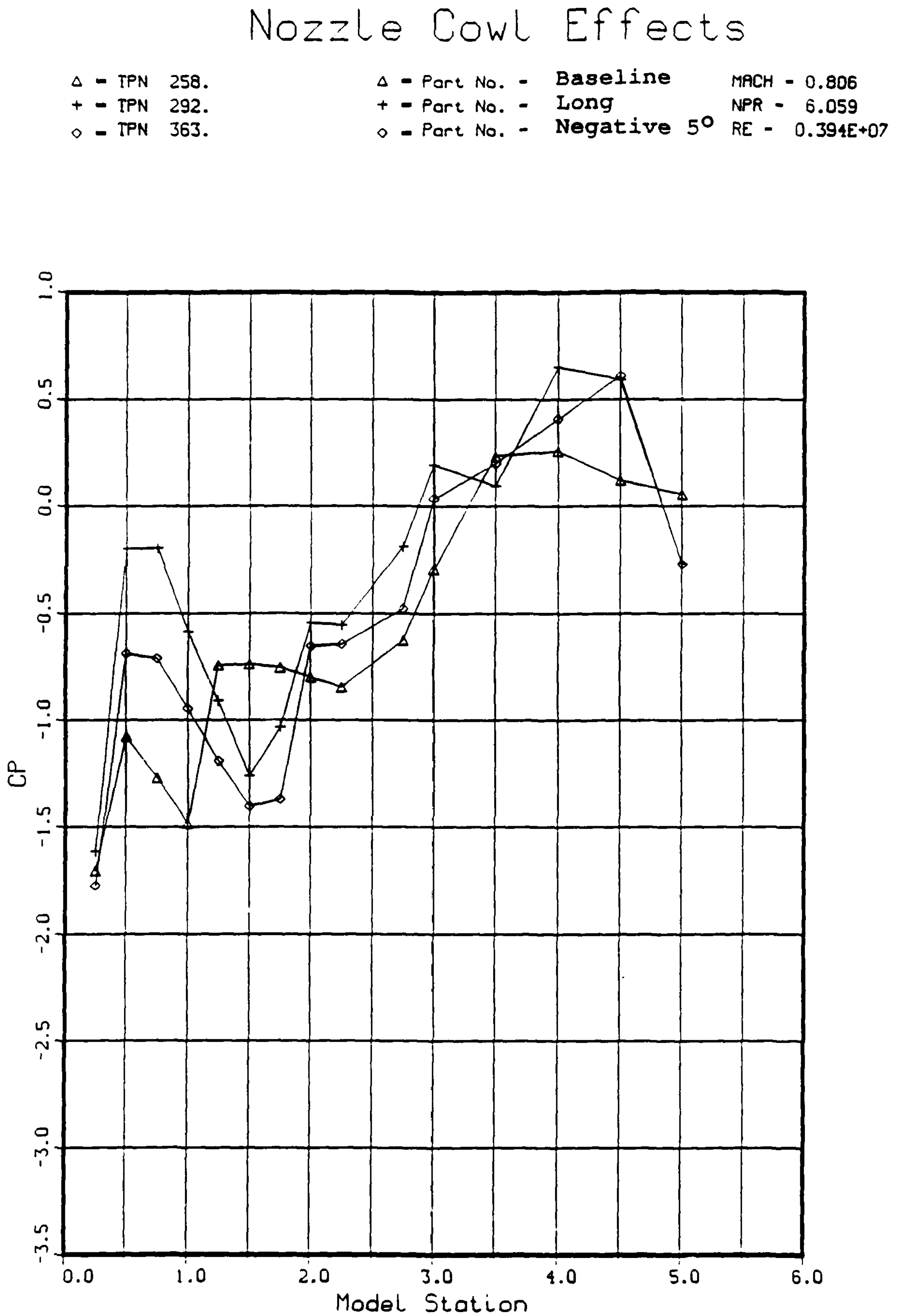

Figure G9. Pressure Coefficients, C_p vs Model Station, Nozzle Cowl Effects: Mach 0.8, NPR = 6.0

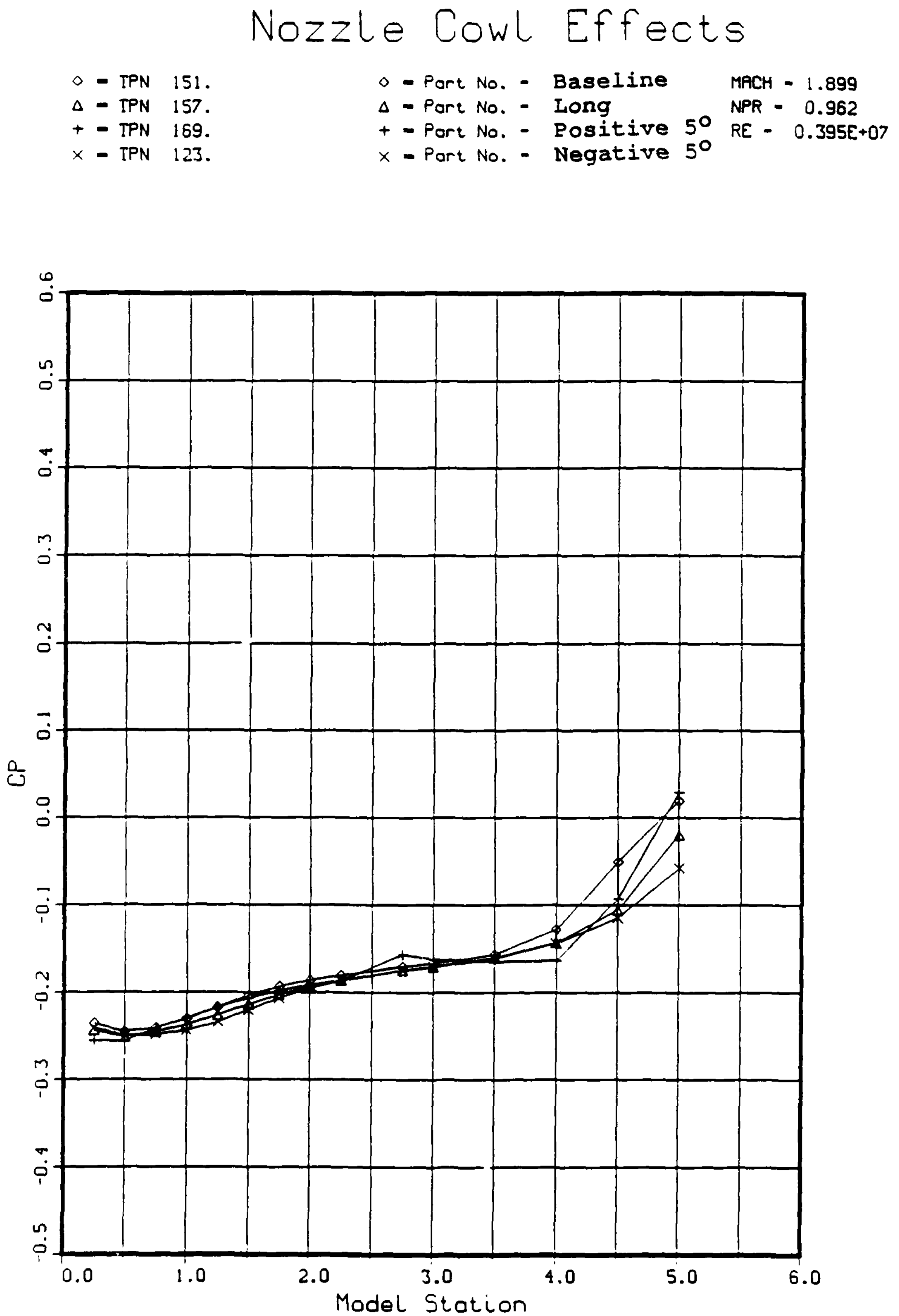

Figure G10. Pressure Coefficients, C_p vs Model Station, Nozzle Cowl Effects: Mach 1.9, NPR = 1.0

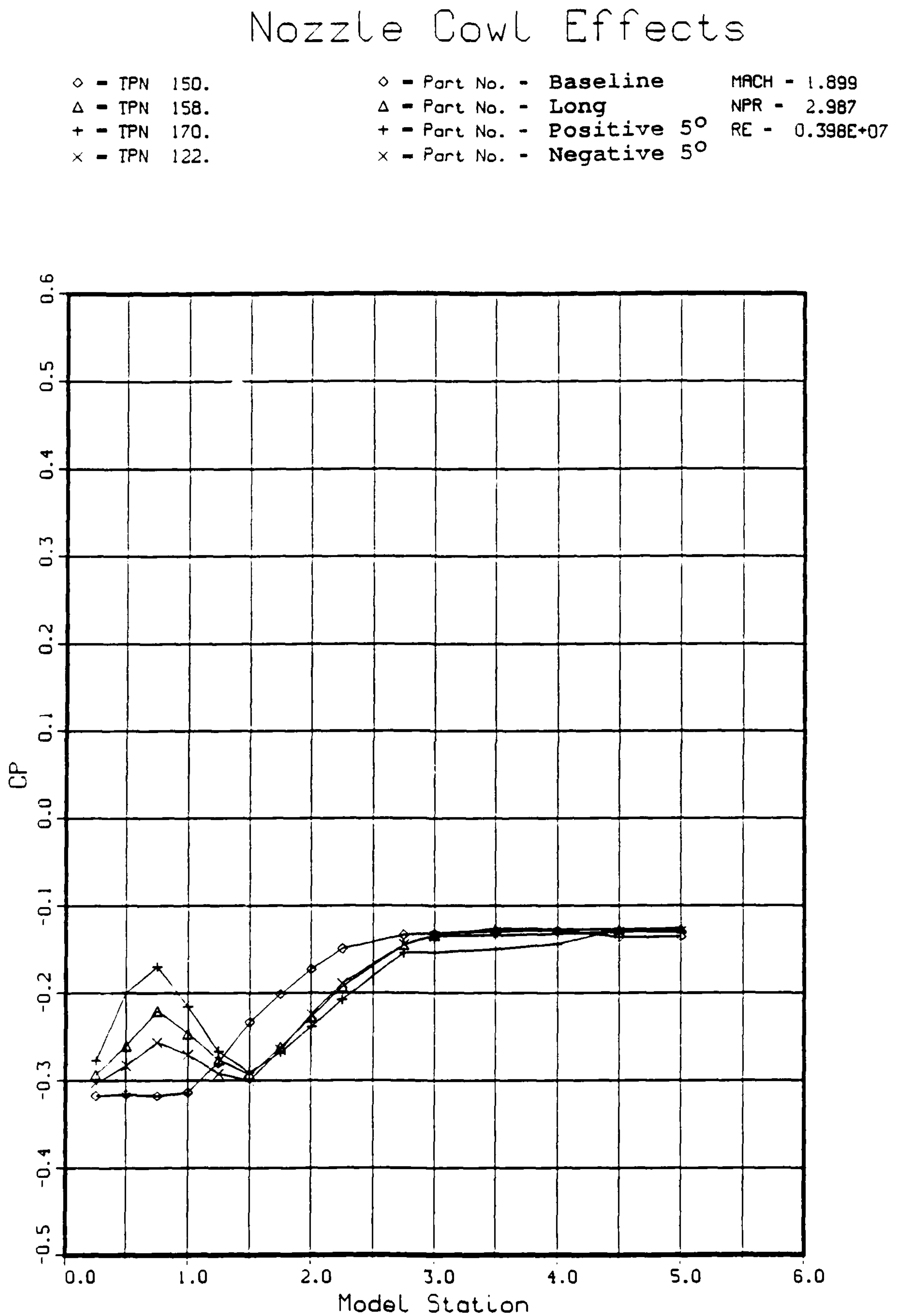

Figure G11. Pressure Coefficients, C_p vs Model Station, Nozzle Cowl Effects: Mach 1.9, NPR = 3.0

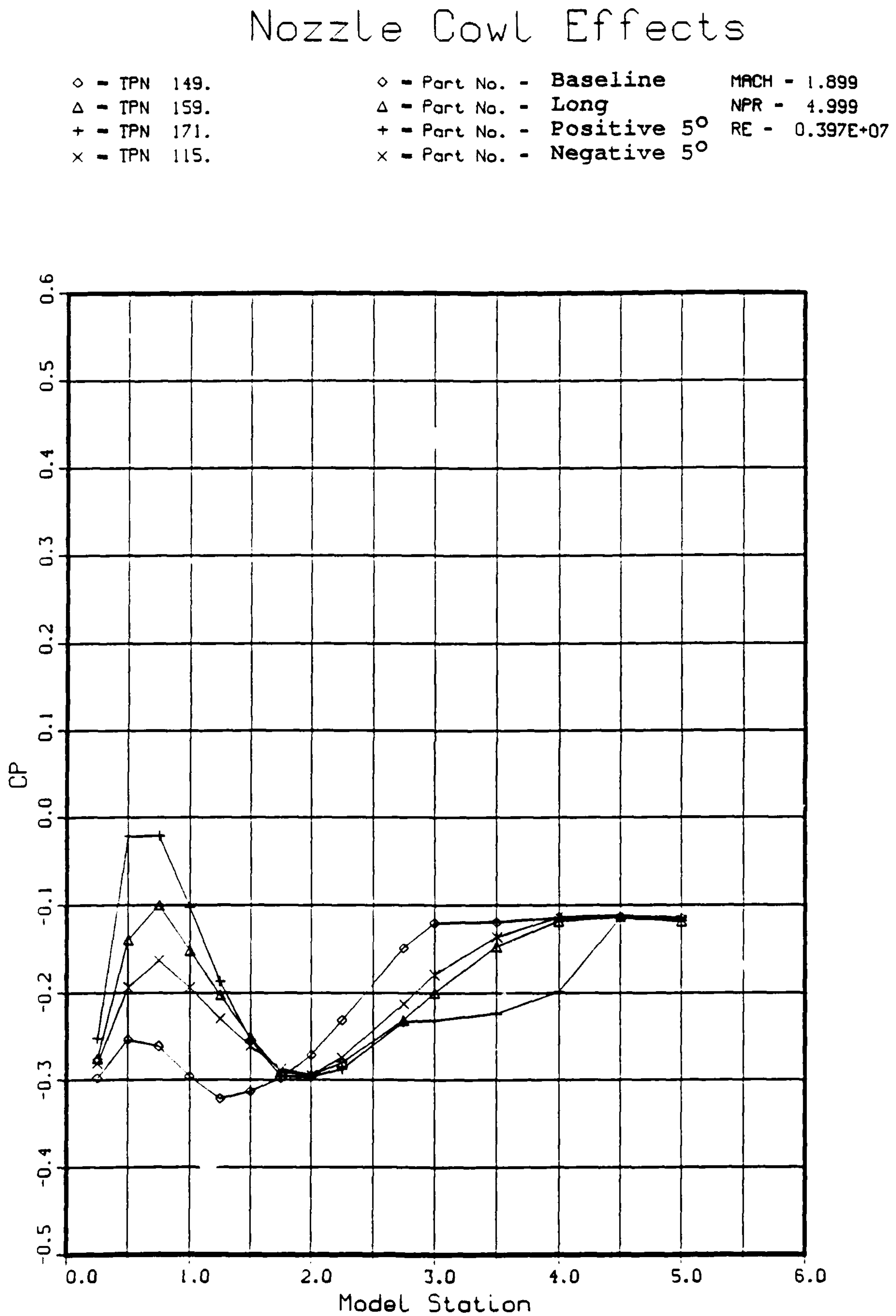

Figure G12. Pressure Coefficients, C_p vs Model Station, Nozzle Cowl Effects: Mach 1.9, NPR = 5.0

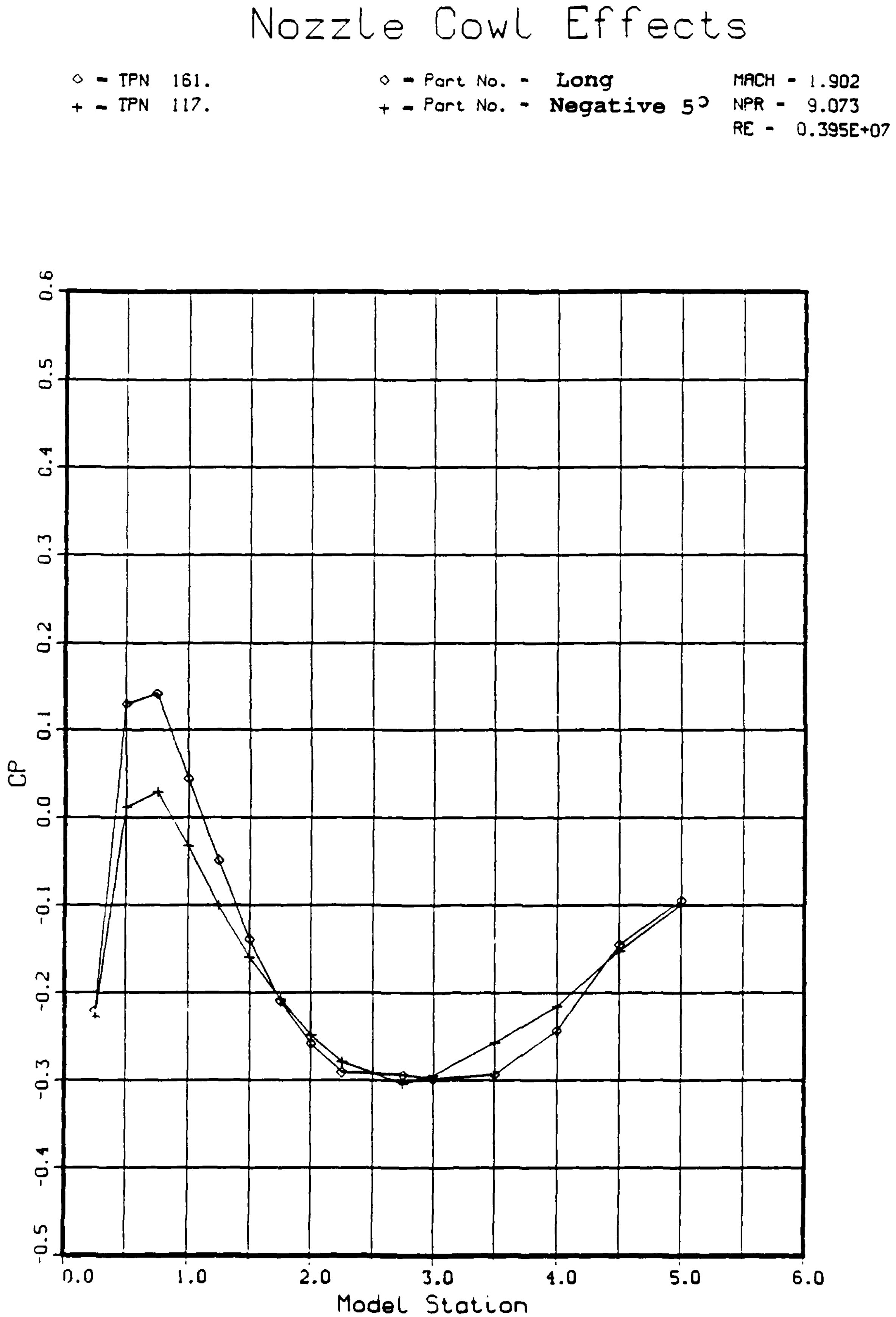

Figure G13. Pressure Coefficients, C_p vs Model Station, Nozzle Cowl Effects: Mach 1.9, NPR = 9.0

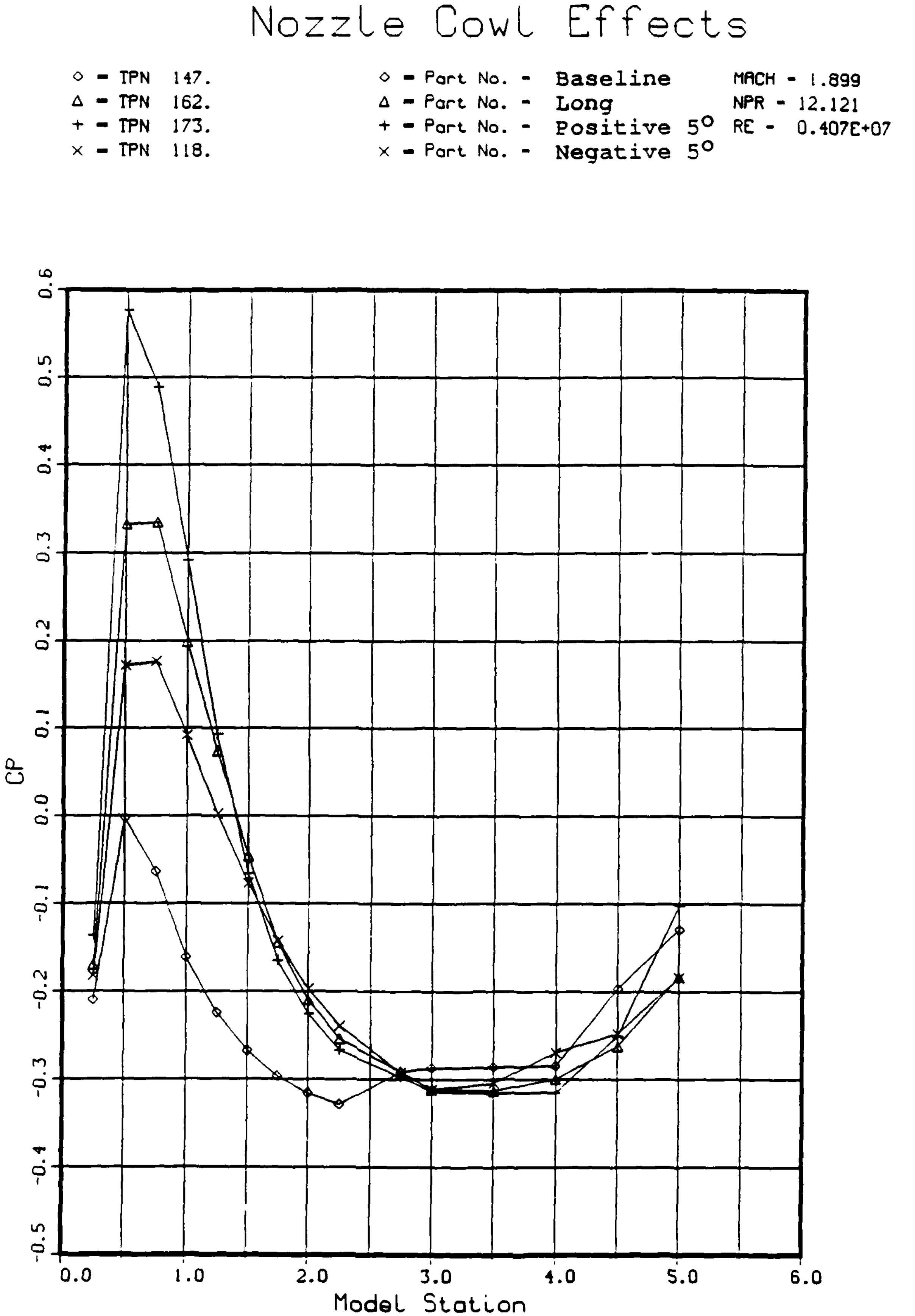

Figure G14. Pressure Coefficients, C_p vs Model Station, Nozzle Cowl Effects: Mach 1.9, NPR = 12.0

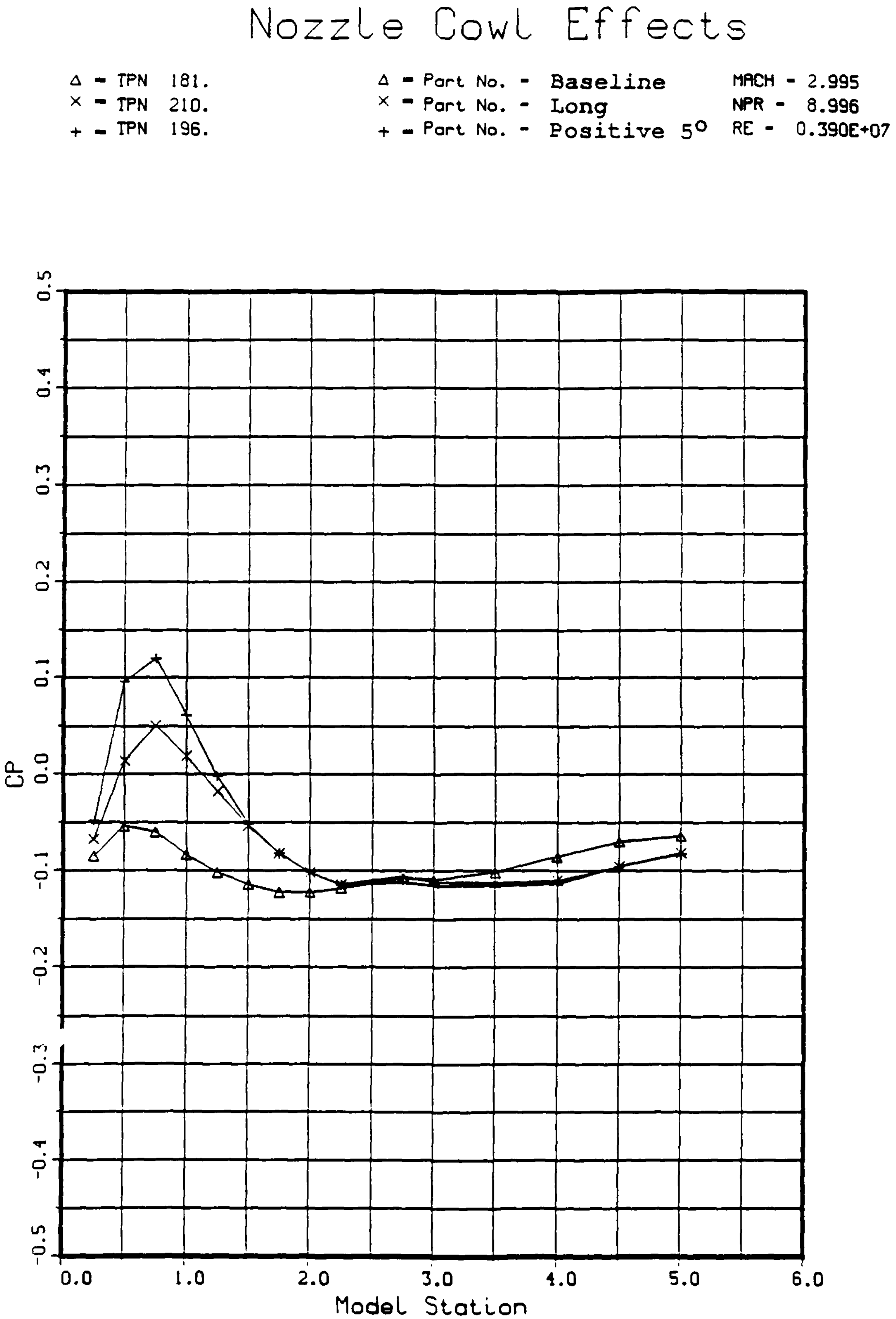

Figure G15. Pressure Coefficients, C_p vs Model Station, Nozzle Cowl Effects: Mach 3.0, NPR = 9.0

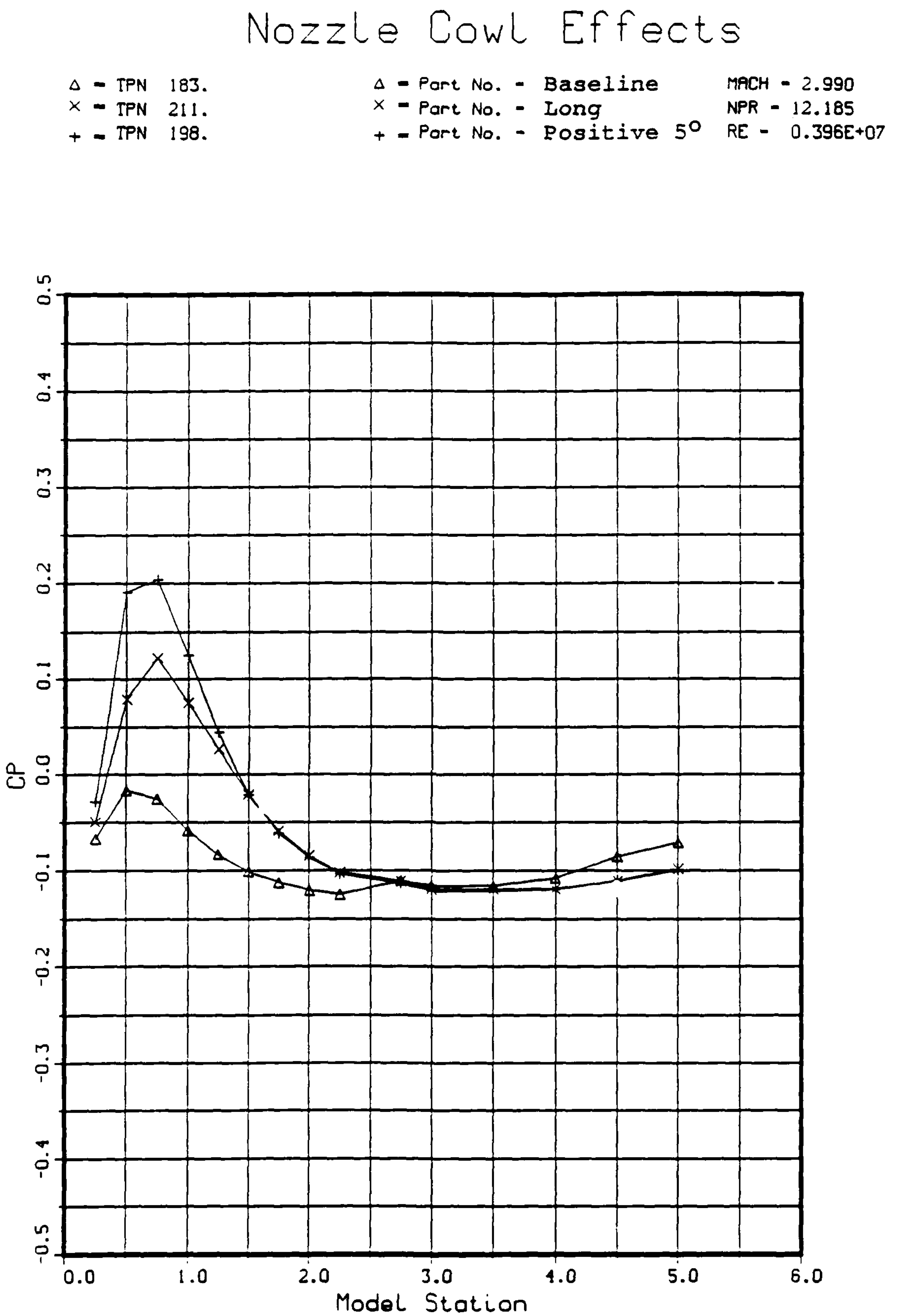

Figure G16. Pressure Coefficients, C_p vs Model Station, Nozzle Cowl Effects: Mach 3.0, NPR = 12.0

Appendix H: Pressure Coefficients, C_p vs Model Station: NPR Effects

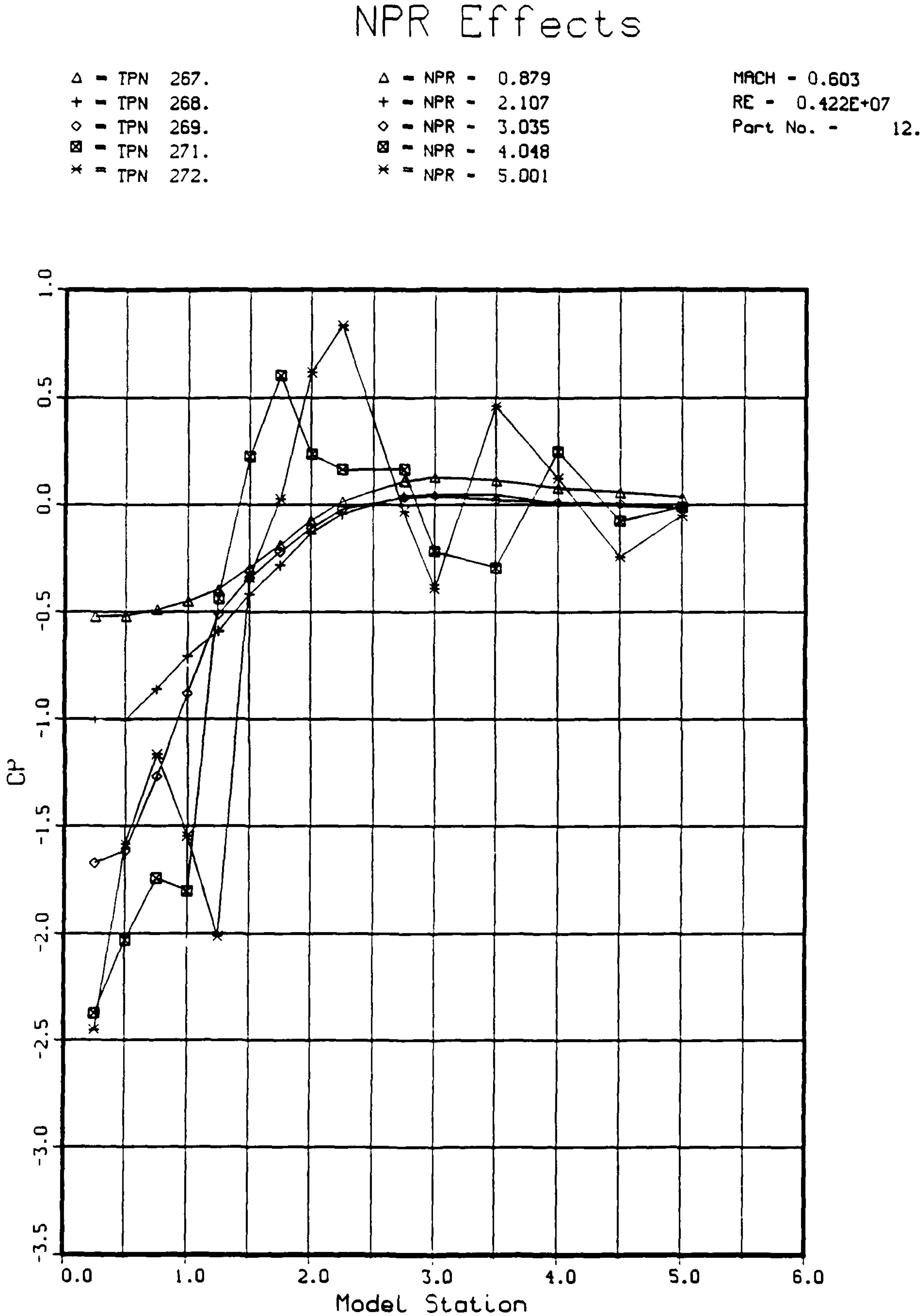

Figure H1. Pressure Coefficients, C_p vs Model Station, NPR Effects: Mach 0.6, L Cowl

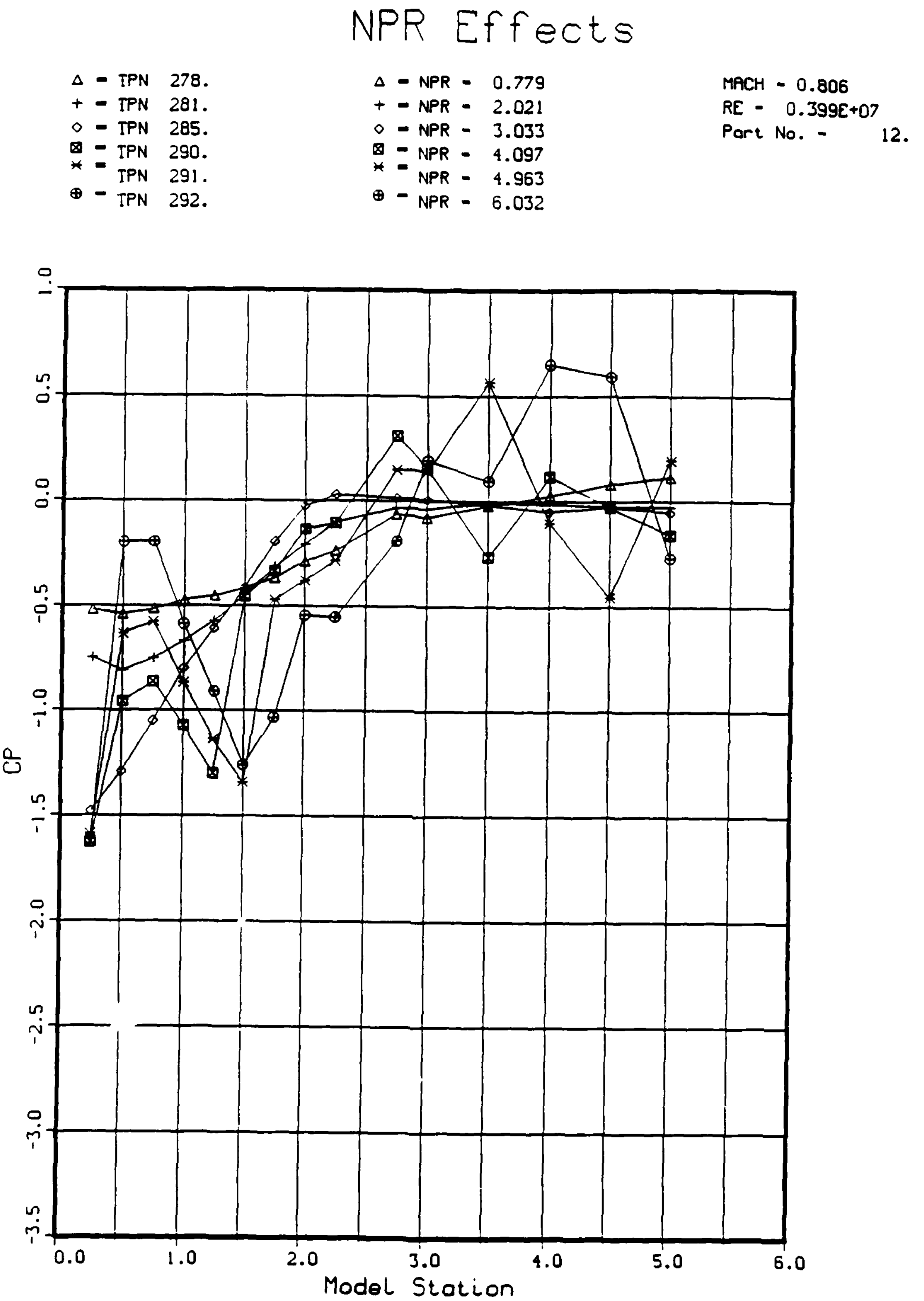

Figure H2. Pressure Coefficients, C_p vs Model Station, NPR Effects: Mach 0.8, L Cowl

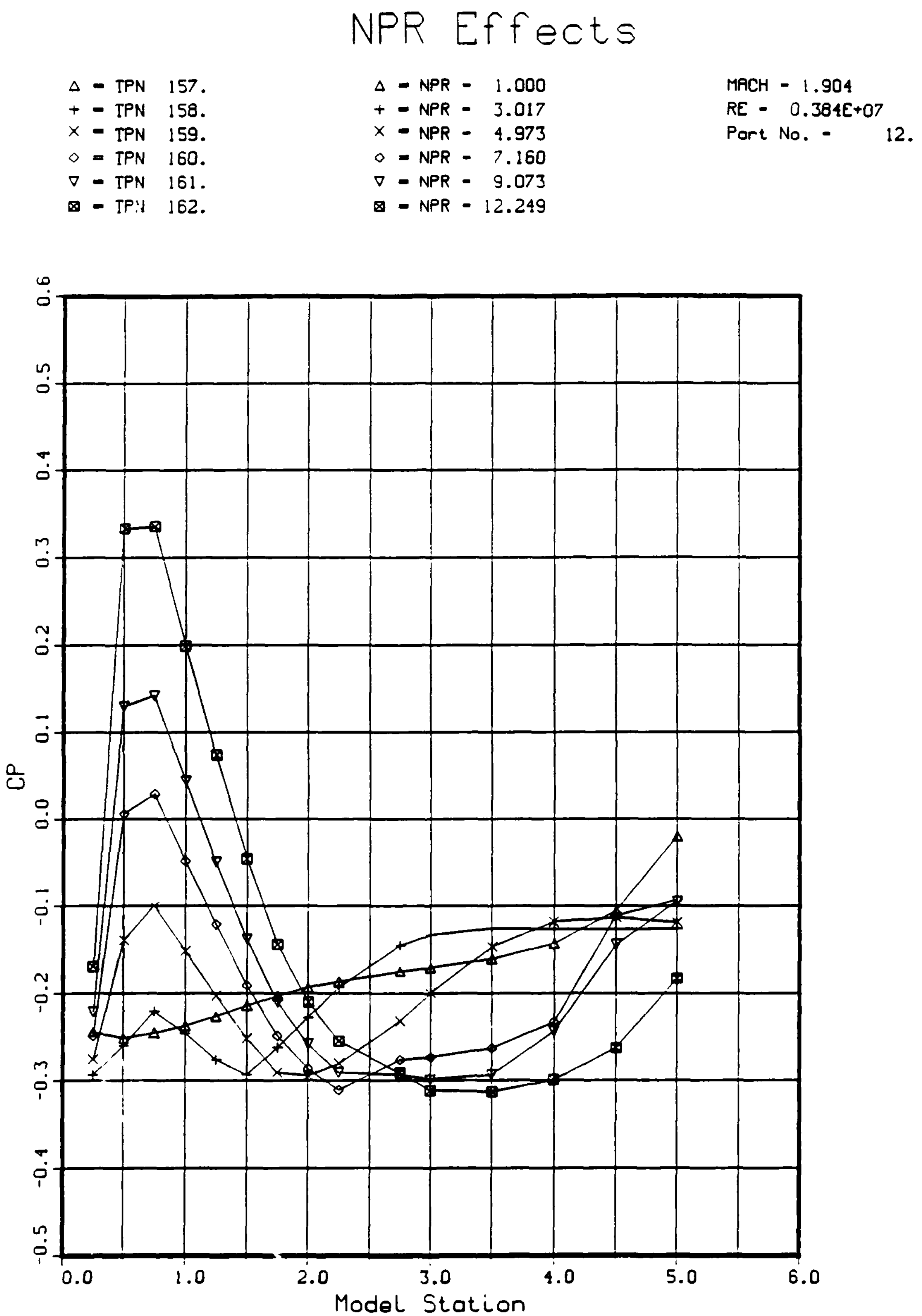

Figure H3. Pressure Coefficients, C_p vs Model Station, NPR Effects: Mach 1.9, L Cowl

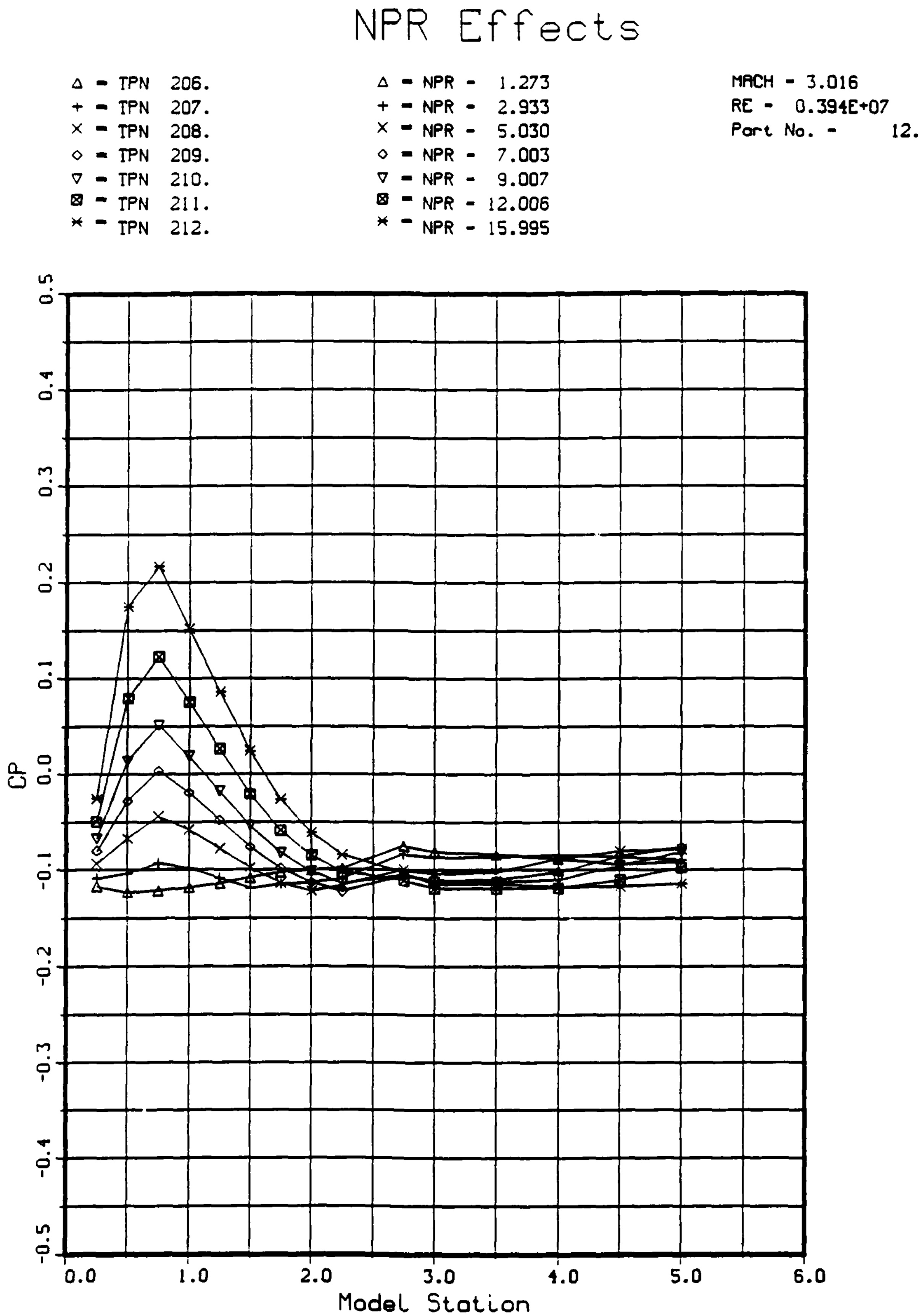

Figure H4. Pressure Coefficients, C_p vs Model Station, NPR Effects: Mach 3.0, L Cowl

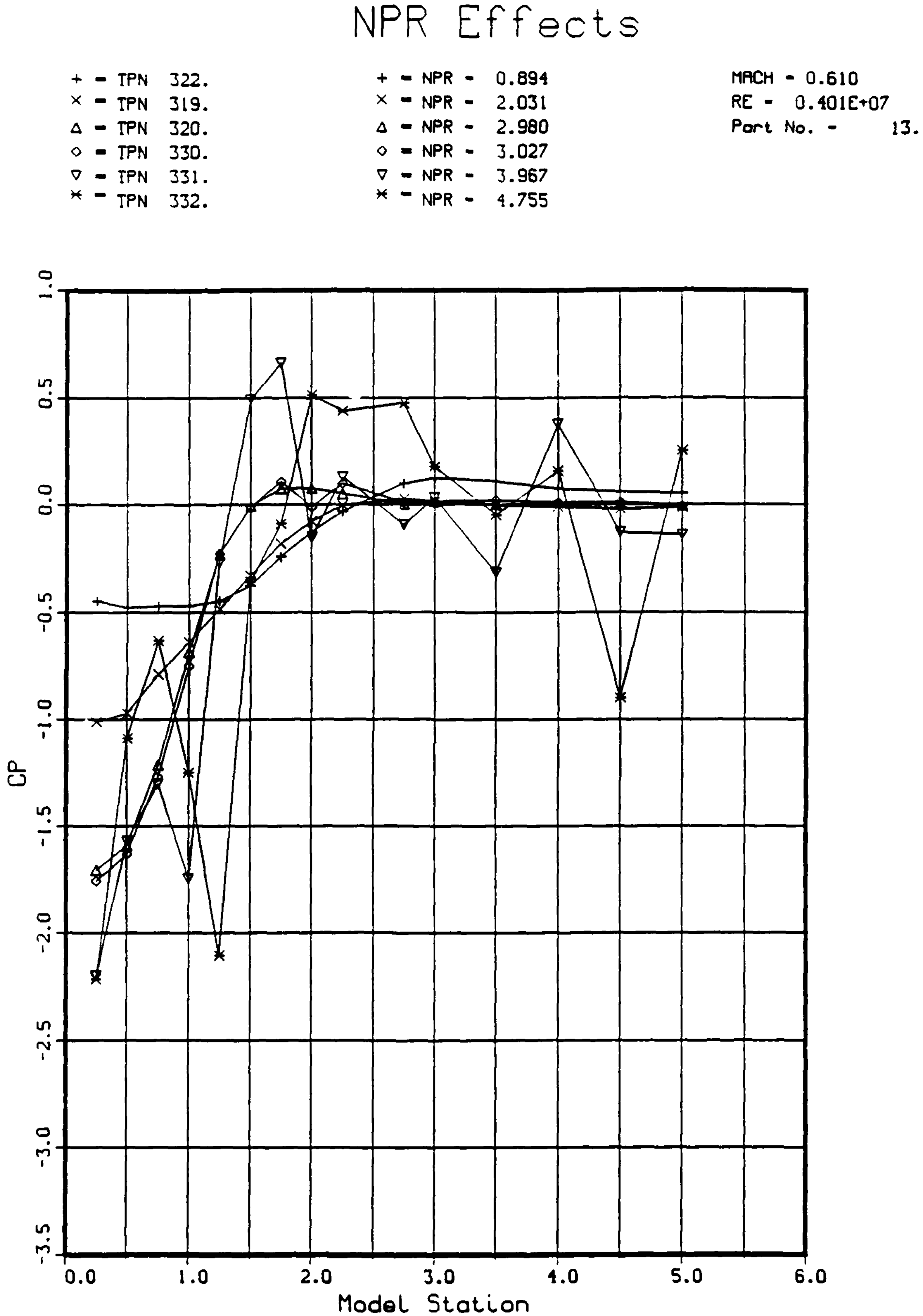

Figure H5. Pressure Coefficients, C_p vs Model Station, NPR Effects: Mach 0.6, +5 Cowl

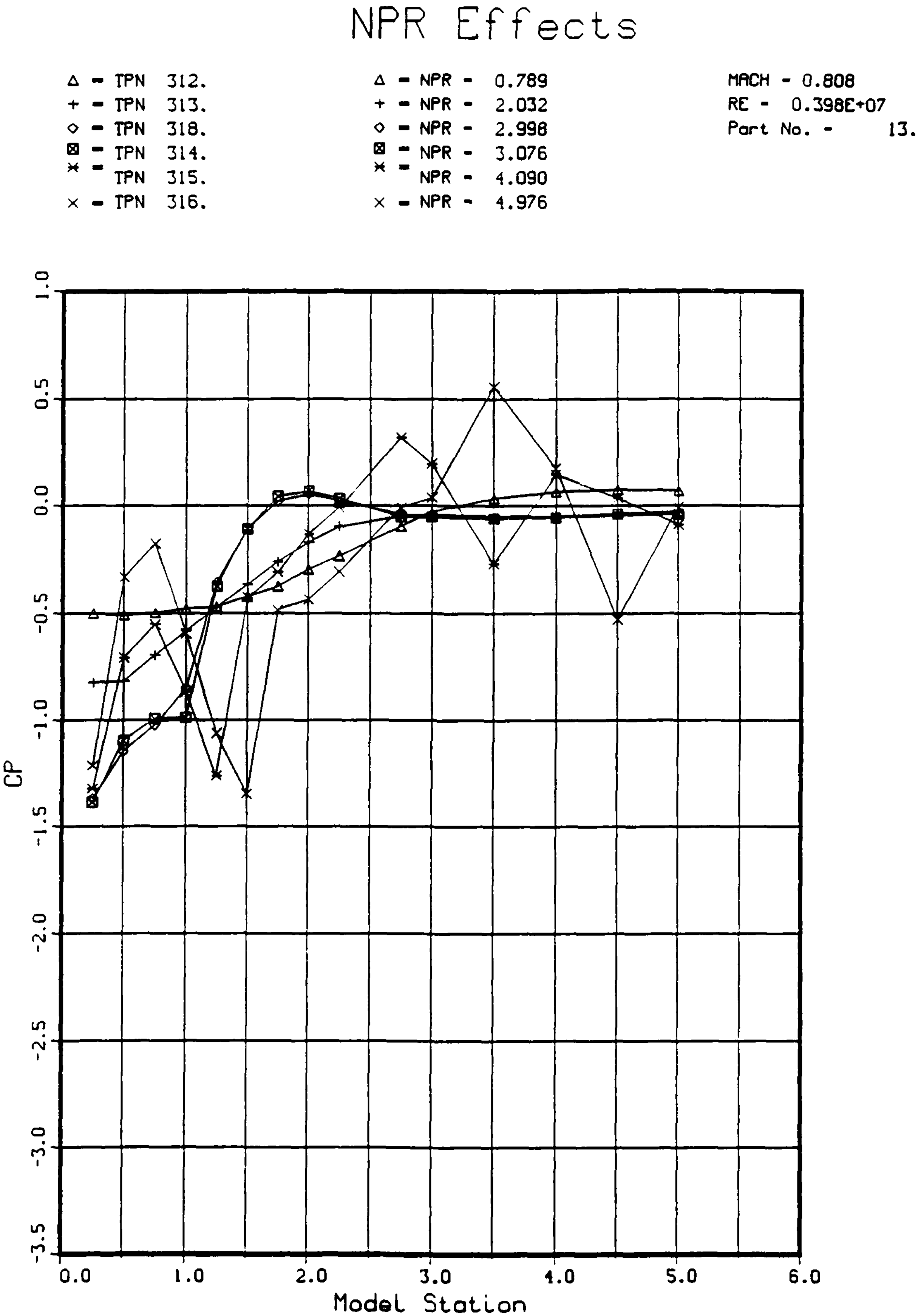

Figure H6. Pressure Coefficients, C_p vs Model Station, NPR Effects: Mach 0.8, +5 Cowl

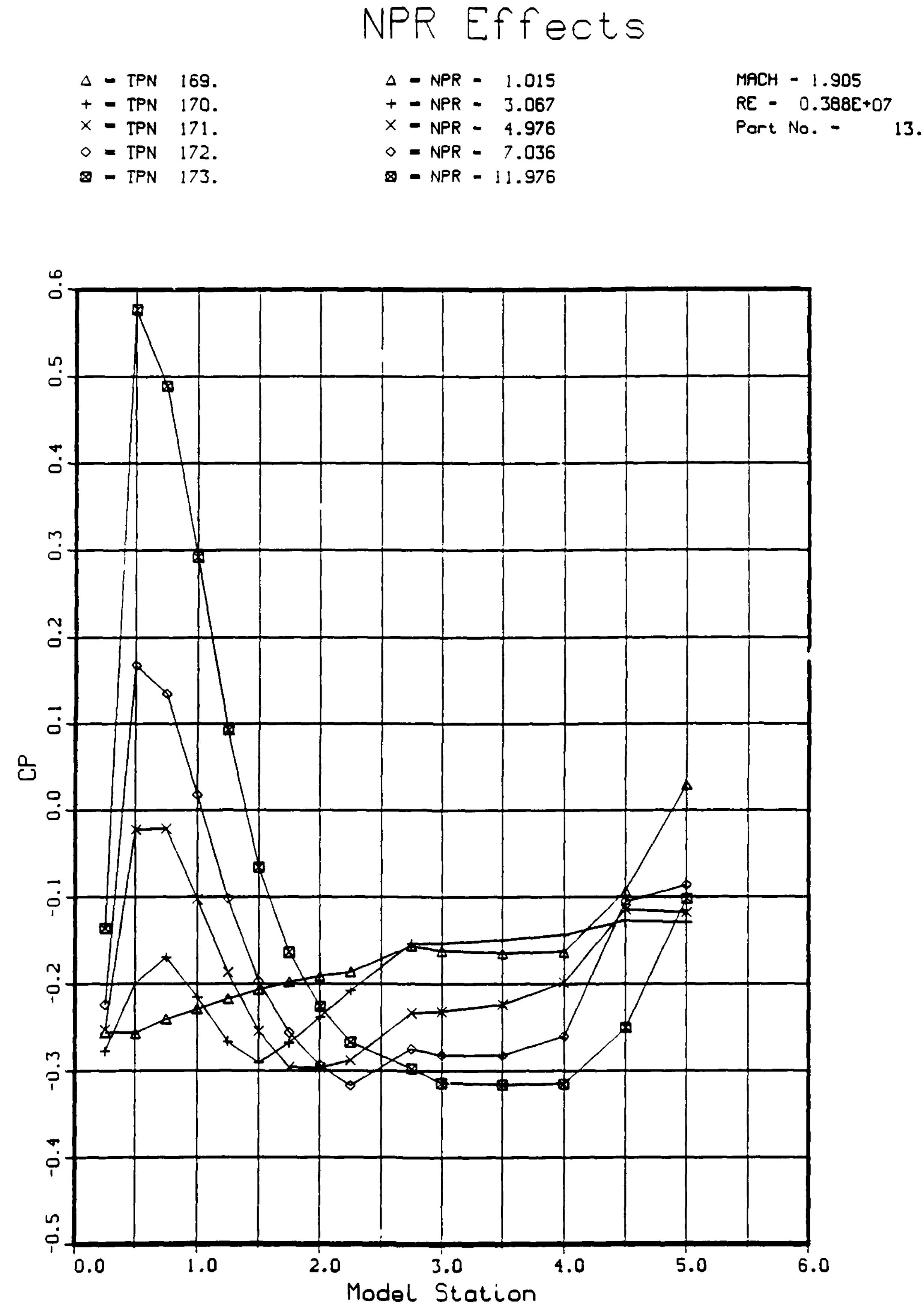

Figure H7. Pressure Coefficients, C_p vs Model Station, NPR Effects: Mach 1.9, +5 Cowl

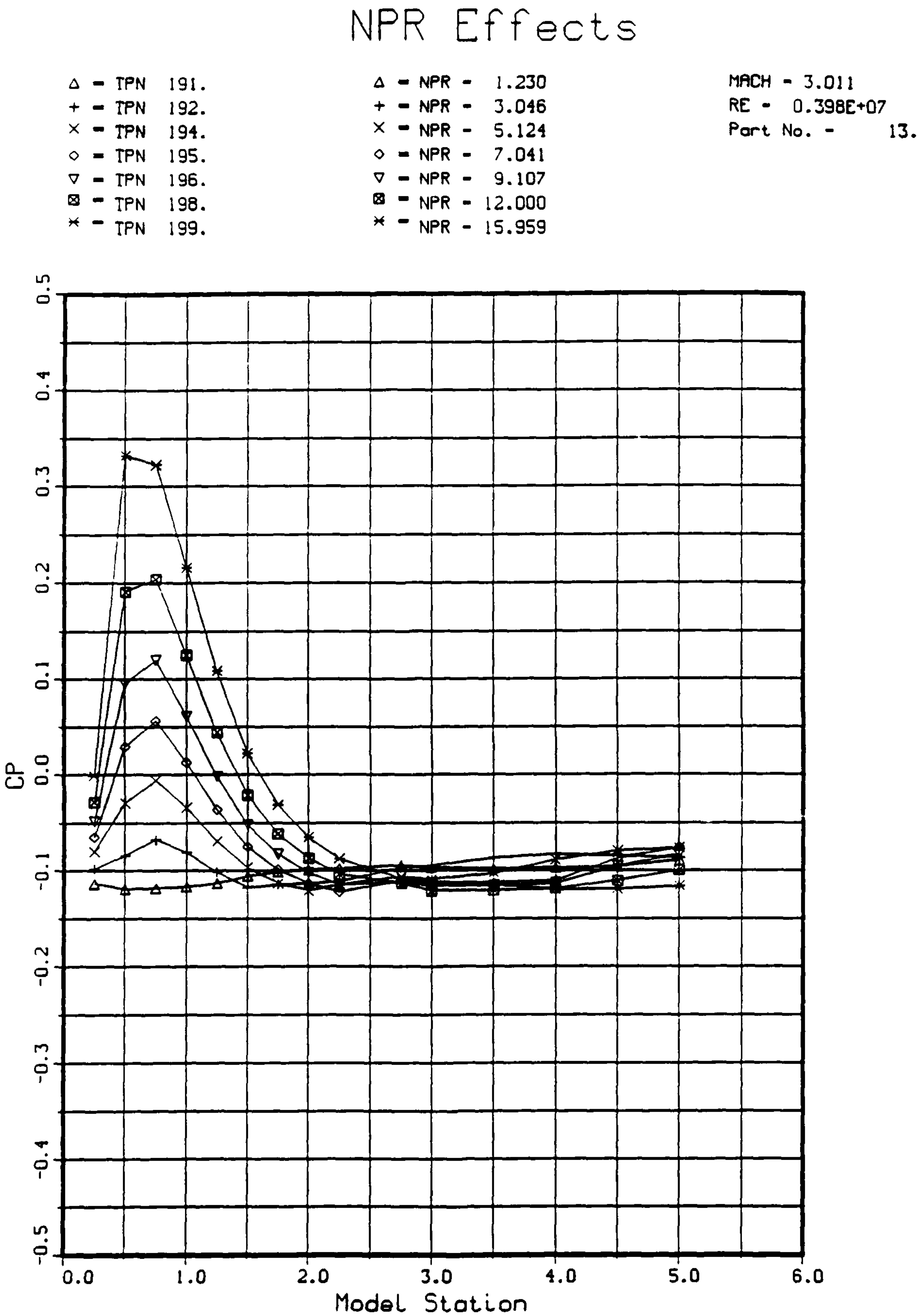

Figure H8. Pressure Coefficients, C_p vs Model Station, NPR Effects: Mach 3.0, +5 Cowl

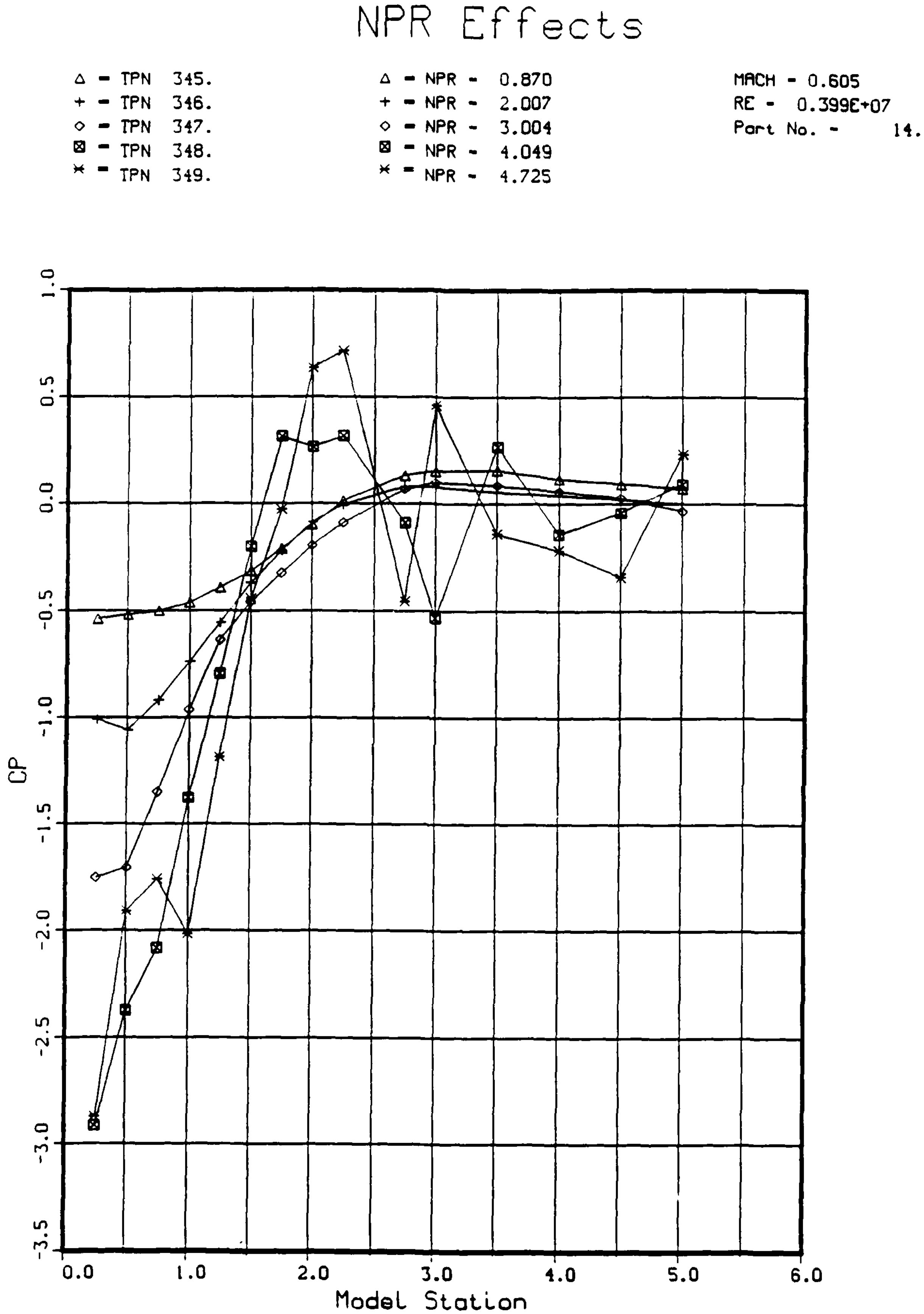

Figure H9. Pressure Coefficients, C_p vs Model Station, NPR Effects: Mach 0.6, -5 Cowl

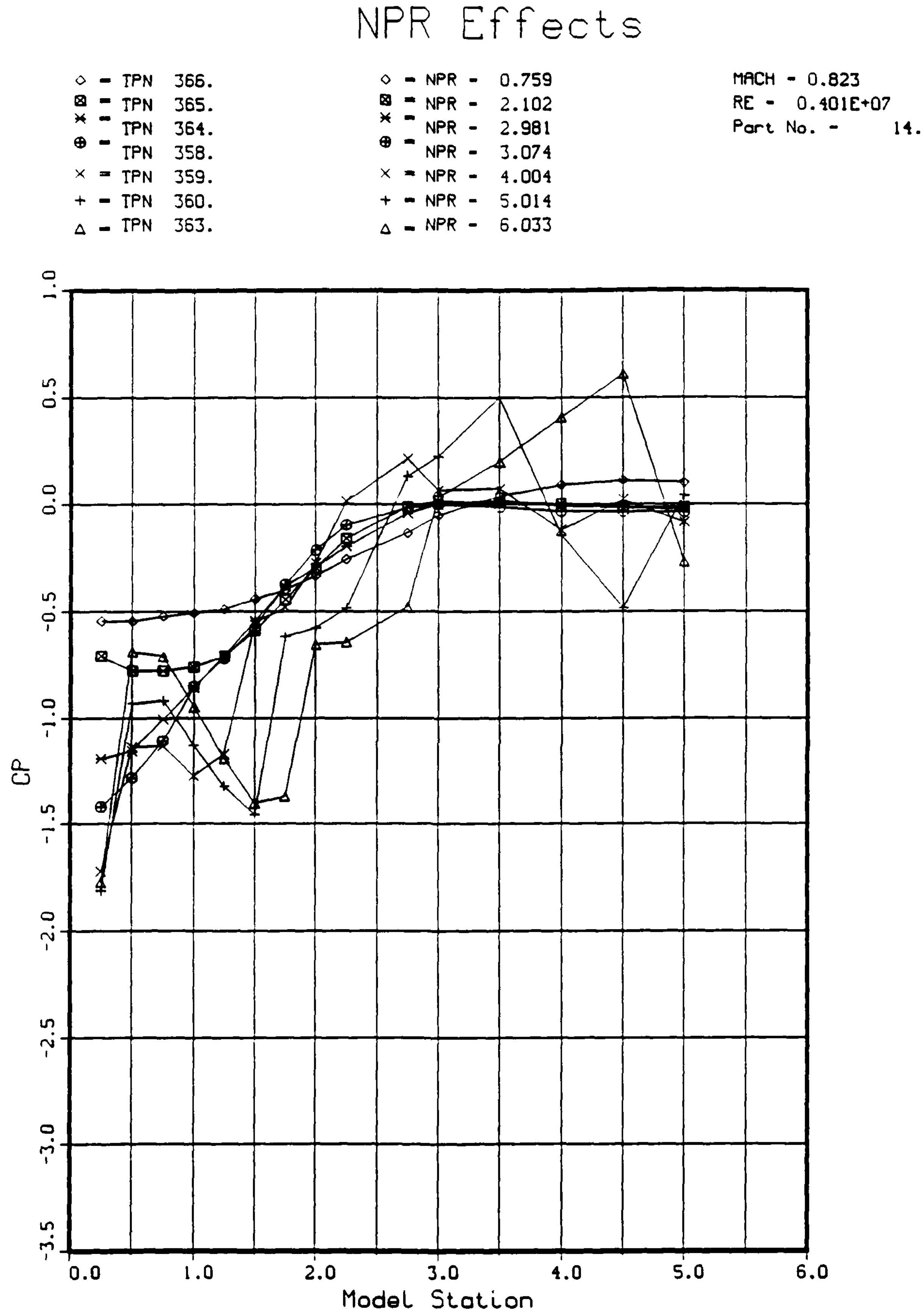

Figure H10. Pressure Coefficients, C_p vs Model Station, NPR Effects: Mach 0.8, -5 Cowl

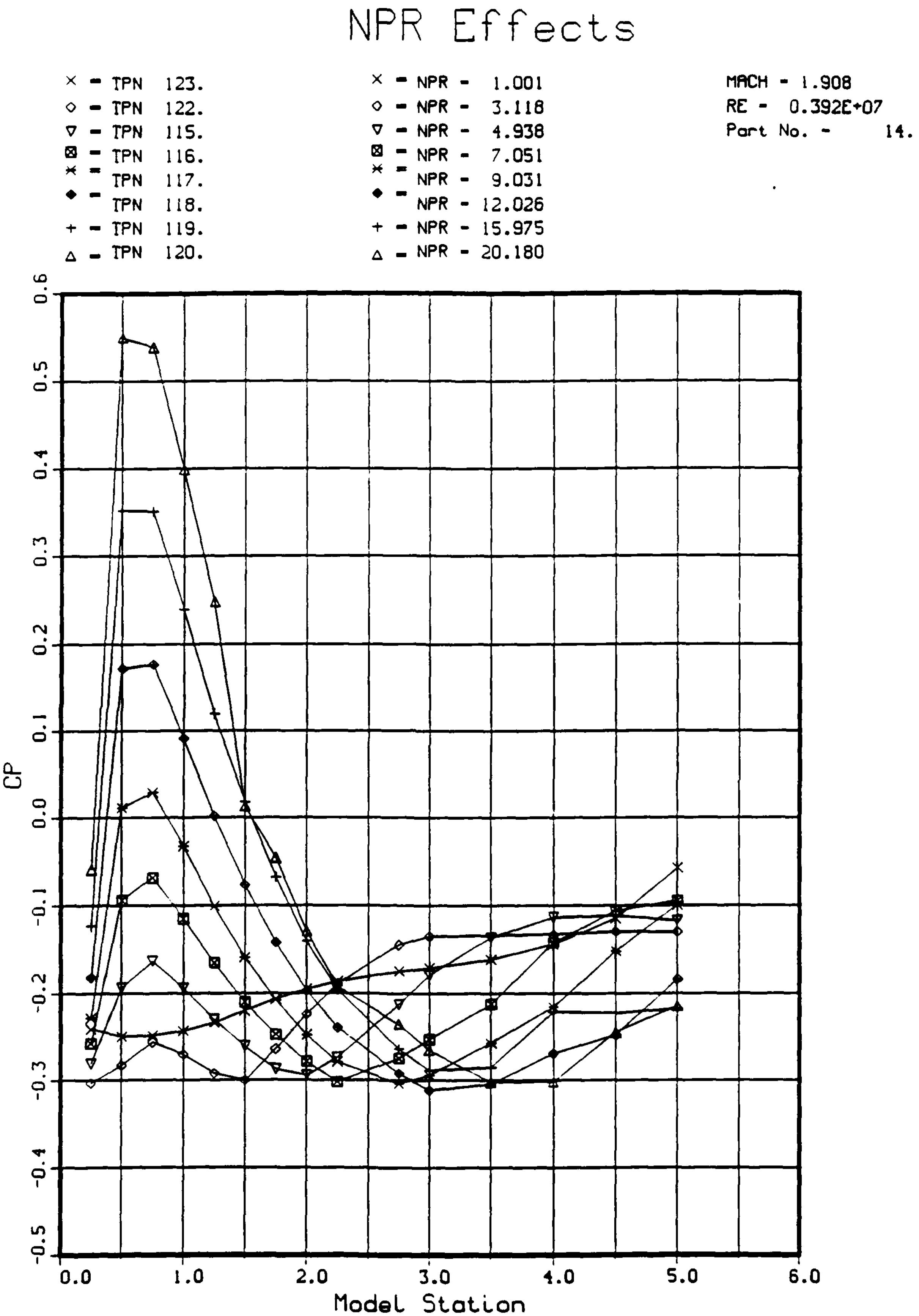

Figure H11. Pressure Coefficients, C_p vs Model Station, NPR Effects: Mach 1.9, -5 Cowl

Vita

Robert Bruce Cochran [redacted] He attended the University of Illinois and received his Bachelor of Science degree in Aeronautical and Astronautical Engineering in 1982. After graduation, he began employment at the Aeronautical Systems Division, USAF, Wright-Patterson AFB as internal aerodynamicist for the Aerodynamics and Performance Branch of the Directorate of Flight Systems Engineering. In January of 1988 he was given the opportunity to enroll in the Graduate Aeronautical Engineering program at the Air Force Institute of Technology.

[redacted]